Department of Physics and Astronomy

A thesis submitted as part of the requirements
for the degree of Master of Science in Astronomy

Ancient Dreams: A Spectroscopic Study of Variable Stars in Binary Systems

---

Author:
Sanjay Sekaran

Senior Supervisor:
Assoc. Prof. Karen Pollard

Associate Supervisor:
Professor Mike Reid

February 2016

“You must have chaos in your soul to give birth to a dancing star.”

— Friedrich Nietzsche

ABSTRACT

This thesis presents the results of the orbital and asteroseismological analysis of three variable stars in binary systems: HD 182640, a system with a candidate γ Doradus primary; HD 3112, a system with a bona fide δ Scuti primary; and HD 147787, a system with a candidate γ Doradus primary. Approximately 2500 spectra of all three stars were obtained from the HERCULES spectrograph, attached to the 1-metre telescope at the University of Canterbury Mount John Observatory. The raw spectra were reduced to radial velocity line profiles through cross-correlation with synthetic spectra.

Orbital analysis of HD 182640 characterised it as a long period (1256 d) binary with an eccentric orbit ($e = 0.43$). A total of 18 pulsational frequencies, explaining 42.9% of the variation across the line profiles, were identified. These frequencies were all characterised as high-degree ($\ell > 4$) modes.

Orbital analysis of HD 3112 characterised it as a short period (7 d) binary with an effectively-circular orbit ($e = 0.01$). A total of 17 pulsational frequencies, explaining 46.3% of the variation across the line profiles, were identified. The mode of the primary pulsation frequency ($f_1 = 20.2802$ d^{-1}) was the only one that was able to be identified. Previously identified ellipsoidal variations may have hindered mode identification efforts.

Orbital analysis of HD 147787 characterised it as a moderate period (40 d) binary with an eccentric orbit ($e = 0.25$). A total of 9 pulsational frequencies, explaining 48.1% of the variation across the line profiles, were identified. The modes of 6 out of the 9 pulsational frequencies, all low-degree ($\ell \leq 3$) modes, were able to be identified. The 3 unidentified frequencies are abnormally low for a γ Doradus star. Previously unidentified ellipsoidal variations may have hindered mode identification efforts.

Declaration

I declare that all of the work presented in this Master's thesis is my own, unless otherwise stated.

I would like to acknowledge the contributions of Dr. Duncan Wright, Dr. Emily Brunsden, Dr. Jovan Skuljian and Mr. Aaron Greenwood in writing and enhancing the MATLAB scripts used in the data reduction process. I would also like to acknowledge Dr. Christoph Bergmann for his help in creating the binary analysis methodology and for providing the radial velocity and orbital fitting codes. All other scientific software used in this analysis has been acknowledged and cited in the appropriate sections of this thesis.

I would also like to express my heartfelt gratitude to my senior supervisor, Associate Professor Karen Pollard, for all of her guidance and advice, and for proofreading this thesis.

Sanjay Sekaran
February 2016

TO AMMA AND APPA,
THE BRIGHTEST BINARY STAR IN MY LIFE.

CONTENTS

LIST OF FIGURES iv

LIST OF TABLES viii

GLOSSARY xi

1 INTRODUCTION 1

1.1 Ancient Dreams of the Universe . . . 1
1.2 Asteroseismology . . . 1
1.3 Stellar Pulsations . . . 3
1.3.1 Driving Mechanisms . . . 3
1.3.2 Radial Pulsations . . . 5
1.3.3 Non-Radial Pulsations . . . 5
1.3.4 Selection Mechanisms of Pulsation Modes and Frequencies . . . 7
1.3.5 Non-Radial Pulsational Geometry . . . 7
1.3.6 Rotational Effects on Pulsations . . . 9
1.3.7 Pulsational Effects on Spectroscopic Data . . . 12
1.4 Variable Star Classes . . . 13
1.4.1 γ Doradus Variable Stars . . . 13
1.4.2 δ Scuti Variable Stars . . . 17
1.5 Binary Stars . . . 19
1.5.1 Binary Orbits . . . 20
1.5.2 Spectroscopic Binaries . . . 23
1.6 Thesis format and goals . . . 26

2 DATA COLLECTION AND ANALYSIS 27

2.1 Observational Data . . . 27
2.1.1 University of Canterbury Mount John Observatory (UC MJO) . . . 27
2.1.2 Observational Timeframe and Target Selection . . . 28
2.1.3 Observational Methodology . . . 29
2.2 Spectroscopic Data Reduction . . . 30
2.2.1 Data Reduction Setup . . . 30

2.2.2 First Data Reduction Pipeline . . . 30
2.2.3 Second Data Reduction Pipeline . . . 32
2.3 Binary Analysis . . . 36
2.3.1 Orbital Analysis . . . 37
2.3.2 Line Profile Correction . . . 40
2.4 Spectroscopic Variability Analysis . . . 41
2.4.1 Frequency Identification . . . 41
2.4.2 Mode Identification . . . 51

3 HD 182640 **57**
3.1 Observations . . . 59
3.2 Binary Analysis . . . 59
3.3 Orbital Analysis . . . 62
3.4 Frequency Identification . . . 63
3.5 Mode Identification . . . 68
3.6 Discussion . . . 75

4 HD 3112 **77**
4.1 Observations . . . 80
4.2 Orbital Analysis . . . 81
4.3 Frequency Identification . . . 83
4.3.1 The 13 d^{-1} to 25 d^{-1} Frequency Range . . . 83
4.3.2 The 0 d^{-1} to 3 d^{-1} Frequency Range . . . 85
4.3.3 Final Frequency Identification . . . 88
4.4 Mode Identification . . . 90
4.5 Discussion . . . 97

5 HD 147787 **101**
5.1 Observations . . . 103
5.2 Orbital Analysis . . . 104
5.3 Frequency Identification . . . 105
5.4 Mode Identification . . . 110
5.5 Discussion . . . 114

6 Conclusion and Future Research **117**
6.1 Conclusion . . . 117
6.2 Future Research . . . 119

Acknowledgements **121**

A Raw FITS Spectrum Examples 123

B Additional Plots and Tables for HD 182640 127

C Additional Plots and Tables for HD 3112 139

D Additional Plots and Tables for HD 147787 159

References 191

List of Figures

1.1 Classes of variable stars on a Hertzsprung-Russell diagram. 4
1.2 Propagation of p-mode and g-mode waves within a sun-like star. 6
1.3 Radial and Non-radial Pulsation Modes. 10
1.4 $\ell = 20$ Pulsation Modes. 11
1.5 Line Profile Variations due to Pulsations. 14
1.6 Theoretical γ Doradus instability strips for stars pulsating with $\ell = 1$ modes. . . . 16
1.7 Theoretical δ Scuti instability strips for stars pulsating with $\ell = 2$ modes. 16
1.8 Schematic diagram of an elliptical orbit. 21
1.9 Eccentric and true anomalies on a diagram of a two-dimensional elliptical orbit. 22
1.10 Radial velocity curves of orbits with different e and ω. 24
1.11 Doppler Shift of Spectral Lines in an SB2 Spectrum. 25

2.1 Barycentric correction values for HD 182640, HD 3112 and HD 147787. 32
2.2 The continuum-fitting process for spectral order 99 of HD 3112. 34
2.3 The mean stellar spectrum of HD 182640. 35
2.4 The mean stellar spectrum of HD 147787 with its corresponding δ-function template. 35
2.5 The cross-correlated line profiles of HD 147787. 37
2.6 The Gaussian-fitting process for HD 3112. 38
2.7 The component orbital fits to the radial velocities of HD 147787. 39
2.8 The line profiles HD 147787 A. 41
2.9 The iterative prewhitening process in FAMIAS using the pixel-by-pixel method. 45
2.10 The iterative prewhitening process in FAMIAS using the second moment of the moment method. 46
2.11 The spectral significance values of the frequencies of HD 3112 identified by SigSpec. 48
2.12 The amplitude and phase profiles of $f_1 = 20.2802$ d^{-1} of HD 3112. 50
2.13 The zero-point fit of HD 182640. 54
2.14 The amplitude and phase profiles of the best-fit mode (1,0) of $f_7 = 0.78074$ d^{-1} of HD 147787. 55

3.1 The cross-correlated line profiles of HD 182640. 58
3.2 The partial Gaussian-fitting processes of HD 182640 B. 60
3.3 The Gaussian-fitting process of HD 182640 A. 60
3.4 The cross-correlated line profiles of HD 182640 A. 62
3.5 The component orbital fits to the radial velocities of HD 182640. 63
3.6 The 0 d^{-1} to 80 d^{-1} frequency range pixel-by-pixel mean Lomb-Scargle periodogram of HD 182640. 64
3.7 The 0 d^{-1} to 10 d^{-1} frequency range spectral window of HD 182640. 64
3.8 The spectral significance values of the frequencies of HD 182640 identified by SIGSPEC. 65
3.9 Zero-point fit of HD 182640. 69
3.10 The amplitude and phase profiles of the best-fit modes of f_1 to f_6 of HD 182640. 72
3.11 The amplitude and phase profiles of the best-fit modes of f_7 to f_{12} of HD 182640. 73
3.12 The amplitude and phase profiles of the best-fit modes of f_{13} to f_{18} of HD 182640. 74

4.1 The cross-correlated line profiles of HD 3112. 79
4.2 The cross-correlated line profiles of HD 3112 A. 80
4.3 The component orbital fits to the radial velocities of HD 3112. 82
4.4 The 0 to 80 d^{-1} frequency range pixel-by-pixel mean Lomb-Scargle periodogram of HD 3112. 83
4.5 The spectral significance values of the frequencies of HD 3112 identified by SIGSPEC. 84
4.6 The 13 to 25 d^{-1} frequency range spectral window of HD 3112. 84
4.7 The 0 d^{-1} to 3 d^{-1} frequency range spectral window of HD 3112. 85
4.8 Zero-point fit of HD 3112. 91
4.9 The v sin i values of the models fit to the zero-point line profile of HD 3112. . . . 92
4.10 The amplitude and phase profiles of the best-fit mode (1,1) of $f_1 = 20.28$ d^{-1} of HD 3112. 93
4.11 The amplitude and phase profiles f_1 to f_6 of HD 3112. 94
4.12 The amplitude and phase profiles of f_7 to f_{12} of HD 3112. 95
4.13 The amplitude and phase profiles of f_{13} to f_{17} of HD 3112. 96

5.1 The cross-correlated line profiles of HD 3112. 102
5.2 The cross-correlated line profiles of HD 147787 A. 103
5.3 The component orbital fits to the radial velocities of HD 147787. 105
5.4 The 0 to 80 d^{-1} frequency range pixel-by-pixel mean Lomb-Scargle periodogram of HD 147787. 106

5.5 The spectral significance values of the frequencies of HD 147787 identified by SIGSPEC. . . . 106
5.6 The 0 to 6 d^{-1} frequency range spectral window of HD 147787. . . . 107
5.7 Zero-point fit of HD 147787. . . . 111
5.8 The v sin i values of the models fit to the zero-point line profile of HD 147787. . . 112
5.9 The amplitude and phase profiles the best-fit modes of f_1 to f_3, and f_4 to f_7 of HD 147787. . . . 113

A.1 Flat-field spectrum example. . . . 124
A.2 Thorium-Argon spectrum example. . . . 125
A.3 Stellar spectrum example. . . . 126

B.1 The first batch of five pixel-by-pixel mean Lomb-Scargle periodograms of HD 182640. . . . 128
B.2 The second batch of five pixel-by-pixel mean Lomb-Scargle periodograms of HD 182640. . . . 129
B.3 The third batch of five pixel-by-pixel mean Lomb-Scargle periodograms of HD 182640. . . . 130
B.4 The fourth batch of three pixel-by-pixel mean Lomb-Scargle periodograms of HD 182640. . . . 131
B.5 The zeroth-moment Lomb-Scargle periodograms of HD 182640. . . . 132
B.6 The first-moment Lomb-Scargle periodograms of HD 182640. . . . 133
B.7 The second-moment Lomb-Scargle periodograms of HD 182640. . . . 134
B.8 The third-moment Lomb-Scargle periodograms of HD 182640. . . . 135
B.9 Reduction in the standard deviation across the line profiles of HD 182640. . . . 137

C.1 The first batch of five pixel-by-pixel mean Lomb-Scargle periodograms of HD 3112 (13 d^{-1} to 25 d^{-1}). . . . 140
C.2 The second batch of five pixel-by-pixel mean Lomb-Scargle periodograms of HD 3112 (13 d^{-1} to 25 d^{-1}). . . . 141
C.3 The third batch of four pixel-by-pixel mean Lomb-Scargle periodograms of HD 3112 (13 d^{-1} to 25 d^{-1}). . . . 142
C.4 The zeroth-moment Lomb-Scargle periodograms of HD 3112 (13 d^{-1} to 25 d^{-1}). 143
C.5 The first batch of five first-moment Lomb-Scargle periodograms of HD 3112 (13 d^{-1} to 25 d^{-1}). . . . 144
C.6 The second batch of three first-moment Lomb-Scargle periodograms of HD 3112 (13 d^{-1} to 25 d^{-1}). . . . 145
C.7 The first batch of five second-moment Lomb-Scargle periodograms of HD 3112 (13 d^{-1} to 25 d^{-1}). . . . 146

C.8 The second batch of five second-moment Lomb-Scargle periodograms of HD 3112 (13 d^{-1} to 25 d^{-1}). 147
C.9 The first batch of five third-moment Lomb-Scargle periodograms of HD 3112 (13 d^{-1} to 25 d^{-1}). 148
C.10 The second batch of four third-moment Lomb-Scargle periodograms of HD 3112 (13 d^{-1} to 25 d^{-1}). 149
C.11 The pixel-by-pixel mean Lomb-Scargle periodograms of HD 3112 (0 d^{-1} to 3 d^{-1}).150
C.12 The first batch of five zeroth-moment Lomb-Scargle periodograms of HD 3112 (0 d^{-1} to 3 d^{-1}). 151
C.13 The second batch of five zeroth-moment Lomb-Scargle periodograms of HD 3112 (0 d^{-1} to 3 d^{-1}). 152
C.14 The first-moment Lomb-Scargle periodograms of HD 3112 (0 d^{-1} to 3 d^{-1}). 153
C.15 The second-moment Lomb-Scargle periodograms of HD 3112 (0 d^{-1} to 3 d^{-1}). . 154
C.16 The third-moment Lomb-Scargle periodograms of HD 3112 (0 d^{-1} to 3 d^{-1}). . . . 155
C.17 Reduction in the standard deviation across the line profiles of HD 3112. 157
C.18 The amplitude and phase profiles of the best-fit mode (2,2) of $f_2 = 18.0661$ d^{-1} of HD 3112. 158

D.1 The first batch of five pixel-by-pixel mean Lomb-Scargle periodograms of HD 147787. 160
D.2 The second batch of five pixel-by-pixel mean Lomb-Scargle periodograms of HD 147787. 161
D.3 The zeroth-moment Lomb-Scargle periodograms of HD 147787. 162
D.4 The first batch of five first-moment Lomb-Scargle periodograms of HD 147787. 163
D.5 The second batch of two first-moment Lomb-Scargle periodograms of HD 147787.164
D.6 The second-moment Lomb-Scargle periodograms of HD 147787. 165
D.7 The first batch of five third-moment Lomb-Scargle periodograms of HD 147787.166
D.8 The second batch of three third-moment Lomb-Scargle periodograms of HD 147787. 167
D.9 Reduction in the standard deviation across the line profiles of HD 147787. 169
D.10 The amplitude and phase profiles of the best-fit mode (2,0) of $f_4 = 0.08$ d^{-1} of HD 147787. 170
D.11 The amplitude and phase profiles of the best-fit mode (2,0) of $f_8 = 0.06$ d^{-1} of HD 147787. 170
D.12 The amplitude and phase profiles of the best-fit mode (2,0) of $f_9 = 0.21$ d^{-1} of HD 147787. 171

List of Tables

2.1 Observational information of the three stars analysed for this thesis. 28

3.1 The fundamental stellar parameters of HD 182640. 58
3.2 The orbital elements of HD 182640. 61
3.3 HD 182640 frequencies found in FAMIAS and SIGSPEC. 67
3.4 The identified pulsational frequencies of HD 182640. 68
3.5 The zero-point fit parameters of HD 182640. 68
3.6 The best-fit modes of each of the 18 analysed frequencies of HD 182640. 71
3.7 The inclination ranges of the best-fitting models of the frequencies of HD 182640. 75

4.1 The fundamental stellar parameters of HD 3112. 79
4.2 The orbital elements of HD 3112. 81
4.3 HD 3112 frequencies found in FAMIAS and SIGSPEC in the 13 d^{-1} to 25 d^{-1} range. 86
4.4 HD 3112 frequencies found in FAMIAS and SIGSPEC in the 0 d^{-1} to 3 d^{-1} range. 89
4.5 The identified pulsational frequencies of HD 3112. 90
4.6 The zero-point fit parameters of HD 3112. 90
4.7 The five best-fitting modes of $f_1 = 20.2802$ d^{-1} of HD 3112. 93
4.8 Comparison of the HD 3112 frequencies in Paparo et al. (1996), De Mey et al. (1998) and this analysis. 97

5.1 The fundamental stellar parameters of HD 147787. 102
5.2 The orbital elements of HD 147787. 104
5.3 HD 147787 frequencies found in FAMIAS and SIGSPEC. 109
5.4 The identified pulsational frequencies of HD 147787. 110
5.5 The zero-point fit parameters of HD 3112. 110
5.6 The best-fit modes of f_1 to f_3, and f_4 to f_7 of HD 147787. 114
5.7 The inclination ranges of the best-fitting models of f_1 to f_3, and f_4 to f_7 of HD 147787. 114

6.1 Summary of frequency and mode identification results of the three stars analysed for this thesis. 117

B.1 The reduction in the standard deviation from successive prewhitening of the pulsation frequencies of HD 182640. 136

C.1 The reduction in the standard deviation from successive prewhitening of the pulsation frequencies of HD 3112. 156

D.1 The reduction in the standard deviation from successive prewhitening of the pulsation frequencies of HD 147787. 168

GLOSSARY

ASCII
: The American Standard Code for Information Interchange is a display scheme for text in computers and other electronic devices. (Referenced on page xi, 40.)

ATLAS9
: Version 9 of the ATLAS code, originally written for the VMS operating system by Dr. Robert Kurucz (Kurucz, 1970). It was ported over to LINUX by Sbordone et al. (2004) and is currently the most widely used code for modeling stellar atmospheres. (Referenced on page xiii.)

COROT
: COnvection ROtation and planetary Transits is a satellite launched by the French Space Agency (CNES) in conjunction with the European Space Agency (ESA) and other governmental agencies. Its objective was to search for extrasolar planets and to detect sun-like oscillations in stars using photometry. It was in operation from 2007 to 2013. (Referenced on page 12, 13, 17.)

FAMIAS
: Frequency And Mode Identification for AsteroSeismology (Zima, 2008a,b) is an analysis program for time-series of photometric and spectroscopic data. It enables the identification of pulsational frequency and modes. (Referenced on page 7, 8, 13, 40, 41, 42, 43, 44, 45, 46, 47, 48, 49, 51, 52, 55, 56, 64, 65, 66, 67, 68, 83, 84, 85, 86, 87, 88, 89, 90, 98, 106, 107, 108, 109, 110, 128, 129, 130, 131, 132, 133, 134, 135, 140, 141, 142, 143, 144, 145, 146, 147, 148, 149, 150, 151, 152, 153, 154, 155, 160, 161, 162, 163, 164, 165, 166, 167.)

FITS
: Flexible Image Transport System (Wells et al., 1981) is a digital file format that has become the de facto standard for astronomical images. Each FITS file contains uncompressed raw image data with an ASCII file header that details all of the relevant information related to the observation. (Referenced on page 29, 30, 123.)

Glossary

Gaia The Gaia satellite, named after the Greek word for Earth, is a space telescope launched by the European Space Agency (ESA) as a successor to the Hipparcos mission. Its objective is to conduct precision photometry, astrometry and spectroscopy of more than 1 billion stars throughout the Milky Way to create a three-dimensional map. It was launched in 2013 and is currently still in operation. (Referenced on page 13, 119.)

HERCULES The High Efficiency and Resolution Canterbury University Large Échelle Spectrograph is the fibre fed échelle spectrograph that is attached to the 1-metre McLellan telescope at UC MJO. (Referenced on page xii, xiii, 27, 33, 101, 123.)

Hipparcos The High Precision PARallax COllecting Satellite is a space telescope launched by the European Space Agency (ESA). Its objective was to conduct precision astrometry of a large number of stars. It was in operation from 1989 to 1993. (Referenced on page xii, 13, 57, 77, 101.)

HRSP The HERCULES Reduction Software Package (Skuljian, 2004) is a C program that was originally developed for the purposes of reducing the data obtained from the HERCULES spectrograph. Although it had been largely superseded by the MATLAB reduction pipelines, the barycentric correction module of version 5.2.9 of the HRSP, `barycorr_HRSP`, is included as one of the subroutines in one of the data reduction pipelines. (Referenced on page 33.)

Kepler The Kepler satellite, named after the German astronomer Johannes Kepler, is a space telescope launched by the National Aeronautical and Space Administration (NASA) of the USA. Its objective is to search for extrasolar planets in or around habitable zones. It was launched in 2009 and is currently still in operation. (Referenced on page 13, 17, 18.)

MATLAB — MATrix LABoratory is a programming language developed by company MathWorks, which specialises in mathematical computing software. It provides a platform for high-level numeric computation, data analysis and visualisation, and algorithm development. The release version used for the analysis described in this thesis is 2013b. (Referenced on page xii, 30, 32, 59, 122.)

MOST — Microvariability and Oscillations of STars is a space telescope launched by the Canadian Space Agency (CSA). It is the first space telescope used purely for asteroseismological purposes. It was launched in 2003 and is currently still in operation. (Referenced on page 13, 17.)

MUSICIAN — Mapping and Understanding Stellar Interiors through a Coordinated International Asteroseismology Network: A project group headed by Associate Professor Karen Pollard at the University of Canterbury funded by the Marsden Fund, granted by the Royal Society of New Zealand. (Referenced on page 28.)

SIGSPEC — SIGnificance SPECtrum (Reegen, 2007, 2011) is a program that computes the significance spectrum for time-series of photometric and spectroscopic data. In addition to identifying pulsational frequencies, it also incorporates a sophisticated anti-aliasing algorithm to reduce the probability of identifying false frequencies (aliases or harmonics). (Referenced on page 40, 41, 42, 47, 48, 49, 65, 66, 67, 68, 75, 83, 84, 85, 86, 87, 88, 89, 90, 106, 107, 108, 109, 110.)

SYNSPEC — SYNthetic SPECtrum is a FORTRAN program that produces synthetic spectra based on ATLAS9 model atmospheres (Zboril, 1996; Hubeny and Lanz, 2011). (Referenced on page 33, 34, 35, 36.)

UC MJO — The University of Canterbury Mount John Observatory is the observatory attached to the Department of Physics and Astronomy at the University of Canterbury. It houses the 1-metre McLellan telescope, linked by optical fibre to the HERCULES spectrograph. (Referenced on page xii, 27, 28, 77.)

Glossary

WIRE The Wide-field Infrared Explorer is a space telescope launched by the National Aeronautical and Space Administration (NASA) of the USA. Its original objective, to conduct an infrared survey of the sky, was changed due to a mechanical fault. It was repurposed to conduct long timebase photometric monitoring of bright variable stars. WIRE was in operation from 1999 to 2011. (Referenced on page 17.)

ZAMS The Zero-Age Main Sequence is the curve along the Hertzsprung-Russell diagram that corresponds to stars which have just started to use hydrogen fusion as their primary source of energy (i.e. they have expended all of the energy gained from gravitational contraction). (Referenced on page 14, 15.)

1 Introduction

"The cosmos is within us. We are made of star-stuff.
We are a way for the universe to know itself."
– Carl Sagan, Cosmos (1980)

1.1 Ancient Dreams of the Universe

Stars: Majestic; Timeless; Ineffable. Every culture on earth that we know of has been influenced by their mysterious, otherworldly natures; those twinkling diamonds in the vast, atramentous blanket of night. Some cultures have ascribed special names to groups of the brightest stars, naming them after beasts both real and mythological. Others have raised grand monuments on earth in homage to their beauty or vast temples to curry their favour, considering them representatives of their gods and goddesses.

If the universe was a sentient creature, the stars can be considered to be its ancient dreams, given form and substance. Mankind has always been fascinated by these pinpricks of light in the fathomless depths of the void. That fascination has resulted in the birth of astronomy, the study of stars. Only after the invention of the telescope has astronomy evolved into a modern science, with multifarious branches both observational and theoretical. As ever, the common goal of these disciplines is to expand the body of knowledge of the universe, *"to know that we know what we know, and to know that we do not know what we do not know"* (Copernicus, 15^{th} Century).

1.2 Asteroseismology

One of the newest branches of astronomy is asteroseismology. The word "asteroseismology" has its roots in ancient greek. It is a combination of three words: "Aster," which means star, "seismos," which means tremor and "logia," which means study. Asteroseismology is therefore the study of the oscillations or "tremors" of each star.

Asteroseismology allows one to determine the internal structure of variable stars through the study of their pulsations. The first mentioning of the desire to probe stellar interiors was in *The Internal Constitution of the Stars* (Eddington, 1926), the now seminal work penned by Sir Arthur Stanley Eddington.

In it, he had lamented that:

> *"At first sight it would seem that the deep interior of the Sun and stars is less accessible to scientific investigation than any other region of the universe. Our telescopes may probe farther and farther into the depths of space; but how can we ever obtain certain knowledge of that which is hidden behind substantial barriers? What appliance can pierce through the outer layers of a star and test the conditions within?"*

Eddington had come to the conclusion that theory, using the laws of physics and mathematics, would be an essential tool in the determination of the internal structure of stars. However, he had also understood that such theoretical modelling must also be supported by observational data. Asteroseismology is a marriage of both of these principles: observing the pulsational characteristics of stars and using theoretical models to describe the mechanisms within them that had produced those pulsations.

The analysis of oscillation frequency spectra of stars enables the determination of the modes of oscillations of each star (Handler, 2013). Different modes penetrate to different depths in each star, giving insights into the stellar interior that is not directly viewable due to their opaque photospheres. The analysis of these frequency spectra also enables the determination or the constraining of stellar parameters such as the inclination, mass, radius, metallicity, temperature and surface gravity, as well as the frequencies and modes of stellar pulsations.

However, spectroscopic asteroseismological analysis is a difficult task and suffers from many limitations. The precise identification of the frequencies and modes of pulsation necessitates the use of large sets of high resolution spectroscopic data, with sufficient temporal coverage of the pulsational phases (Cunha et al., 2007). This difficulty is further compounded by the large computational power requirements of the analysis itself. In addition, the theoretical models of stellar surfaces are rudimentary at best (Zima, 2006) and do not take into account all of the physical conditions[1] of each star. A lack of precise stellar parameters (Cunha et al., 2007), also essential for theoretical modelling, is yet another factor that complicates this task. Greater understanding of the physics governing stellar structures and a larger quantity of broad timebase observational data would enable the development of more sophisticated models that would improve the ability to explain the characteristics of variable stars.

[1] Refer to the section on FAMIAS mode identification assumptions (2.4.2) for more information on the limitations on the theoretical modelling of pulsations in this analysis.

1.3 Stellar Pulsations

It is thought that many, if not all, stars exhibit some sort of variation in their luminosity due to the variations in the internal conditions within all stars (Eyer and Mowlavi, 2008). These variations cause their outer layers to distort, producing luminosity variations or pulsations. Studies (e.g. Starrfield et al., 1983; Gautschy and Saio, 1995, 1996; Beauchamp et al., 1999) have found that most regular variable stars[2] tended to have specific ranges of temperature and luminosity, falling within instability strips on the Hertzsprung-Russell (HR) diagram. Figure 1.1 shows the locations of different classes of variable stars on a HR diagram.

The periodic instability that results in stellar pulsations are caused by internal mechanisms within each star. These mechanisms are known as excitation or driving mechanisms and are generally a variation of heat-engine mechanisms, first postulated by Eddington (1917). Unlike temporary distortions within the stellar interior, which are quickly damped, these mechanisms are active and sustained over long temporal periods. In addition, these mechanisms are cyclical, which means that they incorporate a restoring process that forces a return to equilibrium and keeps the variation regular and stable.

1.3.1 Driving Mechanisms

Three major driving mechanisms for the excitation of pulsations in variable stars have been postulated: the κ mechanism, stochastic driving and the ϵ mechanism (Cox, 1980). The κ mechanism is the most common mechanism producing pulsations in variable stars (Cox, 1980). It operates due to the properties of radiative opacity, denoted by the Greek symbol κ. Most radial layers or zones of the star prevent or delay radiation (originating in the core) from escaping past those layers (they are partially opaque to radiation). Under compression, some layers become more opaque. This causes those layers to absorb energy, causing the star to expand as a whole, distort the shape of the star or both. However, the chemical elements within those layers (typically hydrogen and helium) become more greatly ionised, decreasing the opacity. This cools those layers and contracts them, forcing them back to and past equilibrium, where they once again become less ionised and more opaque, causing the cycle to repeat.

The second major driving mechanism, operating primarily in the Sun, sun-like stars and some red giants, is stochastic driving (Cox, 1980). It is very similar to the κ mechanism in that it involves a heat-engine mechanism. However, in the case of stochastic driving, the mechanism is not strong enough to produce significant variation on its own. This is due to turbulent

[2] Regular variables are variable stars that show consistent variations in luminosity over a fairly long time period, as opposed to semi-regular variables which showcase some irregularities in their pulsational cycles and cataclysmic variables which tend to showcase one-off or highly infrequent variation.

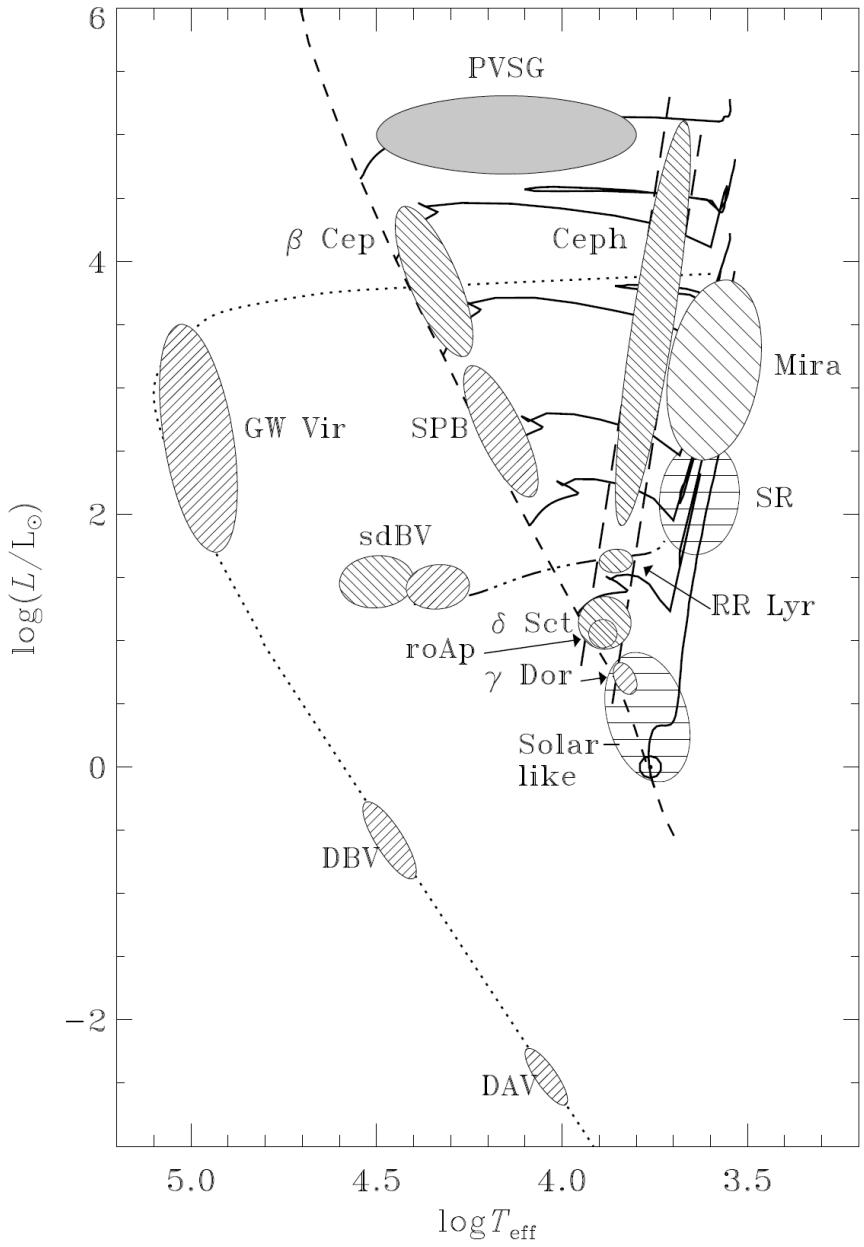

Figure 1.1: Locations of different classes of variable stars on a Hertzsprung-Russell (HR) diagram. From Aerts et al. (2010). (Referenced on page 3, 13, 17, 18.)

convection currents damping the variation in the inner convective zone (Antoci, 2013). Instead, the oscillations are generated by the resonance of the outer convective zone with the variation in the inner convective zone (Antoci, 2013), producing acoustic waves travelling on the surface of the star. This is similar to musical stringed instruments vibrating with their natural frequency in a noisy room.

The third driving mechanism, called the ϵ mechanism, has been theorised to drive pulsations in later-stage, high mass stars but there has been little evidence to support its existence

(Cox, 1980). The mechanism relies on variations in the energy generation rate in the core, which can potentially only occur in very massive stars.

In addition to these three major driving mechanisms, there are others such as convective flux blocking[3] that drive pulsations in certain classes of variable stars. These mechanisms tend to be variants of the three major driving mechanisms.

1.3.2 Radial Pulsations

Stellar pulsations can be divided into two main types: radial and non-radial pulsations. Radial pulsations are pulsations in which the entire star expands and contracts with no change in its shape, similar to a balloon into which air is pumped and released. These pulsations are spherically symmetric with modes that are characterised by the radial order n: the number of concentric nodal shells within each star. Cepheid variables, RR Lyrae stars and δ Scuti stars (such as HD 3112) are among the types of variable stars exhibiting radial pulsations. Cepheids are the most ubiquitous examples of radially pulsating stars and tend to pulsate in the fundamental radial mode (Cox, 1980). This means that there are no nodal shells within most Cepheids (i.e. $n = 0$). Instead, the centre of the star functions as a nodal point.

Stars that pulsate in both the fundamental and the first overtone radial modes simultaneously are particularly useful for asteroseismology. This is because the ratio of the periods of the fundamental and the first overtone in these stars usually differs significantly from those found in stringed instruments (0.5) and in open pipe wind instruments (0.33). For example, this ratio is 0.71 for certain types of Cepheids (Petersen, 1973) and 0.78 for δ Scuti stars (Pigulski et al., 2006). This discrepancy is caused by sound speed gradients within each star, consequences of the different internal compositions. Determining the ratio of these modes allows the inference of the internal structures of each star.

1.3.3 Non-Radial Pulsations

Non-radial pulsations are pulsations in which different regions of the star expand and contract at the same time, distorting the spheroidal shape of the star. These pulsations are therefore non-spherically symmetric with modes that are characterised not only by the radial order n, similar to radial pulsations, but also by the degree ℓ and the azimuthal order m[4] (Aerts et al., 2010). The degree ℓ is the total number of nodal lines present on the surface of the star and the azimuthal order m is the number of nodal lines passing through the poles of the axis of rotation of the star. Technically, radial pulsations also have ℓ and m numbers but these are

[3] Convective flux blocking is a variant of the κ mechanism and drives the pulsations in γ Doradus stars (Guzik et al., 2000; Dupret et al., 2004). Refer to the section on γ Doradus stars (1.4.1) for more information.

[4] ℓ and m are parameters that describe spherical harmonics. Refer to the section on non-radial pulsational geometry (1.3.5) for more information.

equal to zero.

Non-radial pulsations can be further subdivided into three types: p-modes, g-modes and f-modes (Aerts et al., 2010). p-modes are pressure modes, akin to acoustic sound waves and have pressure as their restoring force. g-modes are gravity modes and have buoyancy as their restoring force. f-modes are surface gravity modes, akin to ocean waves but travelling on the surface of the star. The characterisation of a non-radial pulsation mode as either a p-, g- or f-type aids in the creation and refinement of stellar interior models as these modes penetrate to different depths (Handler, 2013).

For example, g-modes penetrate to a greater depth than p-modes (Handler, 2013). Therefore, these g-modes are indicative of the physical conditions deep within a star and information such as the size of the stellar core, the interior rotation profile and variations of the sound speed in the stellar interior can be deduced (Handler, 2013). There are also mixed modes: combinations of p-mode pulsations on the surface and g-mode pulsations in the interior. Balona and Evers (1999), Breger and Bischof (2002) and Handler (2005) have found a number of δ Scuti stars which display such modes. Figure 1.2 shows the propagation of p-mode and g-mode waves within a sun-like star.

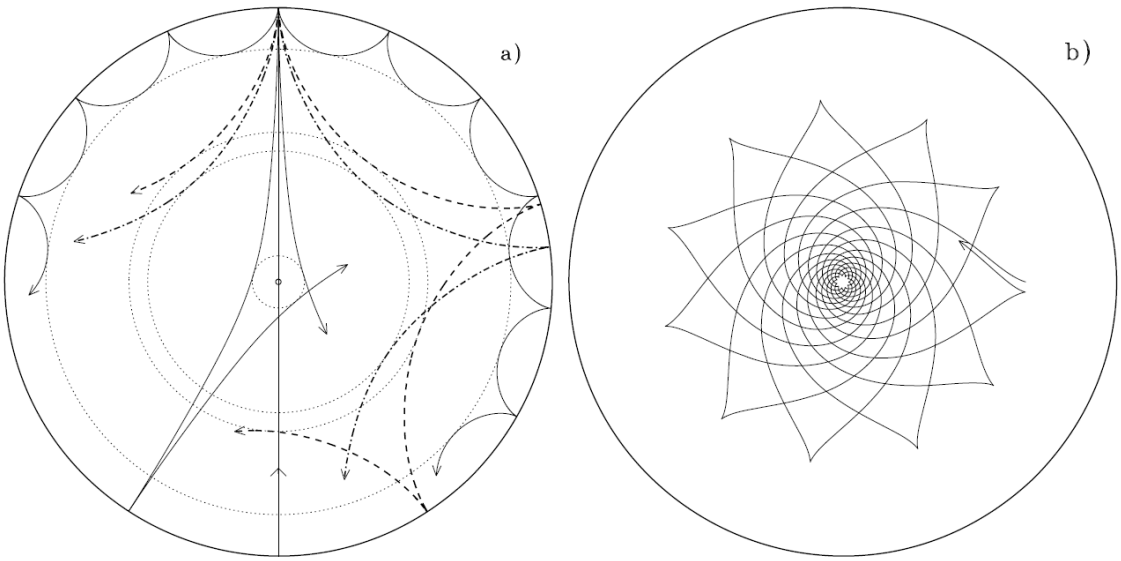

Figure 1.2: The propagation p-mode and g-mode waves within a star. Panel a) shows different p-mode rays (solid, dashed and dash-dotted arrows) with $\ell = 75$, 25, 20 and 2, in the order of increasing penetration depth. These rays undergo become increasingly refracted due to the rapidly increasing density and eventual reflection upon reaching certain boundary shells (indicated by the dotted circles). The arrow passing through the centre of the cross-section represents the behaviour of a radial-mode ray. Panel b) shows the path of a single g-mode ray (note the arrowhead representing the end of the path of the ray). In this cross-section, the pulsation remains confined to the interior of the star and does not propagate to the outer layers, which is not the case for γ Doradus stars represented in this thesis. Diagram taken from Cunha (2007). (Referenced on page 6.)

1.3.4 Selection Mechanisms of Pulsation Modes and Frequencies

Although the modes and frequencies of many stars have been identified, a key question that has yet to be definitively answered is this: Why do some stars pulsate with those modes and frequencies? More specifically, why do most Cepheids pulsate in the fundamental radial mode? Why do γ Doradus stars exhibit low frequency g-mode pulsations and δ Scuti stars exhibit high frequency p-mode pulsations? What are the selection mechanisms behind modes and frequencies?

Most variable stars show strong fundamental frequency pulsations, similar to musical instruments, but not all of them. Some classes stars tend to pulsate in specific overtone modes exclusively over others. All of these effects are a result of the physical properties of each star: the location of nodal shells that prevent the excitation of certain modes (Lund et al., 2014), strong magnetic fields that preferentially excite dipole modes (Kurtz et al., 2011), the damping of interior driving forces by the exterior layers (Antoci, 2013) and many others (Aerts et al., 2010). As more information about the interior of the various variable star classes is collated, the question of why certain modes are excited over others might be answered in the future.

1.3.5 Non-Radial Pulsational Geometry

Non-radial pulsations are typically defined in terms of spherical coordinates. The orientation of a star is defined in terms of the inclination i: the angle between the observer's line-of-sight and the rotational axis. This parameter is typically unknown or imprecise. Therefore, the rotational velocity is also often not well defined. Instead, the projection of the equatorial rotational velocity along the line-of-sight ($v \sin i$) is used as a lower bound on the rotational velocity of the star.

Non-radial pulsations are modelled in the program FAMIAS as spherical harmonics[5] that distort the stellar surface[6] (Zima, 2008b). Spherical harmonics (Y_ℓ^m) are represented mathematically by the product of a trigonometric function ($e^{im\phi} \cos\theta$) and a Legendre function (P_ℓ^m). The equation defining spherical harmonics is:

$$Y_\ell^m = N_\ell^m P_\ell^{|m|} e^{im\phi} \cos\theta \tag{1.1}$$

ℓ is the degree of and m is the azimuthal order (not to be confused with the radial order n) of the spherical harmonic. θ and ϕ are the polar and azimuthal angle in spherical coordinates. $e^{im\phi}$ is the complex exponential form of a trigonometric function ($i = \sqrt{-1}$ is a com-

[5] Spherical harmonics are a set of solutions of Laplace's equation (an equation that describes a scalar field) in three dimensions.

[6] Radial pulsations are also modelled in FAMIAS using spherical harmonics but the result is trivial as there is no distortion of the stellar surface ($P_0^0 = 1$).

plex number and not the inclination). N_ℓ^m is a normalisation constant, defined in FAMIAS (Zima, 2008b) as:

$$N_\ell^m = (-1)^{(m+|m|)/2}\sqrt{\frac{2\ell+1}{4\pi}\frac{(\ell-|m|)!}{(\ell+|m|)!}} \tag{1.2}$$

The Legendre functions (with respect to the random variable x) are defined by the equation:

$$P_\ell^m(x) = (-1)^m(1-x^2)^{m/2}\frac{d^m}{dx^m}P_\ell(x) \tag{1.3}$$

$P_\ell(x)$ is a Legendre polynomial (not to be confused with a Legendre function), defined by Rodrigues' formula as:

$$P_\ell(x) = \frac{1}{2^\ell \ell!}\left(\frac{d^\ell}{dx^\ell}(x^2-1)^\ell\right) \tag{1.4}$$

The Legendre function reduces to the Legendre polynomial when $m = 0$[7]. The pulsational modelling in FAMIAS is carried out under the assumption that the rotational axes are aligned with the coordinate system of the spherical harmonics (i.e. the pulsational axis). Although this is true for most stars (Aerts et al., 2010), it may not necessarily be the case in all stars. For example, in rapidly oscillating Ap (roAp) stars, the pulsation axis is aligned to the magnetic field axis instead of the rotational axis due to the strength of the magnetic field in these stars (Kurtz et al., 2011). There is therefore the possibility that some stars in other variable star classes with strong magnetic fields may exhibit such behaviour as well.

Figure 1.3 shows a snapshot of various radial and non-radial pulsation modes, up to $\ell = 4$. While the observational identification of high-degree modes using spectroscopy is possible (e.g. Mantegazza and Poretti, 2005 have identified modes up to $\ell = 16$), there are a number of observational and technological difficulties, including insufficient spectral resolution (Balona and Evers, 1999; White et al., 2012). In addition, higher-degree modes become progressively more confined to the equatorial region as the azimuthal order increases[8] (as m approaches ℓ). This means that modes with both high degree and azimuthal order would be undetectable at low inclinations (close to pole on). Figure 1.4 illustrates this phenomenon.

The pulsations are also affected by Inclination Angles of Complete Cancellation (IACC) (Chadid et al., 2001): the inclination angles at which there is a cancellation of the effects of a particular pulsation mode in the stellar spectra. This means that for some inclination angle i, $P_\ell^m \cos i = 0$. Similarly, one can define Inclination Angles of Least Cancellation (IALC): the

[7] $P_\ell^0(x) = P_\ell(x)$

[8] This phenomenon is due to the nature of the spherical harmonics: when m approaches ℓ for large ℓ, the number of maxima of $|Y_\ell^m|$ decrease and the θ values at which these maxima occur become closer 90° (i.e. the equatorial region). This can be verified by substituting in the appropriate values in Equations 1.1 to 1.4.

inclination angles at which there is minimal or no cancellation of a particular pulsation mode in the stellar spectra ($P_\ell^m \cos i$ is maximised). An $(\ell, m) = (2, 1)$ mode, for example, has IACC at 0° and 90° and IALC at 45° (Chadid et al., 2001).

Note that these cancellation effects are of the first-order: they only apply to linear quantities such as the monochromatic magnitude[9] of photometric data and the radial velocity[10]. For photometric data that has been recorded with respect to several passbands, which have specific ranges of wavelengths, the comparison of these passbands[11] can mitigate, if not totally eliminate, the effects of IACC. In addition, frequency analysis using the pixel-by-pixel method and the higher-order moments of the moment method would largely mitigate the effects of IACC.

1.3.6 Rotational Effects on Pulsations

Stellar pulsations can be most significantly affected by the rotations of the stars about their axes (García et al., 2014). This is because the pulsations distorting the surfaces of the stars are affected by changes in the geometry of the star[12]. Although other factors, such as turbulence and granulation[13], affect stellar pulsations, they are considered to be relatively minor in comparison with rotational effects. In addition, current understanding of such effects is limited (Gray, 1975, 1988, 2005). As such, these more minor effects will not be taken into account for the purposes of this thesis.

$m = 0$ modes are known as axisymmetric modes as the locations of the nodal lines are symmetric about the pulsation axis, which is assumed to be aligned with the rotation axis[14]. These modes are standing waves and are therefore unaffected by rotation[15]. $m \neq 0$ modes are travelling waves and are divided into two groups: prograde modes ($m > 0$) and retrograde modes ($m < 0$)[16]. Prograde modes travel along the direction of rotation while retrograde modes travel opposite to the direction of rotation. This is of particular concern when the pulsational and

[9] The monochromatic magnitude is an absolute measure of the brightness of a star across a passband. It is defined as the logarithm of the spectral flux density. Refer to Oke and Gunn (1983) for more information.

[10] The radial velocity is equivalent to the first moment of the Moment Method (Aerts, 1996). Refer to the section on the moment method (2.4.1) for more information.

[11] Since IACC only affects the monochromatic magnitude, taking the amplitude ratios of different passbands would eliminate the dependence on i. Refer to Aerts et al. (2010) for more information.

[12] Refer to Aerts et al. (2010) for a definitive list of rotational effects and their mathematical and physical foundations.

[13] Turbulence is the mathematically chaotic flow of a fluid. Granulation is the conglomeration of fluid particles due to viscosity. Both of these phenomena work in conjunction, producing asymmetries and other minor variations in stellar spectral lines. Refer to Gray (1975, 1988, 2005) for more information.

[14] Refer to the section on non-radial pulsational geometry (1.3.5) for more information.

[15] Note that this definition assumes that the star does not deviate from spherical symmetry at equilibrium, which is generally untrue (stars exhibit varying amounts of rotational flattening). Refer to Reese et al. (2006) for more information.

[16] Note that the sign convention for prograde and retrograde modes may be reversed in other papers (e.g. Townsend, 2003b)

rotational periods are similar to each other, as is the case for γ Doradus stars.

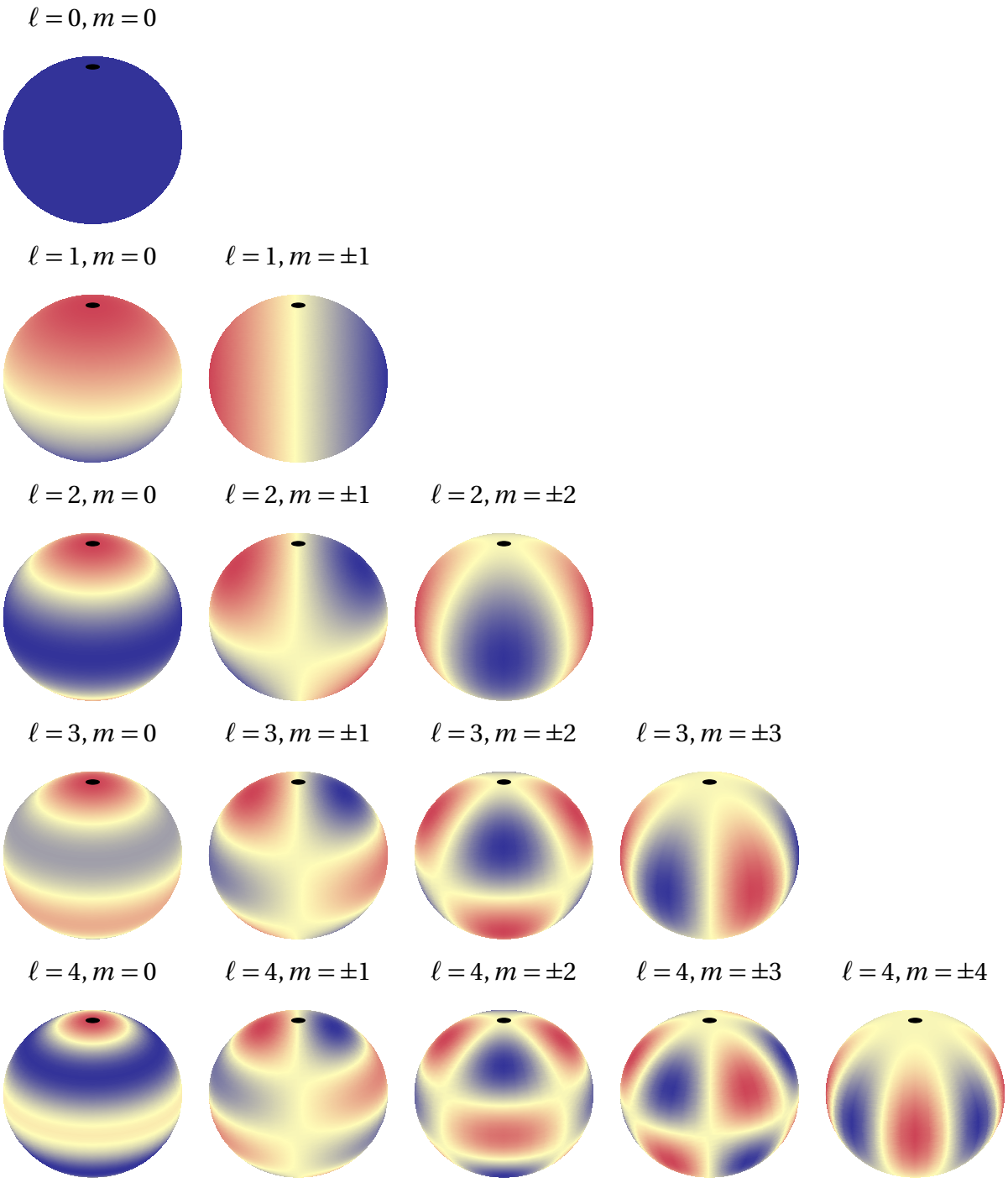

Figure 1.3: Radial and non-radial pulsation modes of a star at an inclination of 60°. These diagrams are the mapping of spherical harmonics onto the surfaces of spheres, with no consideration of rotational effects. The north poles are represented by black ellipses. The degree ℓ and the azimuthal order m of each mode has been printed above each diagram. The yellowish-white lines are the surface nodes while the red and blue areas represent the regions of the star that are moving inwards (or outwards) or cooling (or heating) at a particular time. (Referenced on page 8.)

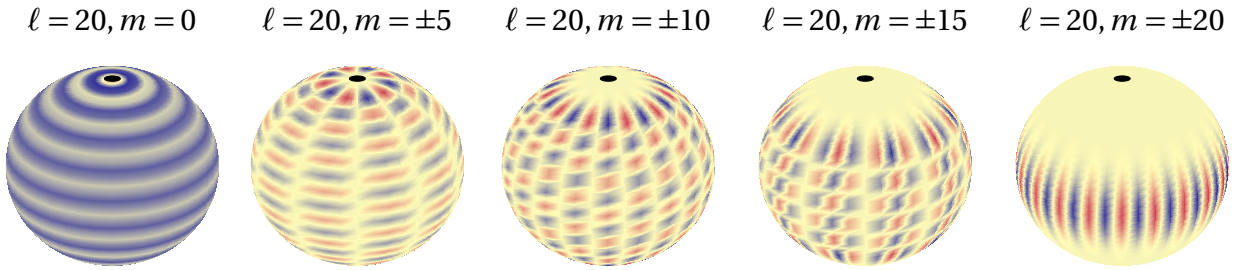

Figure 1.4: $\ell = 20$ pulsation modes of a star at an inclination of 60°. These diagrams are the mapping of spherical harmonics onto the surfaces of spheres, with no consideration of rotational effects. The north poles are represented by black ellipses. The degree ℓ and the azimuthal order m of each mode has been printed above each diagram. The yellowish-white lines are the surface nodes while the red and blue areas represent the regions of the star that are moving inwards (or outwards) or cooling (or heating) at a particular time. Note the progressive confining of the pulsation to the equatorial region as $|m|$ increases. (Referenced on page 8, 12.)

The main structural effect of rotation is the deviation of the pulsationally unperturbed star from spherical symmetry due to rotational flattening. This means that the modelling of stellar pulsations as a single spherical surface harmonic becomes imprecise (Reese et al., 2006). Unfortunately, there are currently no asteroseismological surface models taking this factor into account.

Rotational splitting is another effect of rotation. This phenomenon causes the prograde orders of a mode with a certain ℓ to have higher frequencies and the retrograde orders to have lower frequencies. This is due to simple vector addition: the rotational frequency vector is added to the pulsational frequency for the case of prograde modes and subtracted from the pulsational frequency for the case of retrograde modes (Aerts et al., 2010). Note that the Coriolis force opposes this phenomenon: the frequency of prograde modes are reduced while the frequency of retrograde modes are increased. However, the effects of the Coriolis force is much weaker than the effects of rotational splitting for stars with slow to medium rotational velocities (Saio, 2013). The increase or decrease in frequency varies according to the order of the mode, causing any one frequency to be split into a total of $2\ell + 1$ frequency multiplets.

However, most stars exhibit differential rotation[17] (Gizon and Solanki, 2004; Lund et al., 2014), implying that the splitting process is complicated and non-uniform. The inclination of the star would therefore influence the number of detected multiplet components. In addition, different multiplets are excited to different amplitudes depending on the physical conditions of the star (Miesch, 2005; Lund et al., 2014). Some components may therefore not even be detectable due to the low amplitudes. Comparing the multiplets of modes with different ℓ or

[17] Differential rotation is the rotation of different latitudinal regions of a star at different speeds. This is in contrast with rigid body rotation. The observed rotational splitting therefore depends on the rotation rates of the various regions of the photosphere. Refer Miesch (2005) for more information on differential rotation in the Sun.

n values[18] enable the measurement of the interior rotation rate of the star[19] (Benomar et al., 2015).

A recent study by Chapellier et al. (2012), using CoRoT photometry, showed some evidence that space-based photometry is precise enough for the identification of split frequencies in γ Doradus stars and δ Scuti stars. However, Chapellier et al. (2012) mentioned that the origins of the frequency splitting was highly uncertain and that the star that they had analysed (CoRoT ID 105733033) could possibly be a binary. In addition, the plethora of identified frequencies, many of which are potential aliases, harmonics or combinations thereof[20], made identification of frequency multiplets difficult and imprecise.

Another recent study by Bouabid et al. (2013) proposes an origin for mixed modes[21] in γ Doradus stars and δ Scuti stars. They discovered that frequencies between those typically exhibited by the two classes of stars can be explained by the rotational shifting of prograde g-modes in γ Doradus stars to higher frequency values.

It has been theorised by Townsend (2003b) that prograde tesseral modes[22] of rapidly-rotating stars have reduced photometric amplitudes. This is because the pulsations become increasingly confined to the equatorial region as the rotational velocity increases, due to increasing Coriolis force. This phenomenon is independent of the confining of high-order, high-degree modes to the equatorial region[23] (Figure 1.4) and as such, applies to pulsations of all degrees and azimuthal orders. This means that some of the pulsation modes of rapidly-rotating stars with low inclinations would not be detectable photometrically (Townsend, 2003a,b) or spectroscopically (Townsend, 1997, 2003a; Daszyńska-Daszkiewicz et al., 2007).

1.3.7 Pulsational Effects on Spectroscopic Data

Radial and non-radial pulsations manifest as asymmetric deviations across the spectral lines of a stellar spectrum. These are the result of the minute radial velocity and temperature variations caused by the expansion and contraction of the outer layers of the star. There is a small blueshift in radial velocity when there is expansion and small redshift in radial velocity when there is a contraction along the along the observational line-of-sight. One would also expect the spectroscopic variations to also typically correspond to the photometric variations, but

[18] Some asteroseismological analysis software packages, like TOUCAN (Rodrigo et al., 2015; Suárez et al., 2014), allow for the measurement of n values.

[19] The interior regions (core and radiation zone) of stars are considered to rotate uniformly (as rigid bodies) (Benomar et al., 2015). This was first observed in the Sun (refer to Garaud, 2002; Garaud and Garaud, 2008; Acevedo-Arreguin et al., 2013 for detailed reviews).

[20] Refer to the section on frequency identification (2.4.1) for more information.

[21] Refer to the section on non-radial pulsations ((1.3.3) for more information

[22] Tesseral modes are modes where $|m| \neq \ell$. Prograde tesseral modes are therefore modes where $\ell > m > 0$.

[23] Refer to to the section on non-radial pulsational geometry (1.3.5) for more information.

this does not always seem to be case[24] (Balona, 1998).

The spectra in this analysis are reduced to cross-correlated line profiles[25] for ease of analysis and to increase the signal-to-noise ratios of the individual spectra. Figure 1.5 shows how different pulsation modes distort the shape of the cross-correlated line profiles. The frequencies of these variations are then identified using Fourier analysis and the line profile variations are then modelled as functions of the ℓ and m values of various modes using FAMIAS[26]. As mentioned in the preceding sections, these models are reasonably idealised and do not take into account many physical factors, such as rotational flattening. However, it is assumed that these models are a reasonable approximation for non-radially pulsating and slowly rotating stars.

1.4 Variable Star Classes

1.4.1 γ Doradus Variable Stars

γ Doradus variable stars were first suggested as a new class by Krisciunas in 1993. They were named after the prototypical star γ Doradus, whose variability was first discovered by Cousins and Warren (1963) and later analysed by Cousins et al. (1989). Kaye et al. (1999) and Pollard (2009) are the two most recent reviews of γ Doradus stars and the theoretical and observational challenges faced when analysing such stars.

As of 2011, there were 86 bright bona fide γ Doradus stars (Henry et al., 2011), most of whose variability was originally found through the HIPPARCOS mission (Perryman et al., 1997; Aerts et al., 1998; Waelkens et al., 1998; Eyer and Aerts, 2000). 418 candidates had been identified by COROT (Hareter, 2012) and 207 by KEPLER (Uytterhoeven et al., 2011; Bradley et al., 2015). The MOST satellite has been used for follow up work on some of these stars, primarily collecting long timebase photometric data (Rowe et al., 2006; Sódor et al., 2014). The number of bona fide members is expected to rise significantly with the first data release (mid-2016) from the recently-launched GAIA mission, currently the most advanced space observatory in orbit.

γ Doradus stars are typically Population I[27], late A- to early F-type stars. They are characterised by their g-mode pulsations of high n and low ℓ[28] (Kaye et al., 1999). These stars have

[24] Refer to the sections on non-radial pulsational geometry (1.3.5) and the rotational effects on pulsations (1.3.6) for more information on exceptions to this rule.
[25] Refer to the section on cross-correlation (2.2.3) for more information.
[26] Refer to the section on spectroscopic variability analysis (2.4) for more information on the frequency and mode identification process.
[27] Population I stars, one of the two "populations" of stars originally defined by Baade (1944), are generally young stars with high metallicity.
[28] Refer to the sections on non-radial pulsations (1.3.3) and non-radial pulsational geometry (1.3.5) for more information.

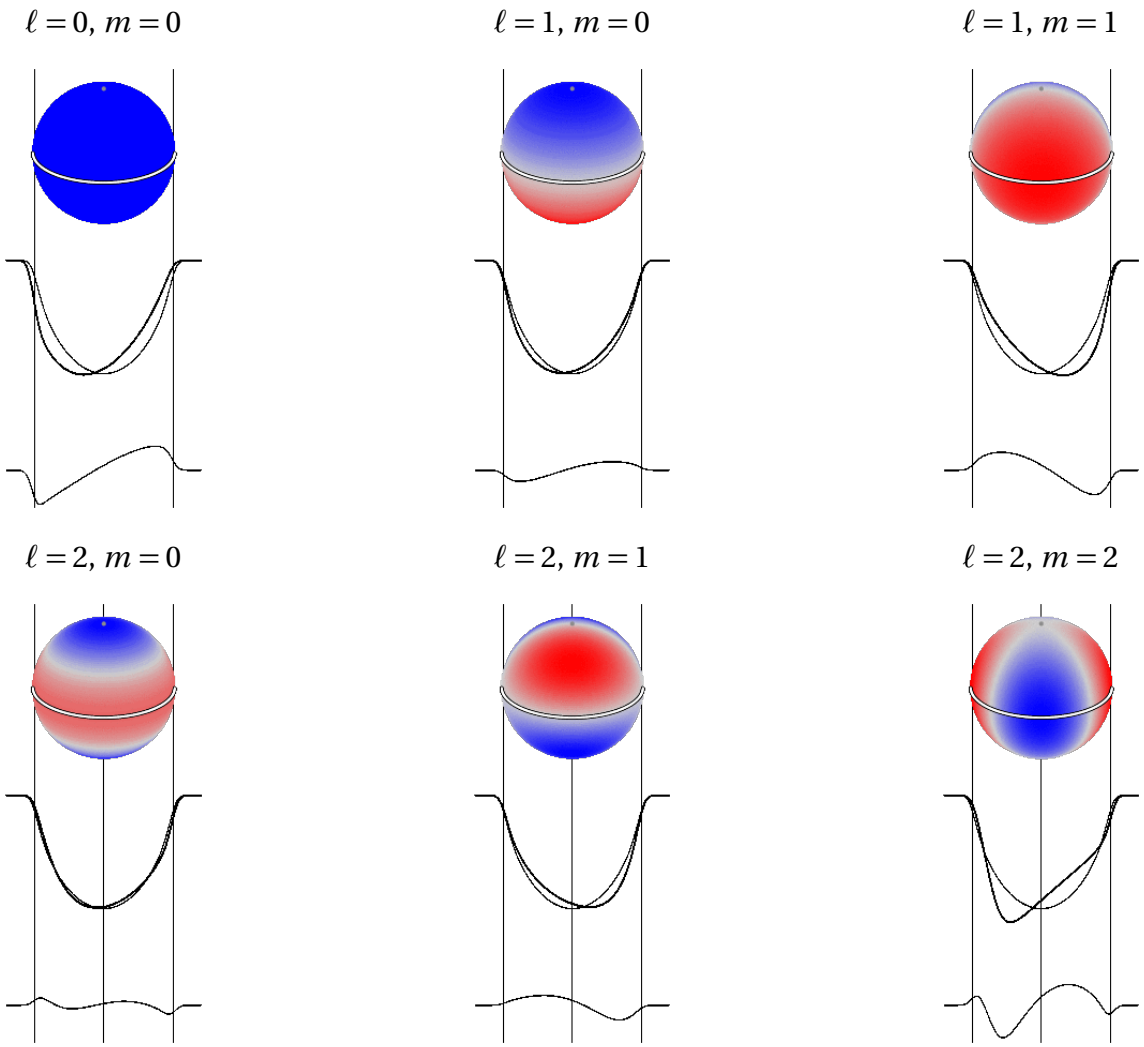

Figure 1.5: An animated diagram showing the line profile variations of various modes due to pulsations. The degree ℓ and the azimuthal order m have been printed above each diagram. The top panels of each diagram are the spherical harmonics, the middle panels are the distorted cross-correlated line profiles and the bottom panels are graphs showing the variation of each line profile from a pulsationally unperturbed line profile (assumed to be Gaussian). The animations can be viewed in Adobe Reader. Animations obtained from Dr. John Telting's website (`http://staff.not.iac.es/~jht/science/nrpform/`). (Referenced on page 13.)

typical frequencies between 0.3 d^{-1} and 3 d^{-1} with luminosity variations of up to 0.1 magnitudes and radial velocity variations of up to several kilometres per second (Guzik et al., 2000). The frequencies of γ Doradus stars are much smaller than those of the fundamental radial modes of A- to F-type stars, which are between 8 d^{-1} and 24 d^{-1}. They are located along the intersection between the classical instability strip and the main sequence branch of the HR diagram (Figure 1.1).

γ Doradus stars tend to have spectral types between A7 and F5, with temperatures between 7200 K and 7700 K for stars on the zero-age main sequence (ZAMS) and 6900 K to 7500 K one

magnitude above the ZAMS (Handler, 1999). Henry et al. (2011) observed that stars belonging to both subgiant (IV) and dwarf (V) luminosity classes could exhibit γ Doradus-like pulsations and found that approximately 22% of A7- to F5-type stars of their sample of 114 stars were bona-fide γ Doradus stars. γ Doradus stars have typical masses of about 1.51 $M_\odot$ to 1.71 $M_\odot$ and typical radii of about 1.43 $R_\odot$ to 2.36 $R_\odot$ (Kaye et al., 1999).

It was first theorised by Guzik et al. (2000), using frozen convection models, that the driving mechanism behind the pulsations of γ Doradus stars was convective flux blocking (Pesnell, 1987), a variant of the κ-mechanism[29]. Dupret et al. (2004) later expanded upon the proposal of Guzik et al. (2000) using a time-dependent treatment of convection, producing instability strips for γ Doradus stars of various masses and luminosities (refer to Figure 1.6). Dupret et al. then refined their models in 2005 and used them to predict the photometric behaviour of five of the most well-studied γ Doradus stars (Dupret et al., 2005b).

γ Doradus stars have a three-layer internal structure: a convective core, an intermediate radiative zone and an outer convective envelope (Guzik et al., 2000). The pulsations in the radiative zone, arising because of opacity variations, attempt to propagate to the outer regions through radiative heat transfer. However, the convective envelope is resistant to the radiative heat transfer from the interior, resulting in a blockage of radiative flux by the convective envelope (Pesnell, 1987). The degree of blockage varies periodically, driving the pulsations in the interior of the star. The g-mode pulsations in γ Doradus stars arise due to this mechanism (Dupret et al., 2006).

γ Doradus stars have been studied quite extensively. Detailed photometric and spectroscopic frequency and mode identifications of stars such as HD 12901 (Brunsden et al., 2012), HD 135825 (Brunsden, 2013), HD 139095 (Greenwood, 2014), HR 8779 (Sódor et al., 2014) and KIC 6462033 (Ulusoy et al., 2014) have been performed. All of the aforementioned stars were reported to display the low frequencies and low degree modes typical of γ Doradus stars. However, some stars such as CoRoT ID 105733033 (Chapellier et al., 2012), BD+18 4914 (Rowe et al., 2006) and KIC 9533489 (Bognár et al., 2015) were also reported to display high-frequency pulsations in addition to the low-frequency pulsations[30]. Further investigation of γ Doradus stars would be useful to determine the origin of the high frequency variation in certain γ Doradus stars.

[29] Refer to the section on driving mechanisms (1.3.1) for more information

[30] These stars are referred to as δ Scuti-γ Doradus hybrids. Refer to the section on δ Scuti stars (1.4.2) for more information.

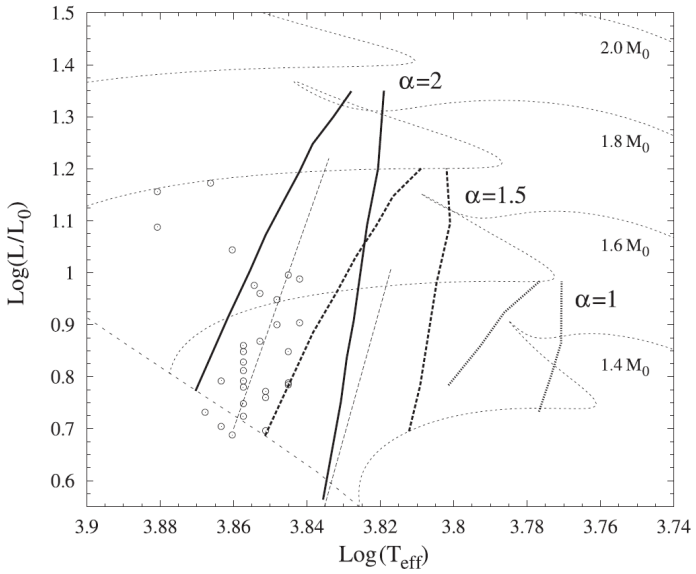

Figure 1.6: Theoretical γ Doradus instability strips for stars vibrating with $\ell = 1$ modes. The thick solid lines denote the instability strips at different values of the mixing-length parameter α[a]. The thin dashed lines denote the results using the less sophisticated frozen convection model of Warner et al. (2003). The circles represent bona fide γ Doradus stars. The dotted lines denote isochrones at the various masses indicated on the right edge of the diagram. From Dupret et al. (2004). (Referenced on page 15, 18.)

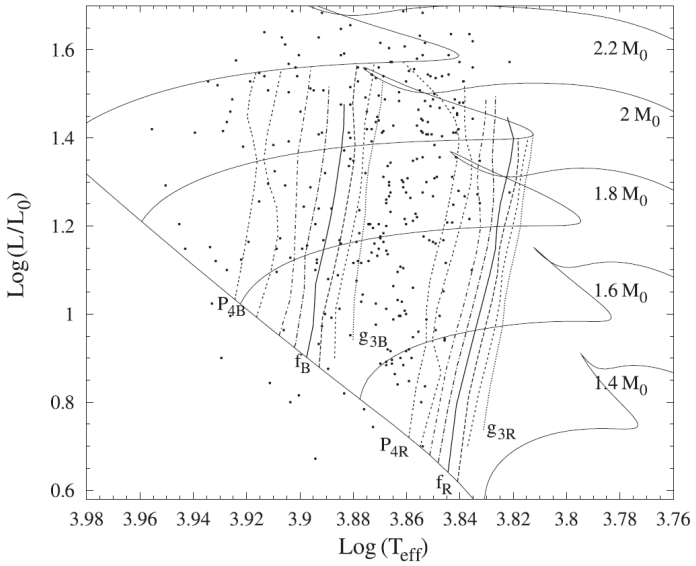

Figure 1.7: Theoretical δ Scuti instability strips for stars vibrating with $\ell = 2$ modes. p, g and f represent the type of mode (either pressure, gravity or surface gravity[b]), the subscripted number represents the order of the mode and the subscripts R and B represent the red and blue edges (arbitrarily defined) of the mode. The points represent observed δ Scuti stars. The solid lines extending from left to right denote isochrones at the various masses indicated on the right edge of the diagram. From Dupret et al. (2004). (Referenced on page 18.)

[a]The mixing-length parameter is the ratio that represents the degree of coherence of a fluid globule (which forms due to viscosity of the fluid) in fluid dynamics.

[b]Refer to the section on non-radial pulsations (1.3.3) for more information.

1.4.2 δ Scuti Variable Stars

δ Scuti stars are a well-established class of variable stars, first defined by Eggen in 1956. They are named after the prototypical star, δ Scuti, whose variability was first discovered by Campbell and Wright (1900). The photometric variability and radial velocity variations were first characterised by Fath (1935) and Colacevich (1935) respectively, more than thirty years after the discovery of the star. Breger (2000), Lampens and Boffin (2000) and Rodríguez and Breger (2001) had published reviews on the δ Scuti class, with Lampens and Boffin (2000) focussing specifically on those present in multi-star systems.

Being such a well-established class, more than 1500 bona fide members and several thousand candidates have been identified and catalogued (Rodríguez et al., 2000; Rodríguez and Breger, 2001; Balona and Dziembowski, 2011). Large quantities of follow-up work has been carried out using satellite data. Analysis of WIRE data has shown that the bright star Altair, also known as α Aquilae, is a δ Scuti star, and the brightest one discovered to date (Buzasi et al., 2005). Data from MOST (Breger et al., 2012b), CoRoT (Kaiser et al., 2009) and Kepler (Bradley et al., 2015), have also been used in a number of in-depth studies on individual members: Rho Puppis (Antoci et al., 2009), HD 174936 (García et al., 2009), KIC 9700322 (Breger et al., 2011), KIC 80541466 (Breger et al., 2012a) and HD 261711 (Zwintz et al., 2013). HD 261711 and KIC 9700322 were reported to display low-degree ($\ell < 3$) non-radial modes. Rho Puppis was also reported to display solar-like pulsations in addition to a dominant radial pulsation mode. KIC 8054146 was also reported to display low frequency g-modes and and high frequency p-modes. All of the aforementioned stars were also reported to display regularities in the spacings between identified frequencies.

δ Scuti stars are typically Population I[31], early A- to early F-type stars. They are characterised by both radial pulsations and p-mode pulsations of low ℓ[32] (Rodríguez and Breger, 2001). These stars have typical frequencies between 3 d^{-1} and 80 d^{-1} with a wide range of luminosity variations: anywhere from 0.001 to 1 magnitude (Rodríguez and Breger, 2001). They are located along the intersection between the classical instability strip and the main sequence branch of the HR diagram (refer to Figure 1.1), similar to γ Doradus stars.

δ Scuti stars tend to have spectral types between A2 and F5 and may belong to giant (III), subgiant (IV) and dwarf (V) luminosity classes (Rodríguez and Breger, 2001). Breger (2000) had estimated that approximately 30% of all A2- to F5-type stars could exhibit δ Scuti-like pulsations. δ Scuti stars have typical masses of about 1.5 $M_\odot$ to 2.5 $M_\odot$ (Aerts et al., 2010).

δ Scuti stars that pulsate with large luminosity amplitudes are grouped into a subclass called High Amplitude Delta Scuti (HADS) stars. Those which pulsate with low luminosity

[31] Refer to the section on γ Doradus stars (1.4.1) for more information.
[32] Refer to the sections on non-radial pulsations (1.3.3) and non-radial pulsational geometry (1.3.5) for more information.

amplitudes are similarly grouped into a subclass called Low Amplitude Delta Scuti (LADS) stars. HADS stars were initially thought to be monoperiodic and hence not too useful for asteroseismology[33]. They were observed to pulsate most strongly in the fundamental radial mode, with typical frequencies of between 8 d^{-1} and 24 d^{-1} for A- to F-type stars. This was refuted by Mathias et al. (1997), who had managed to discover non-radial modes using radial velocity measurements. Poretti (2003) later attributed the variation in the light curves of HADS to non-radial pulsation modes. According to a theoretical model developed by Lee et al. (2008), only 0.3% of δ Scuti stars are expected to be HADS stars, while more than 33% are expected to be LADS stars.

Another interesting subclass that has been defined in recent years is the δ Scuti-γ Doradus hybrid: stars displaying high-frequency p-mode pulsations, characteristic of δ Scuti stars, as well as low-frequency g-mode pulsations, characteristic of γ Doradus stars. Researchers including Rowe et al. (2006), Chapellier et al. (2012), Hareter (2012), Brunsden (2013) and Bognár et al. (2015) have conducted detailed analyses of stars within this subclass. Recent results from the analysis of KEPLER data (Balona, 2014) has revealed a surprising claim: *all* δ Scuti stars display low-frequency pulsations. Balona et al. (2015) conducted detailed modelling of the hybrid stars and concluded that the low-frequency pulsations could not be attributed to rotational effects or anomalous chemical compositions. This means that the concept of a hybrid pulsator would become meaningless: the pulsational characteristics of the δ Scuti class may need to be redefined to include p-, g and mixed-mode non-radial pulsations of both low and high frequencies.

Dupret et al. (2004) computed theoretical δ Scuti instability strips for stars of various masses and luminosities (refer to Figure 1.7) using a time-dependent treatment of convection. In conjunction with Figure 1.6, it can be observed that there is a large degree of overlap between the γ Doradus and δ Scuti instability strips that is not visible in Figure 1.1. This was further extended by Montalbán and Dupret (2007), who incorporated turbulence[34] into the pulsational modelling. There is strong evidence that the p-mode pulsations in δ Scuti stars are driven by the κ mechanism[35], particularly in the second partial ionisation zone of helium. The origin of the g- and mixed-modes in δ Scuti stars is currently unknown (Balona et al., 2015). The new revelations of Balona (2014) and Balona et al. (2015) necessitate additional investigation into the relationship between γ Doradus and δ Scuti stars.

[33] Refer to the section on radial pulsations (1.3.2) for more information
[34] Refer to the section on the rotational effects on pulsations (1.3.6) for more information.
[35] Refer to the section on driving mechanisms (1.3.1) for more information

1.5 Binary Stars

All of the stars analysed for this thesis are part of binary star systems, also called binaries. This means that each system is a pair of stars orbiting their common centre of mass or barycentre. The term "binary" was originally coined by Sir William Herschel in 1802 to refer to a gravitationally bound pair of stars that interact with other stars as an independent system. This definition differentiates binaries from other *double* stars that appear close to each other along the Earth's line-of-sight but are not gravitationally bound[36]. Although each constituent of a binary system is a separate star, they are catalogued as a single star, which is reasonable given that most binary stars are difficult to resolve visually even through the most advanced telescopes.

It has been theorised that approximately 60% – 80% of all stars are members of binary systems (Hogeveen, 1990, 1992). This implies that a large number of variable stars must also be in such systems. As of 2014, there have been more than 500 catalogued binaries with variable components (Zhou, 2014). In addition, of the 59 γ Doradus candidates surveyed by Mathias et al. (2004), more than half were in binary systems.

However, due to the difficulty of analysing binary stars, much less pulsational analysis has been done on variable stars in binary systems. Researchers such as Schrijvers and Telting (2002), Gamarova et al. (2005), Bohm et al. (2008), Sipahi and Dal (2014) and Keen et al. (2015) have performed mode identification of β Cephei, δ Scuti, Herbig Ae, γ Doradus and δ Scuti-γ Doradus hybrid[37] stars in binary systems respectively. Bíró and Nuspl (2005, 2011) have developed a method for the direct mapping of pulsations onto the surfaces of eclipsing binary stars[38] using photometric data. Although this technique has yet to see widespread use, Maxted et al. (2013) have successfully used this in their determination of the frequencies and modes of a stripped red giant[39] in an eclipsing binary system, 1SWASP J024743.37-251549.2A. However, this method only works with photometric data and only works for modes with $\ell - |m| \leq 4$ (Bíró and Nuspl, 2011).

Liakos et al. (2012) have done pulsational analysis of photometric data of eight δ Scuti stars in binary systems and attempted to relate them to the binary orbits. However, the results were non-definitive: no mode identification was performed and only a couple of frequencies were identified for each star. One of the most definitive mode identification efforts was performed by Schmid et al. (2014), who had performed an analysis of the δ Scuti star 4 CVn. They reported 20 pulsational frequencies and performed mode identification of the two dominant frequencies, 7.3764 d^{-1} and 5.8496 d^{-1}, characterising them as $(\ell, m) = (3, -2)$ and $(3, 3)$ modes

[36] These types of *double* stars are known as optical pairs.
[37] Refer to the section on δ Scuti stars (1.4.2) for more information.
[38] An eclipsing binary is a binary star whose orbital plane lies very close to the line-of-sight from the earth, such that each star either completely or partially blocks the light from the other star as they pass in front of each other.
[39] A stripped red giant is a red giant star whose outer layers have been stripped by mass transfer onto its companion star (this implies that these stars are in binary systems).

respectively. Nevertheless, the paucity of efforts in the pulsational analysis of variable stars in binary systems should be remedied.

1.5.1 Binary Orbits

One of the necessary tasks during the analysis of binary stars is the determination of the orbital equations of each component star. These equations describe elliptical Keplerian orbits[40]. The equations of motion can be constructed once the following constant orbital parameters, or orbital elements, are known:

P, the orbital period The time taken for each body to make one complete revolution around the barycentre.

e, the orbital eccentricity The degree of ellipticity of the orbit.

i, the orbital inclination The angle between the orbital plane and the plane normal to the line-of-sight. Not to be confused with the stellar inclination i.

T_0, the time of periastron passage A reference point in time used for calculating other orbital elements.

Ω, the longitude of the ascending node[a] The reflex angle between the ascending node and a fixed reference direction, used for calculating other orbital elements.

ω, the argument of the periastron The angle between the periastron and the ascending node.

a, the semi-major axis Half of the sum of the distance between the periastron and the apastron.

v_γ, the systemic velocity The radial velocity of the barycentre of the system.

K, the radial velocity semi-amplitude Half of the difference between the maximum and minimum radial velocity of an individual star.

[a] The ascending node is the furthest point along the line of intersection between the orbital plane and the plane normal to the line-of-sight (the plane of the sky).

P, T_0, e, ω and $a \sin i$ (the lower bound for a) can be determined from the analysis of spectroscopic data. Figure 1.8 is a visual representation of most of the orbital elements.

There are several conventions for the nomenclature of binary stars. For the purposes of this thesis, the brighter star of each binary (which also happens to be the variable one in all cases) is labelled as the primary and the dimmer star is labelled as the secondary. Quantities pertaining to the primary star are given the subscript 'A' and those pertaining to the secondary star are given the subscript 'B'. For example, the radial velocity semi-amplitude of the primary is represented by the symbol K_A.

[40] These orbits are idealised: the system is assumed to comprise only the two components of the binary and relativistic effects are ignored.

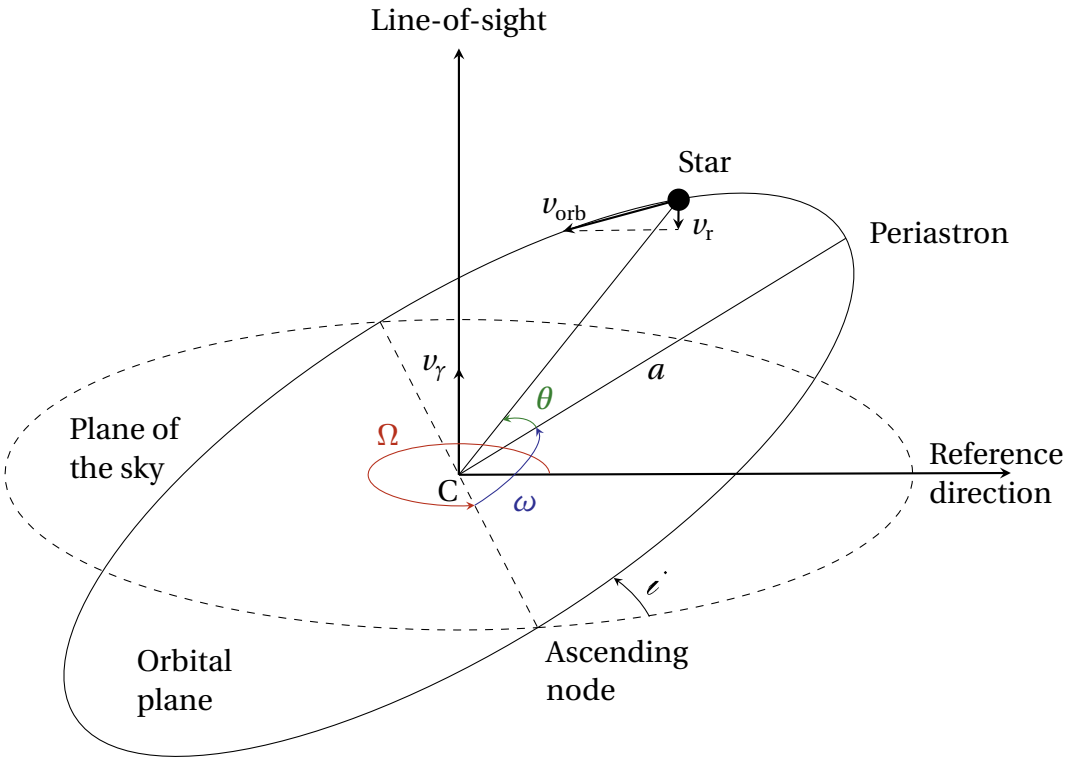

Figure 1.8: A schematic diagram of an elliptical orbit, showcasing most of the orbital elements. The barycentre of the system is marked with the letter C, with the associated systemic velocity v_γ. The radial velocity v_r is the projection of the orbital velocity v_{orb} along the line-of-sight. The angle θ represents the true anomaly. (Referenced on page 20, 21.)

The equation determining the variation of the radial velocity (v_r) (Bergmann, 2015) is:

$$v_r = v_\gamma + K[e\ \cos\omega + \cos(\theta + \omega)] \tag{1.5}$$

The radial velocity semi-amplitude (K) can be calculated using the equation:

$$K = \frac{2\pi a \sin i}{P\sqrt{1-e^2}} \tag{1.6}$$

The only variable in equation 1.5 is the true anomaly θ, the angle between the periastron and the position of the star with respect to the central point of the line of intersection between the orbital plane and the plane of the sky (refer to Figure 1.8).

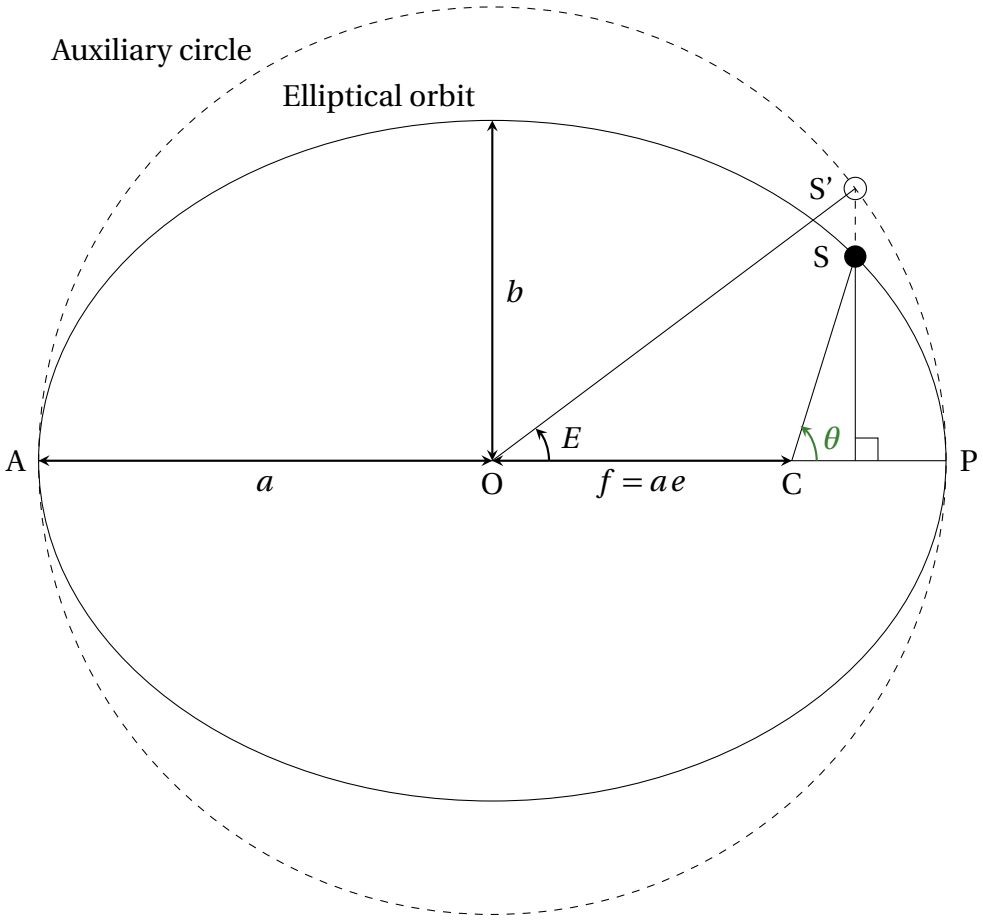

Figure 1.9: The eccentric (E) and true (θ) anomalies on a diagram of a two-dimensional elliptical orbit with $e = 0.25$. The periastron and apastron are marked by the letters P and A. The centre of the ellipse is marked by the letter O and one of the foci of the orbit (the barycentre) is marked with the letter C. The semi-major axis a, semi-minor axis b and the focal distance $f = a\,e$ are indicated on the diagram. Point S represents the position of a star and point S' is the projection of the star onto the auxiliary circle, which is a circle with a radius equal to the semi-major axis of an ellipse and with the same centre. (Referenced on page 23.)

In order to calculate the θ, it is necessary to introduce two new terms: the mean anomaly M and the eccentric anomaly E. The mean anomaly is colloquially referred to as the "orbital phase": it varies from 0 to 2π as the star makes one complete orbit. It can be calculated using the equation:

$$M = \frac{2\pi}{P}(t - T_0) \tag{1.7}$$

t is the time at a particular phase of the orbit. The eccentric anomaly E (indicated on Figure 1.9) can then be calculated using Kepler's equation. Note that this equation is transcendental and cannot be solved analytically. A numerical method (such as the Newton-Raphson method) must be used to obtain a solution.

Kepler's equation takes the following form:

$$M = E - e \sin E \tag{1.8}$$

Once E has been determined, θ can be calculated using the equation[41]:

$$\tan\left(\frac{\theta}{2}\right) = \sqrt{\frac{1+e}{1-e}} \tan\left(\frac{E}{2}\right) \tag{1.9}$$

Figure 1.10 shows how the shape of the radial velocity curve changes with different values of e and ω.

1.5.2 Spectroscopic Binaries

The binary stars analysed for this thesis are spectroscopic binaries. This means that the individual components cannot be resolved, due to the stars being too distant from the Earth, their orbital separation being too small, or a combination thereof. Instead, only a single star is seen through the telescopes. The binarity of the system is given away by the Doppler shift of the spectral lines which depends on the radial velocity along the line-of-sight.

Spectroscopic binaries can be divided into two broad groups: single-lined spectroscopic binaries (SB1s) and double-lined spectroscopic binaries (SB2s). SB1s are spectroscopic binaries where only one set of spectral lines, belonging to the primary star, are visible in the spectra. The presence of the secondary star is inferred by the Doppler shift of the spectral lines of the primary star[42].

SB2s are spectroscopic binaries where two sets of spectral lines, belonging to the primary and secondary star respectively, are visible in the spectra. These lines red- and blue-shift alternately depending on the orbital phase. The spectral lines belonging to the primary star are typically more prominent than those of the secondary star. As such, when the radial velocity of each star along the line-of-sight is small, the spectral line belonging to the secondary star becomes blended with the spectral line of the primary star. All of the stars analysed for this thesis are SB2s and this phenomenon makes pulsational analysis more difficult. Figure 1.11 shows how the spectral lines of an SB2 shift with the binary orbit.

[41] For a rigorous derivation of the equations in this section, please refer to either Ramm (2004) or Bergmann (2015).
[42] Note that other celestial bodies, such as planets, also cause Doppler shifts of the spectral lines of the star. These shifts are much smaller in magnitude as planets are much smaller in mass.

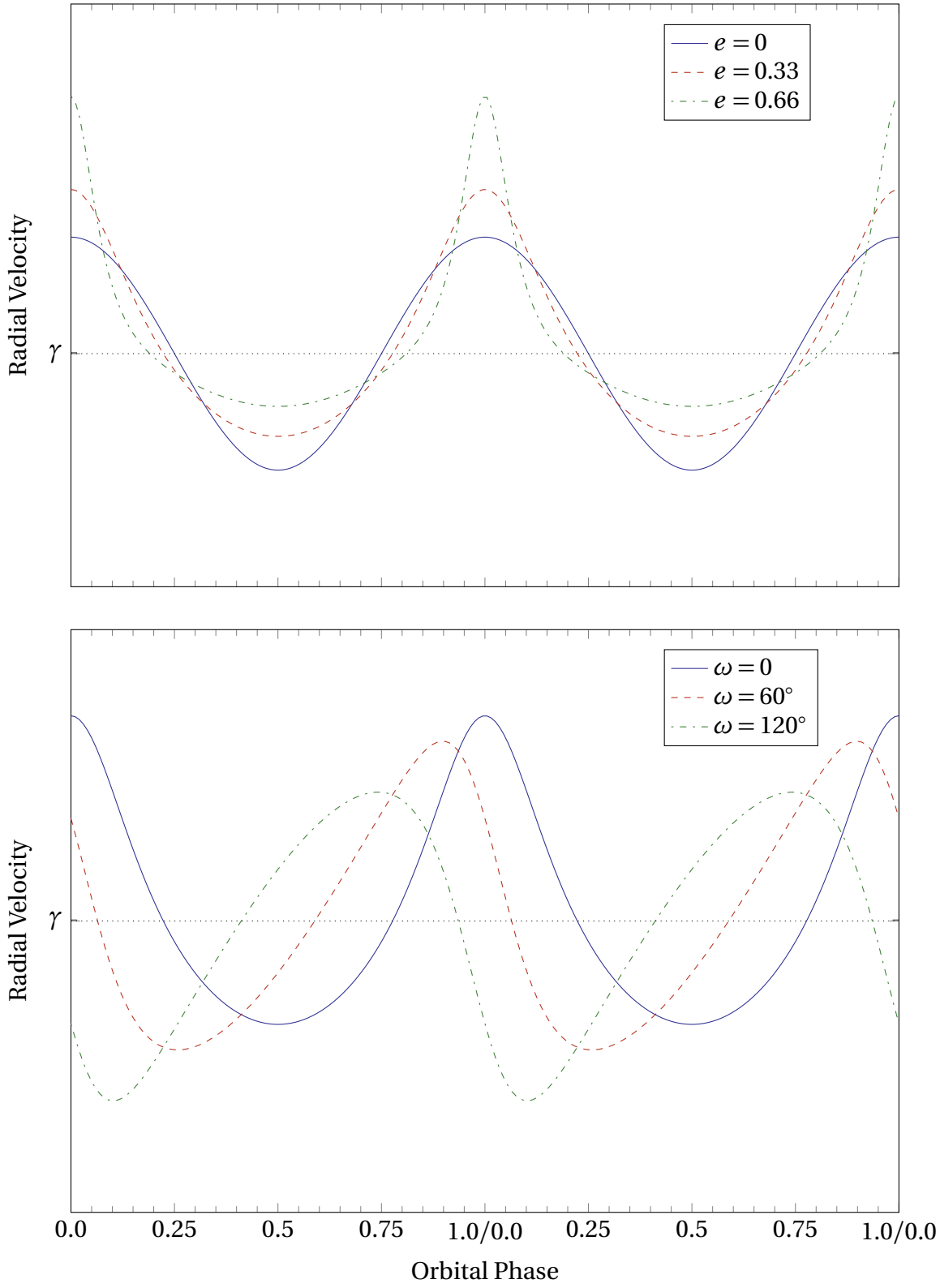

Figure 1.10: Radial velocity curves of orbits with different e and ω. The top panel shows curves with e =0, 0.33 and 0.66, with ω fixed at 0°. The bottom panel shows curves with $\omega = 0°$, 60° and 120°, with e fixed at 0.33. (Referenced on page 23.)

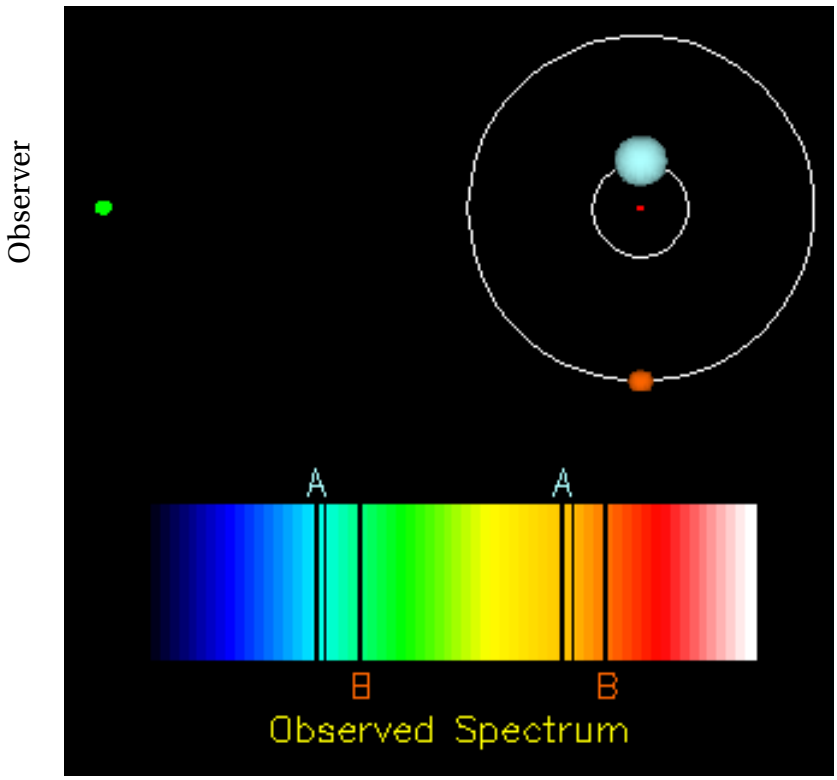

Figure 1.11: An animated diagram illustrating the Doppler shift of spectral lines in an SB2 spectrum. The green dot represents the position of the observer, the larger blue sphere represents the primary star (A) and the smaller red sphere represents the secondary star (B). The spectral lines corresponding to the A and B are colour-coded accordingly and marked on the absorption spectrum below. The animation showing the orbital motion and the corresponding Doppler shift can be viewed in Adobe Reader. Animation obtained with permission from Dr. Richard Pogge (http://www.astronomy.ohio-state.edu/~pogge/Ast162/Movies/specbin.html). (Referenced on page 23.)

1.6 Thesis format and goals

As mentioned in the previous sections, there has been little definitive research done on variable stars in binary systems, particularly γ Doradus and δ Scuti stars. The overarching goal of this research is the precise determination of the frequencies and modes of oscillation of three pulsating stars in binary systems, two γ Doradus stars and one δ Scuti star. The secondary goals of this research are to investigate the relationship between the γ Doradus and δ Scuti classes, based on the analyses of these stars and the revelations of Balona (2014), and the effects, if any, of the binary orbit on the pulsational characteristics of these stars.

A detailed description of the data collection and analysis methodologies is provided in Chapter 2. Two γ Doradus stars and one δ Scuti star, HD 182640, HD 3112 and HD 147787, are analysed and the results detailed in their respective chapters. A brief overview of each star is presented before a thorough evaluation of their orbits and their pulsational frequencies and modes. Brief discussions of the results of the orbital and pulsational analysis are also included at the end of each chapter. This thesis concludes with Chapter 6, where the author's thoughts on the relationship between the γ Doradus and δ Scuti classes and conclusions on the effects of binarity on the pulsational characteristics of variable stars are presented. This chapter also includes a summary of the thesis itself along with suggestions for the expansion and progression of the research scope presented in this thesis.

2 Data Collection and Analysis

2.1 Observational Data

2.1.1 University of Canterbury Mount John Observatory (UC MJO)

All of the data used in this analysis had been collected at the University of Canterbury Mount John Observatory (UC MJO). UC MJO is located on Mount John near the township of Tekapo in New Zealand's South Island. The coordinates of UC MJO are 170° 27.9′ E 43° 59.2′ S, at an elevation of 1029 m above sea level. The spectroscopic data were obtained from the High Efficiency and Resolution Canterbury University Large Échelle Spectrograph (HERCULES), attached by an optical fibre to the 1-metre McLellan Telescope (Hearnshaw et al., 2002).

The HERCULES spectrograph has an efficiency of between 5 % to 15%, depending on seeing and wavelength (Barnes, 2004). It is also capable of a maximum resolving power of $R = 82000$ when attached to the 50 μm diameter optical fibre (Barnes, 2004). However, the observational data used in this thesis were recorded through the 100 μm fibre, which has a resolving power of $R = 41000$ (Barnes, 2004).

The 100 μm optical fibre was used for the observations as the binaries analysed for this thesis (with the exception of HD 182640), had apparent magnitudes from 5 - 6. Using the 50 μm fibre would necessitate significantly longer exposure times, smoothing out the pulsational variations in the spectral lines of the stars and resulting in a decreased ability to detect the frequencies and modes of said pulsations. This outweighs the benefits of the increased resolving power afforded by the 50 μm fibre. In addition, the 100 μm fibre has an acceptance angle of 4.2″ (Hearnshaw, 2009), which allows for increased light throughput compared to the 50 μm fibre. This results in greater signal-to-noise ratios and hence usability of observations taken during poor seeing conditions.

The spectra from HERCULES were recorded on a 4096 by 4096 pixel CCD (Fairchild model 486) chip, with each pixel measuring 15 μm across. This allows échelle spectra over a wavelength range from 380 nm to 880 nm to be recorded in a single exposure (Hearnshaw et al., 2002).

2.1.2 Observational Timeframe and Target Selection

The spectroscopic data in this analysis (totalling approximately 2500 stellar spectra) have been collected in a series of observing runs between 2008 and 2015 (Table 2.1) as part of the MUSICIAN project (Pollard et al., 2014). Three binaries were analysed for this thesis: HD 182640, a system with a candidate γ Doradus primary (Koen and Eyer, 2002); HD 3112, a system with a bona fide δ Scuti primary (De Mey et al., 1998); and HD 147787, a system with a candidate γ Doradus primary (De Cat et al., 2009). Although most of the observations, (particularly those of HD 182640) were done by others, the author had obtained a significant number of spectra (approximately 300) during several observing runs at UC MJO in 2015.

All of the stars chosen for analysis in this thesis displayed significant spectral line profile variation[1] and were noted to be bright enough to produce spectra with high signal-to-noise ratios (>100) with reasonably short exposure times (~10-20 min). This made them good targets for pulsational analysis.

HD 3112 and HD 147787 were chosen as targets for analysis as each had over 100 archived UC MJO spectra and had not been previously analysed in detail. Each binary also had primaries that belonged to a different class of non-radial pulsator (γ Doradus and δ Scuti), enabling a basis of comparison of the orbital effects, if any, of the pulsations of two different classes of pulsators.

HD 182640 has been analysed by Dr. Emily Brusden in her PhD thesis (Brunsden, 2013); she had mentioned that she was unable to determine the frequencies and modes of the pulsations of the primary star, attributing it to a relatively imprecise orbital solution and a lack of observational data as a whole (Brunsden, 2013). Brunsden had also indicated that enough data would have been gathered by the time her thesis was published (July, 2013) to have sufficient temporal coverage of the entire (rather long) orbital period of the star (approximately 1250 days). In light of this new information and in an attempt to solve a previously unsolved mystery, HD 182640 was chosen as one of the targets for analysis.

Table 2.1: The apparent magnitude, typical exposure times, obervational timeframes, number of spectra and the observers of the three binaries analysed for this thesis. (Referenced on page 28, 29, 59, 80, 103.)

Star	m_V	Exp. Times (min)	Timeframe	No. of Spectra	Observers[a]
HD 182640	3.38	1-5	Mar 2009 – Aug 2015	1355	FMG, PMK, KRP, SS
HD 3112	6.12	10	Jul 2014 – Aug 2015	595	EJB, FMG, PMK, SS
HD 147787	5.27	5-30	Feb 2008 – Aug 2015	480	EJB, FMG, PMK, SS

[a]Emily Brunsden (EJB), Fraser Gunn (FMG), Pam Kilmartin (PMK), Karen Pollard (KRP) and Sanjay Sekaran (SS).

[1]Refer to the section on cross-correlation (2.2.3) for more information

2.1.3 Observational Methodology

During each night of observation, three different types of spectra are recorded. Flat-field and thorium-argon images were used for the calibration of the stellar images. All of the raw data were saved as FITS files and archived for future analysis.

Flat-field spectra (e.g. Figure A.1) were obtained by passing white light from an incandescent tungsten lamp through the spectrograph and recording the image with the CCD. Flat-field spectra are relatively featureless (i.e. they have no absorption or emission lines) and were used primarily for spectral order tracing and CCD intensity response correction (during the flat-field spectral processing step). The white tungsten lamp is relatively bright: a 1-second exposure time is sufficient to obtain well-exposed flat-field spectra. At least 10 flat-field spectra[2] were taken either at the beginning or the end of every single night of observation.

Thorium-argon spectra (e.g. Figure A.2) were obtained by passing the light of a thorium-argon emission lamp through the spectrograph and recording it on the CCD. Each thorium-argon spectrum contains several thousand emission lines with well-known wavelengths which, in combination with the flat-field spectra, can be used to determine the wavelengths of the spectral orders of each stellar spectrum (during the stellar spectral processing step). The exposure time for thorium-argon spectra is between 4 to 6 seconds, depending on the brightness of the lamp. This brightness varies depending on the input current (which is set every night to the same level) and the age of the lamp (which grows dimmer over time and must be replaced periodically). Thorium-argon spectra were taken at roughly hourly intervals as well as before and after observing each star.

Stellar spectra (e.g. Figure A.3) were obtained passing the light of the target star through the optical path of the telescope and the spectrograph and recording it on the CCD. The exposure times vary depending on the apparent magnitude of the star being observed and the seeing conditions at the time of observation (refer to Table 2.1). HD 3112 was the only exception to this rule (the exposure times were fixed at 10 min). Increasing the exposure time would render some of the high frequency pulsations[3] (δ Scuti-type pulsations have periods of about 0.5 to 6 hours) more difficult to detect by smoothing them out and the star was too faint to reduce the exposure time, even on the best of nights (in terms of seeing). In order to maximise the signal-to-noise ratios of the recorded stellar spectra, the general observing strategy was to expose the image for a long enough time period such that the exposure meter[4] shows about 1.5 to 2.5 million counts.

[2] This was not always the case: insufficient numbers of flat-field spectra were recorded on some nights. The explanation of how this was dealt with is provided in the section on the data reduction setup (2.2.1).
[3] Refer to the section on δ Scuti stars (1.4.2) for more information.
[4] The exposure meter is a photomultiplier tube that records the number of photoelectrons that are incident on the CCD. This gives the observer an estimate of the degree of exposure of the CCD to different types of incident light.

2.2 Spectroscopic Data Reduction

2.2.1 Data Reduction Setup

The raw stellar images have to be converted into a more useful format in order to be analysed. Spectroscopic data reduction is the removal of data artifacts, variables intrinsic to the observational equipment and the standardisation of observations, including wavelength calibration, for further analysis. This was done through two separate MATLAB code pipelines.

The first data reduction pipeline identifies the type of image (either flat-field, thorium-argon or stellar) from the headers of the FITS files saved in the archives. It then processes all of the images pertaining to each star and extracts the stellar orders of each observation in a flux versus wavelength format. It was originally written by Dr. Duncan Wright (Wright, 2008) with some usability and efficiency enhancements by Mr. Aaron Greenwood (Greenwood, 2014).

The raw data are archived according to the date of the night on which they were recorded. All of the flat-field, thorium-argon and stellar images recorded on a single night are usually processed as a single "run." However, insufficient numbers of flat-field images were taken on some nights. This necessitated the manual indexing of multiple nights of data as a single run. The raw data is reduced on a "run-by-run" basis.

The second data reduction pipeline standardises the wavelength of each order across all of the observations of each star, performs barycentric and systemic velocity correction, performs a continuum fit and finally, merges the stellar orders to produce a normalised stellar spectrum. It then cross-correlates each spectrum with a synthetic spectral template to produce radial velocity line profiles of each observation. This pipeline was written by Dr. Duncan Wright (Wright, 2008) with additions and modifications by Dr. Emily Brunsden (Brunsden, 2013) and some usability and efficiency enhancements by Mr. Aaron Greenwood (Greenwood, 2014).

2.2.2 First Data Reduction Pipeline

Flat-Field Spectral Processing

The flat-field images were first manually examined to ensure that there were no overexposed or underexposed images. An automated statistical comparison was then carried out to ensure that the images had no significant variation from each other. The images were then summed to create a master flat-field image for each run. The blue (short wavelength) section of the master flat-field image, corresponding to the first 1000 rows of the CCD, were then removed as they were too noisy to be useful.

Next, the positions and widths of the spectral orders on the CCD for that run were determined. This enables the locating of those orders on thorium-argon and stellar images later on.

The background signal was then extracted, modelled and subtracted from the master flat-field image by performing cubic spline interpolation[5] through the inter-order regions.

Cosmic-ray removal was then performed to account for the occasional cosmic ray that infiltrates the flat-field images during the 1-second exposures. The intensity values of each pixel of the master flat-field image were used to remove pixel-to-pixel sensitivity variations of the CCD chip in the stellar spectral processing step.

Thorium-Argon Spectral Processing

After the flat-field images were processed, the thorium-argon images were checked to ensure minimal pixel-to-pixel deviations. Overexposed, underexposed and incorrectly saved images that were identified by the check were then discarded. The blue section of the thorium images that correspond to the first 1000 rows of the CCD were removed (as per the reasoning in the flat-field spectral processing step). The emission lines on each image were then located using a calibration matrix containing the pixel coordinates of several thousand lines. The most intense lines of the thorium-argon spectra were in the infra-red region. As such, a large portion of each thorium-argon image was unavoidably overexposed (refer to Figure A.2) and was not used for calibration.

If too few emission lines (less than 600) were located using the matrix, the user would be notified. A new calibration can then be performed using the current thorium-argon image as a template. This was then saved and applied to subsequently analysed thorium-argon images. Once the thorium-argon spectral lines were located, a wavelength solution[6] was obtained by fitting a fourth-order polynomial through the positions of the spectral lines with reference axes defined by the master flat-field image.

Stellar Spectral Processing

Once the wavelength solutions of all of the thorium-argon images were determined, the blue section of the stellar images that correspond to the first 1000 rows of the CCD were removed (as per the reasoning in the flat-field spectral processing step). The background signal was extracted, modelled and subtracted from the stellar images (as per the method in the flat-field spectral processing step). Each stellar order was then extracted using the master flat-field information and cosmic-ray removal was performed.

The wavelength solution for each stellar image was then determined by linearly interpolating the wavelength solutions of the two closest thorium images taken before and after the

[5] Cubic spline interpolation is the fitting of cubic polynomials piecewise between a set of data points to produce a smooth curve.

[6] A wavelength solution is a function that specifies the wavelength ranges for each bin of each order of a stellar spectrum.

stellar image. This was necessary[7] as the wavelength solution depends on the whole telescope/spectrograph/CCD system, which can exhibit minute physical deformations depending on the temperature and pressure changes throughout the course of a night or a run.

The final wavelength solution and the flat-field information was used to calculate the wavelengths and to normalise the intensities of each bin[8] of each order of each stellar spectrum. The data corresponding to each observation were then saved as separate MATLAB readable `.mat` files and were processed later by the second data reduction pipeline.

2.2.3 Second Data Reduction Pipeline

Wavelength and Velocity Correction

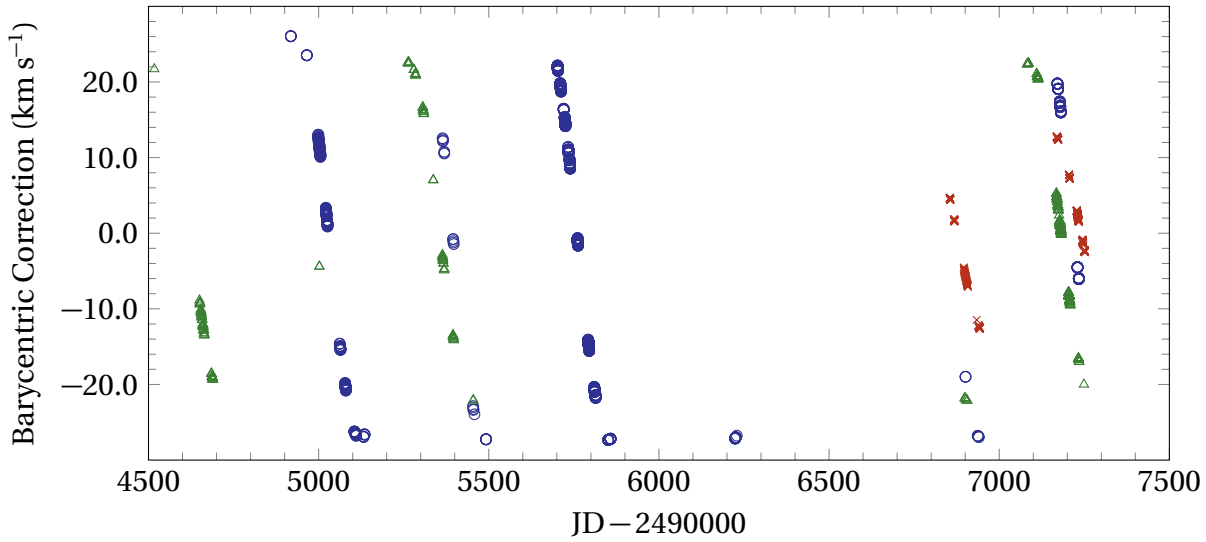

Figure 2.1: Barycentric correction values for HD 182640 (blue circles), HD 3112 (green triangles) and HD 147787 (red crosses), with respect to the Julian dates of each observation. (Referenced on page 32.)

The next step in the reduction would be to standardise the spectral orders. To do that, the `.mat` files of each observation were loaded and the wavelength range of each order[9] across all of the observations was equalised. This was done by first locating the order with the smallest wavelength range across all of the observations and trimming away the wavelength bins of the other orders that were not within the wavelength range of the smallest order. Next, barycen-

[7] The spectral lines can shift by up to 0.1 pixels (Ramm, 2004) during the course of a night. This corresponds to a maximum wavelength shift of 1 Å

[8] A bin is a computational data structure that contains information pertaining to a region in a two- or three-dimensional image. In the case of stellar images, a single bin contains the intensity and wavelength values of a single pixel.

[9] Only 40 spectral orders (orders 84-124) were processed by the second data reduction pipeline, corresponding to a wavelength range of 4550-6850 Å. The other orders had too few and weak spectral lines to be useful and were thus discarded.

tric correction[10] was performed using the barycentric correction module of the HERCULES Reduction Software Package (HRSP), written by Dr. Jovan Skuljian (Skuljian, 2004). Figure 2.1 shows the variation of the barycentric correction values for each star with the Julian date.

The order-to-order differences[11] were then removed by dividing each order by the median intensity of a particular order across all observations. A variable-degree polynomial was then fitted to each order to approximately normalise each order (to simplify the continuum fitting process). The wavelength bins were then Doppler shifted to correct for the systemic velocity[12].

Continuum Fitting and Spectral Order Merging

Continuum fitting is the identification of the continuum level of each stellar order for the purposes of normalising the stellar spectra. This was done manually by comparing the mean stellar spectrum with a synthetic spectrum of a star with the same effective temperature ($T_{\rm eff}$), metallicity ([Fe/H]) and logarithm of surface gravity ($\log g$)[13], generated by the program SYNSPEC (Zboril, 1996; Hubeny and Lanz, 2011).

Each order was fitted with a variable-order polynomial[14] created by cubic spline interpolation through manually-defined points on the mean spectrum. Each order of each observation was then divided by the continuum-fitting function to normalise them. A final cosmic-ray removal, to catch any cosmic rays that may have made it past the other filters, was then carried out before the orders were merged to produce continuous and normalised stellar spectra. Figure 2.2 is a snapshot of the continuum-fitting process for HD 3112 and Figure 2.3 is the mean stellar spectrum of HD 182640.

[10] Barycentric correction is the correction of data for the effect of the Earth's movement around the barycentre of the Solar System.
[11] The spectral orders have overlapping wavelength ranges. The intensity values of the wavelength bins in these regions are sometimes markedly different.
[12] The stellar parameters used in the reduction process are typically the approximate mean or mode of the published literature values. Refer to the section on binary orbits (1.5.1) for more information
[13] The stellar parameters used in the reduction process are typically the approximate mean or mode of the published literature values.
[14] Each polynomial had a minimum degree of six.

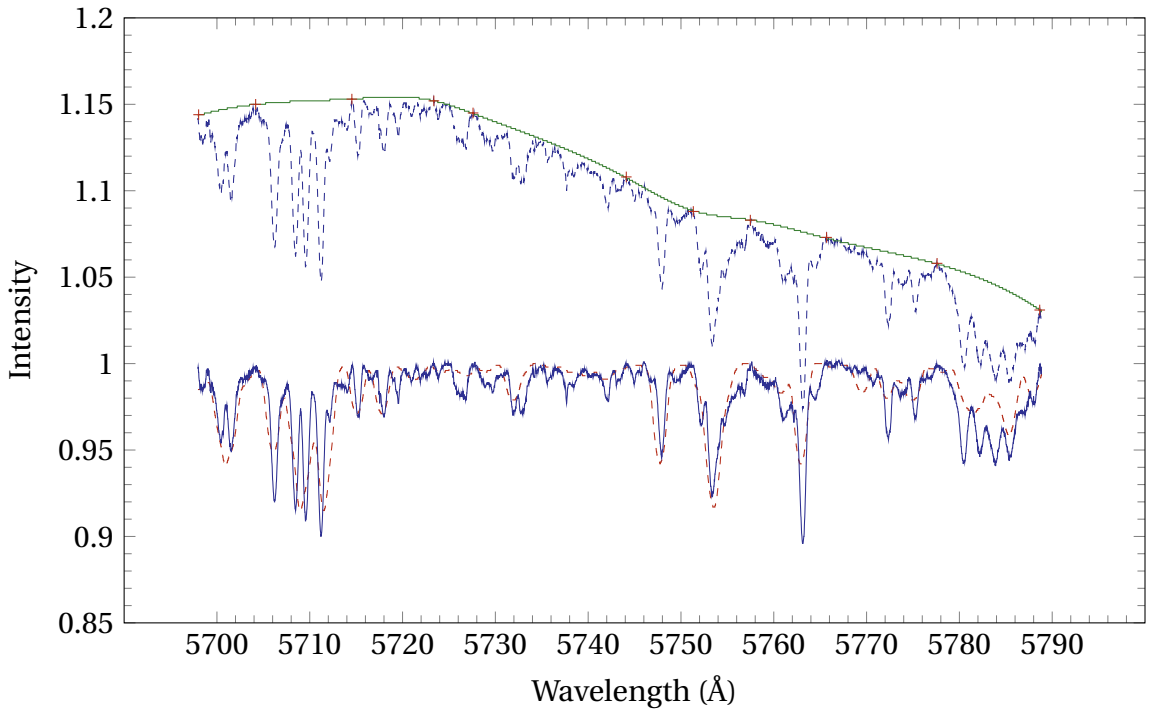

Figure 2.2: A snapshot of the continuum-fitting process for spectral order 99 of HD 3112. The dashed blue line is the non-continuum fitted spectral order, the red plusses are the manually-defined continuum points and the solid green line is the continuum level. The intensity values have been offset by +0.1 for comparison. The solid blue line is the normalised spectral order and the dashed red line is the synthetic spectral order generated by SYNSPEC. (Referenced on page 33.)

Cross-Correlation

The final step in the data-reduction process is the creation of cross-correlated[15] line profiles of each stellar observation. Cross correlating multiple spectral lines increases the signal-to-noise ratio while retaining periodic line profile variations. These line profiles were then used for spectroscopic variability analysis: the identification of the frequencies and modes of pulsation for each star.

Before that can be done, several spectral regions around telluric lines[16], broad hydrogen lines (Hα, Hβ and $H\gamma$) and weak lines (spectral lines narrower than 0.5 mÅ) were removed from each stellar spectrum. Cross-correlating the telluric lines would reproduce the barycentric motion of the Earth due to their terrestrial origin. The broad hydrogen lines exhibit Stark broadening, which smooths out the variation in the wings of each spectral line. They hence do not display the same pulsational variation as other stellar lines. In addition, these lines are so

[15] Cross-correlation is a mathematical function that describes the similarity between two other functions with respect to the lag of one relative to the other.

[16] Telluric lines are absorption lines in a stellar spectrum that are the result of elements in the Earth's atmosphere absorbing the light from the star.

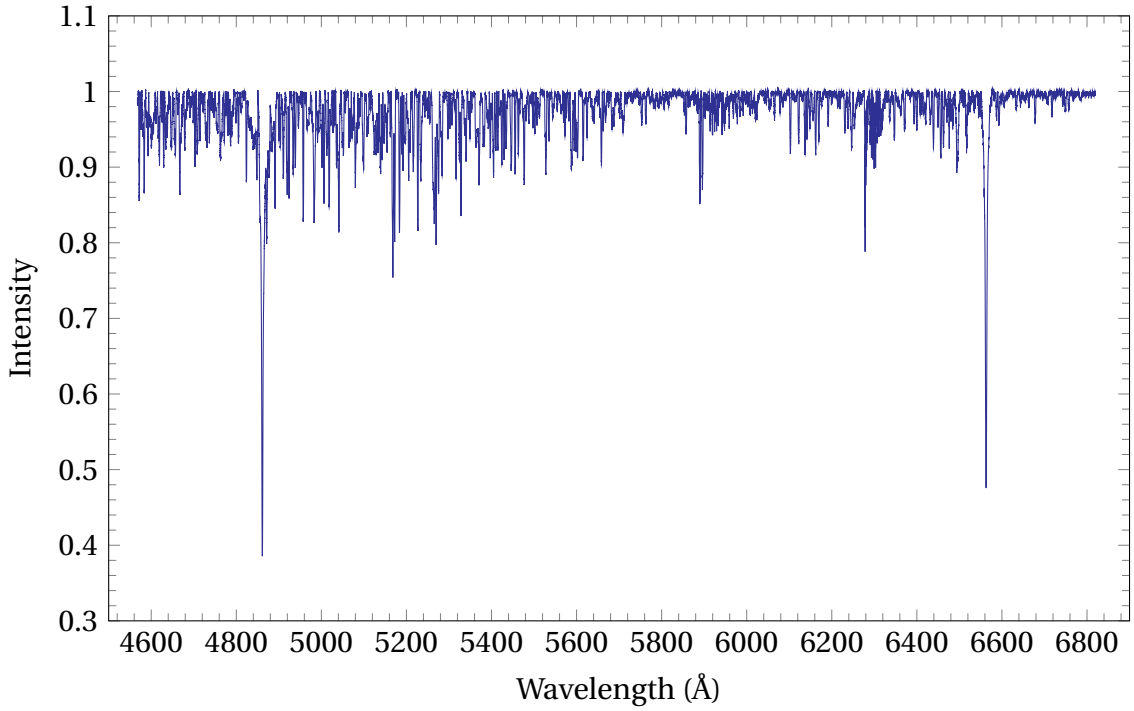

Figure 2.3: The mean stellar spectrum of HD 182640. (Referenced on page 33.)

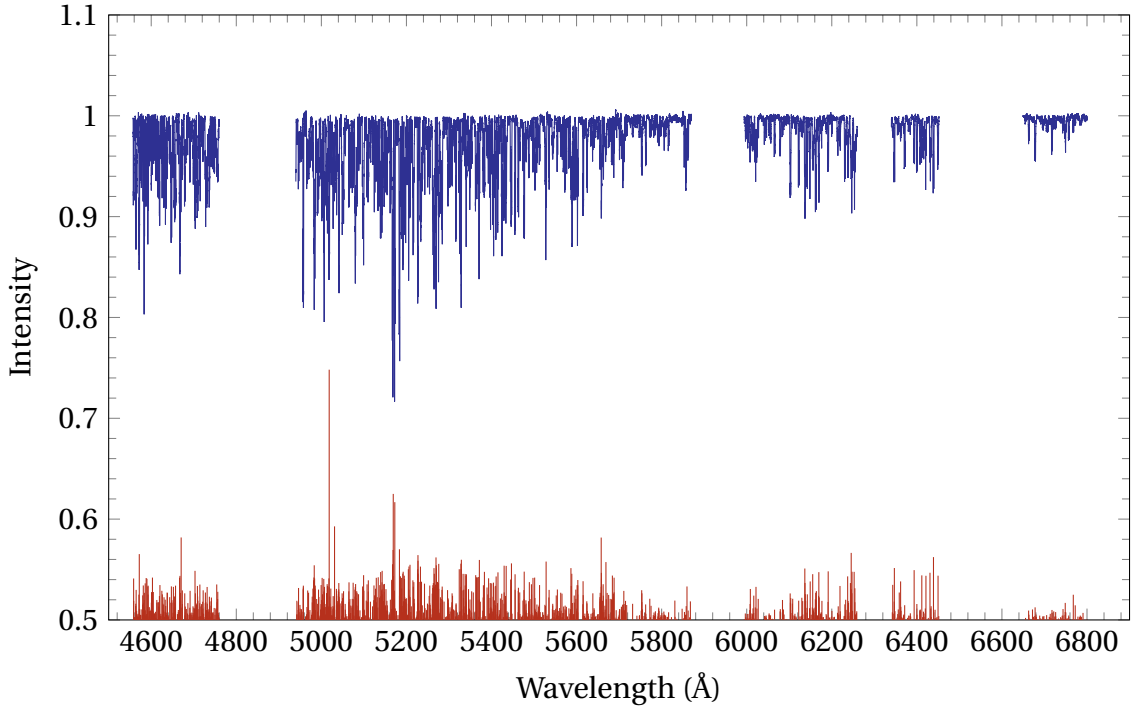

Figure 2.4: The mean stellar spectrum (in blue) of HD 147787, with the hydrogen and telluric regions removed. The δ-function template (in red), used for cross-correlation, was generated from a line list created by SYNSPEC. Note that the scaling of the delta functions in this figure is arbitrary. (Referenced on page 36.)

broad that they are blended with many of the lines that are adjacent to them, distorting their shape. Weak lines were omitted because they did not display significant pulsational variation, due to the low signal-to-noise ratios of these lines. Approximately 2000-5000 stellar spectral lines are left after these lines are removed.

A template of δ-functions (Wright, 2008) was created from a spectral line list drawn from SYNSPEC (approximately 1500 lines). The line depth of these δ-functions were then scaled according to the depths of the corresponding lines in the mean stellar spectrum. Using the rotational broadening functions of Gray (2005), the δ-functions were rotationally broadened by the v sin i of the star[17]. The cross-correlation process was then carried out by determining the amount, in radial velocity space, by which the template had to be shifted in order to match with each stellar spectrum. Once this was done, spectra with low signal-to-noise ratios (<40) were discarded as they would make the spectroscopic variability analysis more difficult[18]. Figure 2.4 is a plot of the mean spectrum of HD 147787 with the hydrogen and telluric regions removed, along with the δ-function template used for cross-correlation.

The range of radial velocities of the line profiles was selected from -150 km s^{-1} to 150 km s^{-1}. This encompasses the signals of the both primary and secondary stars in all observations while removing a large portion of the "flat" wings of the profiles which contain little information. Figure 2.5 shows all of the cross-correlated line profiles of HD 147787 on a single set of axes, together with the mean line profile.

2.3 Binary Analysis

Before the line profiles can be analysed to determine the frequencies and modes of oscillation, the signal of the secondary star in each binary must be removed from the line profiles. In addition, the signal of the primary star must be Doppler shifted to correct for the radial velocity. The binaries analysed for this thesis have non-variable secondary stars. As such, the signal of the secondary star in the line profiles can be approximated[19] by a Gaussian of fixed height and fixed width. The signal of the primary star also exhibits pulsational deviation from a Gaussian profile, preventing precise Gaussian fitting. However, this deviation is not significant enough to render the Gaussian fitting method unusable. Nevertheless, it is a factor which must be accounted for.

[17] The stellar parameters used in the reduction process are typically the approximate mean or mode of the published literature values.

[18] Low signal-to-noise spectra increase the chance that a false frequencies and modes are identified during the frequency and mode identification process.

[19] The signal of the secondary star varies slightly with each observation due to instrument and reduction errors. It is therefore not possible to perfectly match the signal of each secondary with a Gaussian of fixed height and width.

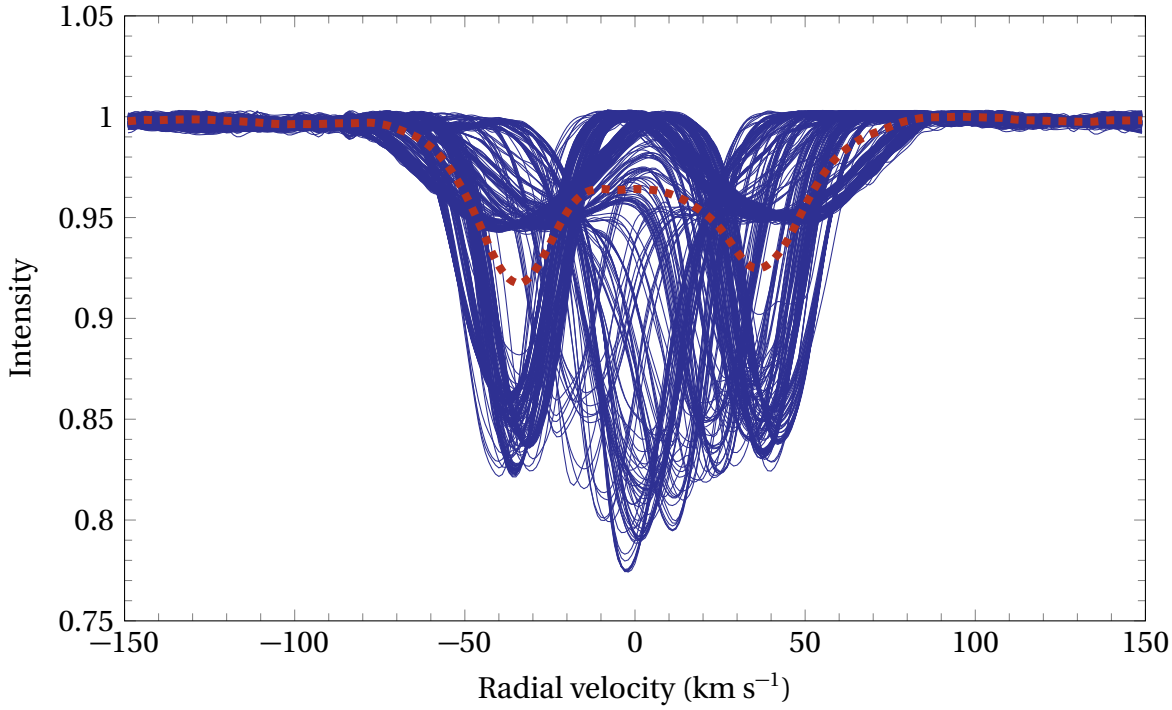

Figure 2.5: The cross-correlated line profiles (solid blue) of HD 147787, with the mean line line profile (dashed red). (Referenced on page 36.)

2.3.1 Orbital Analysis

The first step in this process is the determination of the radial velocities of each component of each binary system[20]. To do that, a Gaussian-fitting code from Bergmann (priv. comm.) was used to fit two Gaussians to the line profiles. The central positions of each Gaussian are the recorded as the respective radial velocities. While this allowed the relatively accurate measurement of velocities for the observations with well-separated peaks (high radial velocity separation), the velocity measurement for the observations with merged peaks (low radial velocity separation) was highly inaccurate as the heights and the widths of the Gaussians are unconstrained. Figure 2.6 shows the Gaussian fitting process for one of the observations of HD 3112.

A preliminary orbital fit was first computed using an orbital-fitting code from Bergmann (priv. comm.). Any radial velocities that deviated significantly from the initial fit were identified visually and flagged. A second orbital fit was then performed using the "good" radial velocities[21]. Figure 2.7 shows the component orbital fits to the velocities of HD 147787. Note that the scatter of the velocities of the primary is greater than that of the secondary due to the

[20] Note that the orbital analysis and line profile correction process for HD 182640 is slightly different from that which is described here. Refer to the section on the orbital analysis of HD 182640 (3.3) for more information.
[21] Note that these fits are weighted according to bootstrap errors calculated during the Gaussian-fitting process.

pulsations.

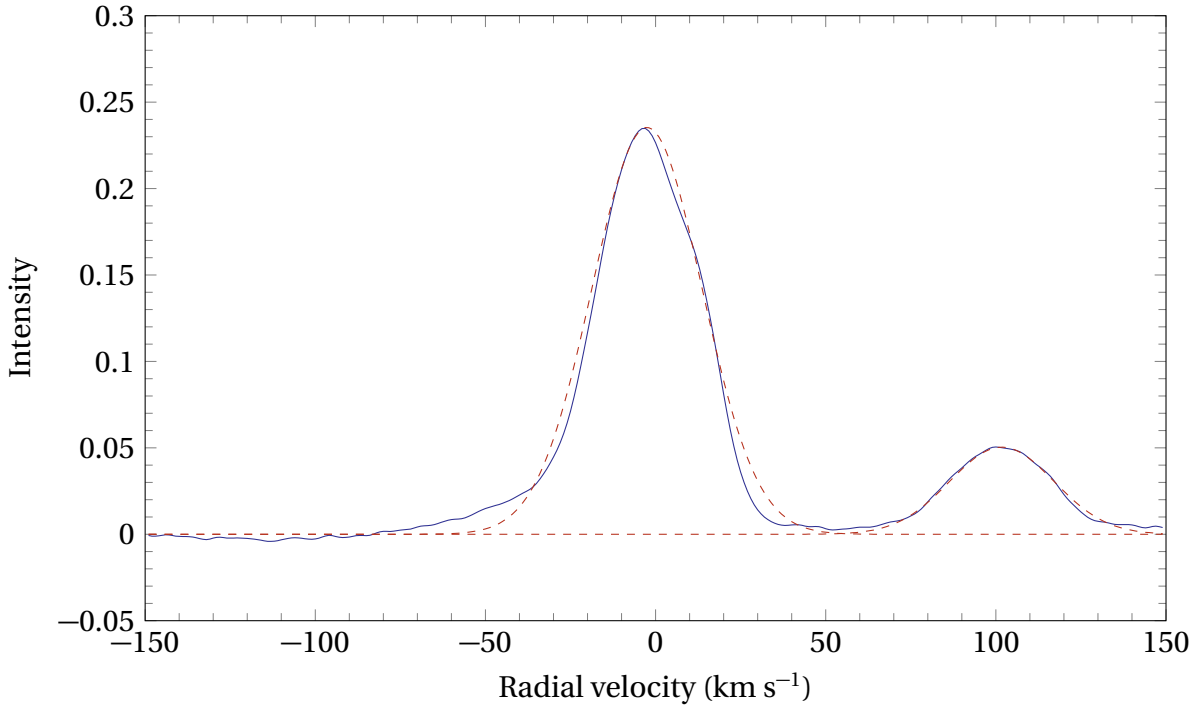

Figure 2.6: The Gaussian-fitting process for one of the line profiles of HD 3112. The solid blue line is a single cross-correlated line profile and the dashed red lines are the best-fit Gaussians to each peak. Note that the Gaussian fit to the primary peak is not as good as the Gaussian fit to the secondary peak. (Referenced on page 36.)

After the orbital fits to the velocities of each component were performed, the orbital elements of the system can be determined. This was done by using the weighted mean method. As the name suggests, the system orbital elements are calculated by taking the weighted mean of the component orbital elements.

The weighted mean ($\bar{x}$) of the orbital element x can be calculated using the equation:

$$\bar{x} = \frac{\sum_{i=1}^{n} w_i x_i}{\sum_{i=1}^{n} w_i} \tag{2.1}$$

x_i is the value of orbital element of the i^{th} component of the system, w_i is the weight assigned to the orbital element of the i^{th} component and n is the total number of components, which in the case of binaries is 2. The weights assigned to each orbital component are determined by taking the square of the reciprocal of the uncertainty estimate ($1/\sigma^2$) for each component orbital element.

The equation therefore simplifies to the following form:

$$\bar{x} = \frac{\frac{x_1}{\sigma_1^2} + \frac{x_2}{\sigma_2^2}}{\frac{1}{\sigma_1^2} + \frac{1}{\sigma_2^2}} \tag{2.2}$$

The corresponding uncertainty of the weighted mean ($\bar{\sigma}$) can be calculated using:

$$\bar{\sigma}^2 = \sigma_1^2 + \sigma_2^2 \tag{2.3}$$

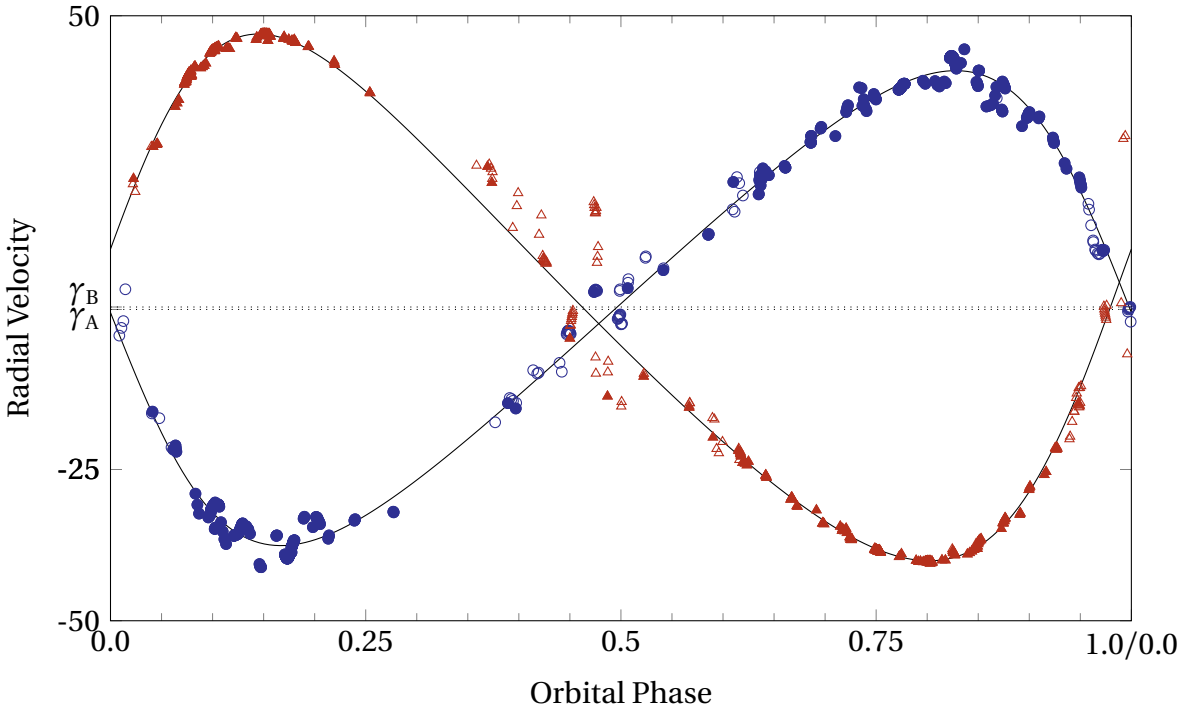

Figure 2.7: The component orbital fits (solid black lines) to the measured radial velocities of HD 147787. The blue circles and the red triangles represent the primary and secondary radial velocities respectively. The filled circles and triangles are the velocities that were used for the second orbital fitting. The dotted black lines represent the component systemic velocities (which in this case are very close). (Referenced on page 37.)

2.3.2 Line Profile Correction

The radial velocities of each component of each observation were then calculated from the individual orbital fits. Even though the measured velocities for the well-separated observations is fairly accurate, each velocity measurement is subject to some degree of measurement error. However, the scatter of velocities about the orbital fit curves is expected to be fairly uniform, given sufficient orbital phase coverage. As such, using the calculated velocities mitigates the effect of measurement errors.

The signal of the secondary star was then removed from the line profiles by subtracting Gaussians from each line profile. These Gaussians have heights and widths equal to the mean height and width of the Gaussians fitted to the secondary star of the well-separated line profiles, and central positions specified by the calculated secondary radial velocities. The line profiles were then Doppler shifted by the calculated primary radial velocities, resulting in a set of single-peaked line profiles displaying only pulsational variation[22].

As mentioned during the description of the cross-correlation process, the wings of the line profiles do not contain much information. As such, the range of radial velocities of the corrected line profiles of each star was further reduced depending on the breadth of the line profile[23]. The line profiles for each star were then saved as two different sets of `.dat` files (ASCII files). The first set of `.dat` files contain the radial velocity and intensity values of each individual observation of each star, which will be input into the FAMIAS frequency and mode identification software. The second set of `.dat` files contain the intensity values and Julian dates of each radial velocity bin of all of the observations of each star, along with the signal-to-noise ratios of each observation which will be input into the SIGSPEC frequency identification software. Figure 2.8 shows all of the line profiles of HD 147787 A, one of the end results of the line profile correction process.

[22] Although the line profiles were corrected for the orbital motion, residual variations in the radial velocity still remain and appear in the Lomb-Scargle periodograms produced by FAMIAS and SIGSPEC during the subsequent pulsational analysis. Refer to the section on spectroscopic variability analysis (2.4) for more information.

[23] The reduced ranges of radial velocities for HD 182640, HD 3112 and HD 147787 are: -120 km s^{-1} to 120 km s^{-1}, -50 km s^{-1} to 50 km s^{-1} and -40 km s^{-1} to 40 km s^{-1} respectively.

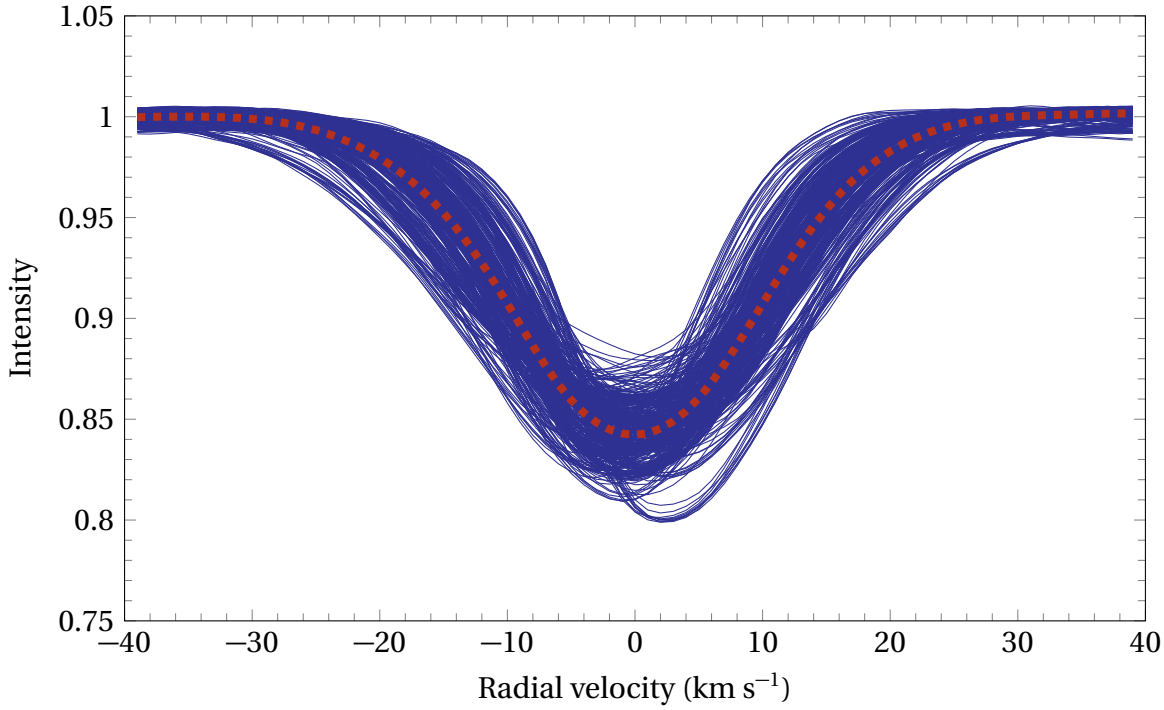

Figure 2.8: The cross-correlated line profiles (solid blue) of HD 147787 A, with the mean line profile (dashed red). (Referenced on page 40.)

2.4 Spectroscopic Variability Analysis

2.4.1 Frequency Identification

Once the secondary star had been removed from the line profiles, the line profiles were analysed to determine the pulsational frequencies and modes of each pulsating star. Frequency identification is typically complicated by the presence of aliases and harmonics.

Aliases are false frequencies that arise due to data sampling. There is 1-day aliasing of the frequencies identified due to the fact that observations are taken on a nightly basis. Harmonics are frequencies that are an integral multiple of another frequency. In some cases, both the harmonic (or the harmonic of an alias) and the fundamental frequency may be identified as real frequencies (although only one is real).

Frequency identification was done using two programs: Frequency And Mode Identification for AsteroSeismology (FAMIAS) and SIGnificance SPECtrum (SIGSPEC). Each program has its advantages and disadvantages but enhance the confidence in the overall frequency identification process when used in tandem.

FAMIAS (Zima, 2008a,b) uses Fourier analysis to produce Lomb-Scargle periodograms[24]

[24]Lomb-Scargle periodograms are periodograms produced from a least-squares fit of sinusoidal functions to spectral data, similar to Fourier analysis.

from the line profiles. These periodograms may be based on the pixel-by-pixel method (Mantegazza, 2000; Zima, 2006) or on the moment method (Balona, 1986; Aerts, 1996; Briquet and Aerts, 2003).

SIGSPEC (Reegen, 2007, 2011) is similar to FAMIAS in that it can also produce Lomb-Scargle periodograms, but is only able to analyse a two-dimensional dataset, such as the pixel-by-pixel variations, rather than a series of line profiles. It does, however, incorporate an anti-aliasing algorithm that reduces the chance of detecting a false frequency (aliases or harmonics). The frequency identification capabilities of SIGSPEC are a useful addition to the use of FAMIAS alone and assist in the frequency selection methodology.

The Pixel-by-Pixel Method

The pixel-by-pixel method, developed by Mantegazza (2000), is a method for determining patterns of variation in a line profile by analysing the change in intensity of each pixel of a time series of observations and performing a least-squares fit of sinusoidal functions to the data (creating a Lomb-Scargle periodogram) for each pixel. The mean of the Lomb-Scargle periodograms of each pixel is then computed, enabling the identification of the strongest frequencies across all pixels.

The pixel-by-pixel method is better at identifying sectoral mode ($m = \pm\ell$) than zonal mode ($m = 0$) frequencies[25] (Aerts et al., 2010). It is also better at identifying frequencies with high ℓ than the moment method as the pixel-by-pixel method is less susceptible to cancellation effects[26] (Aerts et al., 2010). In addition, this method is less affected by asymmetrical line profile variation (Brunsden, 2013) than the moment method. As such, the pixel-by-pixel method is regarded, in this analysis, as the more reliable of the two frequency identification methods.

The Moment Method for Frequency Identification

The moment method, developed by Balona (1986) and modified by Aerts (1996) and Briquet and Aerts (2003), involves the analysis of the various moments (measurements of a certain characteristic) of a line profile. The zeroth moment is a measurement of the equivalent width; the first moment is a measurement of the radial velocity; the second moment is a measurement of the variance or overall width; and the third moment is a measurement of the skewness.

Although moments of higher order exist and are easily calculable, they are linear combinations of the first to third moments and tend to be more susceptible to noise (Aerts et al., 1992; Aerts, 1996). Similar to the pixel-by-pixel method, Lomb-Scargle periodograms are computed for each moment of the line profiles to determine any periodicity in the variation of the mo-

[25] Refer to the section on non-radial pulsations (1.3.3) for more information

[26] Refer to the section on non-radial pulsational geometry (1.3.5) for more information.

ments.

Frequency Identification in FAMIAS

The `.dat` files containing the observations of each star were first loaded into FAMIAS. The next step would be to determine the frequency range for the analysis. Due to the recent revelations by Balona (2014)[27] of the presence of γ Doradus-like pulsations in all δ Scuti stars, it became necessary to investigate the 0 d^{-1} to 80 d^{-1} range. This encompassed the typical frequency ranges of both the γ Doradus and δ Scuti classes.

A single Lomb-Scargle periodogram for each star was computed using the the pixel-by-pixel method and the frequency ranges containing most of the frequency peaks were visually identified. The frequency range was then narrowed[28] to the visually identified range, which is different for each star, and used for the rest of the analysis.

Lomb-Scargle periodograms were computed using the pixel-by-pixel method and the zeroth to third moments of the the moment method. The highest-peak frequencies of each periodogram were automatically identified by FAMIAS and removed through prewhitening[29]. The residuals from the prewhitening process were then used to compute additional periodograms. This process was then iterated until no significant peaks existed above the noise floor of each periodogram.

FAMIAS is able to compute the significance level for periodograms of the different moments of the moment method[30]. Any frequency peaks below the significance level associated with a signal-to-noise ratio of 4 would have to be treated with caution[31]. Due to the fact that FAMIAS is not able to detect aliases or their harmonics, each frequency was examined to determine which of the frequencies were real and which were artefacts of the data sampling. Figure 2.9 and 2.10 show some of the pixel-by-pixel mean Lomb-Scargle periodograms and the Lomb-Scargle periodograms of the second moment of HD 182640 respectively, displaying the iterative prewhitening process in FAMIAS.

[27] Refer to the section on δ Scuti stars (1.4.2) for more information.

[28] This is because the larger frequency range increases the chance of false frequency detections and increases computation time with little information gain.

[29] Prewhitening is a commonly used technique in signal processing that aims to make a time-series more uniform by removing the most prominent sources of non-uniformity. In the Lomb-Scargle periodograms in this thesis, the highest-peak frequencies are the most prominent features in the periodogram.

[30] It is not possible for FAMIAS to compute the significance level for the mean periodograms obtained from pixel-by-pixel analysis as the dataset is two-dimensional.

[31] According to Aerts et al. (2010), the significance level at a signal-to-noise ratio of 4 corresponds to a 99.9% confidence level of having found a real peak rather than one due to white noise.

Error estimates of the frequencies obtained from FAMIAS were obtained from the following equation (Montgomery and Odonoghue, 1999):

$$\sigma(f) = \sqrt{\frac{6}{N}} \frac{1}{\pi T} \frac{\sigma(m)}{A} \tag{2.4}$$

$\sigma(f)$ is the standard deviation of the frequency, N is the number of observations, T is the observational timebase, $\sigma(m)$ is the standard deviation of the noise and A is the mean oscillation amplitude for that frequency. $\sigma(m)$ can be calculated using the following equation (Montgomery and Odonoghue, 1999):

$$\sigma(m) = \sqrt{\frac{N}{2}} \sigma(A) \tag{2.5}$$

$\sigma(A)$ is the standard deviation of the amplitude A, which is calculated by FAMIAS during the least-squares fitting process[32]. Substituting this relation into Equation 2.6 reduces it to:

$$\sigma(f) = \frac{\sqrt{3}}{\pi T} \frac{\sigma(A)}{A} \tag{2.6}$$

The observational timebase T is the total time between the first and last observation of each star. It can be calculated by taking the difference in the Julian dates of the last (T_f) and first (T_i) observations of the star:

$$T = T_\mathrm{f} - T_\mathrm{i} \tag{2.7}$$

[32] Refer to the section on frequency selection methodology (2.4.1) for more information.

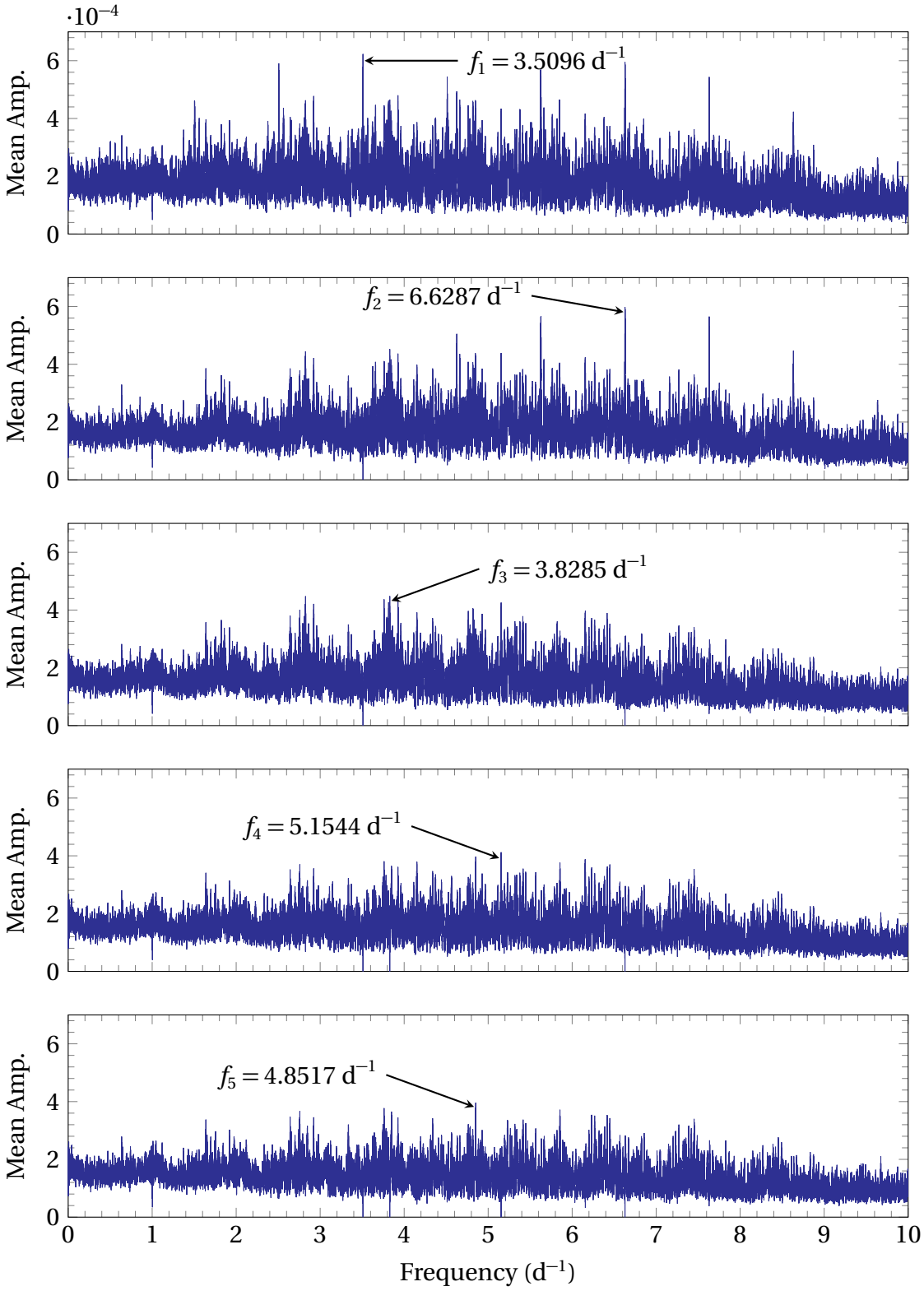

Figure 2.9: The pixel-by-pixel mean Lomb-Scargle periodograms of HD 182640, showcasing the identification and iterative prewhitening of the five strongest frequencies identified using the the pixel-by-pixel method in FAMIAS. (Referenced on page 63, 64, 127.)

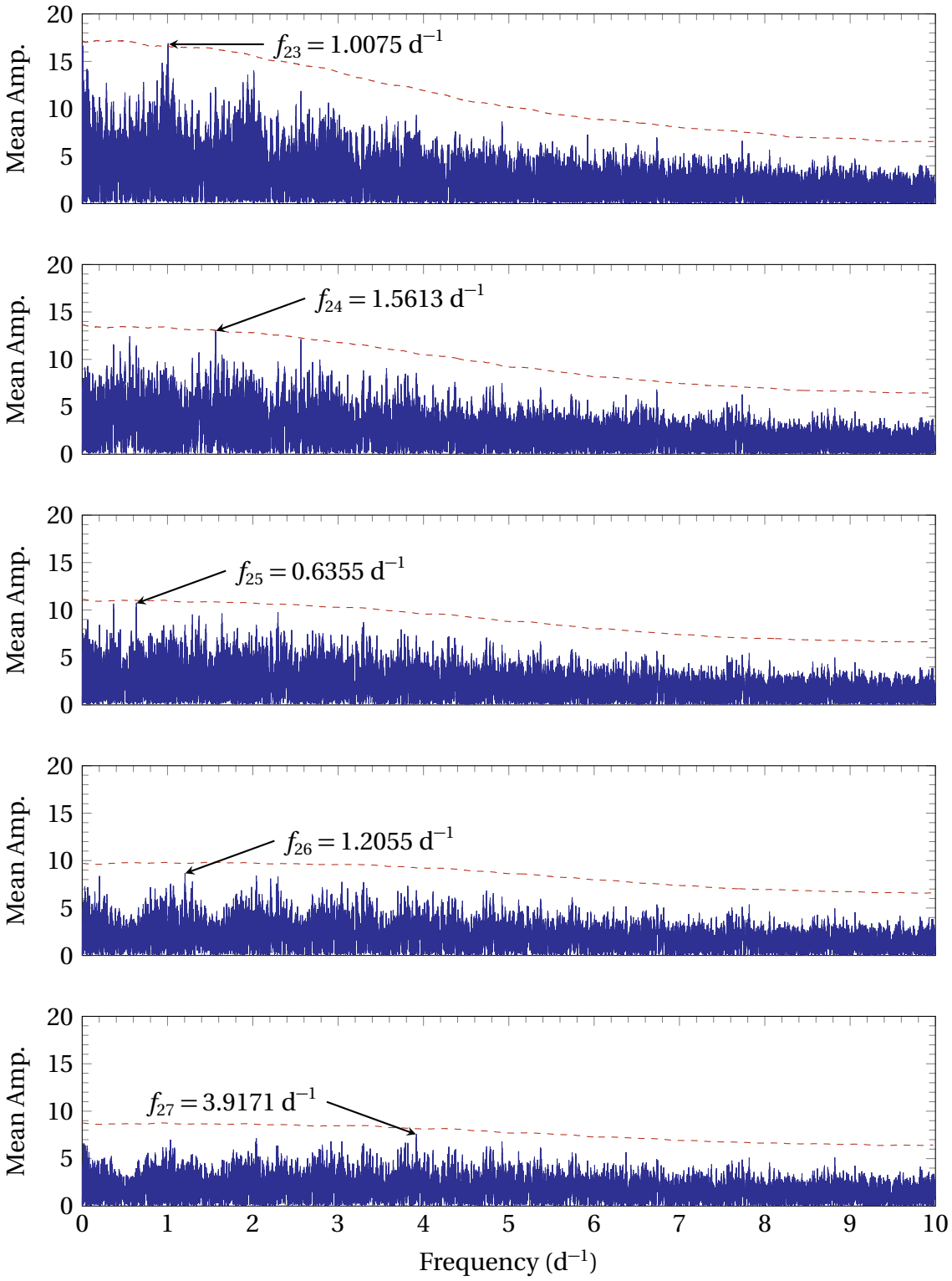

Figure 2.10: The second-moment Lomb-Scargle periodograms (solid blue) of HD 182640, showcasing the identification and iterative prewhitening of the five frequencies identified using the second moment of the the moment method in FAMIAS. The dashed red line represents the significance level at a signal-to-noise ratio of 4. (Referenced on page 43.)

Frequency Identification in SIGSPEC

The `.dat` files of each radial velocity bin of all of the observations of each star were loaded into SIGSPEC. Similar to FAMIAS, Lomb-Scargle periodograms based on the the pixel-by-pixel method are produced iteratively by SIGSPEC. However, instead of simply determining and removing the highest-peak frequency in each periodogram, SIGSPEC calculates the spectral significance (sig) at an amplitude (A) of the periodogram for different frequencies:

$$\mathrm{sig}(A) = -\log_{10}[\Phi_{\mathrm{FA}}(A)] \tag{2.8}$$

$\Phi_{\mathrm{FA}}(A)$, the False-Alarm Probability, is the probability that the frequency peak of amplitude A had been generated by white noise. A spectral significance of 4 would therefore mean that the False-Alarm Probability is 10^{-4}.

The frequency range was restricted to that determined during the initial phase of frequency identification in FAMIAS. For each pixel, SIGSPEC first identifies all frequencies above a sig of 4. All frequencies with a sig of at least half of that of the frequency of the highest sig were checked using an anti-aliasing algorithm. This algorithm identifies the combination of frequencies that produced the smallest residual variation. The frequency with the highest sig in the combination is then selected and used in the prewhitening and periodogram recomputation process, as described in the section on frequency identification in FAMIAS.

This process was iterated until the sig of the detected frequencies fell below 4. This ensured that all frequencies identified in SIGSPEC had a False-Alarm Probability of less than 0.1%. The spectral significance calculation and the anti-aliasing algorithm utilised by SIGSPEC make it less likely that an alias frequency is identified, enabling the cross-checking of frequencies identified by FAMIAS. Figure 2.11 shows the spectral significance values of the frequencies of HD 3112 identified by SIGSPEC.

Error estimates of the frequencies obtained from SIGSPEC were obtained from the following equation (Kallinger et al., 2008):

$$\sigma(f) = \frac{1}{T\sqrt{\mathrm{sig}}} \tag{2.9}$$

$\sigma(f)$ is the standard deviation of the frequency and T is the observational timebase, defined earlier in the section on frequency identification in FAMIAS and calculated using Equation 2.7.

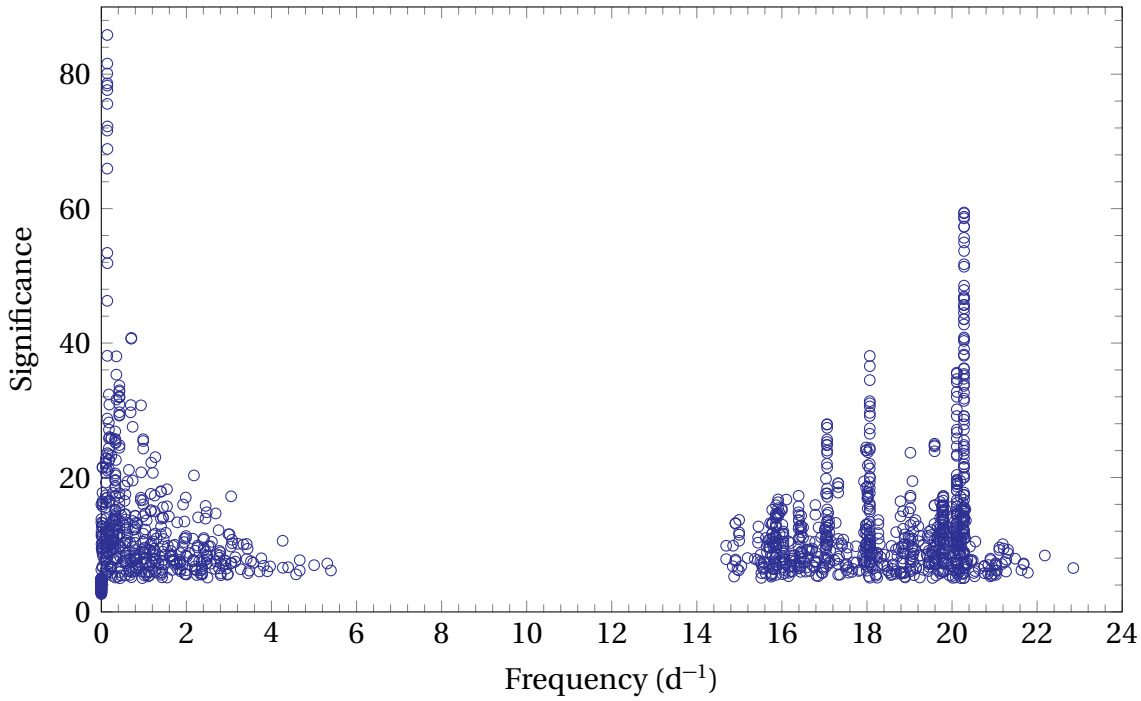

Figure 2.11: The spectral significance values of the frequencies of HD 3112 identified by SIGSPEC. Each blue circle represents a single pixel in which a frequency was identified at a particular significance. (Referenced on page 47.)

Frequency Selection Methodology

Frequencies obtained from FAMIAS and SIGSPEC were analysed to determine whether they were indeed real pulsation frequencies. The likelihood of an identified frequency being a real one was ranked according to the following criteria, from most likely to least likely:

1. Frequencies that were identified in both SIGSPEC and the pixel-by-pixel method in FAMIAS.
2. Frequencies that were identified in both SIGSPEC and one or more moments of the moment method in FAMIAS.
3. Frequencies that were identified in both the pixel-by-pixel method and one or more moments of the Moment Method in FAMIAS.
4. Frequencies that were identified only in the pixel-by-pixel method in FAMIAS.
5. Frequencies that were identified only in one or more moments of the moment method in FAMIAS.
6. Frequencies that were identified only in one of the moments of the moment method in FAMIAS.
7. Frequencies that were identified in SIGSPEC with low spectral significance.

Frequencies identified in SIGSPEC with high spectral significance were regarded as more reliable due to the anti-aliasing algorithm incorporated in the software. Frequencies identified using the pixel-by-pixel method were also regarded as more reliable as the pixel-by-pixel method produces the lowest noise levels of all of the analysis methods (Brunsden et al., 2012). In some cases, multiple frequencies with roughly equivalent spectral significance are identified in SIGSPEC. In those cases, the frequency that was detected in a larger number of pixels was regarded as a more likely pulsational frequency. Although there is a possibility of SIGSPEC identifying a frequency of high spectral significance without a similar identification in FAMIAS, this is unlikely to occur. In practice, only the frequencies that had fallen within the first five categories were considered as candidates for pulsational frequencies.

In addition to considering the methods and programs used in frequency identification, the presence of aliases and harmonics must also be taken into account, especially for frequencies detected only using FAMIAS. Frequencies that were integer multiples of each other and frequencies that were of the form $1+f$, $1-f$, $2+f$, $2-f$ and so on, where f is another identified frequency, need to be treated with caution.

FAMIAS uses a Levenberg-Marquadt algorithm to perform least-squares fits to the data for a frequency or combination of frequencies, using the formula (Zima, 2008b):

$$y_i = Z + \sum_i A_i \sin\left[2\pi(F_i t + \phi_i)\right] \tag{2.10}$$

Z is the fitted zero point[33], and y_i, A_i, F_i and ϕ_i are the intensity values, amplitude, frequency and phase of the i^{th} fitted frequency. This fit was applied to each pixel of the spectrum separately[34] and the amplitude and phase profiles of each frequency was optimised.

The least-squares fitting, in addition to being necessary for mode identification, also provides another layer of alias detection. If the frequencies chosen were real, the transitions in the amplitude fits are more likely to be in similar locations to those in the phase fits. Least-squares fits were therefore performed for each chosen frequency independently to obtain the individual amplitude and phase profiles. Any frequency that displayed irregular profiles was likely an alias and was discarded. In addition, the true pulsational frequencies should be independent of one another. This was verified by adding or removing different candidate frequencies from the least-squares fit and comparing the amplitude and phase fits for each frequency. If there were any significant changes in shape in those fits during the process of adding and removing frequencies, it could be deduced that one of the frequencies was likely to be an alias.

[33] A zero-point fit is the least-squares fit of a rotationally broadened synthetic line profile to the phase-independent mean line profile (i.e. the zero-point line profile).

[34] The fitting was done for each pixel separately as that is the primary requirement of the FPF method. Refer to the section on mode identification (2.4.2) for more information.

Figure 2.12 shows the observed amplitude and phase of the frequency $f = 20.2802$ d^{-1} for HD 3112. Note the good match in the transitions of the amplitude and phase fits, indicative of a real pulsational frequency.

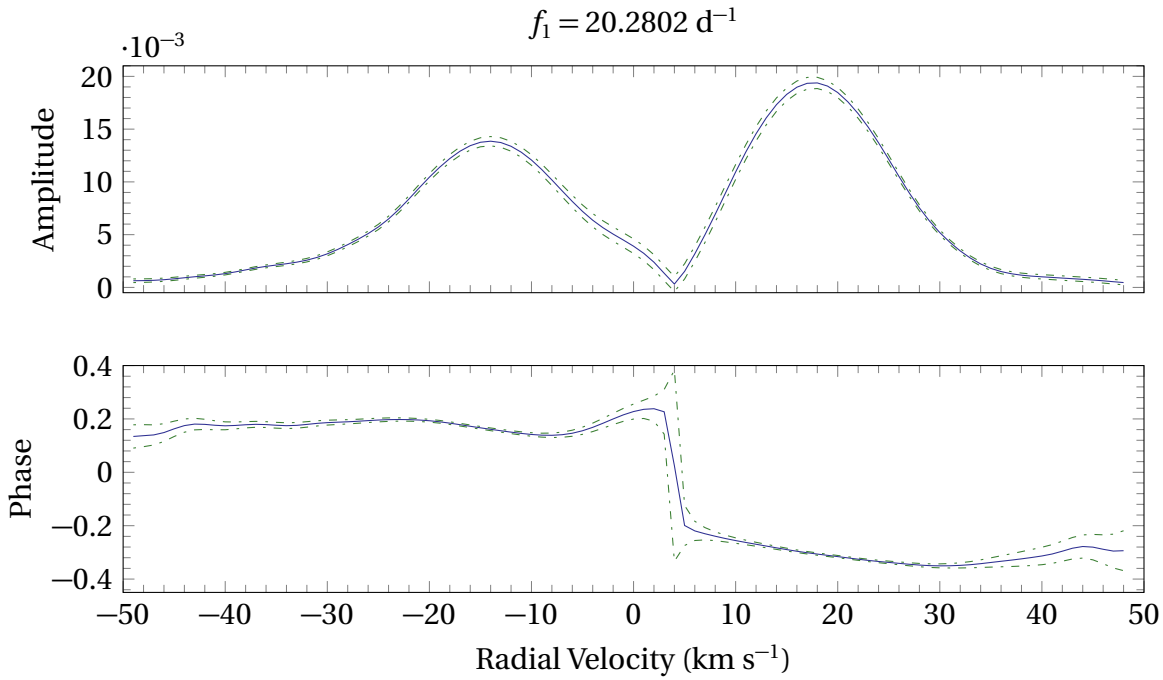

Figure 2.12: The amplitude and phase profiles of $f_1 = 20.2802$ d^{-1} of HD 3112. The solid blue lines are the observed profiles and the dash dotted green lines represent the statistical uncertainty. (Referenced on page 50.)

A method of measuring of the success of the frequency identification process is the determination of the percentage of variation of each star explained by the identified frequencies. This means that the least-squares fits of a combination of all the identified pulsational frequencies should be able to largely predict the shape of the line profile of the star at any point in time.

The percentage of variation explained by a frequency was determined by calculating the percentage reduction of the mean standard deviation after the removal of a particular frequency from the line profiles (during the iterative prewhitening process). This calculation was also used as yet another method of alias detection: alias frequencies typically explained a smaller percentage of variation than real ones. The frequency identification process could only be considered to be successful if a significant percentage of the line profile variations was explained by the identified frequencies.

2.4.2 Mode Identification

Once the real pulsational frequencies were identified, the determination of the modes of oscillation for each pulsation frequency was carried out. Although many methods are available for mode identification, the Fourier Parameter Fit (FPF) method in FAMIAS was used. This is because the FPF method was determined by Wright (2008) to be superior to the moment method for stars with medium to high rotational velocities ($v \sin i > 30\,\mathrm{km\,s^{-1}}$). FAMIAS has been successfully used to identify p-mode pulsations (Desmet et al., 2009) and, more recently, had been adapted for the identification of the g-mode pulsations of γ Doradus stars stars (Brunsden, 2013; Greenwood, 2014).

The Fourier Parameter Fit (FPF) Method

The Fourier Parameter Fit (FPF) method was developed by Zima (2006) as an extension of the pixel-by-pixel method of Mantegazza (2000). Synthetic profiles of various modes[35] and using different stellar parameters[36] were created and fitted to the least-squares fits of the zero-point, standard deviation and phase for each frequency[37] using a genetic algorithm[38].

The fitting then proceeds on a pixel-by-pixel basis: each pixel across the zero-point, standard deviation and phase profiles is fitted independently. The algorithm searches the specified parameter space until the best-fit parameters are found, as determined by the lowest χ^2 value for each fit. Note that the χ^2 values in this thesis, as reported by FAMIAS, are the *reduced* χ^2 values[39]. This was calculated using the equation (Zima, 2008b):

$$\chi^2 = \frac{1}{2n_\lambda - N} \sum_{i=1}^{n_\lambda} \left[\frac{(A^o_{R,i} - A^s_{R,i})^2}{\sigma^2_{R,i}} + \frac{(A^o_{I,i} - A^s_{I,i})^2}{\sigma^2_{I,i}} \right] \tag{2.11}$$

n_λ is the number of pixels across the line profile, N is the estimated number of free parameters, A is a phasor [40] and σ is the observational standard deviation. The indices o, s, R, and I represent the observational and synthetic values, and the real and imaginary values respectively. Therefore, $A^o_{R,i}$ is the i^{th} component of the observationally-determined real component of a phasor and $\sigma^2_{R,i}$ is the corresponding observational variance (square of the standard devi-

[35] These modes are essentially different permutations of the degree ℓ and the azimuthal order m.
[36] Radius (R), mass (M), T_{eff}, $\log g$, [Fe/H] and $v \sin i$
[37] The least-squares fits, performed for each pixel separately, are prerequisites to the mode identification process and are described in the ection (2.4.1).
[38] A genetic algorithm is an iterative optimisation algorithm that attempts to mimic natural selection in the attempt to find a best-fit solution. After each iteration, the weakest solutions are discarded and the strongest ones used in the next iteration.
[39] Each χ^2 value has been divided by the estimated number of free parameters.
[40] A phasor is a complex number which represents a sinusoidal function with a time-invariant amplitude, angular frequency and initial phase.

ation) of the i^{th} component of the observationally-determined real component of the phasor.

The Moment Method for Mode Identification

The moment method for mode identification (Zima, 2008b) is an adaptation of the moment method for frequency identification, as described by Briquet and Aerts (2003). Similar to the FPF method, synthetic line profiles of the various modes using different stellar parameters are generated. Instead of determining the goodness-of-fit of the zero-point, standard deviation and phase for each pixel independently, the observational[41] and synthetic profiles were decomposed into combinations of the first and second moments (radial velocity and variance) of a line profile. These moments are used for the χ^2 calculation in the genetic algorithm. The χ^2 value for the moment method was calculated using the equation (Zima, 2008b):

$$\chi^2 = \frac{1}{2N}\sum_{i=1}^{N}\left[\left(\frac{<v^1>_o - <v^1>_s}{\sigma_{<v^1>_o}}\right)^2 + \left(\frac{<v^2>_o - <v^2>_s}{\sigma_{<v^2>_o}}\right)^2\right] \tag{2.12}$$

N is the number of observations, $<v^1>$ is the first moment, $<v^2>$ is the second moment and $\sigma_{<v^1>_o}$ and $\sigma_{<v^1>_o}$ are the corresponding observational standard deviations for the first and second moments respectively. The indices o and s are represent the observational and synthetic values respectively.

FAMIAS Mode Identification Assumptions

FAMIAS makes a number of assumptions in its modelling of the modes of stellar pulsations. These are detailed in Zima (2008b), and include the following:

- The model star is spherically symmetric and initially unperturbed, with no magnetic deformation of the surface and with a uniform rotation that is slow enough rotation such that higher order (second-order and above) Coriolis effects can be neglected.
- The stellar pulsations can be described by the superimposition of spherical harmonics[42] onto the unperturbed surface of the model star.
- The line profiles are symmetric and display limb darkening[43] according to the equations of Claret (2000).
- For the FPF method, the line profiles are rotationally broadened Gaussians with variable line widths caused by surface temperature variations.

[41] Note that the least-squares fits of each frequency must be calculated using the first moment (radial velocity) of the moment method in order for the mode identification to be performed using this method.
[42] Refer to the section on non-radial pulsational geometry (1.3.5) for more information
[43] Limb darkening is the stellar phenomenon in which the central part of the star appears brighter than the edges. The amount of limb darkening is wavelength and stellar type dependent and has been observationally-characterised and modelled reasonably by astronomers.

It is clear from these assumptions that the model star is highly idealised and does not take into consideration many factors such as rotational flattening or turbulence and granulation[44]. The assumption of first-order Coriolis terms implies that the mode identification for rapidly rotating stars may be imprecise. These models represents good initial solutions until more sophisticated models are developed.

Mode Identification Methodology

The mode identification process was initiated by first inputting the following stellar parameters: radius (R), mass (M), $T_{\rm eff}$, $\log g$, [Fe/H] and $v \sin i$. Although it is possible to optimise all of these parameters in a fit, typically only the $v \sin i$ has a significant effect on the shape of the synthetic line profiles (Zima, 2006). The other parameters were therefore fixed at values obtained from the literature. The central wavelength[45] was set at 5000 Å (the approximate mean wavelength value of the cross-correlated region of the stellar spectra). The actual value itself is not of concern for this analysis as the line profile variations are largely unaffected by limb darkening (Schrijvers et al., 1997).

Since the FPF method was used for mode identification, a zero-point fit (Zima, 2008a) was performed to determine the best-fit (lowest χ^2) $v \sin i$, equivalent width, intrinsic width and velocity offset of the zero-point line profile. This enabled the fixing of those parameters that influence the shape of all of the line profiles of a particular star, reducing the parameter space that had to be searched in the subsequent steps. Figure 2.13 shows the zero-point fit of the line profile of HD 182640.

Once this was done, the pulsation modes for each frequency could be identified. Models with different permutations of degree (ℓ) and azimuthal number (m) within a user-defined range were fitted to the observational amplitude and phase profiles for individual frequencies. The velocity amplitude ($v_{\rm amp}$), phase (ϕ) and inclination (i) were also set as free parameters during the mode identification. Once the best-fit solutions for the individual frequencies were determined, ℓ, m, $v_{\rm amp}$ and ϕ for the best-fit mode of each frequency were set as fixed parameters. A fit with the inclination as the only variable was then performed to determine if the inclination converged for each frequency.

Figure 2.14 shows the best-fit mode to the standard deviation and phase profiles of $f_7 = 0.78074$ d^{-1} of HD 147787. Deviations in the phase fits during phase transitions of ± 1, observable in this figure, are mathematical artefacts that arise during the modelling process and are largely irrelevant in the analysis. In addition to the goodness-of-fit, careful consideration of each model's physicality was required during the mode identification process. Firstly, models

[44] Refer to the section on the rotational effects on pulsations (1.3.6) for more information

[45] The central wavelength determines the limb darkening coefficients applied to the fit (Zima, 2008b), which may slightly affect the $v \sin i$ and intrinsic width of the line profiles.

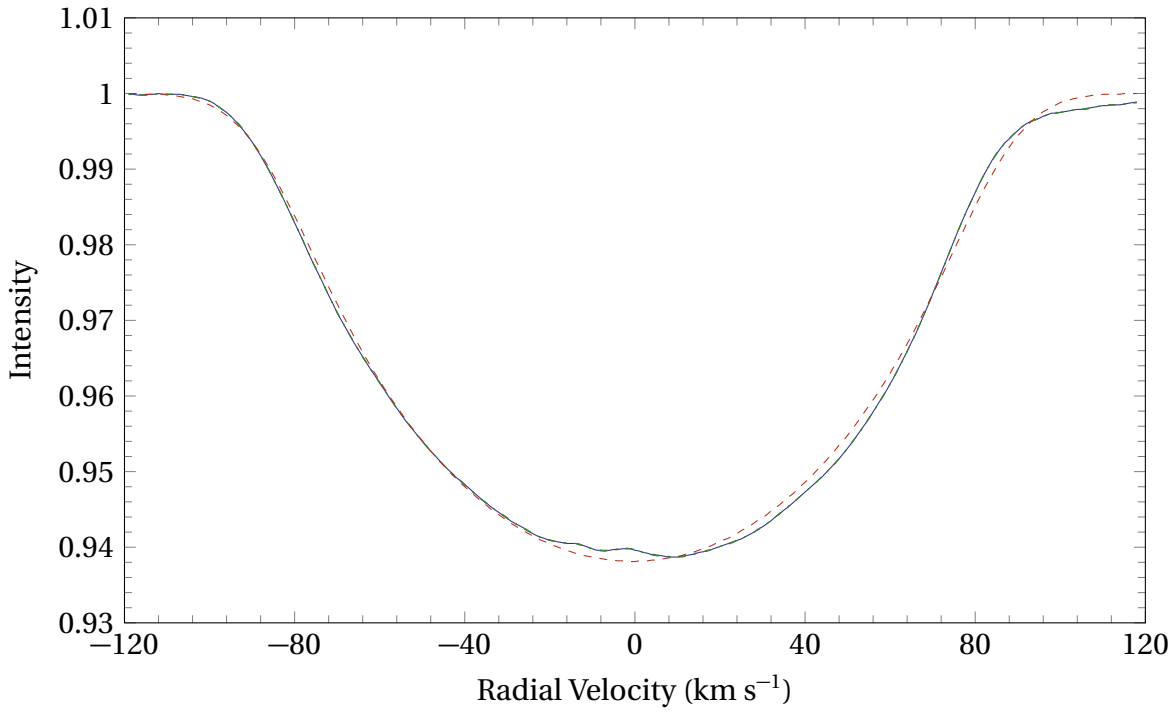

Figure 2.13: The zero-point fit of the HD 182640 line profiles. The solid blue line represents the zero-point line profile, the two dash dotted green lines (partially obscured by the solid blue line) represent the statistical uncertainty and the dashed red line represents the best-fit synthetic zero-point line profile. Note the relativity good visual fit of the synthetic line profile to the zero-point line profile (albeit with a high $\chi^2 = 2290.82$). (Referenced on page 53.)

with inclination values that result in equatorial rotational velocities greater than the Keplerian breakup velocity (v_{crit}) must be discarded. The equation used to calculate v_{crit} is described in Schulz (2012):

$$v_{\text{crit}} = \sqrt{\frac{GM}{R}} \tag{2.13}$$

G is the gravitational constant and M and R are the mass and radius of the star respectively. This value puts a lower bound (i_{crit}) on the inclination values of the star, given by the equation:

$$i_{\text{crit}} = \arcsin\left(\frac{v \sin i}{v_{\text{crit}}}\right) \tag{2.14}$$

Secondly, retrograde modes ($m < 0$) where the pulsational frequency is larger than the rotational frequency of the star cannot exist as such modes are defined as prograde modes. Equivalently, prograde modes ($m > 0$) where the pulsational frequency is smaller than the rotational frequency of the star cannot exist as such modes are defined as retrograde modes.

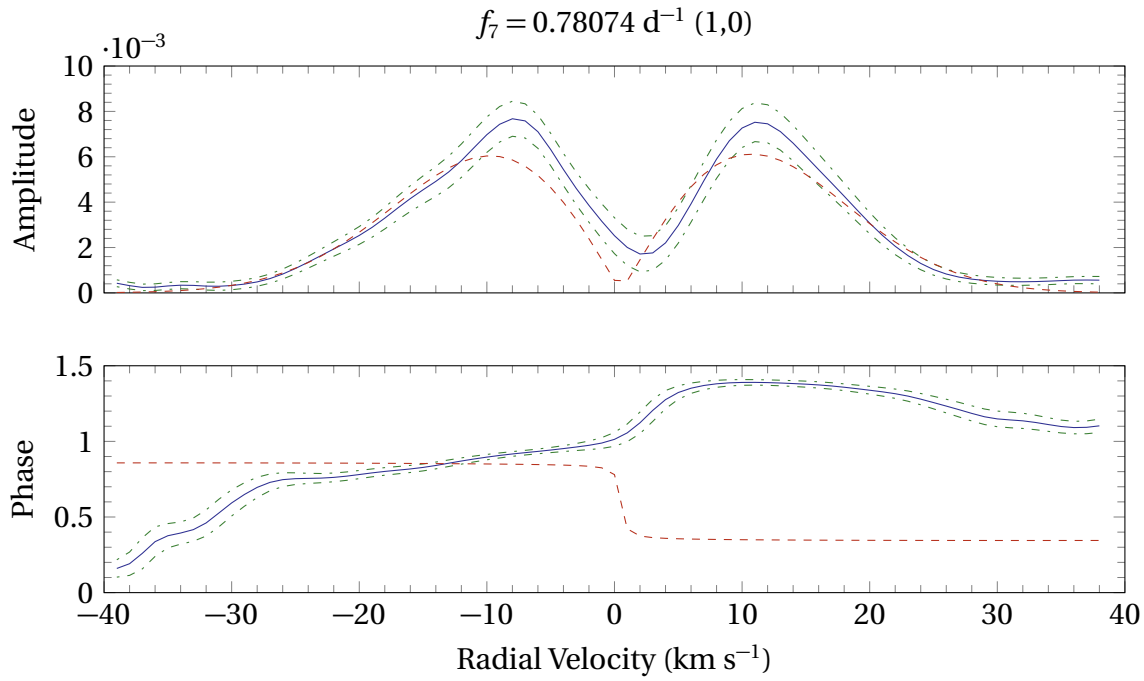

Figure 2.14: The amplitude and phase profiles of the best-fit mode (1,0) of $f_7 = 0.78074$ d^{-1} of HD 147787. The solid blue lines are the observational profiles, the dash dotted green lines represent the statistical uncertainty and the dashed red lines represent the best-fit synthetic profiles. Note the deviation in the synthetic phase profile; a mathematical artefact that arises during the modelling process. (Referenced on page 53.)

The rotational frequency f_{rot} is calculated using the equation:

$$f_{\text{rot}} = \frac{v}{2\pi R} \tag{2.15}$$

R is the radius of the star and v is the equatorial rotational velocity, obtained by dividing $v \sin i$ by the sine of the inclination ($\sin i$). However, because the inclination is often not well defined, the rotational frequency of the star is often highly uncertain. An additional assumption for the rotational frequency in FAMIAS is that:

$$\left| \frac{f_{\text{rot}}}{f_{\text{co-rot}}} \right| \leq 0.5 \tag{2.16}$$

$f_{\text{co-rot}}$ is the co-rotating frequency, which can be calculated using the following equation (Dziembowski and Goode, 1992):

$$f_{\text{co-rot}} = f_{\text{obs}} - m(1-C)f_{\text{rot}} + D\frac{m^2 f_{\text{rot}}^2}{2\pi f_{\text{obs}}} \tag{2.17}$$

f_{obs} is the observed pulsational frequency, C is the Coriolis term, D is the centrifugal term and

m is the azimuthal order of the pulsational mode. For pulsations of high radial order (the non-radial pulsations of γ Doradus), C can be approximated by $1/\ell(\ell+1)$, where ℓ is the degree of the pulsation mode, and D is approximately zero. This reduces Equation 2.17 to:

$$f_{\text{co-rot}} = f_{\text{obs}} + m\frac{1-\ell(\ell+1)}{\ell(\ell+1)}f_{\text{rot}} \tag{2.18}$$

For δ Scuti stars, the assumption $C = 0$ and $D = 0$ (used by FAMIAS in its pulsational modelling process) (Zima, 2008b) was adopted. This reduces Equation 2.17 to:

$$f_{\text{co-rot}} = f_{\text{obs}} - m f_{\text{rot}} \tag{2.19}$$

According to Zima (2008b), the pulsational frequency can only considered to be reliable if the $|f_{\text{rot}}/f_{\text{co-rot}}| \leq 0.5$ condition is met. However, Shrijvers et al. (1997) had indicated that as long as $|f_{\text{rot}}/f_{\text{co-rot}}| \leq 1$, the pulsational frequency can be considered to be a reasonable approximation.

Since f_{rot} is highly uncertain, $|f_{\text{rot}}/f_{\text{co-rot}}|$ is similarly not well-defined and the criterion of $|f_{\text{rot}}/f_{\text{co-rot}}| \leq 0.5$ is not a good discriminator for the exclusion of certain pulsation modes. As such, it can be concluded that $|f_{\text{rot}}/f_{\text{co-rot}}| \leq 0.5$ could be a minor discriminator between two modes that are very close in χ^2 and that as long as $|f_{\text{rot}}/f_{\text{co-rot}}| \leq 1$, the mode can be considered to be physical.

All probable radial modes (particular those of HD 3112, a δ Scuti star) were also verified by calculating the frequency of the fundamental radial mode and determining if the frequency of the identified radial mode was of a similar order or a multiple of the fundamental radial mode frequency (i.e. a harmonic). The equation used to calculate the fundamental radial mode is Cox (1980):

$$f_{\text{rad}} = K\sqrt{\frac{GM}{R^3}} \tag{2.20}$$

f_{rad} is the frequency of the fundamental radial mode, G is the gravitational constant, M is the mass of the star and K is a proportionality constant. K was set to be 2.065, which is a reasonable approximation for sun-like stars (Cox, 1980).

The next three chapters describe the results of the orbital analysis, and the frequency and mode identification results for three stars: HD 182640 – a bright, known long-orbit SB2[46] with a γ Doradus primary; HD 3112 – a known 7-day orbit SB2 with a δ Scuti primary; and HD 147787 – a known 40-day orbit SB2 with a γ Doradus primary.

[46]Refer to the section on spectroscopic binaries (1.5.2) for more information.

3 HD 182640

HD 182640[1] is one of the brightest stars ($m_V = 3.38$, Paunzen, 2015) in the constellation of Aquila, which is the Latin word for *eagle*. HD 182640 is also known as Denebokab, which the Arabic phrase for *the tail of the eagle*. It has a spectral type of F0IV (Agati et al., 2015) and is located at the coordinates 19h 25m 29.9s, +03° 56′ 53.2″ (J2000 epoch[2], van Leeuwen, 2007) at a distance of 15.5 ± 0.5 pc from the Sun (van Leeuwen, 2007), according to HIPPARCOS astrometric parallax measurements.

Variations in the radial velocity of HD 182640 were first recorded by Campbell and Curtis in 1903. The first mentioning of the binarity of HD 182640 was by Alden (1936), who proposed an orbital period of 1250 d through astrometric analysis. Osvalds (1958) performed another astrometric study of HD 182640 and found a similar orbital period. A complete set of orbital elements was most recently published by Kamper et al. (1989) from a set of 40 data points taken over 5.2 yr. These elements were used by Brunsden (2013) in her orbital analysis. However, she was unable to precisely model the orbit of HD 182640.

There seem to be some conflicts in the literature regarding the variability of HD 182640. The first mentioning of the variability of HD 182640 was in 1923 by Henroteau. He discovered a spectroscopic pulsation period of 0.1571 d, corresponding to a frequency of 6.365 d^{-1}, and classified it as a β Canis Majoris variable. Frolov (1970) later performed a spectroscopic study and found a very similar pulsation frequency of 6.31 d^{-1} and classified HD 182640 as a δ Scuti variable star. This classification was supported by King and Liu (1990), based on its similarity to the δ Scuti star they were studying (AI Canum Venaticorum). A study conducted by Baade and Kjeldsen (1997) found no radial velocity variations but found high azimuthal order[3] ($6 < m < 10$) variation in the line profiles, positing that these could be a result of g-mode pulsations characteristic of the then-newly defined γ Doradus class of variable stars. HD 182640 was first proposed as a candidate γ Doradus star by Koen and Eyer (2002), who found a photometric frequency of 0.95672 d^{-1}. The most recent pulsational analysis was by Brunsden (2013), who reported four likely pulsation frequencies: 3.67 d^{-1}, 2.21 d^{-1}, 1.43 d^{-1} and 4.37 d^{-1}.

A study of nearby stars conducted by Fuhrmann (2008) characterised HD 182640 B as a late K-type dwarf star with a $m_V = 8.31$, a temperature of 4100 K, a mass of 0.67 $M_\odot$ and a radius of 0.61 $R_\odot$.

[1] Other designations for this star include HR 7377, HIP 95501, delta Aquilae and δ Aql.
[2] An epoch is a reference point for astronomical quantities (in this case, celestial coordinates) that vary with time. The coordinates of the star are with reference to the J2000 epoch, defined as 12:00 UT on 1 January, 2000.
[3] Refer to the section on non-radial pulsations (1.3.3) for more information

Table 3.1: The fundamental stellar parameters of HD 182640, used during spectroscopic data reduction and mode identification. The minimum and maximum literature values of each parameter and the value used in this analysis (typically the approximate mean or the mode of the literature values) are listed. (Referenced on page 59, 68.)

Parameter	Min. Literature Value	Max. Literature Value	Value Used
$T_{\rm eff}$ (K)	6790 (Muñoz et al., 2013)	7413 (Önehag, 2008)	7000
$\log[g$ (cm s^{-2})]	3.87 (Schröder et al., 2009)	4.35 (Katz et al., 2011)	4.0
Radius ($R_\odot$)	1.5 (Pasinetti-Fracassini et al., 2001)	2.04 (Fuhrmann, 2008)	1.75
Mass ($M_\odot$)	1.65 (Fuhrmann, 2008)	1.75 (Brunsden, 2013)	1.7
[Fe/H] (dex)	−0.18 (Katz et al., 2011)	0.11 (Ammons et al., 2006)	0.0
$v \sin i$ (km s^{-1})	80 (Glebocki and Gnacinski, 2005)	91 (Zorec and Royer, 2012)	85
v_γ (km s^{-1})	−35.59 (Erspamer and North, 2003)	−29.9 (Gliese and Jahreiß, 1991)	-30.0

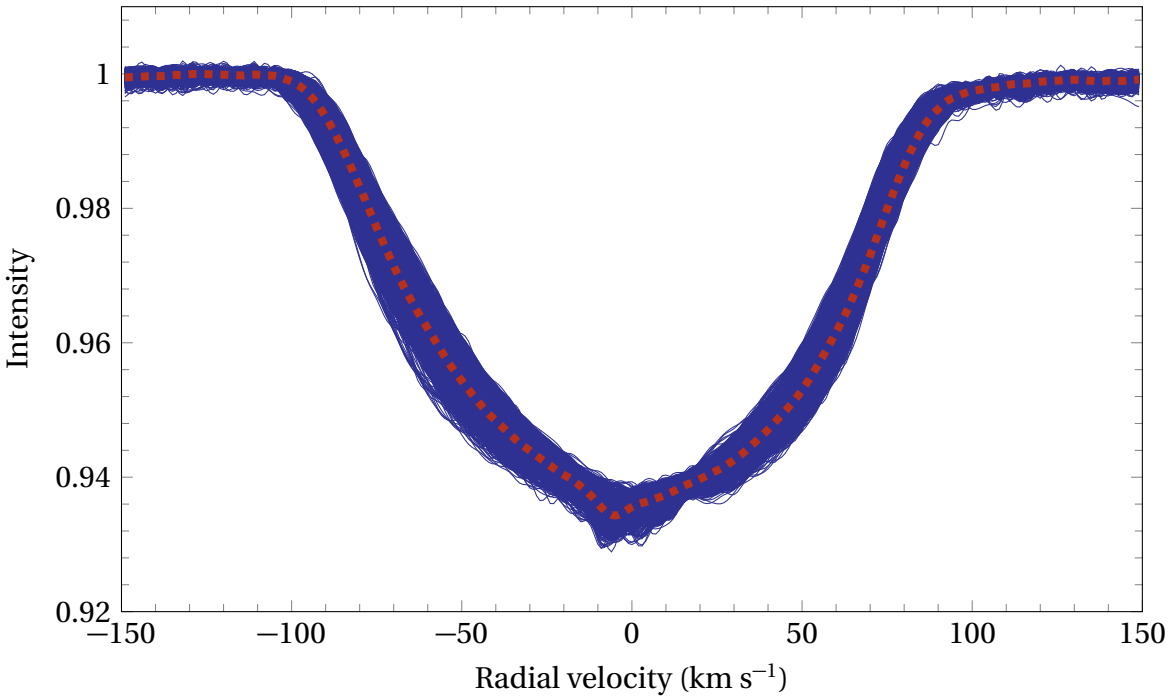

Figure 3.1: The cross-correlated line profiles (solid blue) of HD 182640, with the mean line profile (dashed red). (Referenced on page 59.)

3.1 Observations

A total of 1355 observations[4] of HD 182640 were collected between March 2009 and August 2015. It was decided to discard spectra below a signal-to-noise ratio of 100[5] in order to retain only the highest quality spectra. 1298 spectra remained for orbital and pulsational analysis. Table 3.1 shows a summary of the stellar parameters obtained from the literature and the values used as inputs during the spectroscopic data reduction process[6]. Figure 3.1 shows all of the cross-correlated line profiles of HD 182640, together with the mean line profile. Due to the broadness of the line profile of the primary, the signal of the much fainter secondary star appears as a prominent "bump" close to the minimum of each line profile.

3.2 Binary Analysis

HD 182640 is a very interesting SB2[7] as the line profiles of the primary and secondary are perpetually merged due to the broadness of the primary line profile. Therefore, it is not possible to use the method described in the section on binary analysis (2.3) as there are no line profiles with well-separated peaks.

As such, a different approach was taken with this star. It was observed that the peak of the "bump" in each line profile was also the minimum point of each line profile. However, even though the secondary star is non-variable, the line profile of the star showed a great degree of deviation from a typical Gaussian shape. This is due to the low intensity of the line profile of the secondary, leaving it more susceptible to noise, and the pulsations of the primary star.

A three-step approach was created to deal with this problem and involved the use of the MATLAB code `peakfit.m`, created by Prof. Em. Tom O' Haver. It was observed that a small region around the peak of the secondary seemed undistorted and that the asymmetry in the line profile only occurred at the "base" of the line profile. A partial unconstrained Gaussian[8] was then fitted to a ± 5 km s^{-1} range of the minimum point of each line profile. Fitting a small region around the peak of each secondary line profile enables a more precise velocity measurement of the secondary star. The left panel of Figure 3.2 is a snapshot of the first step. Note that even with this measure, the fit is relatively poor.

The orbital fitting code of Bergmann (priv. comm.) was then used to fit a orbit to the velocities of the secondary. Model velocities for the secondary star were then calculated from

[4] Refer to Table 2.1 for more details

[5] This was particularly important due to the susceptibility of the signal of the secondary star to noise. Refer to the section on cross-correlation (2.2.3) for more information on why low signal-to-noise spectra were discarded.

[6] Refer to the section on the second data reduction pipeline (2.2.3) for more information.

[7] Refer to the section on spectroscopic binaries (1.5.2) for more information.

[8] `peakfit.m` allows for the fitting of Gaussians without requiring that the signal return to the baseline minimum at the edges.

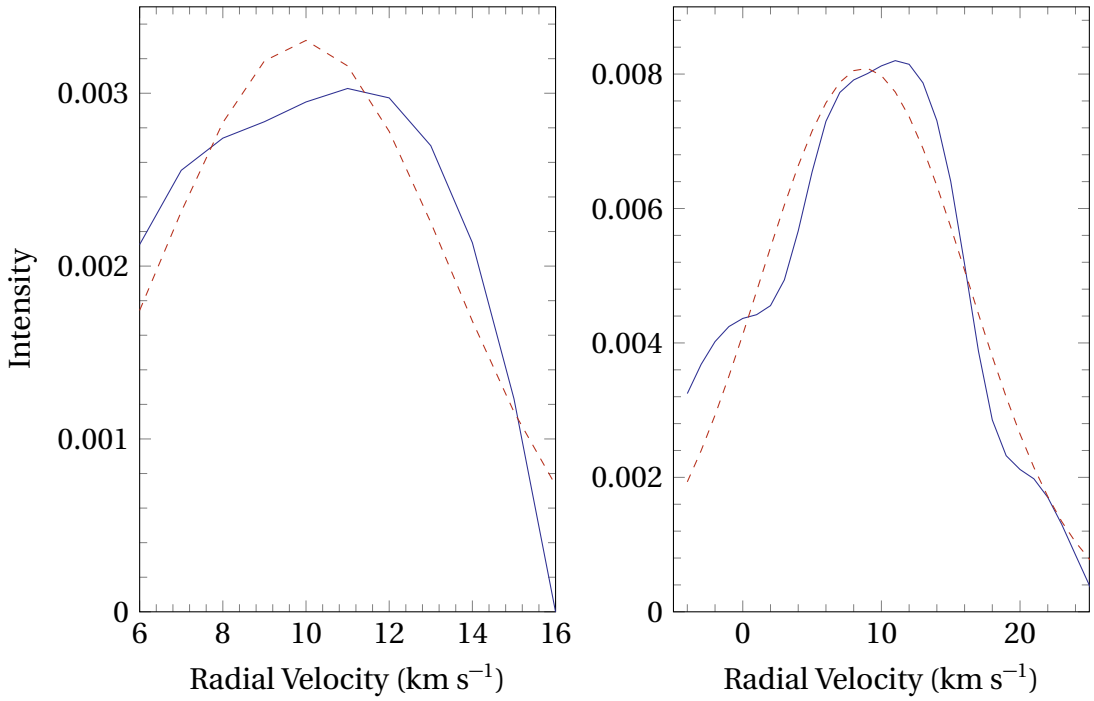

Figure 3.2: Snapshots of the partial Gaussian-fitting processes of HD 182640 B. The solid blue lines are inverted portions of the line profiles and the dashed red lines are the fitted partial Gaussians. The left panel shows the fitting of a partial Gaussian for velocity measurement and the right panel shows the fitting of a partial Gaussian for height and width measurement. (Referenced on page 59, 61.)

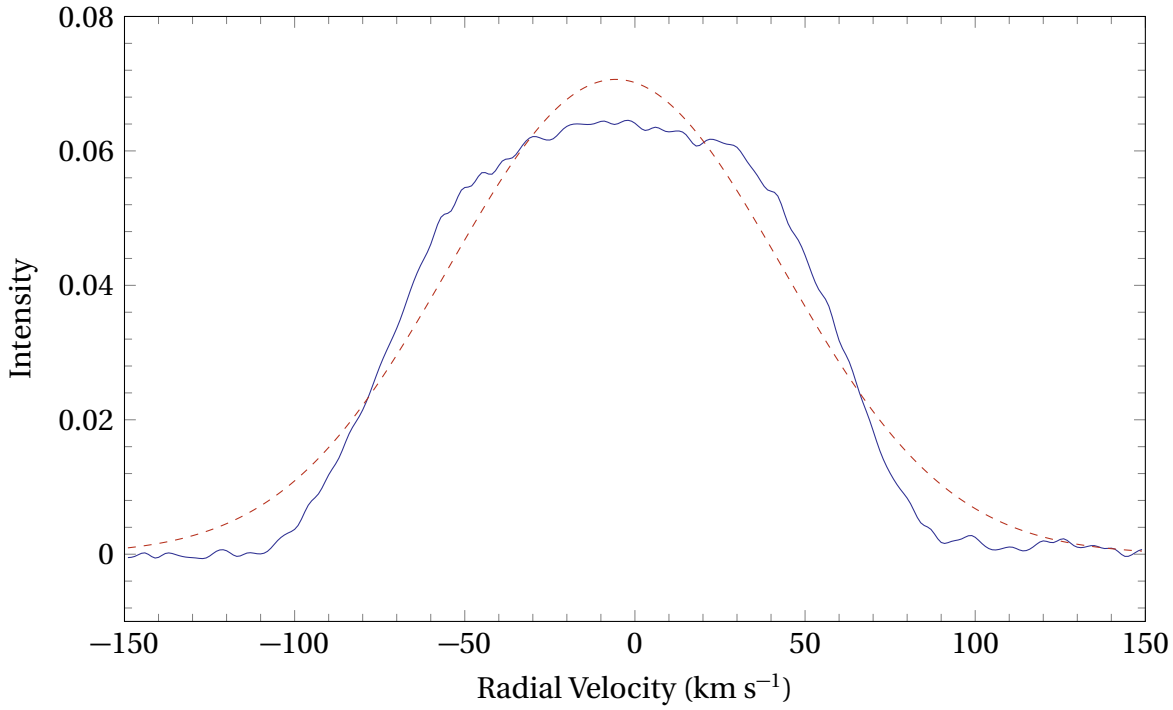

Figure 3.3: The Gaussian-fitting process of HD 182640 A, for the purposes of velocity measurement. The solid blue line is one of the inverted line profiles and the dashed red line is the fitted Gaussian. (Referenced on page 61.)

the orbital fit[9].

The second step was to constrain the parameters of the Gaussian that is used to approximate the secondary line profile. It was once again observed that the "bump" in each line profile occupied an approximate ±15 km s^{-1} range of the minimum point. Similar to the first step, a partial unconstrained Gaussian was fitted to a ±15 km s^{-1} range of the minimum point of each line profile, giving a set of height and width parameters for each Gaussian. Since the secondary peak is small and more susceptible to noise, the individual height and width parameters greater than 1σ away from the mean height and width were removed and the mean height and width recomputed. The right panel of Figure 3.2 is a snapshot of the second step. Note the asymmetrical deviations at the base of the line profile. The signal of the secondary star was removed from the line profiles by subtracting Gaussians, with the central positions equal to the calculated radial velocities and with dimensions equal to the mean height and width of the secondary peak across all of the line profiles.

The final step in the process was to measure the velocities of the primary and Doppler shift the line profiles to correct for the orbital motion. This step is relatively straightforward: a single unconstrained Gaussian was fitted to each line profile to measure the radial velocities. An orbit was once again fitted to these velocities using the orbital code of Bergmann (priv. comm.) and model velocities for the primary star calculated. Figure 3.3 is a snapshot of the third step. Note the poor fit of the Gaussian to the line profile due to the non-Gaussian broadening of the primary. The calculated velocities were used to Doppler shift the primary line profiles, resulting in a set of line profiles of HD 182640 A corrected for the orbital motion. Figure 3.4 shows all of the line profiles of HD 182640 A, together with the mean line profile.

Table 3.2: The orbital elements of HD 182640. (Referenced on page 62.)

Orbital Element	**HD 182640 A**	**HD 182640 B**	**Weighted Mean**
P (d)	1279 ± 6	1252 ± 3	1256 ± 6
e	0.44 ± 0.01	0.432 ± 0.009	0.43 ± 0.02
T_0 (JD−2450000)	56237 ± 7	56187 ± 4	56198 ± 8
ω (°)	195 ± 2	4 ± 1	–
v_γ[a] (km s^{-1})	-0.22 ± 0.04	-2.03 ± 0.07	-0.72 ± 0.08
K (km s^{-1})	4.07 ± 0.06	9.0 ± 0.1	–
χ^2	94.93	181.41	

[a]The v_γ values here are calculated after systemic velocity correction during the wavelength and velocity correction process, carried out by the second data reduction pipeline during the initial spectroscopic data reduction.

[9]Refer to the section on line profile correction (2.3.2) for more information

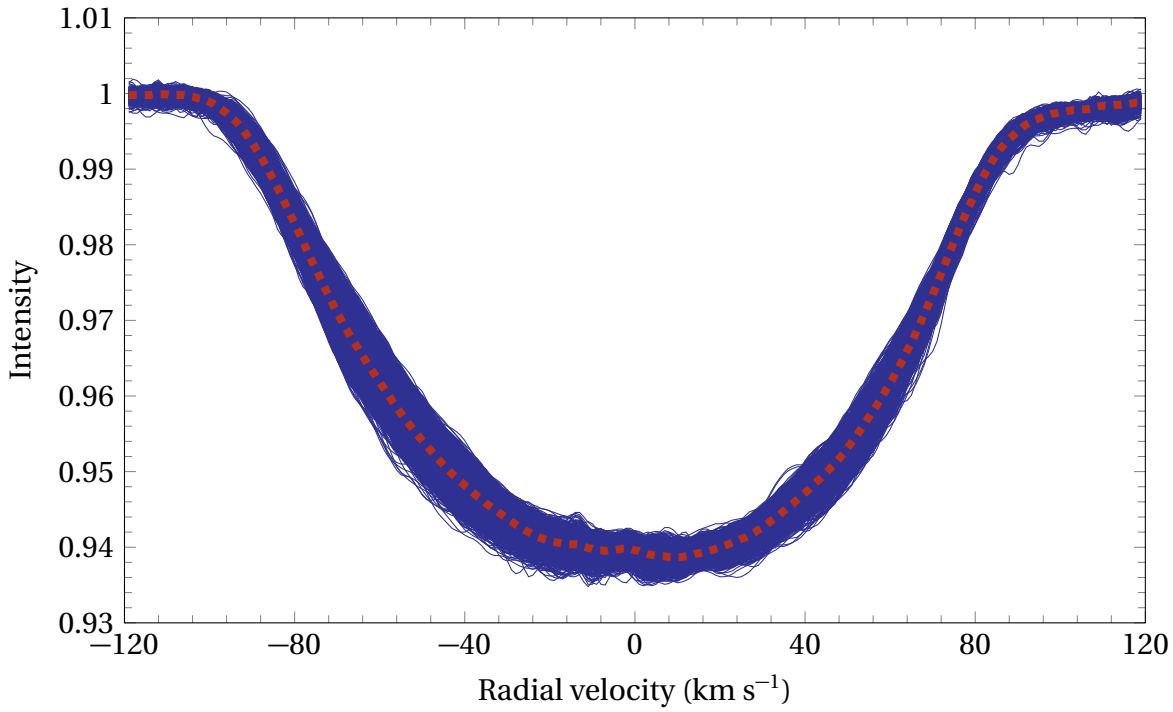

Figure 3.4: The cross-correlated line profiles (solid blue) of HD 182640 A, with the mean line profile (dashed red). Note the relatively successful removal of the signal of the secondary star from the line profiles. (Referenced on page 61.)

3.3 Orbital Analysis

The orbital fitting code of Bergmann (priv. comm.) was used to fit orbits to the measured primary and secondary radial velocities. There is a large degree of scatter of the velocities of both components due to the reasons mentioned in the binary analysis section (3.2) of this chapter. The component orbital elements and system orbital elements, calculated using the weighted mean of the component orbital elements[10], are detailed in Table 3.2 and the phased radial velocities and fitted component orbits are shown in Figure 3.5.

There are clear discrepancies between the component orbital elements that should not exist in theory. There is a 2.2% difference between P_A and P_B and a 3.6% difference between e_A and e_B. These values are within ±5% of each other and are therefore still reasonably close. ω_A and ω_B differ by 191° instead of 180° as expected. The most significantly different orbital elements are $v_{\gamma A}$ and $v_{\gamma B}$, with a difference of 1.81 km s^{-1}. These differences can be explained by the great degree of velocity scatter of both components, a consequence of the pulsations of the primary and the weak signal of the secondary star, resulting in poor orbital fits to the velocities. More precise velocity measurements would be useful in obtaining more accurate

[10]The weighted mean and its associated uncertainty estimate can be calculated using Equations 2.2 and 2.3 respectively. Refer to the section on binary orbits (1.5.1) for more information.

orbital elements.

Nevertheless, the value of $\bar{P} = 1256 \pm 6$ d agrees reasonably well with those of Kamper et al. (1989) and Fuhrmann (2008) (1251±1 d and 1251.3 d respectively). The value $\omega_A = 195 \pm 2°$ is also in agreement with that obtained by Kamper et al. ($191 \pm 14°$). $\bar{e} = 0.43 \pm 0.02$ also agrees, within the uncertainties, with that obtained by Kamper et al. (0.36 ± 0.07). However, given that their orbit was obtained from a fit of 40 velocities of the primary, it is unlikely that their e value is more accurate that those presented in this analysis.

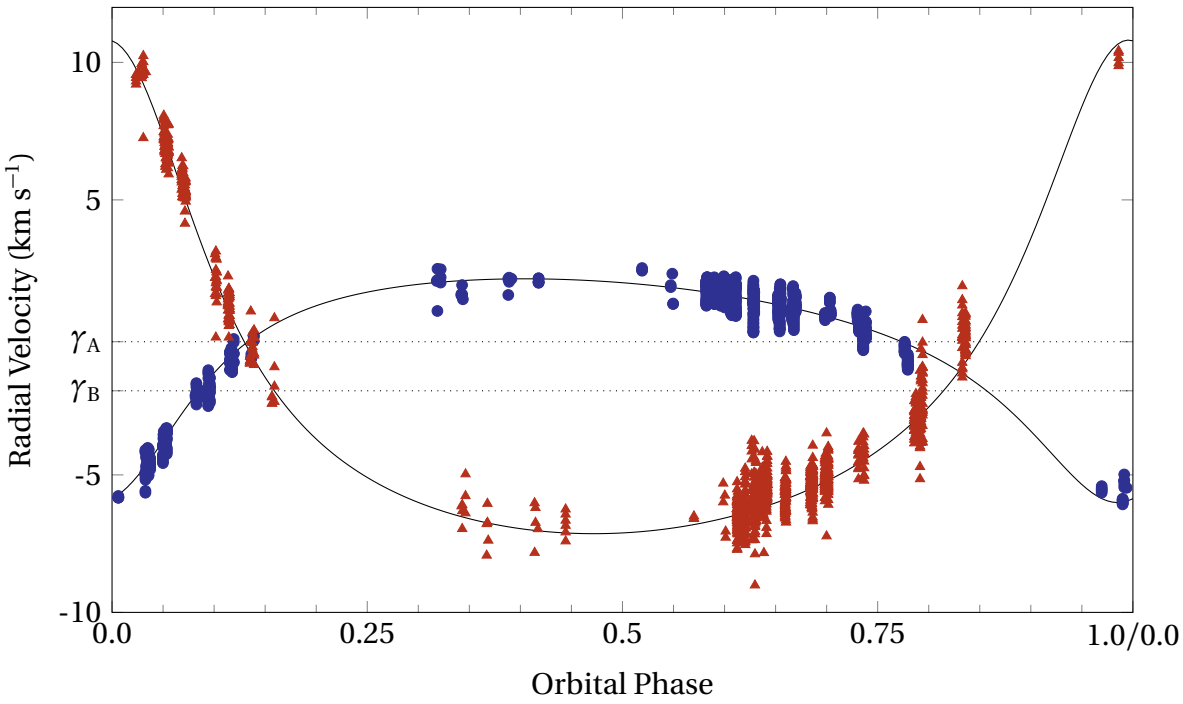

Figure 3.5: The component orbital fits (solid black lines) to the measured radial velocities of HD 182640. The blue circles and red triangles represent the primary and secondary velocities respectively. The dotted black lines represent the component systemic velocities. (Referenced on page 62.)

3.4 Frequency Identification

Figure 3.6 is the 0 d^{-1} to 80 d^{-1} frequency range pixel-by-pixel mean Lomb-Scargle periodogram of HD 182640[11], computed to determine the frequency ranges where the star shows the greatest variation[12]. It can be observed that most of the variation occurs in the 0 d^{-1} to 10 d^{-1} frequency range. Although there is some minor variation in the 25 d^{-1} to 40 d^{-1} frequency range, it was deemed by visual inspection to be below the noise level for the definitive identification of any frequencies. As such, the 0 d^{-1} to 10 d^{-1} frequency range was selected for analysis.

[11] It is assumed that all periodograms and mode identifications refer to the primary star.
[12] Refer to the section on frequency identification (2.4.1) for more information.

Figure 3.7 shows the 0 d^{-1} to 10 d^{-1} frequency range spectral widow of HD 182640, indicating the dominant frequency pattern that arose from the data sampling. Note the significant one-day aliasing that occurs. Figures B.1 to B.4 show the FAMIAS computed pixel-by-pixel mean Lomb-Scargle periodograms, and Figures B.5 to B.8 show the FAMIAS computed zeroth- to third-moment Lomb-Scargle periodograms respectively. Figure 3.8 shows the spectral significance of frequencies identified in the frequency range of 0 d^{-1} to 10 d^{-1}.

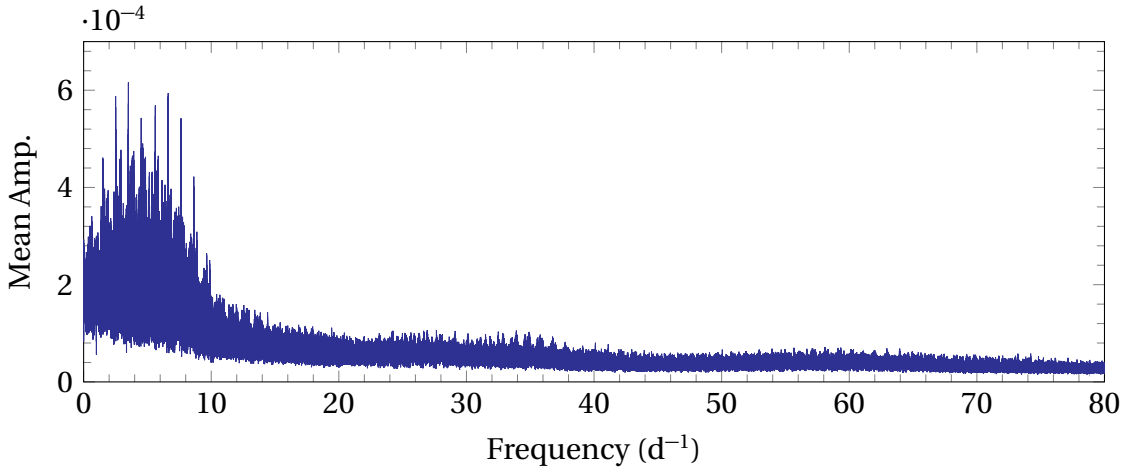

Figure 3.6: The 0 to 80 d^{-1} frequency range pixel-by-pixel mean Lomb-Scargle periodogram of HD 182640 computed by FAMIAS. (Referenced on page 63.)

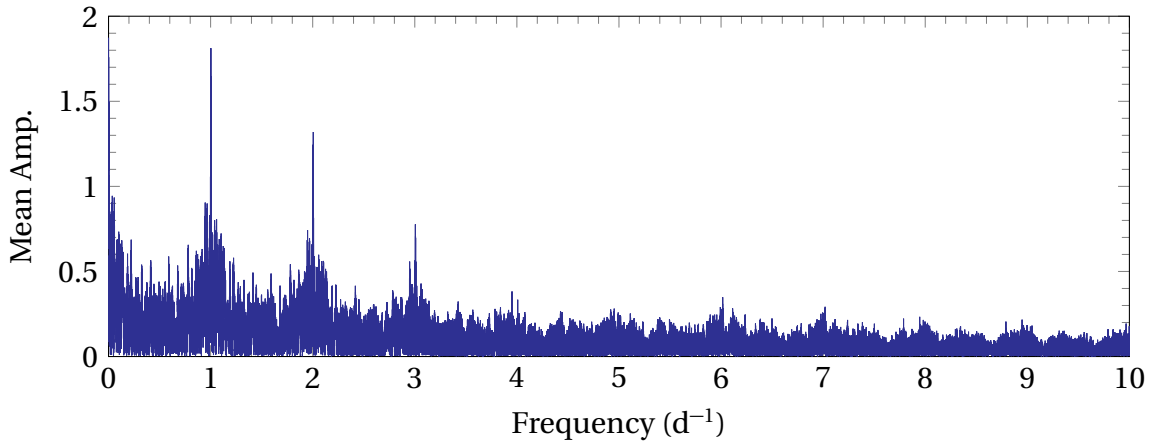

Figure 3.7: The 0 to 10 d^{-1} frequency range spectral window of HD 182640 computed by FAMIAS. (Referenced on page 63.)

It can be seen from the periodograms and from the spectral significance results that the binary orbit frequency and its one-day alias (0.0008 d^{-1} and 1.0008 d^{-1}) are still present[13]. The orbital frequency manifests itself as high spectral significance peaks around the 0 d^{-1} and 1 d^{-1}

[13]This also occurs for HD 3112 and HD 147787.

region in Figure 3.8 and medium amplitude frequency peaks in the 0 d^{-1} and 1 d^{-1} region of Figures B.1 to B.4.This is due residual variation from the line profile correction process.

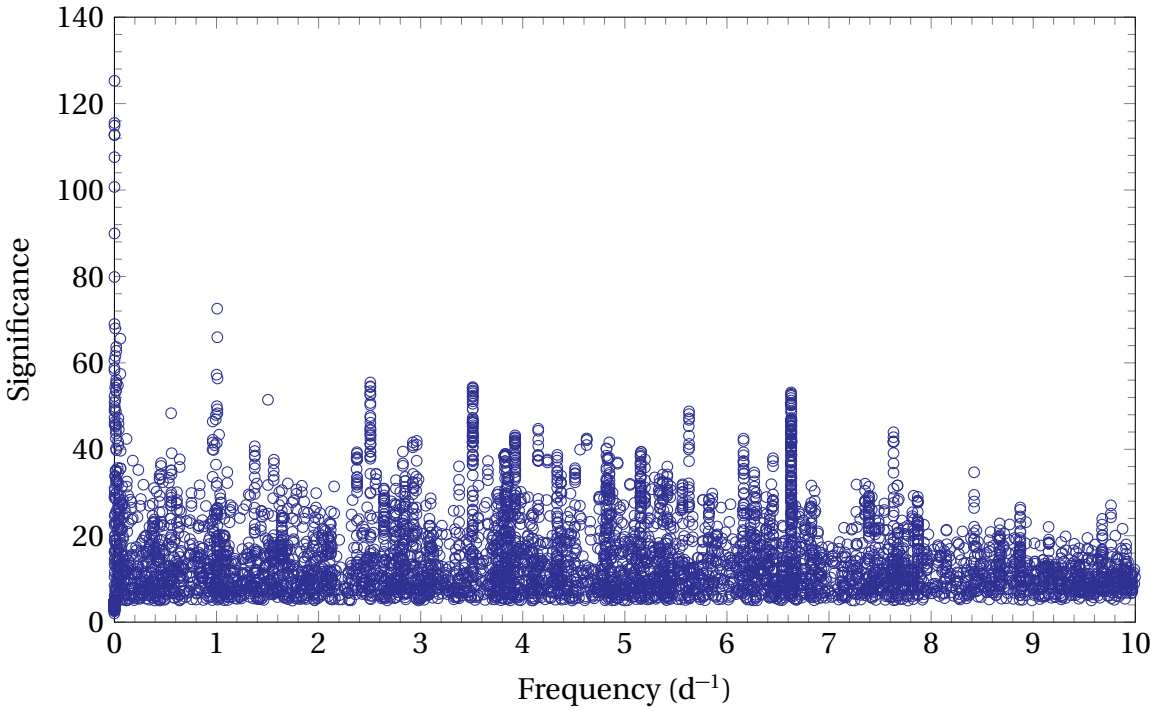

Figure 3.8: The spectral significance values of the frequencies of HD 182640 identified by SIGSPEC. Each blue circle represents a single pixel in which a frequency was identified at a particular significance. (Referenced on page 63, 64, 65, 75.)

It is also evident that the one-day aliases are still present in the Figure 3.8 and in some cases have equivalently large spectral significance values. However, the assumption that real frequencies explain a greater proportion of line profile variations, and are detected in a larger number of pixels according to the SIGSPEC results, was used to distinguish the real frequency from the aliases. Table 3.3 is a list all of the identified frequencies in FAMIAS, using the various identification methods and their corresponding SIGSPEC values.

An interesting point of note is that some of these frequencies that seem like 1-day aliases of each other (e.g. $f_3 = 3.8285$ d^{-1} and $f_5 = 4.8517$ d^{-1}) are real pulsational frequencies as the prewhitening of one did not remove the peak of the other in the periodograms, implying that they are indeed independent. Another point of note is that the strongest frequencies detected using the the pixel-by-pixel method are not detected using the the moment method.

In fact, the only frequencies detected using the the pixel-by-pixel method that have analogues detected using the moment method are:

$f_7 = 2.6420$ d^{-1}: $f_{24} = 1.5613$ d^{-1} and $f_{32} = 1.6622$ d^{-1} as potential aliases.
$f_8 = 3.9257$ d^{-1}: $f_{21} = 3.9171$ d^{-1} and $f_{29} = 3.9017$ d^{-1}.

$f_{19} = 0.0392$ d^{-1} and $f_{23} = 1.0075$ d^{-1} have corresponding SIGSPEC frequencies with high significance (46 and 73) respectively. However, in addition to being detected below the significance level associated with a signal-to-noise ratio of 4, these frequencies were not identified in any other frequency identification method. $f_{23} = 1.0075$ d^{-1} also seems to be an alias of the binary orbit

A total of 18 frequencies were identified as real pulsation frequencies, based on the criteria described in the section on frequency selection methodology (2.4.1). These frequencies and their corresponding uncertainties, calculated using Equations 2.6 for FAMIAS and 2.9 for SIGSPEC, are listed in Table 3.4. The observational timebase T was calculated using Equation 2.7, giving the value $T = 2718$ d. According to Brunsden (2013) and Greenwood (2014), SIGSPEC uncertainty estimations are overestimations and FAMIAS uncertainty estimations are underestimations. As such, a mean of the two uncertainty estimates would be closer to the true uncertainty of the identified frequencies and was therefore calculated and included in Table 3.4. The mean error estimates obtained are in the range of 0.00004 ± 0.00001 d^{-1}. The reduction in the standard deviation from successive prewhitening of pulsation frequencies is listed in Table B.1. The combination of these 18 pulsational frequencies explain 42.9% of variation across the line profiles of HD 182640, illustrated by Figure B.9.

Table 3.3: A summary of the HD 182640 frequencies found in FAMIAS and SIGSPEC. The corresponding amplitudes and uncertainties in the amplitudes A and $\sigma(A)$ calculated in FAMIAS and the maximum spectral significance of the identified frequency in SIGSPEC for the real pulsational frequencies are also listed. (Referenced on page 65.)

	FAMIAS			SIGSPEC	
	Frequency (d^{-1})	A	$\sigma(A)$	**Frequency (d^{-1})**	**Maximum Sig.**
	Pixel-by-Pixel				
f_1	3.5096	0.1521	0.0082	3.51	54
f_2	6.6287	0.1315	0.0077	6.629	53
f_3	3.8285	0.0952	0.0082	3.829	39
f_4	5.1544	0.1066	0.0080	5.154	39
f_5	4.8517	0.0687	0.0082	4.848	42
f_6	6.4157	0.0644	0.0078	6.416	22
f_7	2.6420	0.0933	0.0077	2.64	31
f_8	3.9257	0.0812	0.0082	3.926	43
f_9	2.7579	0.0771	0.0080	2.758	33
f_{10}	6.2677	0.0688	0.0079	6.268	35
f_{11}	7.8706	0.0649	0.0074	7.869	29
f_{12}	6.6690	0.0709	0.0083	6.669	27
f_{13}	4.1005	0.0694	0.0078	4.101	25
f_{14}	3.1229	0.0591	0.0078	3.123	20
f_{15}	5.3162	0.0542	0.0077	5.312	23
f_{16}	4.3371	0.0552	0.0082	4.338	39
f_{17}	7.4895	0.0516	0.0077	7.487	26
f_{18}	9.6744	0.0475	0.0079	9.676	24
	Zeroth Moment				
f_{19}	0.0392			0.0397	46
	First Moment				
f_{20}	2.6773			2.64	31
f_{21}	0.3904			0.3905	24
f_{22}	3.3281			3.329	6
	Second Moment				
f_{23}	1.0075			1.006	73
f_{24}	1.5613			1.562	38
f_{25}	0.6355			0.6365	24
f_{26}	1.2055			1.206	9
f_{27}	3.9171			3.926	43
	Third Moment				
f_{28}	1.1186			1.1182	15
f_{29}	3.9017			3.926	43
f_{30}	5.3782			5.372	34
f_{31}	2.1894			2.175	15
f_{32}	1.6622			1.661	9

Table 3.4: The identified pulsational frequencies of HD 182640, with the corresponding FAMIAS, SIGSPEC and mean uncertainty estimates. (Referenced on page 66, 66.)

	Frequency (d^{-1})	**FAMIAS $\sigma(f)$ (d^{-1})**	**SIGSPEC $\sigma(f)$ (d^{-1})**	**$\bar{\sigma}(f)$ (d^{-1})**
f_1	3.50963	0.00001	0.00005	0.00003
f_2	6.62872	0.00001	0.00005	0.00003
f_3	3.82854	0.00002	0.00006	0.00004
f_4	5.15437	0.00002	0.00006	0.00004
f_5	4.85172	0.00002	0.00006	0.00004
f_6	6.41574	0.00002	0.00008	0.00005
f_7	2.64204	0.00002	0.00007	0.00004
f_8	3.92570	0.00002	0.00006	0.00004
f_9	2.75791	0.00002	0.00006	0.00004
f_{10}	6.26770	0.00002	0.00006	0.00004
f_{11}	7.87060	0.00002	0.00007	0.00005
f_{12}	6.66905	0.00002	0.00007	0.00005
f_{13}	4.10050	0.00002	0.00007	0.00005
f_{14}	3.12290	0.00003	0.00008	0.00005
f_{15}	5.31620	0.00003	0.00008	0.00005
f_{16}	4.33710	0.00003	0.00006	0.00004
f_{17}	7.48950	0.00003	0.00007	0.00005
f_{18}	9.67440	0.00003	0.00008	0.00005

3.5 Mode Identification

Table 3.5: The zero-point fit parameters of HD 182640. (Referenced on page 68.)

Parameter	**Value**
$v \sin i$ (km s^{-1})	86.4
Equivalent Width (km s^{-1})	7.86
Intrinsic Width (km s^{-1})	10.96
Velocity Offset (km s^{-1})	-0.56
χ^2	2290.82

The initial stellar parameters input prior to mode identification are listed in Table 3.1. The $v \sin i$, equivalent width, intrinsic width and velocity offset, calculated by performing a zero-point fit in FAMIAS[14], are listed in Table 3.5. Figure 3.9 shows the zero-point fit of HD 182640. Note the relativity good visual fit of the synthetic line profile to the zero-point line profile, albiet with a high $\chi^2 = 2291$. This is likely due to the slight distortion of the zero-point profile at the base. Using Equations 2.13 and 2.14, the Keplerian breakup velocity and associated critical minimum inclination are $v_{crit} = 430.6$ and $i_{crit} = 11.57°$ respectively.

[14]Refer to the section on mode identification methodology (2.4.2) for more information.

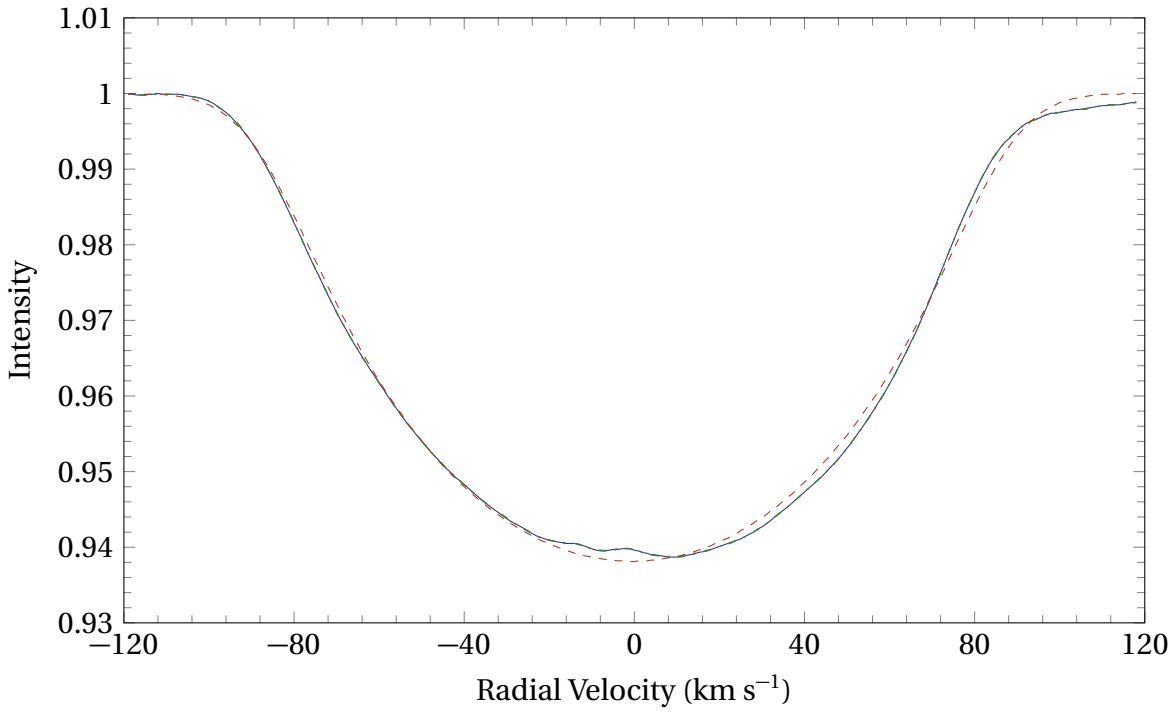

Figure 3.9: The zero-point fit of the HD 182640. The solid blue line represents the zero-point line profile, the two dash dotted green lines (partially obscured by the solid blue line) represent the statistical uncertainty and the dashed red line represents the best-fit synthetic zero-point line profile. Note the relativity good visual fit of the synthetic line profile to the zero-point line profile (albeit with a high $\chi^2 = 2290.82$). (Referenced on page 68, 76.)

Due the current status of HD 182640 as a candidate γ Doradus star[15], a parameter space consisting of modes from $0 < \ell < 3$ and $-3 < m < 3$ (the typical range for such stars) was searched at the beginning of the mode identification process. The inability to fit the observed amplitude and phase profile of the strongest frequency ($f_1 = 3.50963$ d^{-1}) using this approach necessitated the expansion of the searched parameter space to $0 < \ell < 9$ and $-9 < m < 9$. Due to the large parameter space and the often-asymmetrical observational amplitudes of many of the frequencies, it was found that the best-fit (lowest χ^2) model were sometimes poor visual fits to the amplitude profiles. As such, the ℓ and m value of the model with the best visually-fitting amplitude profile was selected as the best-fit model[16]. These values were then subsequently fixed and a second fit with a variable velocity amplitude, phase and inclination was performed to optimise those parameters.

Table 3.6 lists the best-fit modes of each individual frequency with their associated χ^2 values, inclinations, velocity amplitudes and phases. In addition, the rotational frequency $f_{\rm rot}$

[15]Refer to the section on γ Doradus stars (1.4.1) for more information.

[16]It was observed that the synthetic amplitude profiles of $\ell > 4$ models were visually more varied those of lowerℓ models. Refer to the section on the mode identification (5.4) of HD 147787 for some examples of low ℓ mode synthetic amplitude profiles.

and the co-rotating frequency $f_{\text{co-rot}}$ were calculated using Equations 2.15 and 2.18 in order to determine the physicality of each mode. These are also listed in Table 3.6. The observational amplitudes and phases for each frequency along with the best-fitting synthetic amplitude and phase profiles are shown in Figures 3.10 to 3.12.

One can observe immediately that all of these modes have inclinations that are significantly above i_{crit}. In addition, all of the frequencies are significantly greater than f_{rot} at the modelled inclination of the best-fit modes[17]. However, most of the calculated $f_{\text{co-rot}}$ values are negative, which contradicts the prograde nature of the best-fit modes. Nevertheless, the identified pulsation modes are reliable, based on Equation 2.16, as the ratio $|f_{\text{rot}}/f_{\text{co-rot}}|$ for all of the frequencies is below 0.5.

However, not all of these modes were well-fitted. While most of the modes have a $\chi^2 < 25$, the best-fit modes of $f_1 = 3.50963\ \text{d}^{-1}$, $f_2 = 6.62872\ \text{d}^{-1}$ and $f_4 = 5.15437\ \text{d}^{-1}$ have high χ^2 values (35.18, 69.33 and 27.05 respectively). This is likely due to the larger degree of asymmetry in the observational amplitude and phase profiles of these frequencies compared to the other frequencies. The best-fit modes of $f_6 = 6.41574\ \text{d}^{-1}$, $f_{10} = 6.26770\ \text{d}^{-1}$, $f_{15} = 5.31620\ \text{d}^{-1}$ and $f_{16} = 4.33710\ \text{d}^{-1}$ are also visually poor. Many of the synthetic phase profiles, while having the same general shape as the observational phase profile, are offset from the observational phase profiles by different amounts. However, it should be noted that an offset of ± 1 in phase is equivalent to an offset of 0 since the phase is periodic.

It was also found that the inclination values of the models with the best-fit ℓ and m values converged to specific ranges. Table 3.7 lists the range of inclination values for each frequency. Most of the best-fit inclination ranges fell within the 30° to 50° range (except for the inclinations ranges of f_{12}, f_{17} and f_{18}). It is therefore reasonable to conclude that the true inclination of HD 182640 is somewhere in the 30° to 50° range. This corresponds to a rotational velocity of 113 km s^{-1} to 173 km s^{-1} (25% to 40% of $v_{\text{crit}} = 430.6$ km s^{-1}). This is above the average for F0-type stars (95 km s^{-1}, McNally, 1965), but entirely reasonable.

[17] Refer to the section on mode identification methodology (2.4.2) for more information.

Table 3.6: The best-fit modes of each of the 18 analysed frequencies of HD 182640, with the corresponding rotational frequencies at the modelled inclinations. (Referenced on page 69, 69.)

Mode	χ^2	Inclination	Vel. Amp. (km s^{-1})	Phase	f_{rot} (d^{-1})	$f_{\text{co-rot}}$ (d^{-1})
$f_1 = 3.50963$ d^{-1}						
(7, 5)	35.18	42.48	0.645	0.890	1.45	−3.59
$f_2 = 6.62872$ d^{-1}						
(5, 1)	69.33	39.80	0.645	0.331	1.52	5.15
$f_3 = 3.82854$ d^{-1}						
(6, 6)	8.61	35.79	1.290	0.370	1.67	−5.95
$f_4 = 5.15437$ d^{-1}						
(9, 7)	27.05	45.16	0.645	0.945	1.38	−4.38
$f_5 = 4.85172$ d^{-1}						
(6, 6)	9.95	35.79	0.645	0.283	1.67	−4.93
$f_6 = 6.41574$ d^{-1}						
(9, 7)	21.89	30.43	0.645	0.039	1.93	−6.92
$f_7 = 2.64204$ d^{-1}						
(6, 6)	23.27	45.16	0.645	0.669	1.38	−5.42
$f_8 = 3.92570$ d^{-1}						
(8, 8)	17.48	46.50	0.645	0.984	1.35	−6.69
$f_9 = 2.75791$ d^{-1}						
(6, 6)	12.19	42.48	0.645	0.535	1.45	−5.71
$f_{10} = 6.26770$ d^{-1}						
(6, 6)	23.75	30.43	0.645	0.906	1.93	−5.02
$f_{11} = 7.87060$ d^{-1}						
(6, 2)	11.05	52.52	0.645	0.339	1.23	5.47
$f_{12} = 6.66905$ d^{-1}						
(5, 2)	23.69	63.23	0.645	0.709	1.09	4.56
$f_{13} = 4.10050$ d^{-1}						
(8, 8)	13.52	45.16	0.645	0.039	1.38	−6.76
$f_{14} = 3.12290$ d^{-1}						
(7, 7)	10.79	41.81	0.645	0.945	1.46	−6.94
$f_{15} = 5.31620$ d^{-1}						
(5, 5)	12.91	23.74	1.290	0.260	2.42	−6.40
$f_{16} = 4.33710$ d^{-1}						
(8, 8)	11.16	41.14	0.645	0.031	1.48	−7.37
$f_{17} = 7.48950$ d^{-1}						
(6, 3)	9.43	75.94	0.645	0.457	1.01	4.54
$f_{18} = 9.67440$ d^{-1}						
(7, 4)	6.66	75.94	0.645	0.173	1.01	5.72

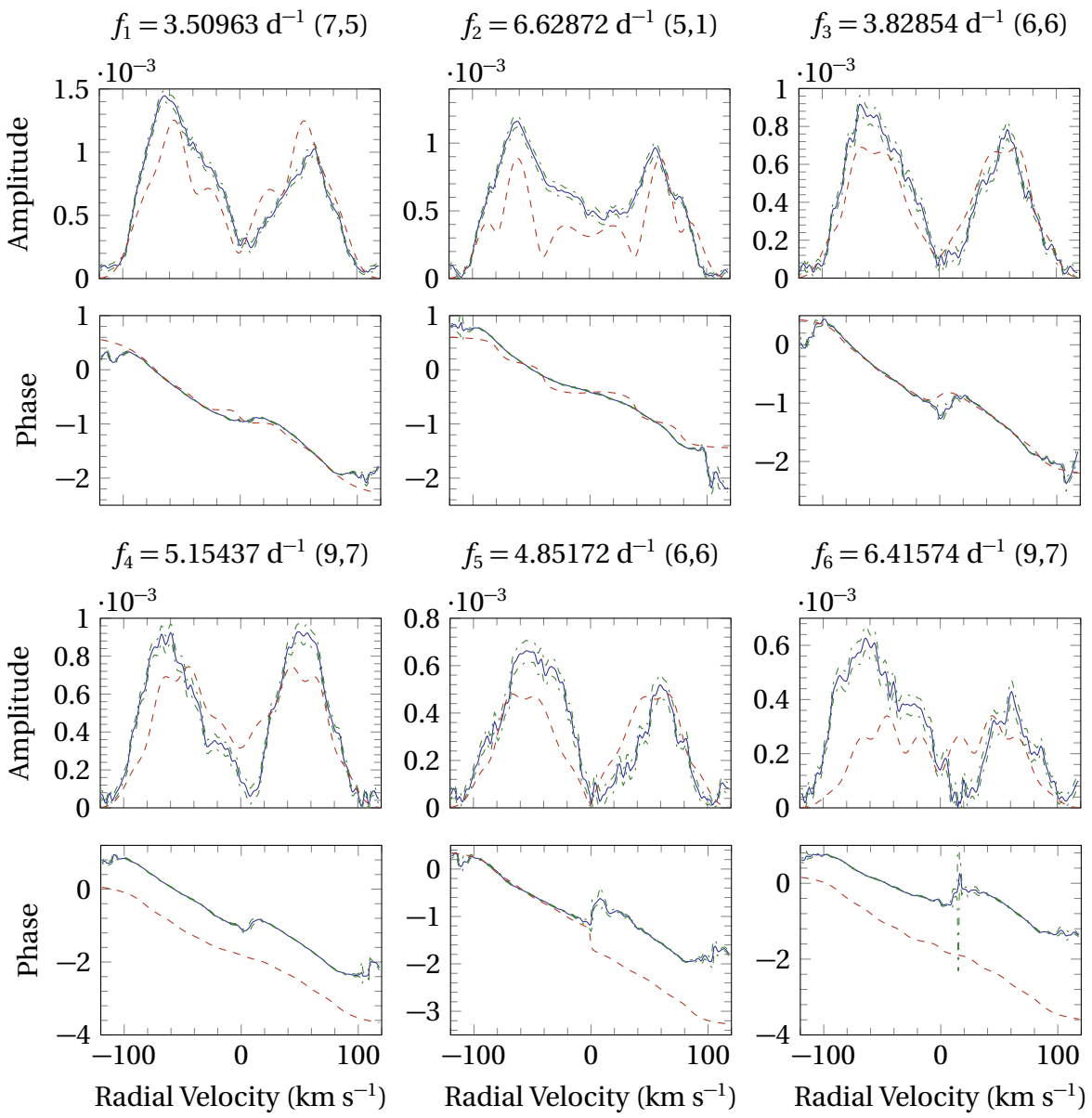

Figure 3.10: The amplitude and phase profiles of the best-fit modes of f_1 to f_6 of HD 182640. The solid blue lines are the observational profiles, the dash dotted green lines represent the statistical uncertainty and the dashed red lines represent the best-fit synthetic profiles. (Referenced on page 69, 76.)

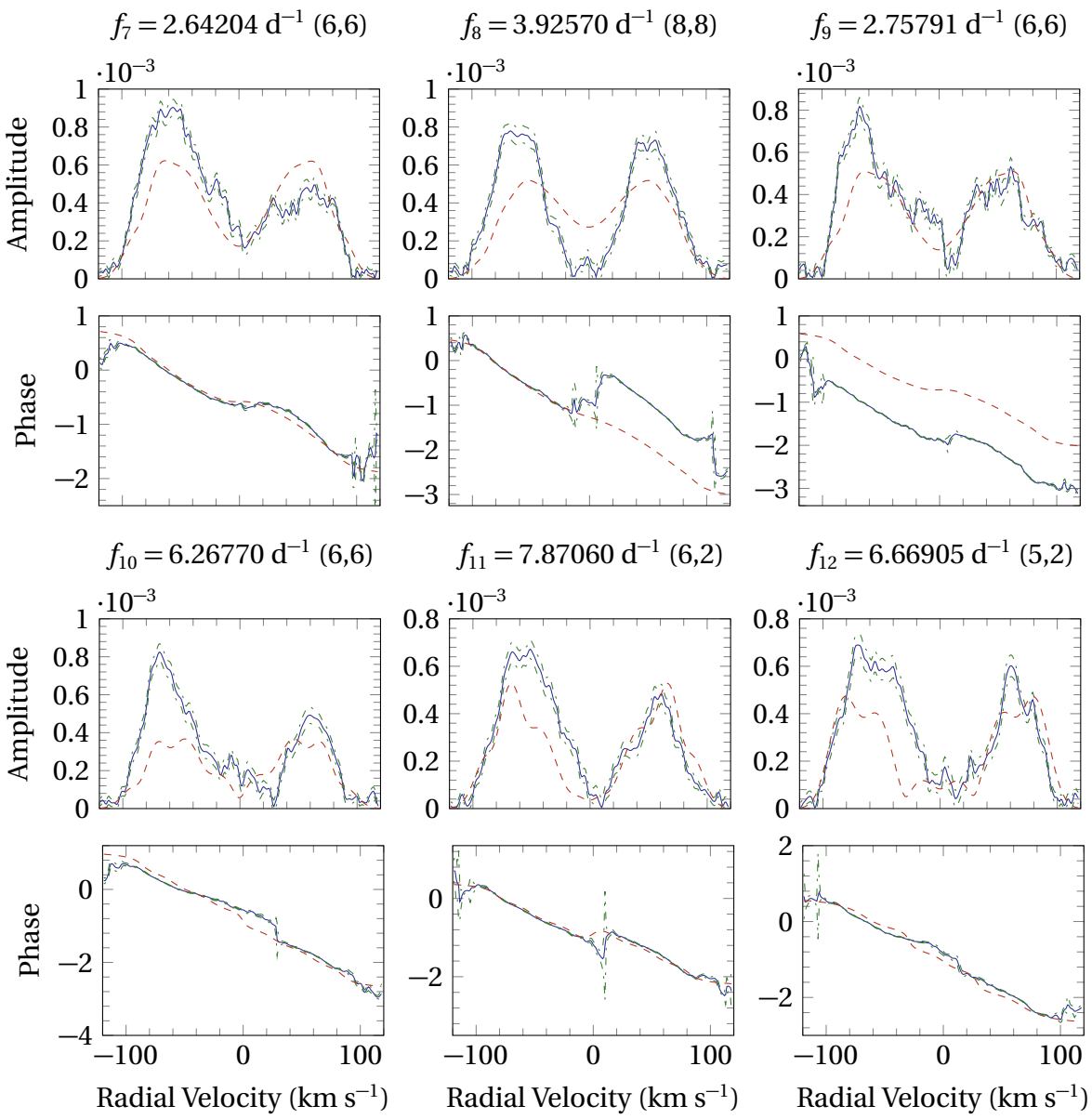

Figure 3.11: The amplitude and phase profiles of the best-fit modes of f_7 to f_{12} of HD 182640. The solid blue lines are the observational profiles, the dash dotted green lines represent the statistical uncertainty and the dashed red lines represent the best-fit synthetic profiles. (Referenced on page 69, 76.)

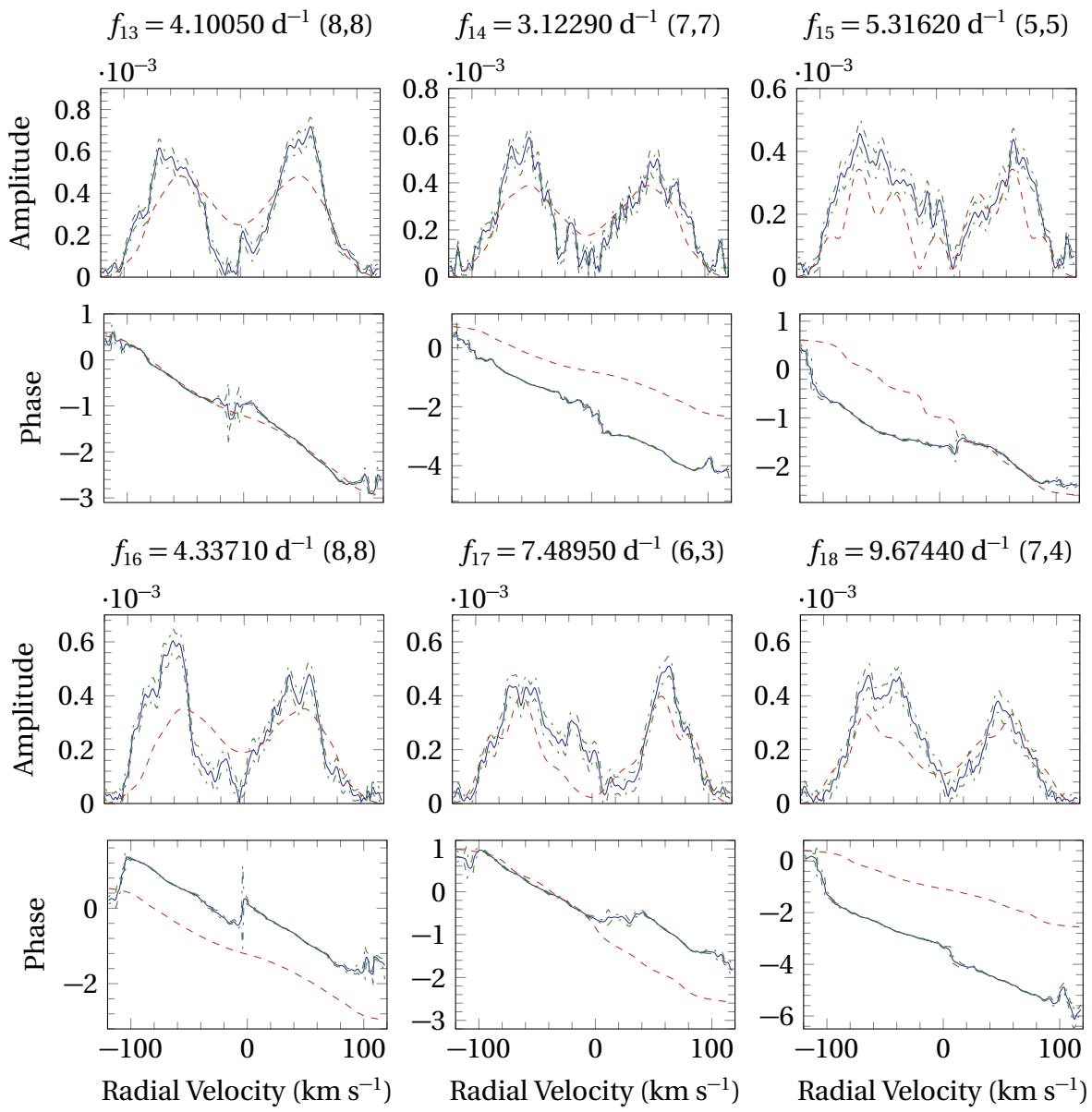

Figure 3.12: The amplitude and phase profiles of the best-fit modes of f_{13} to f_{18} of HD 182640. The solid blue lines are the observational profiles, the dash dotted green lines represent the statistical uncertainty and the dashed red lines represent the best-fit synthetic profiles. (Referenced on page 69, 76.)

Table 3.7: The inclination ranges of the best-fitting models of the individual frequencies of HD 182640. (Referenced on page 70.)

	Frequency (d^{-1})	Inclination range (°)
f_1	3.50963	37 – 47
f_2	6.62872	35 – 45
f_3	3.82854	25 – 45
f_4	5.15437	37 – 50
f_5	4.85172	20 – 42
f_6	6.41574	25 – 35
f_7	2.64204	35 – 50
f_8	3.92570	35 – 52
f_9	2.75791	30 – 45
f_{10}	6.26770	20 – 35
f_{11}	7.87060	45 – 65
f_{12}	6.66905	55 – 78
f_{13}	4.10050	30 – 50
f_{14}	3.12290	30 – 45
f_{15}	5.31620	18 – 30
f_{16}	4.33710	35 – 45
f_{17}	7.48950	65 – 90
f_{18}	9.67440	70 – 90

3.6 Discussion

The results of the frequency and mode identifications are interesting, to the say the least. Most of the identified frequencies (except for $f_7 = 2.64204$ d^{-1} and $f_9 = 2.75791$ d^{-1}) are outside of the typical γ Doradus[18] range of 0.3 d^{-1} to 3 d^{-1}. In fact, most of these frequencies are within the lower end of the spectrum of the typical frequency range of δ Scuti stars[19] (3 d^{-1} to 80 d^{-1}). This seems to support the claims of Frolov (1970) and King and Liu (1990), who had classified HD 182640 as a δ Scuti star. However, the results from SIGSPEC (Figure 3.8) show a number of high spectral-significance frequencies in the 0 d^{-1} to 3 d^{-1}. As such, it is not possible to definitively conclude that HD 182640 is a δ Scuti star. These frequencies are of much lower amplitude (and hence did not emerge during frequency analysis for this thesis) and could be identified with the analysis of a larger dataset or with higher-quality spectra.

Nevertheless, some of the frequencies obtained are similar to previously published results. The frequency 6.365 d^{-1} (Henroteau, 1923) and 6.31 d^{-1} (Frolov, 1970) are potentially aliases of $f_2 = 6.62872$ d^{-1}. The frequency 4.37 d^{-1} (Brunsden, 2013) seems correspond to $f_{16} = 4.33710$ d^{-1} and the frequencies 3.67 d^{-1} and 2.21 d^{-1} (Brunsden, 2013) seem to be aliases of $f_7 = 2.64204$ d^{-1} and $f_9 = 2.75791$ d^{-1} respectively.

[18] Refer to the section on γ Doradus stars (1.4.1) for more information.
[19] Refer to the section on δ Scuti stars (1.4.2) for more information.

The inability to find strong frequencies using the various moments of the the moment method is also an interesting point. In fact, the Lomb-Scargle periodograms of the various moments were dominated by noise (Figures B.5 to B.8). This was alluded to by Baade and Kjeldsen (1997), who had found no variations in the radial velocity (the first moment). This could probably be due to distortions in the line profiles, particularly near the minimum point, making it difficult to extract periodicities from the moment values.

One of the difficulties encountered during the mode identification process is the noise (the distorted appearance of the line profiles) and asymmetry in the observational zero-point, amplitude and phase profiles[20]. This resulted in poor mode identifications for some of the frequencies (Figures 3.10 to 3.12). The noise in the observational zero-point, amplitude and phase probably arose from distortions in the individual line profiles[21]. Higher signal-to-noise spectra of the star would improve the quality of the least-squares fits and correspondingly, the mode identification. This may be aided by longer exposure times for this star.

The identified modes are also slightly uncertain because most of the $f_{\text{co-rot}}$ values are negative, contradicting the prograde nature of the modes. However, the f_{rot} values are in agreement with the prograde nature of the modes as they were all lower than the pulsational frequencies. Further investigation would be useful to confirm the veracity of the mode identification.

It is also interesting that all of the best-fit modes are high-ℓ modes. In fact, none of the best-fit modes had $\ell < 5$ and is in agreement with the results of Baade and Kjeldsen (1997). High ℓ modes have been observed in δ Scuti stars (Mantegazza and Poretti, 2005), as well as β Cephei and SPB stars (Dziembowski et al., 1993). However, none have been observed in γ Doradus stars. This could imply that HD 182640 is a hybrid pulsator (Chapellier et al., 2012), which according to Balona et al. (2015), is equivalent to classifying it as a δ Scuti star. However, Balona et al. (2015) had mentioned that the low-frequency variation that they had observed in δ Scuti stars is significantly weaker than the high-frequency variation[22]. Given the strength of the low-frequency variation, particularly in the 0 d^{-1} to 3 d^{-1} range, observed in HD 182640, it would, once again, be unwise to conclude that HD 182640 is a δ Scuti star.

Given the long orbital period (1252 d), low radial velocity semi-amplitudes (< 10 km s^{-1}) and low mass of the companion star (0.67 $M_\odot$, Fuhrmann, 2008), it is unlikely that the binarity of HD 182640 has any effect on the pulsational characteristics of HD 182640 A, other than complicating the analysis.

[20] Refer to the section on mode identification methodology (2.4.2) for more information.
[21] This can be inferred from the zero-point line profile itself (Figure 3.9).
[22] This is in contrast with the low frequency variation observed in HD 3112. Refer to the section on the frequency identification (4.3) of HD 3112 for more information.

4 HD 3112

HD 3112[1] is a moderately bright ($m_V = 6.11$, Paunzen, 2015) star in the constellation of Tucana, which is the Latin word for *toucan* (a type of bird). It has a spectral type of A7IV (Chang et al., 2013) and is located at the coordinates 00h 33m 23.4s, -71° 1′ 58.5″ (J2000 epoch[2], van Leeuwen, 2007) at a distance of 130 ± 5 pc from the Sun (van Leeuwen, 2007), according to HIPPARCOS astrometric parallax measurements. Its position in the sky makes HD 3112 circumpolar[3] when observed from UC MJO.

HD 3112 is a fairly well-studied star. Photometric variability was first recorded by Cousins and Lagerwey in 1971. They reported variations of up to 0.06 magnitudes with short periods of 70 min to 80 min, corresponding to frequencies of 18.0 d^{-1} to 20.5 d^{-1}. This was later confirmed by Stobie and Shobbrook (1976), who noted a main frequency of 20.28 d^{-1} as well as several other frequencies that varied in an irregular fashion, depending on the timebase of the analysed observations, and classified HD 3112 as a δ Scuti star. Kurtz (1980) later posited that the frequency variability could be due to the beating of frequencies and, through the analysis of a 7-year dataset, found that the main frequency of 20.281 ± 0.004 d^{-1} was constant over the entire time period. His analysis also found seven other frequencies from 15 d^{-1} to 21 d^{-1} but mentioned that they were not definitive.

Paparo et al. (1996) later conducted an analysis of a much larger photometric dataset (more than 2300 observations) and found not only nine stable frequencies in the 13 d^{-1} to 25 d^{-1} range, but also another three frequencies in the 0 d^{-1} to 5 d^{-1} range: 0.14206 d^{-1}, 0.28151 d^{-1} and 0.99350 d^{-1}. They had also noted that the frequency spacings were very close and attributed that to rotational splitting[4]. The first mentioning of the potential binarity of HD 3112 was also in Paparo et al. (1996), who found that the infrared and ultraviolet spectra of the star displayed some "unusual" behaviour and posited that HD 3112 could possibly be a binary system with a late F-type companion.

The binarity of the system was later confirmed by Sterken (1997), who expanded upon the work of Paparo et al. (1996). He found a binary period of 7.04 d and attributed two of the low frequencies found by Paparo et al. (1996) (0.14206 d^{-1} and 0.28151 d^{-1}) to the binary orbit. He also classified HD 3112 as an ellipsoidal binary, based on its similarity to the bona-fide

[1] Other designations for this star include HR 139, HIP 2629, theta Tucanae and θ Tuc.
[2] An epoch is a reference point for astronomical quantities (in this case, celestial coordinates) that vary with time. The coordinates of the star are with reference to the J2000 epoch, defined as 12:00 UT on 1 January, 2000.
[3] Circumpolar stars are stars that do not set (i.e. fall below the horizon) when observed from a specific latitude. This is due to their proximity to one of the two celestial poles and the latitude at which the star is observed.
[4] Refer to the section on the rotational effects on pulsations (1.3.6) for more information.

ellipsoidal binary HD 96008. In addition, he proposed that the strongest frequency 20.28 d^{-1} was a fundamental radial mode[5] and that the others could be $\ell = 2$ modes[6].

The first spectroscopic study of HD 3112 was published by Sterken et al. (1997) and reported several fundamental stellar parameters such as $T_{\rm eff}$, [Fe/H] and $\log g$. The study also reported the pulsational radial velocity amplitude of the frequency 20.28 d^{-1}: 6 km s^{-1} to 8 km s^{-1}. A follow-up study by De Mey et al. (1998) included the determination the orbital elements of the system as well as a spectroscopic frequency analysis using 148 spectra taken during the month of September 1996. They found four main pulsational frequencies in the spectroscopic data: 20.28 d^{-1}, 18.82 d^{-1}, 20.78 d^{-1} and 19.05 d^{-1}. De Mey et al. (1998) also found that the frequency 20.28 d^{-1} is a radial mode and indicated that 18.82 d^{-1} is probably a high degree mode ($\ell > 3$). Possible evolution scenarios were also discussed: De Mey et al. (1998) suggested that HD 3112 is a post-mass-transfer binary that was once semi-detached, and is currently detached but experiencing ellipsoidal variation.

Templeton et al. (2000) calculated various different pulsational models for HD 3112 that incorporated second-order rotation effects[7]. They were able to approximately reproduce all of the pulsation modes of the star and supported the claims made by Sterken (1997), Sterken et al. (1997) and De Mey et al. (1998) that 20.28 d^{-1} is a radial mode, characterising it as a high-overtone mode ($n = 4$). They also found a large number of mixed-mode frequencies. Templeton et al. (2000) also calculated ranges for the equatorial rotational velocity (70 km s^{-1} to 90 km s^{-1}).

The work of Paparó and Sterken (2000) builds on this, incorporating amplitude ratios for the frequencies found by Paparo et al. (1996) and including a more thorough mode identification attempt. They mentioned that the rotational splitting explanation of Templeton et al. (2000) could not fully explain all of the observed frequencies and modes, and that the mode identification itself was non-definitive.

Templeton et al. (2000) characterised HD 3112 B as a post-red giant branch star[8] with $\log g = 3$, a temperature of 7000 K, a mass of 0.2 $M_\odot$ and a radius of 1.9 $R_\odot$.

[5] Refer to the section on radial pulsations (1.3.2) for more information
[6] Refer to the section on non-radial pulsations ((1.3.3) for more information
[7] Refer to the section on the rotational effects on pulsations (1.3.6) for more information.
[8] A post-red giant branch star is a star that has evolved off the red giant branch (RGB) of the HR diagram. In this case, the mass transfer from HD 3112 B to HD 3112 A has caused HD 3112 B to exhibit characteristics of post-RGB stars without going through the typical evolutionary cycle.

Table 4.1: The fundamental stellar parameters of HD 3112, used during spectroscopic data reduction and mode identification. The minimum and maximum literature values of each parameter and the value used in this analysis (typically the approximate mean or the mode of the literature values) are listed. (Referenced on page 80, 90.)

Parameter	Min. Literature Value	Max. Literature Value	Value Used
$T_{\rm eff}$ (K)	7053 (McDonald et al., 2012)	7650 (Wright et al., 2003)	7500
$\log[g$ (cm s^{-2})]	3.8 (Sterken et al., 1997)	4.2 (Lafrasse et al., 2010)	3.85
Radius ($R_\odot$)	1.7 (De Mey et al., 1998)	2.7 (De Mey et al., 1998)	2.2
Mass ($M_\odot$)	1.9 (Sterken et al., 1997)	2.2 (Templeton et al., 2000)	2.0
[Fe/H] (dex)	0.02 (Sterken et al., 1997)	0.02 (Sterken et al., 1997)	0.02
$v \sin i$ (km s^{-1})	52 (Hoffleit and Warren, 1995)	80 (Glebocki and Gnacinski, 2005)	52
v_γ (km s^{-1})	2.3 (de Bruijne and Eilers, 2012)	4.0 (Abt and Biggs, 1972)	2.3

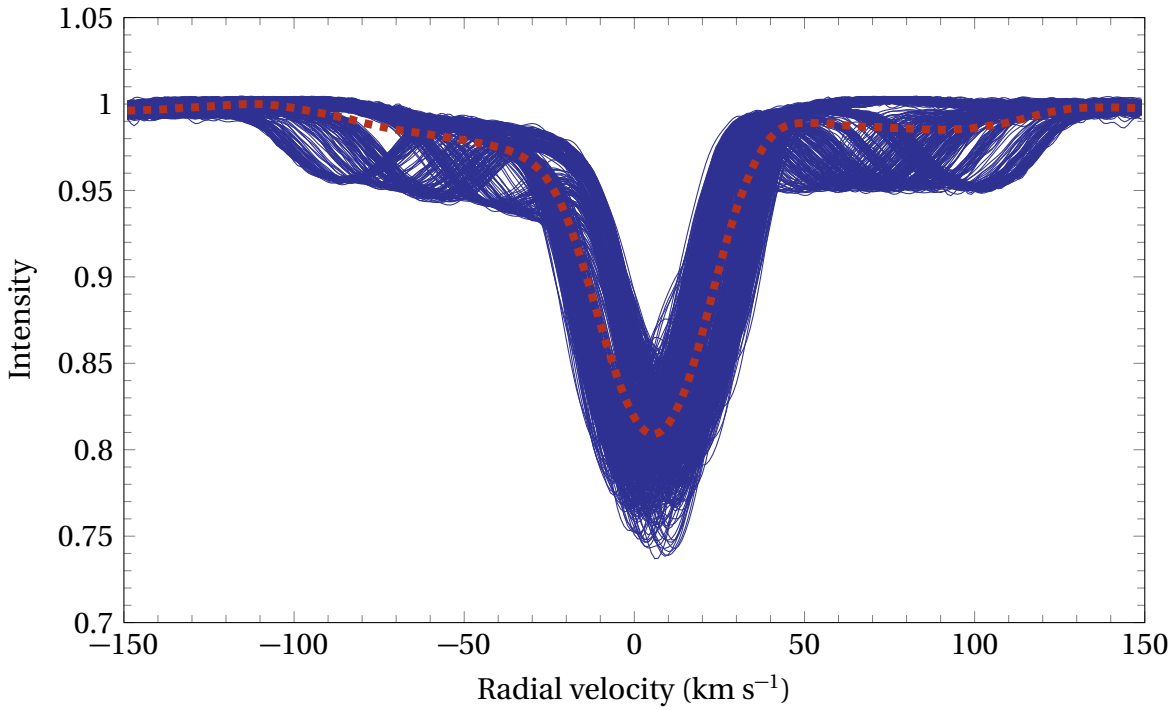

Figure 4.1: The cross-correlated line profiles (solid blue) of HD 3112, with the mean line profile (dashed red). (Referenced on page 80.)

4.1 Observations

A total of 595 observations[9] of HD 3112 were collected between July 2014 and August 2015. Fortuitously, there were no spectra with a signal-to-noise ratio of less than 40[10]. Table 4.1 shows a summary of the stellar parameters obtained from the literature and the values used as inputs during the spectroscopic data reduction process[11]. Figure 4.1 shows all of the cross-correlated line profiles of HD 3112, together with the mean line profile. The signal of the secondary star was removed using the method described in the section on binary analysis (2.3). Figure 4.2 shows the result of this process: it displays all of the cross-correlated line profiles of HD 3112 A, together with the mean line profile.

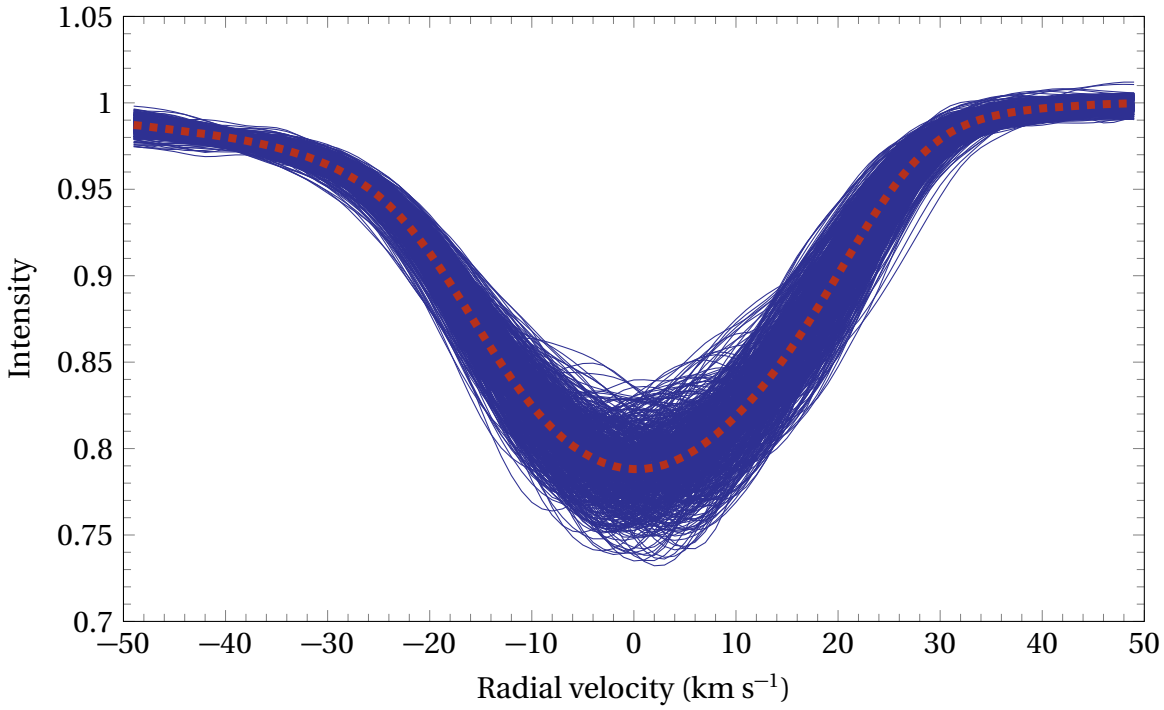

Figure 4.2: The cross-correlated line profiles (solid blue) of HD 3112 A, with the mean line profile (dashed red). Note the relatively successful removal of the signal of the secondary star from the line profiles. (Referenced on page 80.)

[9] Refer to Table 2.1 for more details

[10] Refer to the section on cross-correlation (2.2.3) for more information on why low signal-to-noise spectra were discarded.

[11] Refer to the section on the second data reduction pipeline (2.2.3) for more information.

Table 4.2: The orbital elements of HD 3112. (Referenced on page 81, 90.)

Orbital Element	HD 3112 A	HD 3112 B	Weighted Mean
P (d)	7.107 ± 0.001	7.10760 ± 0.00004	7.108 ± 0.001
e	0.01 ± 0.01	0.0148 ± 0.0008	0.01 ± 0.01
T_0 (JD−2450000)	57229 ± 1	57247.94 ± 0.05	57248 ± 1
ω (°)	100 ± 60	148 ± 3	–
v_γ [a] (km s^{-1})	6.0 ± 0.1	9.46 ± 0.05	8.8 ± 0.1
K (km s^{-1})	8.0 ± 0.1	93.72 ± 0.05	–
χ^2	214.88	2.97	

[a]The v_γ values here are calculated after systemic velocity correction during the wavelength and velocity correction process, carried out by the second data reduction pipeline during the initial spectroscopic data reduction.

4.2 Orbital Analysis

The orbital fitting code of Bergmann (priv. comm.) was used to fit orbits to the measured primary and secondary radial velocities[12]. Of the 595 velocities of each component, 472[13] were used for the orbital fitting. There is some scatter of the radial velocities of the primary due to the pulsations but the secondary velocities are relatively precise. The component orbital elements and system orbital elements, calculated using the weighted mean of the component orbital elements[14], are detailed in Table 4.2 and the phased radial velocities and fitted component orbits are shown in Figure 4.3.

Most of the orbital elements are in agreement with each other. P_A and P_B, as well as e_A and e_B are in very close agreement. ω_A and ω_B differ by 48° instead of 180° as expected due to the low eccentricity, essentially implying a circular orbit for which the argument of the periastron ω is not defined. The values of ω_A and ω_B therefore did not converge in the orbital fit. The only orbital elements that are significantly different are $v_{\gamma A}$ and $v_{\gamma B}$, with a difference of 3.5 km s^{-1}. One of the assumptions in the Gaussian-fitting process is that the line profile variations of the primary average out with sufficient overall phase coverage of the pulsations[15]. However, the mean line profile of HD 3112 is slightly asymmetric (refer to Figure 4.8). This means that the measured velocities will be offset by a certain amount, and might explain the significant difference between $v_{\gamma A}$ and $v_{\gamma B}$.

Comparing the orbital elements in this analysis to the orbital elements reported in De Mey et al. (1998), it can be seen that the period $\bar{P} = 7.108 \pm 0.001d$ and eccentricity $\bar{e} = 0.01 \pm 0.01$

[12]Refer to the section on binary analysis (2.3) for more information on how the velocities were measured.
[13]The velocities that were excluded from the orbital fitting were the ones that deviated significantly from the preliminary orbital fit. These typically correspond to the the velocities measured from the line profiles with merged peaks (low radial velocity separation). Refer to the section on orbital analysis (2.3.1) for more information.
[14]The weighted mean and it's associated uncertainty estimate can be calculated using Equations 2.2 and 2.3 respectively. Refer to the section on binary orbits (1.5.1) for more information.
[15]Refer to the section on binary analysis (2.3) for more information.

are in close agreement with the values 7.1036 d and 0.02 in De Mey et al. (1998). $v_{\gamma A} = 6.0 \pm 0.1$ km s^{-1} and $v_{\gamma B} = 9.46 \pm 0.05$ km s^{-1} differ from those of De Mey et al. (1998) (9.5 km s^{-1} and 7.31 km s^{-1}). $K_A = 8.0 \pm 0.1$ km s^{-1} and $K_B = 93.72 \pm 0.05$ km s^{-1} are also different from those reported by De Mey et al. (1998) (8.57 km s^{-1} and 95.6 km s^{-1}). This could possibly be due to the fact that the orbital elements of De Mey et al. (1998) were calculated after fixing the eccentricity at zero. Given that the dataset used in this analysis to calculate the orbital elements is approximately three times larger than that of De Mey et al. (1998) (472 vs 148), it can be concluded that the orbital elements in this analysis are more accurate that those of De Mey et al. (1998). The mass ratio q, obtained by plotting the velocities of the HD 3112 A vs HD 3112 B and taking the gradient of the best-fit line through the points, was calculated and the value $q = 0.085$ was obtained. This is consistent with the value $q = 0.0896$ reported by De Mey et al. (1998).

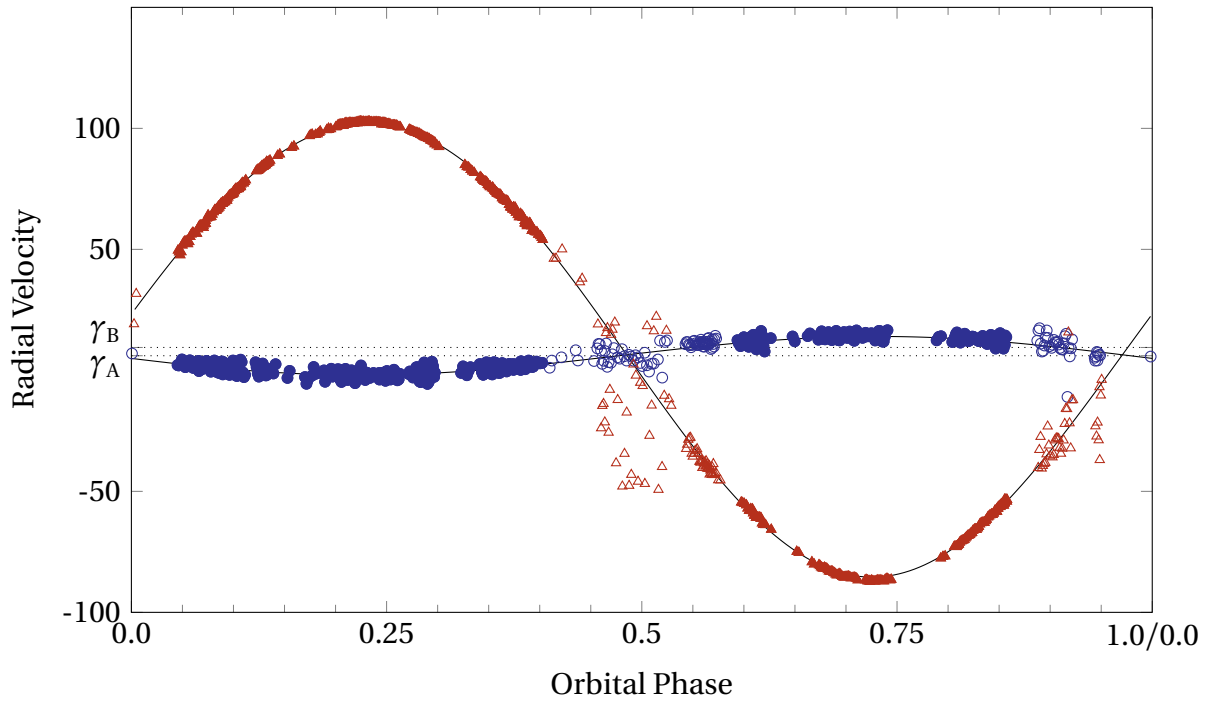

Figure 4.3: The component orbital fits (solid black lines) to the measured radial velocities of HD 3112. The blue circles and the red triangles represent the primary and secondary radial velocities respectively. The filled circles and triangles are the velocities that were used for the orbital fitting. The dotted black lines represent the component systemic velocities. (Referenced on page 81.)

4.3 Frequency Identification

Figure 4.4 is the 0 d^{-1} to 80 d^{-1} frequency range pixel-by-pixel mean Lomb-Scargle periodogram of HD 3112[16], computed to determine the frequency ranges where the star shows the greatest variation[17]. It can be observed that the strongest variation occurs in the 13 d^{-1} to 25 d^{-1} frequency range. There is also some strong variation in the 0 to 3 d^{-1} frequency range. Although there is some minor variation in the 35 d^{-1} to 45 d^{-1} frequency range, it was deemed by visual inspection to be below the noise level for the definitive identification of any frequencies. As such, the 13 d^{-1} to 25 d^{-1} and the 0 d^{-1} to 3 d^{-1} frequency ranges was selected and analysed separately. Figure 4.5 shows the spectral significance of frequencies identified in the frequency range of 0 d^{-1} to 25 d^{-1}. Interestingly, there were no significant frequencies identified in the 6 d^{-1} to 14 d^{-1} range in SIGSPEC.

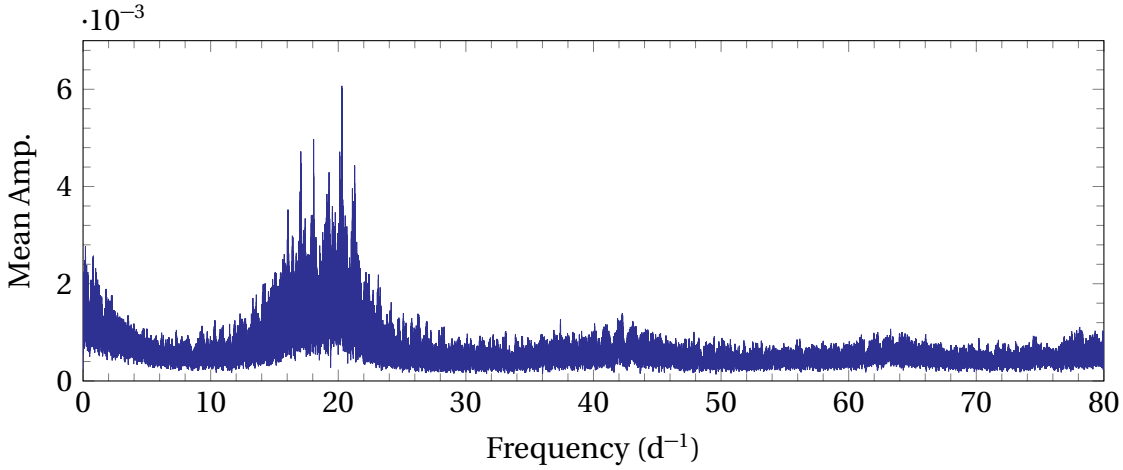

Figure 4.4: The 0 to 80 d^{-1} frequency range pixel-by-pixel mean Lomb-Scargle periodogram of HD 3112 computed by FAMIAS. (Referenced on page 83.)

4.3.1 The 13 d^{-1} to 25 d^{-1} Frequency Range

Figure 4.6 shows the 13 d^{-1} to 25 d^{-1} frequency range spectral widow of HD 3112, indicating the dominant frequency pattern that arose from the data sampling in that range. Although there is some one-day aliasing, there seems to be sufficient random variation that the aliasing is not as significant a factor in this frequency range. The low level of aliasing can also be seen from the SIGSPEC results (Figure 4.5), where the primary frequency in the 13 d^{-1} to 25 d^{-1} frequency range ($f_1 = 20.2802$ d^{-1}) is of much higher spectral significance than its 1-day alias (19.2810 d^{-1}). Figures C.1 to C.3 are the FAMIAS computed pixel-by-pixel mean Lomb-Scargle

[16] It is assumed that all periodograms and mode identifications refer to the primary star.
[17] Refer to the section on frequency identification (2.4.1) for more information.

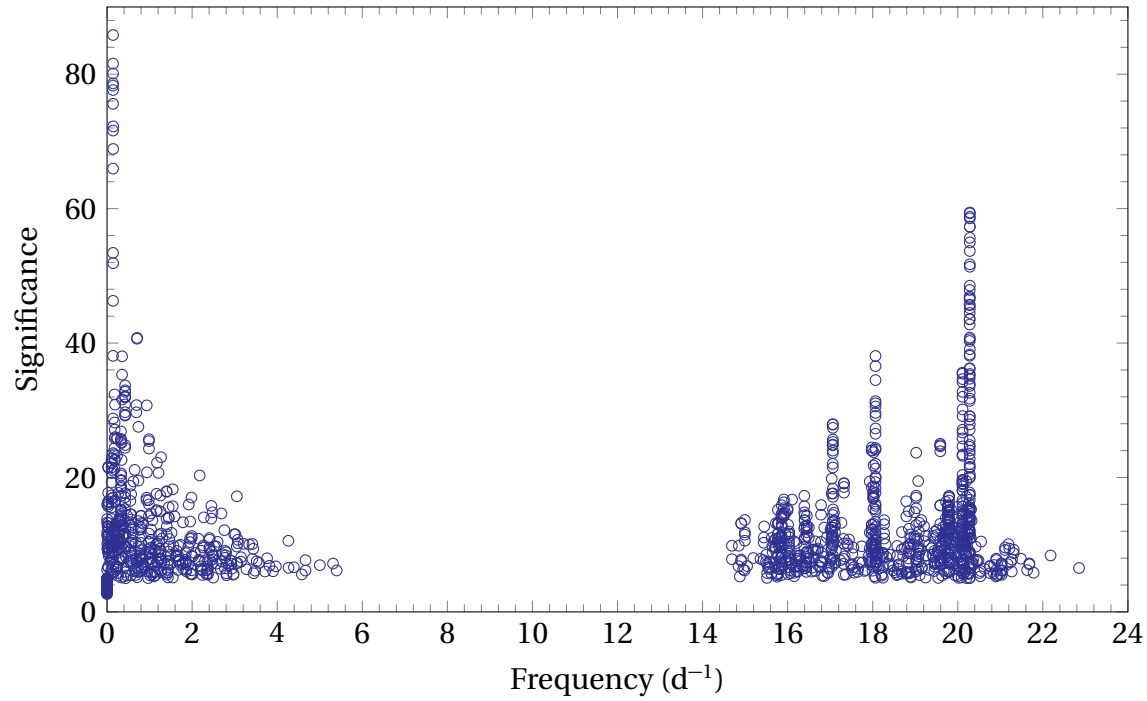

Figure 4.5: The spectral significance values of the frequencies of HD 3112 identified by SIGSPEC. Each blue circle represents a single pixel in which a frequency was identified at a particular significance. (Referenced on page 83, 83, 87.)

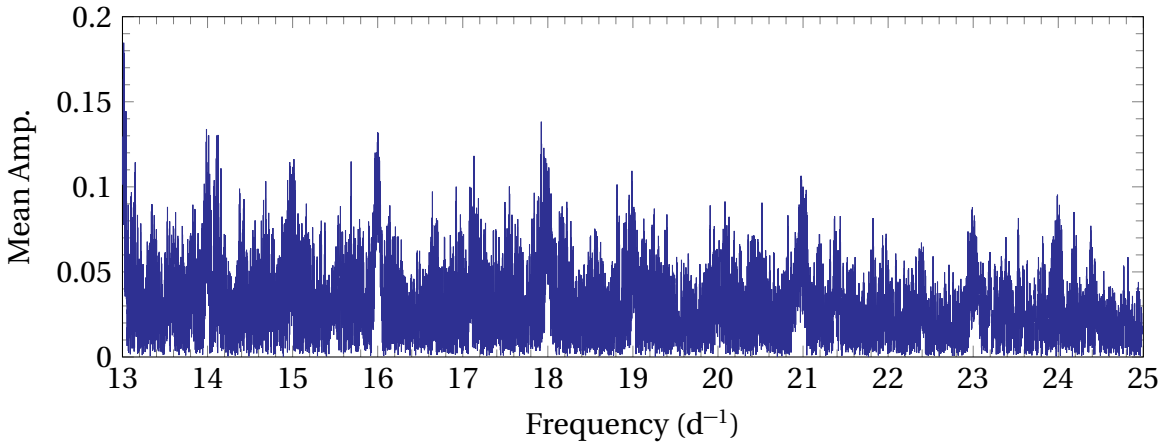

Figure 4.6: The 13 to 25 d^{-1} frequency range spectral window of HD 3112 computed by FAMIAS. (Referenced on page 83.)

periodograms, and Figures C.4 to C.10 are the FAMIAS computed zeroth- to third-moment Lomb-Scargle periodograms of the 13 d^{-1} to 25 d^{-1} frequency range respectively. Table 4.3 lists all of the identified frequencies in 13 d^{-1} to 25 d^{-1} frequency range in FAMIAS, using the various identification methods and their corresponding SIGSPEC values.

It can be seen that all of the frequencies identified in this range using the pixel-by-pixel method had analogues that were identified in multiple moments of the moment method:

$f_1 = 20.2802$ d^{-1}: $f_{19} = 20.2798$ d^{-1}, $f_{22} = 20.2800$ d^{-1}, $f_{31} = 20.2795$ d^{-1} and $f_{40} = 20.2829$ d^{-1}.
$f_2 = 18.0661$ d^{-1}: $f_{18} = 18.0658$ d^{-1}, $f_{23} = 18.0622$ d^{-1} and $f_{41} = 18.0661$ d^{-1}.
$f_3 = 20.1118$ d^{-1}: $f_{25} = 20.1117$ d^{-1} and $f_{30} = 20.1117$ d^{-1}.
$f_4 = 19.7947$ d^{-1}: $f_{26} = 19.7919$ d^{-1} and $f_{32} = 19.7915$ d^{-1}.
$f_6 = 19.5885$ d^{-1}: $f_{39} = 19.5202$ d^{-1} and $f_{43} = 19.5410$ d^{-1}.
$f_7 = 15.7692$ d^{-1}: $f_{21} = 15.7098$ d^{-1} and $f_{35} = 15.7103$ d^{-1}.
$f_8 = 15.8596$ d^{-1}: $f_{20} = 15.8523$ d^{-1} and $f_{27} = 15.8623$ d^{-1}.
$f_9 = 17.3184$ d^{-1}: $f_{29} = 17.3184$ d^{-1}.
$f_{10} = 19.0910$ d^{-1}: $f_{28} = 19.1007$ d^{-1}.
$f_{12} = 19.0212$ d^{-1}: $f_{33} = 18.0307$ d^{-1} and $f_{46} = 21.0328$ d^{-1} as aliases.
$f_{13} = 20.2329$ d^{-1}: $f_{47} = 20.2558$ d^{-1}.

4.3.2 The 0 d^{-1} to 3 d^{-1} Frequency Range

Figure 4.7 shows the 0 d^{-1} to 3 d^{-1} frequency range spectral widow of HD 3112, indicating the dominant frequency pattern that arose from the data sampling in that range. Note that the aliasing in this frequency range is much more significant than in the 13 d^{-1} to 25 d^{-1} range. Figure C.11 shows the FAMIAS computed pixel-by-pixel mean Lomb-Scargle periodograms, and Figures C.12 to C.16 show the FAMIAS computed zeroth- to third-moment Lomb-Scargle periodograms of the 0 d^{-1} to 3 d^{-1} frequency range respectively. Table 4.4 lists all of the identified frequencies in 0 d^{-1} to 3 d^{-1} frequency range in FAMIAS, using the various identification methods and their corresponding SIGSPEC values.

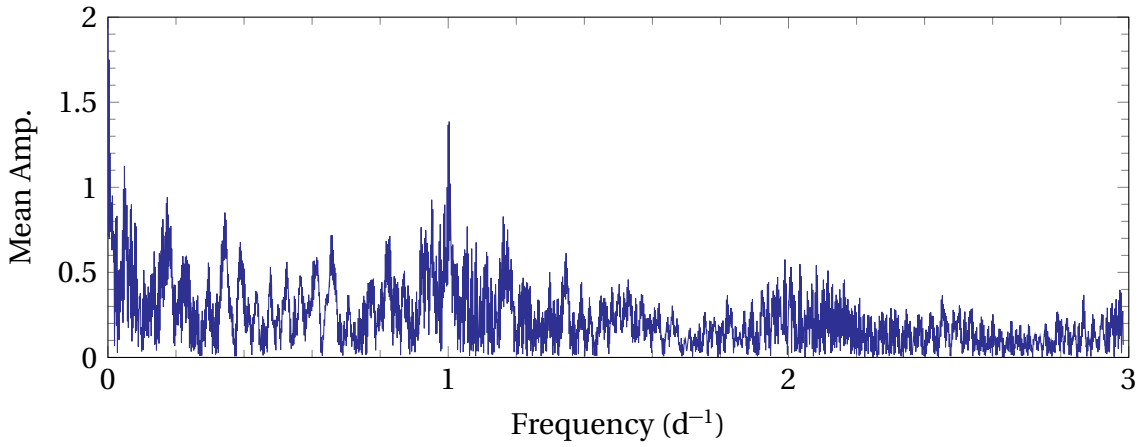

Figure 4.7: The 0 d^{-1} to 3 d^{-1} frequency range spectral window of HD 182640 computed by FAMIAS. (Referenced on page 85.)

Table 4.3: A summary of the HD 3112 frequencies found in FAMIAS and SIGSPEC in the 13 d^{-1} to 25 d^{-1} range. The corresponding amplitudes and uncertainties in the amplitudes A and $\sigma(A)$ calculated in FAMIAS and the maximum spectral significance of the identified frequency in SIGSPEC for the real pulsational frequencies are also listed. (Referenced on page 83.)

	FAMIAS			SIGSPEC	
	Frequency (d^{-1})	**A**	**$\sigma(A)$**	**Frequency (d^{-1})**	**Maximum Sig.**
	Pixel-by-Pixel				
f_1	20.2802	0.6548	0.0362	20.28	59
f_2	18.0661	0.3602	0.0408	18.07	38
f_3	20.1118	0.5276	0.0385	20.11	36
f_4	19.7947	0.2527	0.0360	19.79	18
f_5	17.0591	0.2423	0.0375	17.06	28
f_6	19.5885	0.2316	0.0369	19.59	25
f_7	15.7692	0.2687	0.0360	15.77	15
f_8	15.8596	0.2146	0.0349	15.86	16
f_9	17.3184	0.1769	0.0346	17.32	19
f_{10}	19.0910	0.1847	0.0398	19.09	13
f_{11}	15.5819	0.1792	0.0365	15.57	7
f_{12}	19.0212	0.2169	0.0420	19.02	24
f_{13}	20.2329	0.1588	0.0375	20.20	19
f_{14}	18.8509	0.1665	0.0375	18.85	15
	Zeroth Moment				
f_{18}	18.0658			18.07	38
f_{19}	20.2798			20.28	59
f_{20}	15.8523			15.86	16
f_{21}	15.7098			15.72	13
	First Moment				
f_{22}	20.2800			20.28	59
f_{23}	18.0622			18.07	38
f_{24}	17.9790			17.98	25
f_{25}	20.1117			20.11	36
f_{26}	19.7919			19.79	18
f_{27}	15.8623			15.86	16
f_{28}	19.1007			19.09	13
f_{29}	17.3184			17.32	19
	Second Moment				
f_{30}	20.1117			20.11	36
f_{31}	20.2795			20.28	59
f_{32}	19.7915			19.79	18
f_{33}	18.0307			18.02	24
f_{34}	19.2415			19.24	11
f_{35}	15.7031			15.70	11
f_{36}	22.5097				
f_{37}	16.4432			16.45	14

Continued on the next page...

Continued from the previous page...

	FAMIAS			SIGSPEC	
	Frequency (d^{-1})	***A***	***σ*(*A*)**	**Frequency (d^{-1})**	**Maximum Sig.**
f_{38}	16.1505			16.15	11
f_{39}	19.5202			19.51	12
	Third Moment				
f_{40}	20.2829			20.28	59
f_{41}	18.0661			18.07	38
f_{42}	17.9790			17.98	25
f_{43}	19.5410			19.54	9
f_{44}	18.2439			18.24	9
f_{45}	15.3844			15.36	8
f_{46}	21.0328			21.03	7
f_{47}	20.2558			20.25	13
f_{48}	15.9910			16.00	15

An interesting point of note is that a large number of frequencies that were found in the zeroth moment of the moment method. This implies a large amount of low-frequency variation in the equivalent width of the line profiles.

It can be seen from the periodograms of the 0 d^{-1} to 3 d^{-1} frequency range and from the spectral significance results that the binary orbit frequency ($f_{orb} = 0.14$ d^{-1}) is still present[18]. The orbital frequency manifests itself as a high spectral significance peak at 0.14 d^{-1} in Figure 4.5 and a high amplitude frequency peak at 0.14 d^{-1} in Figures C.11 to C.12. This is due to residual variation from the line profile correction process and made frequency identification more difficult. To deal with this, the pixel-by-pixel Lomb-Scargle periodograms were first prewhitened by $f_{orb} = 0.14$ d^{-1}. This ensured that any further frequency detections would be real pulsation frequencies.

All of the frequencies that were identified in this range using the pixel-by-pixel method had analogues that were identified in multiple moments of the moment method:

$f_{15} = 0.2816$ d^{-1}: $f_{50} = 0.2814$ d^{-1}, with $f_{68} = 0.7391$ d^{-1} as an alias.
$f_{16} = 0.2371$ d^{-1}: $f_{60} = 0.2419$ d^{-1} and $f_{62} = 0.2305$ d^{-1}, with $f_{56} = 1.2649$ d^{-1} as an alias.
$f_{17} = 0.5629$ d^{-1}: $f_{52} = 0.5807$ d^{-1} and $f_{65} = 0.5631$ d^{-1}.

An unexpected result is the identification of $f_{15} = 0.2816$ d^{-1}, which at first glance seems to be the first overtone of $f_{orb} = 0.14$ d^{-1} (i.e. $2f_{orb}$), as an independent pulsation frequency. If $f_{15} = 0.2816$ d^{-1} was indeed a harmonic of $f_{orb} = 0.14$ d^{-1}, prewhitening by $f_{orb} = 0.14$ d^{-1} would have removed the peak of $f_{15} = 0.2816$ d^{-1} from the pixel-by-pixel mean Lomb-Scargle periodograms (Figure C.11). In addition, the prewhitening of $f_{50} = 0.2814$ d^{-1} did not remove

[18] This also occurs for HD 182640 and HD 147787.

the peak of $f_{\rm orb} = 0.14\,{\rm d}^{-1}$ from the zeroth-moment Lomb-Scargle periodograms (Figure C.12), further reinforcing its status as an independent frequency.

4.3.3 Final Frequency Identification

A total of 17 frequencies were identified as real pulsation frequencies, based on the criteria described in the section on frequency selection methodology (2.4.1). These frequencies and their corresponding uncertainties, calculated using Equations 2.6 for FAMIAS and 2.9 for SIGSPEC, are listed in Table 4.5. The observational timebase T was calculated using Equation 2.7, giving the value $T = 396$. As mentioned in the section on frequency identification (3.4) in the chapter on HD 182640, SIGSPEC uncertainty estimations are overestimations and FAMIAS uncertainty estimations are underestimations. As such, a mean of the two uncertainty estimates would be closer to the true uncertainty of the identified frequencies and was therefore calculated and included in Table 4.5. The mean error estimates obtained are in the range of $0.0004 \pm 0.0002\,{\rm d}^{-1}$, which is relatively precise. The reduction in the standard deviation from successive prewhitening of pulsation frequencies is listed in Table C.1. The combination of these 17 pulsational frequencies explain 46.3% of variation across the line profiles of HD 3112, illustrated by Figure C.17.

Table 4.4: A summary of the HD 3112 frequencies found in FAMIAS and SIGSPEC in the 0 d^{-1} to 3 d^{-1} range. The corresponding amplitudes and uncertainties in the amplitudes A and $\sigma(A)$ calculated in FAMIAS and the maximum spectral significance of the identified frequency in SIGSPEC for the real pulsational frequencies are also listed. (Referenced on page 85.)

	FAMIAS			SIGSPEC	
	Frequency (d^{-1})	A	$\sigma(A)$	**Frequency (d^{-1})**	**Maximum Sig.**
	Pixel-by-Pixel				
f_{orb}	0.1412			0.1408	86
f_{15}	0.2816	0.3165	0.0394	0.2814	14
f_{16}	0.2371	0.1515	0.0349	0.2367	26
f_{17}	0.5629	0.1382	0.0345	0.5662	18
	Zeroth Moment				
f_{49}	0.1896			0.1884	31
f_{50}	0.2814			0.2814	14
f_{orb}	0.1436			0.1408	86
f_{51}	0.1113			0.1072	23
f_{52}	0.5807			0.5662	18
f_{53}	2.4785			2.479	15
f_{54}	1.3881			1.381	8
f_{55}	2.8786			2.865	7
f_{56}	1.2649			1.269	23
f_{57}	1.6482			1.642	9
	First Moment				
f_{58}	0.0014			0.001632	16
f_{59}	0.3302			0.3272	27
f_{60}	0.2419			0.2367	26
f_{61}	2.3173			2.301	8
	Second Moment				
f_{orb}	0.1407			0.1408	86
f_{62}	0.2305			0.2367	26
f_{63}	1.9919			1.992	11
	Third Moment				
f_{64}	0.1937			0.1899	26
f_{65}	0.5631			0.5662	18
f_{66}	1.0156			1.0159	8
f_{67}	2.3181			2.301	8
f_{68}	0.7391			0.7364	28

Table 4.5: The identified pulsational frequencies of HD 3112, with the corresponding FAMIAS, SIGSPEC and mean uncertainty estimates. (Referenced on page 88, 88.)

	Frequency (d^{-1})	**FAMIAS $\sigma(f)$ (d^{-1})**	**SIGSPEC $\sigma(f)$ (d^{-1})**	**$\bar{\sigma}(f)$ (d^{-1})**
f_1	20.2802	0.00008	0.0003	0.0002
f_2	18.0661	0.0002	0.0004	0.0003
f_3	20.1118	0.0001	0.0004	0.0003
f_4	19.7915	0.0002	0.0006	0.0004
f_5	17.0591	0.0002	0.0005	0.0004
f_6	19.5885	0.0002	0.0005	0.0004
f_7	15.7692	0.0002	0.0007	0.0004
f_8	15.8596	0.0002	0.0006	0.0004
f_9	17.3184	0.0003	0.0006	0.0004
f_{10}	19.0910	0.0003	0.0007	0.0005
f_{11}	15.5819	0.0003	0.001	0.0006
f_{12}	19.0212	0.0003	0.0005	0.0004
f_{13}	20.2329	0.0003	0.0006	0.0005
f_{14}	18.8509	0.0003	0.0007	0.0005
f_{15}	0.2816	0.0002	0.0007	0.0004
f_{16}	0.2371	0.0003	0.0005	0.0004
f_{17}	0.5629	0.0003	0.0006	0.0005

4.4 Mode Identification

Table 4.6: The zero-point fit parameters of HD 3112. (Referenced on page 90.)

Parameter	**Value**
$v \sin i$ (km s^{-1})	2.52
Equivalent Width (km s^{-1})	8.23
Intrinsic Width (km s^{-1})	15.82
Velocity Offset (km s^{-1})	-0.97
χ^2	3106.08

The initial stellar parameters input prior to mode identification are listed in Table 4.1. The $v \sin i$, equivalent width, intrinsic width and velocity offset, calculated by performing a zero-point fit in FAMIAS[19], are listed in Table 4.6. Figure 4.8 shows the zero-point fit of HD 3112. Note the poor visual fit of the synthetic line profile to the zero-point line profile, with a correspondingly high $\chi^2 = 3106.08$. This is due to the asymmetry in the zero-point line profile itself. Another issue of concern is the very low best-fit $v \sin i = 2.52$ km s^{-1}, which is radically different from the range of literature values (52 km s^{-1} to 80 km s^{-1})[20]. In fact, the $v \sin i$ parameter itself was poorly constrained during the zero-point fit.

[19]Refer to the section on mode identification methodology (2.4.2) for more information.
[20]Refer to Table 4.2 for more information.

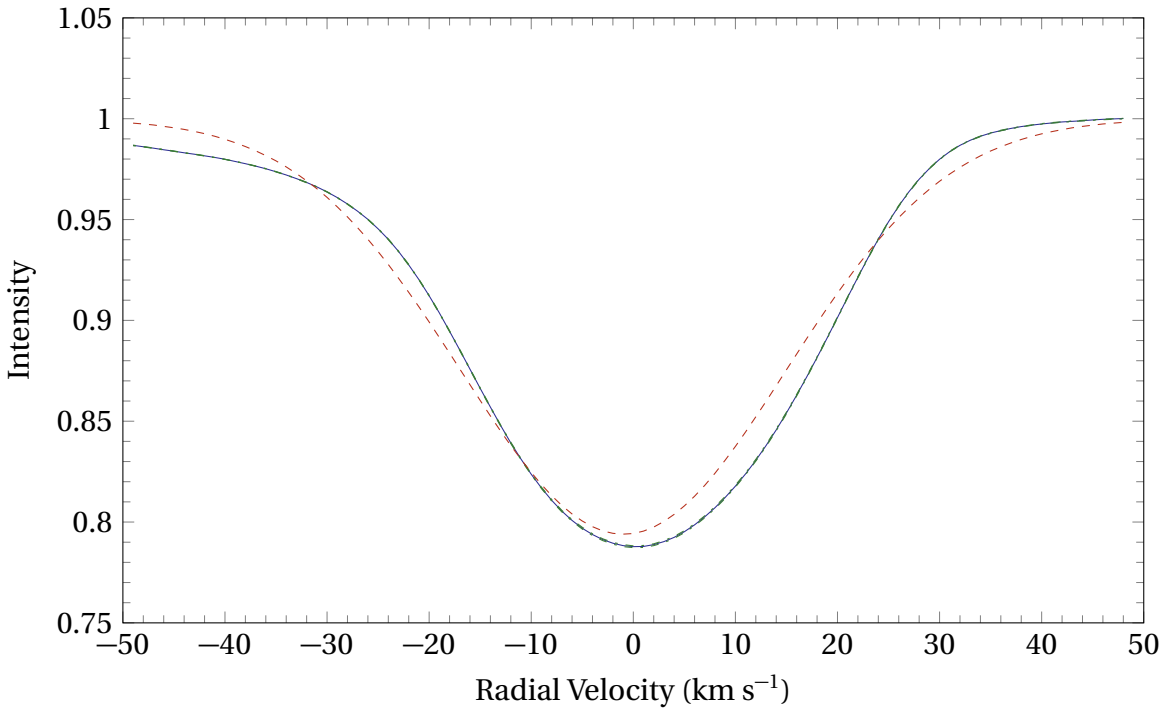

Figure 4.8: The zero-point fit of the HD 3112. The solid blue line represents the zero-point line profile, the two dash dotted green lines (partially obscured by the solid blue line) represent the statistical uncertainty and the dashed red line represents the best-fit synthetic zero-point line profile. Note the poor visual fit of the synthetic line profile to the zero-point line profile (with a correspondingly high $\chi^2 = 3106.08$). (Referenced on page 81, 90.)

Figure 4.9 shows the v sin i values of the models calculated during the zero-point fit, with their associated χ^2 values. It can be seen that the range of v sin i values of the best-fitting models is between 0 km s^{-1} to 20 km s^{-1}, which is relatively large. Equations 2.13 and 2.14 were used to calculate the Keplerian breakup velocity and associated critical minimum inclination. Considering the large range of v sin i values of the best-fitting models, it would be more useful to give a range of i_{crit} values instead of a single one. As such, the Keplerian breakup velocity and range of the critical minimum inclination, based on 0 km s^{-1} $< v$ sin $i <$ 20 km s^{-1}, are $v_{\text{crit}} = 416.6$ and $0° < i_{\text{crit}} < 2.75°$.

Despite the poor constraints on the v sin i, the zero-point fit parameters were fixed before mode identification of the individual frequencies were performed to reduce the parameter space during the amplitude and phase fits[21]. The results of the mode identification were disappointing: the only frequency that could be definitively identified was $f_1 = 20.2802$ d^{-1} (Figure 4.10). Table 4.7 lists the five best-fitting modes of $f_1 = 20.2802$ d^{-1} and their associated χ^2 values, inclinations, velocity amplitudes and phases. In addition, the rotational frequency f_{rot} and the co-rotating frequency $f_{\text{co-rot}}$ were calculated using Equations 2.15 and 2.19 in or-

[21] Refer to the section on mode identification methodology (2.4.2) for more information

der to determine the physicality of each non-radial mode[22] was calculated, using Equation 2.15, to determine the physicality of each mode. These pulsation modes are reliable, based on Equation 2.16, as the ratio $|f_{\text{rot}}/f_{\text{co-rot}}|$ for all of the frequencies is below 0.5.

All of the other frequencies had fitted synthetic amplitude profiles that did not match their observational amplitude profiles visually (e.g. $f_2 = 18.0661$ d^{-1}, Figure C.18). This is surprising, considering the relatively undistorted observational amplitude and phase profiles of each frequency, displayed in Figures 4.11 to 4.13.

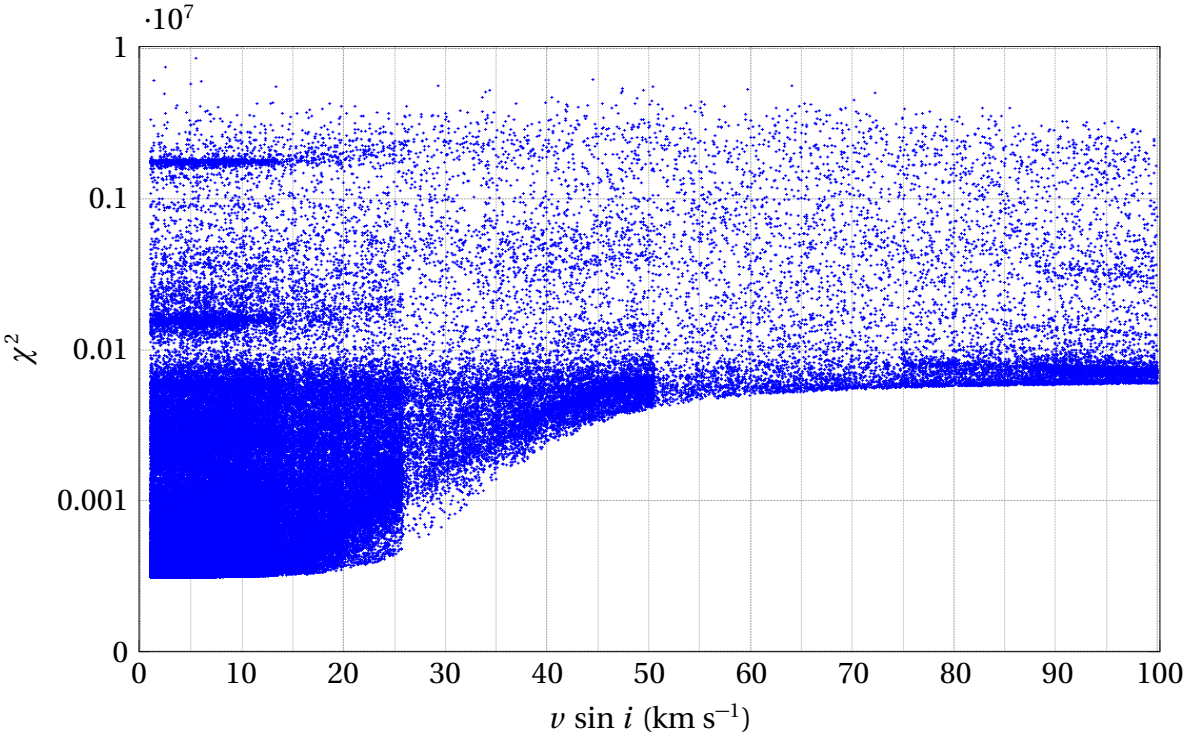

Figure 4.9: The v sin i values of the models fit to the zero-point line profile of HD 3112, with their associated χ^2 values, computed during the zero-point fit of the HD 3112. Each blue dot represents a single model that was fitted to the zero-point line profile of HD 3112. Note the poor constraints on the v sin i values during the fit. (Referenced on page 91.)

[22] Note that the inclination values can only be constrained in models of non-radial modes, due to their particular geometry. Refer to the section on non-radial pulsational geometry (1.3.5) for more information.

Table 4.7: The best-fit modes of $f_1 = 20.2802$ d^{-1} of HD 3112, with the corresponding rotational frequencies at the modelled inclination values for the non-radial modes. (Referenced on page 91.)

Mode	χ^2	**Inclination**	**Vel. Amp. (km s^{-1})**	**Phase**	f_{rot} **(d^{-1})**	$f_{\text{co-rot}}$ **(d^{-1})**
$f_1 = 20.2802$ d^{-1}						
(1, 1)	40.887	60.55	6.45	0.677	0.03	20.25
(2, 2)	40.975	77.95	9.03	0.181	0.02	20.23
(1, 1)	40.998	59.88	6.45	0.677	0.03	20.25
(2, 2)	41.041	87.99	8.38	0.181	0.02	20.23
(0, 0)	41.044	5.00	5.81	0.181		

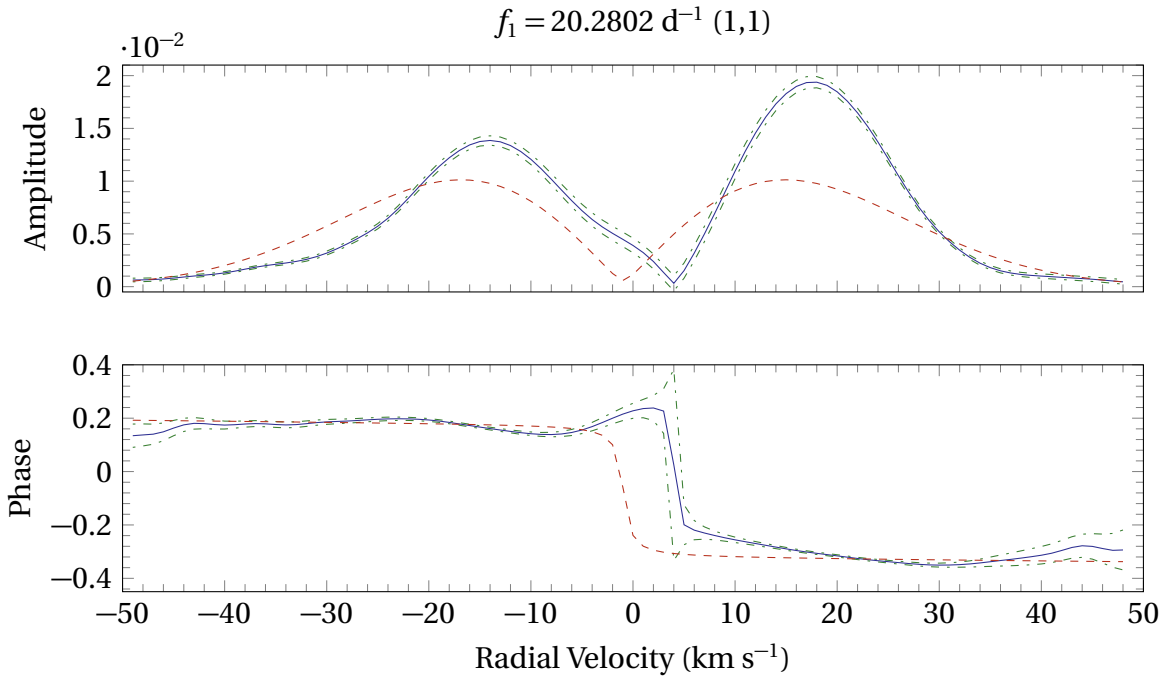

Figure 4.10: The amplitude and phase profiles of the best-fit mode (1,1) of $f_1 = 20.28$ d^{-1} of HD 3112. The solid blue lines are the observational profiles, the dash dotted green lines represent the statistical uncertainty and the dashed red lines represent the best-fit synthetic profiles. Note that the synthetic amplitude and phase profiles visually match the observational profiles relatively well (although the phase shifts do not match). (Referenced on page 91.)

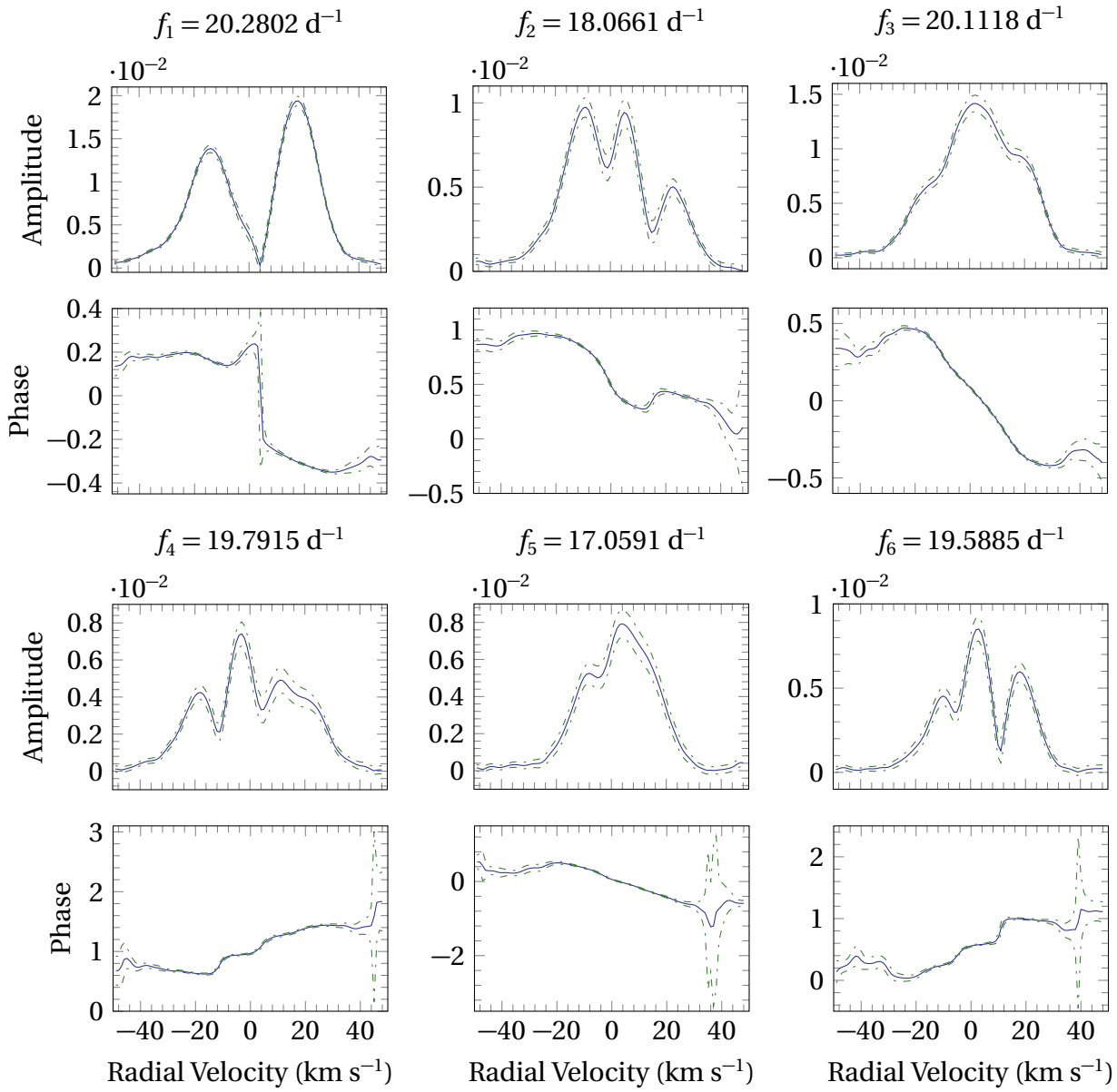

Figure 4.11: The amplitude and phase profiles of f_1 to f_6 of HD 3112. The solid blue lines are the observational profiles and the dash dotted green lines represent the statistical uncertainty. (Referenced on page 92.)

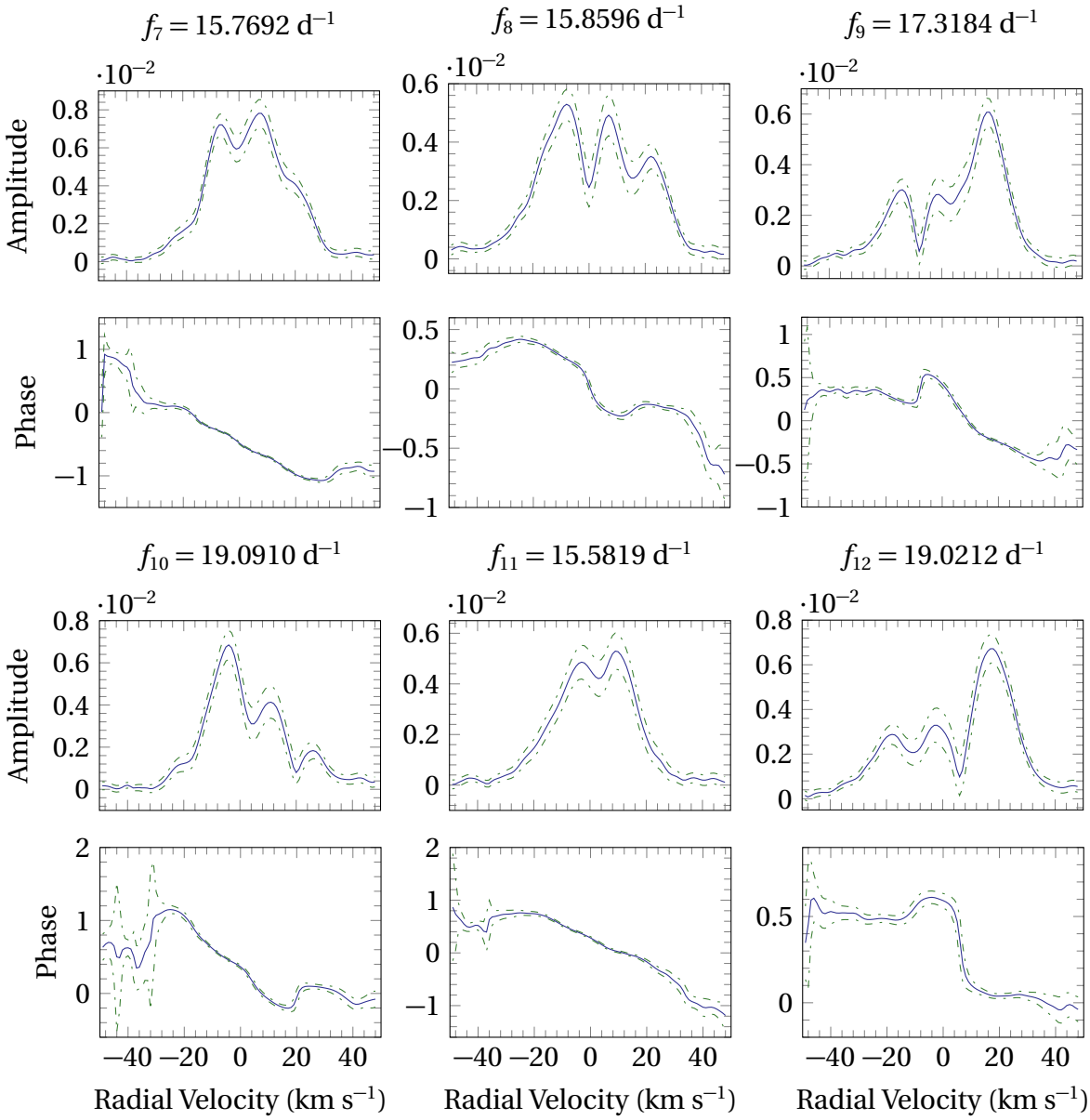

Figure 4.12: The amplitude and phase profiles of f_7 to f_{12} of HD 3112. The solid blue lines are the observational profiles, the dash dotted green lines represent the statistical uncertainty.

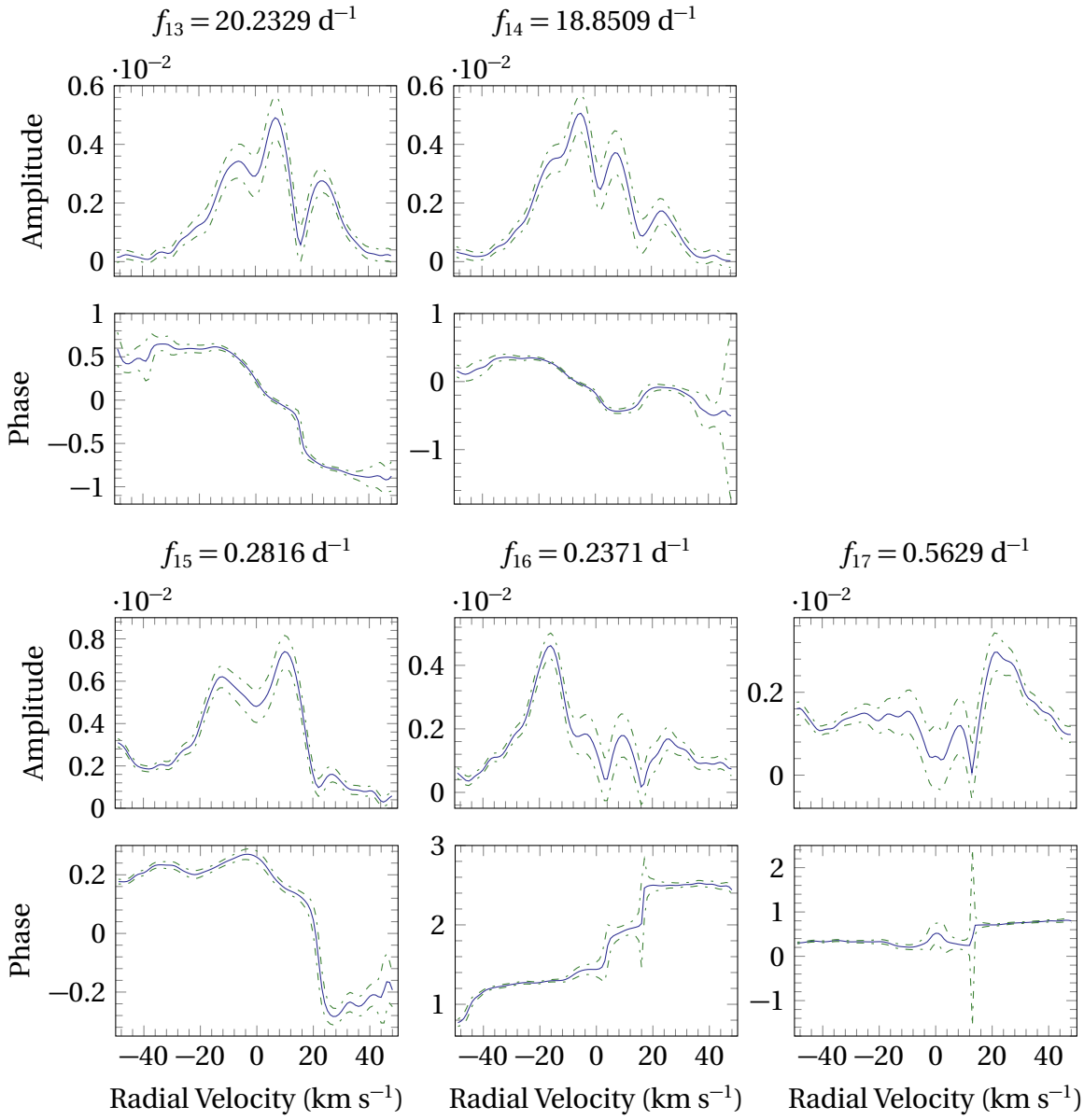

Figure 4.13: The amplitude and phase profiles of f_{13} to f_{18} of HD 3112. The solid blue lines are the observational profiles and the dash dotted green lines represent the statistical uncertainty. (Referenced on page 92.)

4.5 Discussion

The results of the frequency identification show that in addition to the high-frequency variation typically exhibited by δ Scuti stars[23], HD 3112 also displays significant low-frequency variation, reinforcing the claim by Balona (2014) that all δ Scuti stars are hybrids. In addition, most of the frequencies found in this analysis agree with the photometric frequencies found by Paparo et al. (1996) and the spectroscopic frequencies found by De Mey et al. (1998). Table 4.8 shows a comparison of the frequencies of this analysis with those of Paparo et al. (1996) and De Mey et al. (1998).

Table 4.8: Comparison of the HD 3112 frequencies in Paparo et al. (1996), De Mey et al. (1998) and this analysis. (Referenced on page 97.)

Frequency (d^{-1})	
Paparo et al. (1996)	**This Analysis**
$f_1 = 0.28151$	$f_{15} = 0.2816$
$f_2 = 0.14215$	$f_{\rm orb} = 0.1412$
$f_3 = 17.06289$	$f_5 = 17.0591$
$f_4 = 18.06302$	$f_2 = 18.0661$
$f_5 = 19.02045$	$f_{12} = 19.0212$
$f_6 = 15.86246$	$f_8 = 15.8596$
$f_7 = 20.28061$	$f_1 = 20.2802$
$f_8 = 19.79407$	$f_4 = 19.7915$
$f_9 = 15.94618$	
$f_{10} = 20.11136$	$f_3 = 20.1118$
$f_{11} = 17.54177$	$f_{11} = 15.5819$
$f_{12} = 17.85668$	$f_{14} = 18.8509$
$f_{13} = 0.99350$	
De Mey et al. (1998)	**This Analysis**
$f_1 = 20.27$	$f_1 = 20.2802$
$f_2 = 18.82$	$f_{14} = 18.8509$
$f_3 = 20.78$	$f_4 = 19.7915$
$f_{4a} = 18.14$	$f_{10} = 19.0910$
$f_{4b} = 19.09$	$f_{10} = 19.0910$

An interesting result is that the frequency $f_{15} = 0.2816$ d^{-1} is an independent pulsation frequency and not attributable to the binary orbit[24] (even though it appears to the first overtone of the orbital frequency) . This is in contrast with the claim made by Sterken et al. (1997), who had attributed it to the binary orbit.

The low $v \sin i = 2.52$ km s^{-1} of the best-fit model of the zero-point fit is an interesting result, particularly in the light of the work of Templeton et al. (2000), who quoted an equatorial

[23] Refer to the section on δ Scuti stars (1.4.2) for more information.
[24] Refer to the section on frequency analysis (4.3) in this chapter (HD 3112) for more information.

velocity of 70 km s^{-1} to 90 km s^{-1}. Accepting $v \sin i = 2.52$ km s^{-1} as the true value would imply an inclination range of $1.6° < i < 2.1°$, which is very low. Even if one were to consider the upper limit of the $v \sin i$ values determined by the zero-point fit (20 km s^{-1}), the corresponding inclination range would be $12.8° < i < 16.6°$, which is still very close to pole-on. Templeton et al. (2000) had posited that the $v \sin i$ of the star should be lower than the values quoted in the literature (52 km s^{-1}, Hoffleit and Warren, 1995, and 80 km s^{-1}, Glebocki and Gnacinski, 2005), based on the narrow line profiles reported by Sterken et al. (1997).

The $v \sin i$ of the star can be estimated from the standard deviation $\sigma_{\rm obs}$ of the zero-point line profile (Gray, 2005):

$$v \sin i = \sqrt{\sigma_{\rm obs}^2 - \sigma_0^2} \tag{4.1}$$

σ_0 is the standard deviation of the error, which is assumed to be Gaussian and small in comparison to $\sigma_{\rm obs}$. $\sigma_{\rm obs}$ can be calculated from the full width at half maximum (FWHM) using the equation FWHM$= 2\sqrt{2 \ln 2}\sigma_{\rm obs}$. This reduces Equation 4.1 to:

$$v \sin i = \frac{\rm FWHM}{2\sqrt{2 \ln 2}} \tag{4.2}$$

Using FWHM$= 47$ km s^{-1}, the value $v \sin i = 19.96$ km s^{-1} was obtained. This is consistent with the maximum value of the range determined by the zero-point fit (20 km s^{-1}) and is clearly different from 52 km s^{-1} (Hoffleit and Warren, 1995), and 80 km s^{-1} (Glebocki and Gnacinski, 2005). Additional $v \sin i$ measurements would be useful in determining the truth of the matter.

The best-fit mode of $f_1 = 20.2802$ d^{-1} is a (1,1) mode, which differs from the claims of Sterken (1997), Sterken et al. (1997), De Mey et al. (1998) and Templeton et al. (2000), who had all characterised it as a radial mode. Using Equation 2.20, the frequency of the fundamental radial mode was calculated as 48.5716 d^{-1}, which is more than twice of $f_1 = 20.2802$ d^{-1}. Regardless, the fifth-best-fitting mode of $f_1 = 20.2802$ d^{-1} is a radial mode with a very close χ^2 value to the best-fitting one (41.044 vs 40.887). The velocity amplitude of the radial mode (5.81 km s^{-1}), as well as all of the best-fit modes, is also reasonably close to the 6 km s^{-1} to 8 km s^{-1} range estimate reported by Sterken et al. (1997). Considering the poor zero-point fit and the lack of constraints on the $v \sin i$, it is very possible that $f_1 = 20.2802$ d^{-1} could be a radial mode. However, it is not possible to definitively conclude this and additional spectroscopic data would be useful in this endeavour.

The inability to identify modes other than those of the strongest frequency $f_1 = 20.2802$ d^{-1} can be explained by the claim that HD 3112 experiences ellipsoidal variations (Paparo et al., 1996; Sterken et al., 1997; Templeton et al., 2000) due to the close proximity of the companions. This prevents the accurate modelling of pulsation modes in FAMIAS, which assumes

that the star is spherically symmetric when pulsationally unperturbed[25]. This may have been compounded by the low $v \sin i = 2.52$ km s^{-1} of the best-fit model of the zero-point fit, which happens to be significantly different from the $v \sin i = 52$ km s^{-1} used for cross-correlation[26].

If the $v \sin i < 20$ km s^{-1} as was calculated during the zero-point fit, the inclination of the star must correspondingly be very low ($i < 16.6°$). According to Wright et al. (2011), $m > 0$ modes of a star are unobservable when $i < 16°$. This would explain the difficulty in mode identification and additionally, lends credence to the argument that $f_1 = 20.2802$ d^{-1} is a radial mode. However, this can only be resolved definitively if more sophisticated models incorporating ellipsoidal variations are developed.

[25] Refer to the section on FAMIAS mode identification assumptions (2.4.2) for more information on the limitations on the theoretical modelling of pulsations in this analysis.
[26] Refer to the section on cross-correlation (2.2.3) for more information.

5 HD 147787

HD 147787[1] is a moderately bright ($m_V = 5.30$, Paunzen, 2015) star in the constellation of Triangulum Australe, which is the Latin phrase for *southern triangle* (not to be confused with the constellation Triangulum). It has a spectral type of F4IV (Samus et al., 2009) and is located at the coordinates 16h 27m 57.3s, -64° 03′ 28.6″ (J2000 epoch[2], van Leeuwen, 2007) at a distance of 40 ± 1 pc from the Sun (van Leeuwen, 2007), according to HIPPARCOS astrometric parallax measurements.

Compared to HD 182640 and HD 3112, HD 147787 is far less well studied. HD 147787 was first noted as a spectroscopic binary[3] at Lick Observatory in San Jose, California, in 1914. The orbital elements of the system were first published by Jones in 1928, who noted an orbital period of 39.9 d, a systemic velocity of −5.07 km s^{-1}, an eccentricity of 0.28 and a mass ratio[4] $q = 0.218$. No further mention of HD 147787 was found in the literature until it was listed as a visual double star in the third revision of the bright star catalogue (Hoffleit, 1964). Landolt (1969) later reported a low magnitude visual companion (HD 147787 C) at a separation of 24.7″[5]. Its large visual separation from the binary and its faint magnitude renders it irrelevant to the analysis presented in this thesis.

The first mention of the variability of HD 147787 was in Aerts et al. (1998), who noted two main pulsation frequencies in the photometry of HD 147787 (1.4556 d^{-1} and 2.9464 d^{-1}) and classified as a candidate γ Doradus[6] star. A spectroscopic study of candidate γ Doradus stars was later carried out by De Cat et al. (2006), who reported an orbital period of 39.9 d, a systemic velocity of −4.9 km s^{-1}, an eccentricity of 0.59 and the radial velocity semi-amplitudes K_A = 61 km s^{-1} and $K_B = 67$ km s^{-1}. They did not perform any frequency or mode identification.

A follow-up study on HD 147787 by De Cat et al. (2009), using 316 spectra from the HARPS and HERCULES spectrographs, reported a period of 39.88 d, a systemic velocity of −4.1 km s^{-1}, an eccentricity of 0.253 and the radial velocity semi-amplitudes K_A = 38.4 km s^{-1} and $K_B = 43.9$ km s^{-1}. They had also calculated the v sin i of the primary and secondary as 7 km s^{-1}and 33 km s^{-1} respectively and had noted two frequencies: 0.6897 d^{-1} and 1.304 d^{-1}.

[1] Other designations for this star include HR 6109, HIP 80645, iota Trianguli Australis and ι TrA.
[2] An epoch is a reference point for astronomical quantities (in this case, celestial coordinates) that vary with time. The coordinates of the star are with reference to the J2000 epoch, defined as 12:00 UT on 1 January, 2000.
[3] Refer to the section on spectroscopic binaries (1.5.2) for more information.
[4] The mass ratio is the ratio of the mass of the secondary to that of the primary.
[5] Zacharias et al. (2013) quotes a $m_V = 9.75$ for HD 147787 C.
[6] Refer to the section on γ Doradus stars (1.4.1) for more information.

Table 5.1: The fundamental stellar parameters of HD 147787, used during spectroscopic data reduction and mode identification. The minimum and maximum literature values of each parameter and the value used in this analysis (typically the approximate mean or the mode of the literature values) are listed. (Referenced on page 103, 110.)

Parameter	Min. Literature Value	Max. Literature Value	Value Used
$T_{\rm eff}$ (K)	6733 (McDonald et al., 2012)	7190 (Ammons et al., 2006)	7000
$\log[g$ (cm s^{-2})]	3.97 (Casagrande et al., 2011)	4.32 (Lafrasse et al., 2010)	4.15
Radius ($R_\odot$)	2.1 (Allende and Lambert, 1999)	2.1 (Allende and Lambert, 1999)	2.1
Mass ($M_\odot$)	1.38 (Lambert and Reddy, 2004)	1.72 (Allende and Lambert, 1999)	1.7
[Fe/H] (dex)	−0.23 (Holmberg et al., 2009)	−0.01 (Suchkov and Makarov, 2002)	−0.1
$v \sin i$ (km s^{-1})	7.0 (De Cat et al., 2009)	19.0 (Glebocki and Gnacinski, 2005)	13.0
v_γ (km s^{-1})	−7.4 (Abt and Biggs, 1972)	−4.1 (De Cat et al., 2009)	−5.0

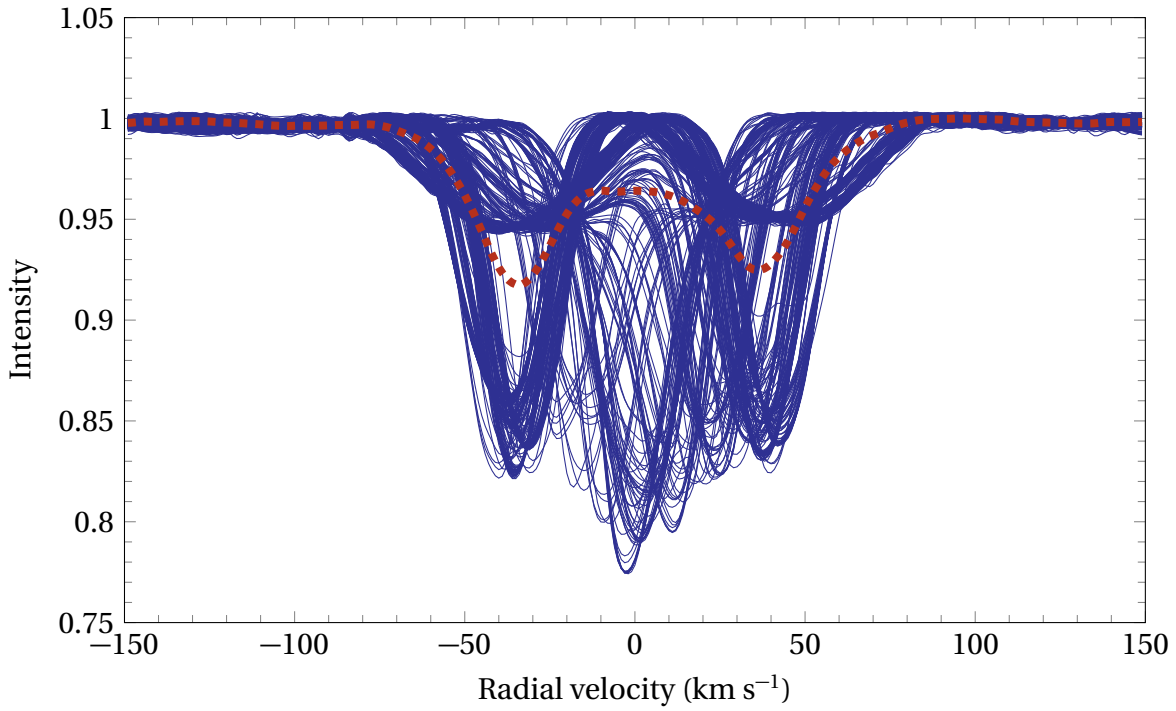

Figure 5.1: The cross-correlated line profiles (solid blue) of HD 3112, with the mean line profile (dashed red). (Referenced on page 103.)

5.1 Observations

A total of 480 observations[7] of HD 147787 were collected between February 2008 and August 2015. After discarding spectra with a signal-to-noise ratio of less than 40[8], 443 spectra remained for orbital and pulsational analysis. Table 5.1 shows a summary of the stellar parameters obtained from the literature and the values used as inputs during the spectroscopic data reduction process[9]. Figure 5.1 shows all of the cross-correlated line profiles of HD 147787, together with the mean line profile. The signal of the secondary star was removed using the method described in the section on binary analysis (2.3). Figure 5.2 shows the result of this process: it displays all of the cross-correlated line profiles of HD 147787 A, together with the mean line profile.

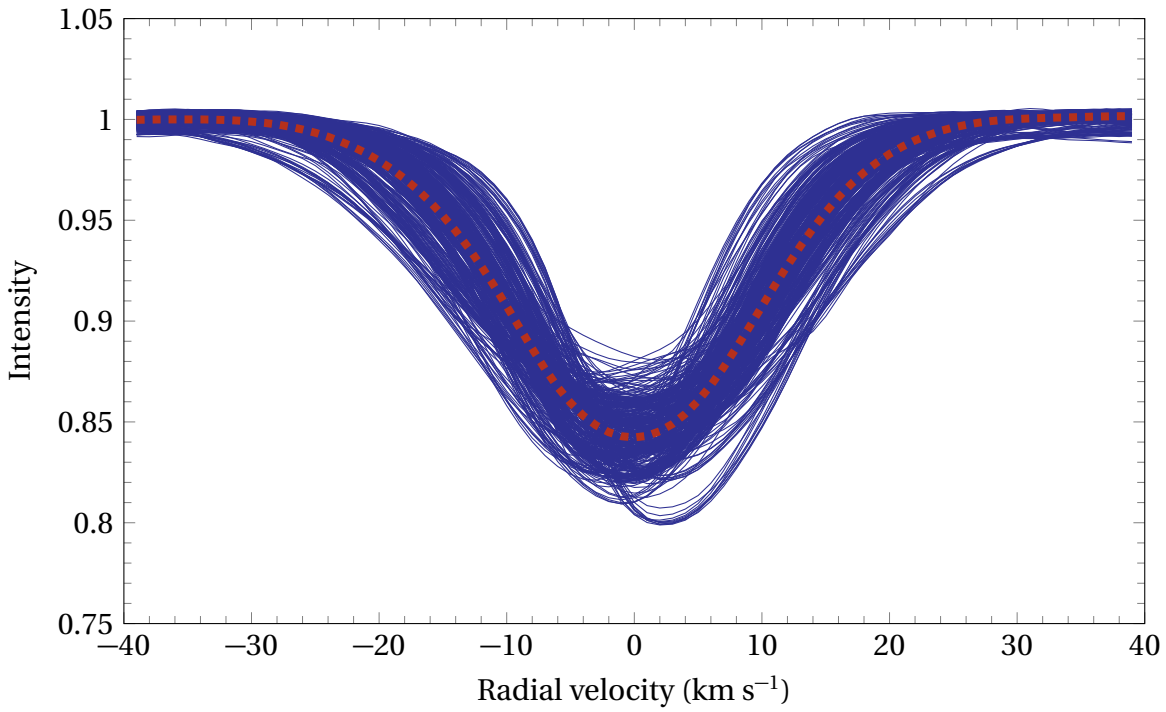

Figure 5.2: The cross-correlated line profiles (solid blue) of HD 147787 A, with the mean line profile (dashed red). Note the relatively successful removal of the signal of the secondary star from the line profiles. (Referenced on page 103.)

[7] Refer to Table 2.1 for more details

[8] Refer to the section on cross-correlation (2.2.3) for more information on why low signal-to-noise spectra were discarded.

[9] Refer to the section on the second data reduction pipeline (2.2.3) for more information.

Table 5.2: The orbital elements of HD 147787. (Referenced on page 104.)

Orbital Element	HD 147787 A	HD 147787 B	Weighted Mean
P (d)	39.881 ± 0.001	39.8844 ± 0.0007	39.883 ± 0.001
e	0.252 ± 0.004	0.250 ± 0.003	0.251 ± 0.005
T_0 (JD−2450000)	57174.0 ± 0.1	57174.9 ± 0.1	57174.6 ± 0.2
ω (°)	91 ± 1	281 ± 1	–
v_γ [a] (km s^{-1})	1.9 ± 0.2	1.5 ± 0.1	1.6 ± 0.3
K (km s^{-1})	39.2 ± 0.1	43.5 ± 0.1	–
χ^2	967.82	10.47	

[a]The v_γ values here are calculated after systemic velocity correction during the wavelength and velocity correction process, carried out by the second data reduction pipeline during the initial spectroscopic data reduction.

5.2 Orbital Analysis

The orbital fitting code of Bergmann (priv. comm.) was used to fit orbits to the measured primary and secondary radial velocities[10]. Of the 443 velocities of each component, 353[11] were used for the orbital fitting. There is some scatter of the radial velocities of the primary due to the pulsations but the secondary velocities are relatively precise. The component orbital elements and system orbital elements, calculated using the weighted mean of the component orbital elements[12], are detailed in Table 5.2 and the phased radial velocities and fitted component orbits are shown in Figure 5.3.

Most of the orbital elements are in agreement with each other. P_A and P_B, as well as e_A and e_B are in very close agreement. ω_A and ω_B differ by 190° instead of 180° as expected. The only orbital elements that are slightly different are $v_{\gamma A}$ and $v_{\gamma B}$, with a difference of 0.4 km s^{-1}, which is almost within the uncertainties. This could be due to the poor fit of the primary velocities compared to that of the secondary, which is largely unmitigable due to the pulsations of the primary.

The orbital elements in this analysis are in close agreement with the orbital elements reported in De Cat et al. (2009). The period $\bar{P} = 39.883 \pm 0.001$ d and eccentricity $\bar{e} = 0.251 \pm 0.005$ are in close agreement with the values in De Cat et al. (2009) (39.88 d and 0.253). The true systemic velocity of HD 147787[13] is given by: $v_\gamma = -5.0 + 1.6 = -3.4 \pm 0.3$ km s^{-1}. This is slightly different to that reported by De Cat et al. (2009) (−4.1 km s^{-1}). $K_A = 39.2 \pm 0.1$ km s^{-1} and $K_B = 43.5 \pm 0.1$ km s^{-1} are also very close to those reported by De Cat et al. (2009) (38.4 km s^{-1}

[10]Refer to the section on binary analysis (2.3) for more information on how the velocities were measured.
[11]The velocities that were excluded from the orbital fitting were the ones that deviated significantly from the preliminary orbital fit. These typically correspond to the the velocities measured from the line profiles with merged peaks (low radial velocity separation). Refer to the section on orbital analysis (2.3.1) for more information.
[12]The weighted mean and it's associated uncertainty estimate can be calculated using Equations 2.2 and 2.3 respectively. Refer to the section on binary orbits (1.5.1) for more information.
[13]This value is obtained by taking the sum of the velocity input during the radial velocity correction during the wavelength and velocity correction process and the systemic velocity calculated during the orbital analysis.

and 43.9 km s^{-1}).

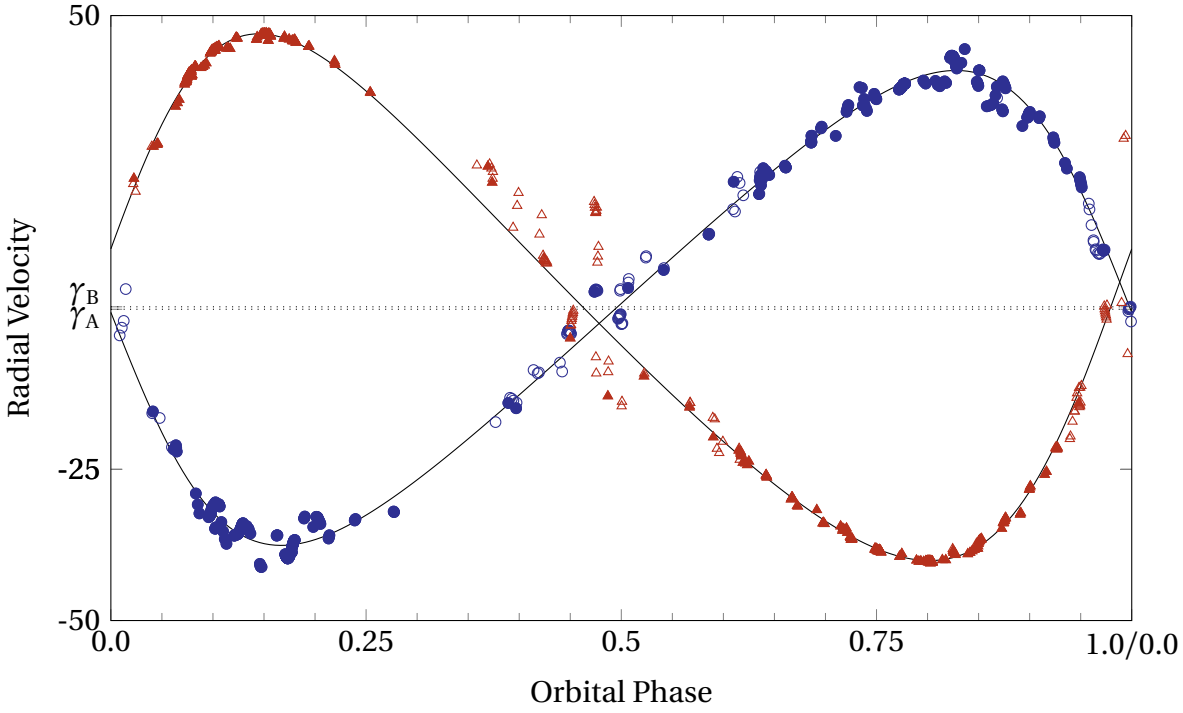

Figure 5.3: The component orbital fits (solid black lines) to the measured radial velocities of HD 147787. The blue circles and the red triangles represent the primary and secondary radial velocities respectively. The filled circles and triangles are the velocities that were used for the orbital fitting. The dotted black lines represent the component systemic velocities. (Referenced on page 104.)

5.3 Frequency Identification

Figure 5.4 is the 0 d^{-1} to 80 d^{-1} frequency range pixel-by-pixel mean Lomb-Scargle periodogram of HD 147787[14], computed to determine the frequency ranges where the star shows the greatest variation[15]. It can be observed that the strongest variation occurs in the 0 d^{-1} to 6 d^{-1} frequency range. Although there is some minor variation in the 10 d^{-1} to 15 d^{-1}, 20 d^{-1} to 25 d^{-1}, 40 d^{-1} to 50 d^{-1} and 60 d^{-1} to 70 d^{-1} frequency ranges, it was deemed by visual inspection to be below the noise level for the definitive identification of any frequencies. As such, the 0 d^{-1} to 6 d^{-1} frequency range was selected for analysis. Figure 5.5 shows the spectral significance of frequencies identified in the frequency range of 0 d^{-1} to 25 d^{-1}. There were effectively no significant frequencies identified beyond 6 d^{-1}.

[14]It is assumed that all periodograms and mode identifications refer to the primary star.
[15]Refer to the section on frequency identification (2.4.1) for more information.

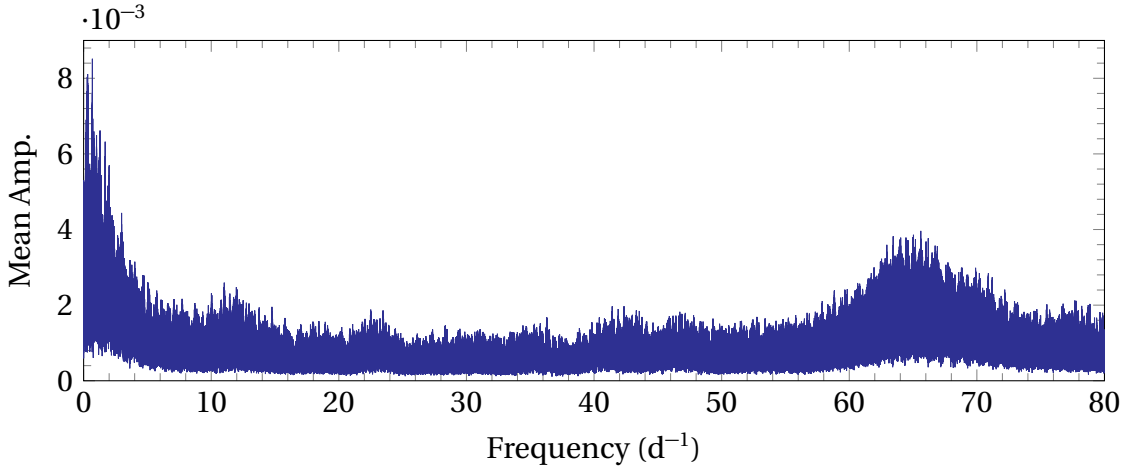

Figure 5.4: The 0 to 80 d^{-1} frequency range pixel-by-pixel mean Lomb-Scargle periodogram of HD 147787 computed by FAMIAS. (Referenced on page 105.)

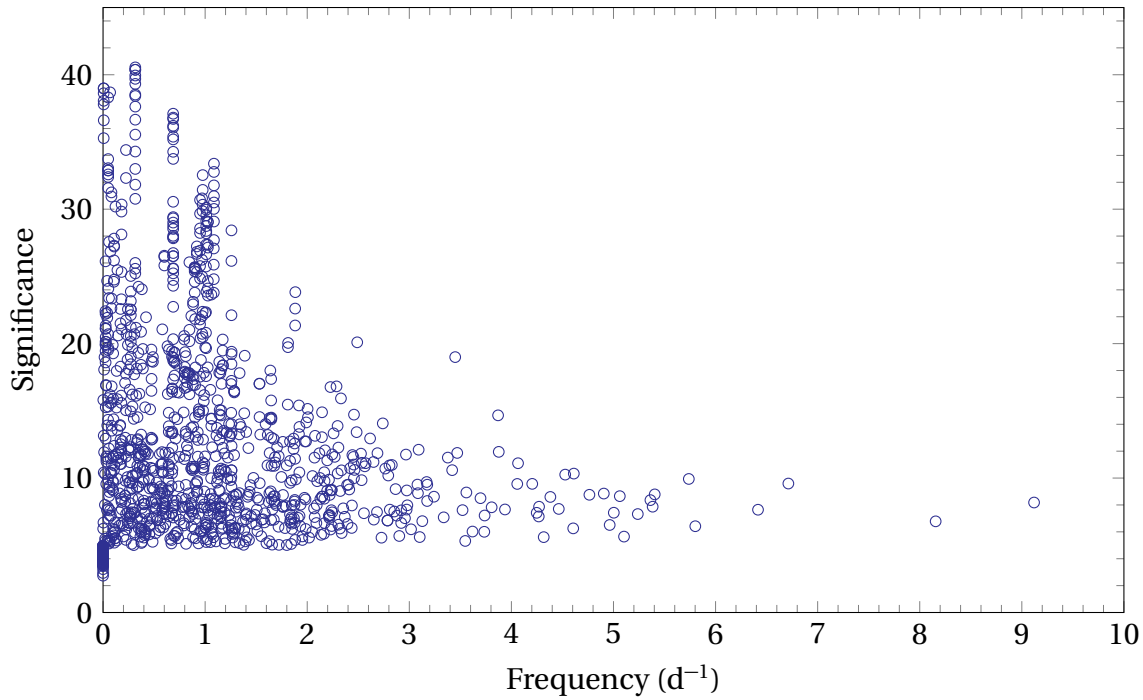

Figure 5.5: The spectral significance values of the frequencies of HD 147787 identified by SIGSPEC. Each blue circle represents a single pixel in which a frequency was identified at a particular significance. (Referenced on page 105, 107, 107, 115.)

Figure 5.6 shows the 0 d^{-1} to 6 d^{-1} frequency range spectral widow of HD 147787, indicating the dominant frequency pattern that arose from the data sampling in that range. Note the significant one-day aliasing that occurs. Figures D.1 and D.2 show the FAMIAS computed pixel-by-pixel mean Lomb-Scargle periodograms, and Figures D.3 to D.8 show the FAMIAS computed zeroth- to third-moment Lomb-Scargle periodograms respectively. Table 5.3 lists all of

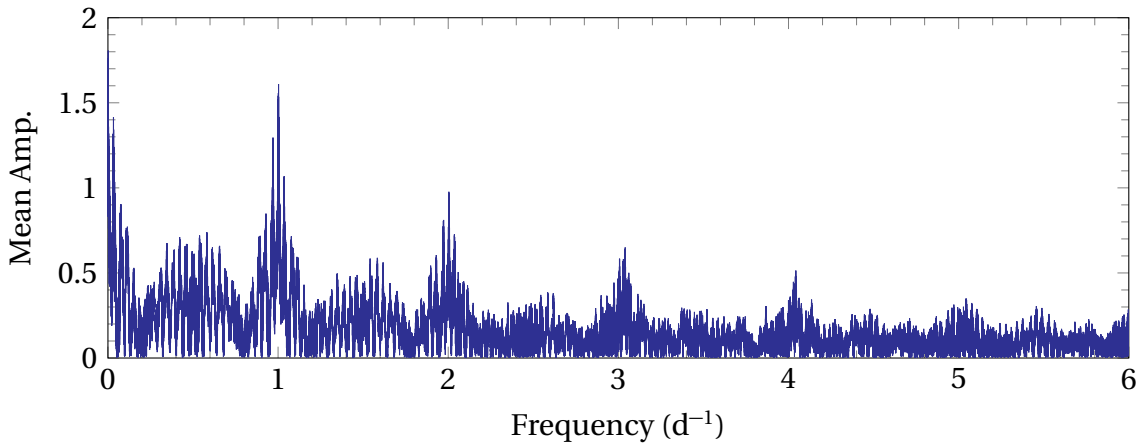

Figure 5.6: The 0 to 6 d^{-1} frequency range spectral window of HD 147787 computed by FAMIAS. (Referenced on page 106.)

the identified frequencies using the various identification methods and their corresponding SIGSPEC values.

It is evident that the one-day aliases are still present in the Figure 5.5 and in some cases have equivalently large spectral significance values. However, the assumption that real frequencies explain a greater proportion of line profile variations, and are detected in a larger number of pixels according to the SIGSPEC results, was used to distinguish the real frequency from the aliases. It can also be seen from the periodograms and particularly from the spectral significance results that the binary orbit frequency ($f_{\rm orb} = 0.0251$ d^{-1}) is still present[16]. The orbital frequency manifests itself as a high spectral significance peak at 0.02 ± 0.01 d^{-1} in Figure 5.5 and a high amplitude frequency peak in the 0.02 ± 0.01 d^{-1} region in Figures D.3 to D.1. This is due to residual variation from the line profile correction process and made frequency identification more difficult. However, this signal is not particularly strong compared to the pulsational frequencies in this case.

Several frequencies identified using the pixel-by-pixel method had analogues that were identified in multiple moments of the moment method:

$f_1 = 0.6870$ d^{-1}: $f_{26} = 1.6917$ d^{-1} as an alias.
$f_2 = 0.9374$ d^{-1}: $f_{18} = 0.9358$ d^{-1}.
$f_4 = 0.0819$ d^{-1}: $f_{22} = 0.0828$ d^{-1}, with $f_{25} = 0.9202$ d^{-1} as an alias.
$f_5 = 0.8818$ d^{-1}: $f_{12} = 0.9016$ d^{-1} with $f_{31} = 0.0997$ d^{-1} as an alias.
$f_8 = 0.0579$ d^{-1}: $f_{10} = 0.0490$ d^{-1}, $f_{23} = 0.0587$ d^{-1} and $f_{32} = 0.9522$ d^{-1}.
$f_9 = 0.2103$ d^{-1}: $f_{17} = 1.1830$ d^{-1} with $f_{34} = 2.1870$ d^{-1} as an alias.

[16] This also occurs for HD 182640 and HD 3112.

It is interesting that $f_1 = 0.6870$ d^{-1} and $f_6 = 0.6780$ d^{-1}, which are very close, were both identified as pulsational frequencies using the pixel-by-pixel method. Another interesting point is the identification of very low frequencies as pulsational frequencies ($f_4 = 0.0819$ d^{-1} and $f_8 = 0.0579$ d^{-1}).

A total of 9 frequencies were identified as real pulsation frequencies, based on the criteria described in the section on frequency selection methodology (2.4.1). These frequencies and their corresponding uncertainties, calculated using Equations 2.6 for FAMIAS and 2.9 for SIGSPEC, are listed in Table 5.4. The observational timebase T was calculated using Equation 2.7, giving the value $T = 396$. As mentioned in the section on frequency identification (3.4) in the chapter on HD 182640, SIGSPEC uncertainty estimations are overestimations and FAMIAS uncertainty estimations are underestimations. As such, a mean of the two uncertainty estimates would be closer to the true uncertainty of the identified frequencies and was therefore calculated and included in Table 5.4. The mean error estimates obtained are in the range of 0.03 ± 0.01 d^{-1}, which is relatively precise. The reduction in the standard deviation from successive prewhitening of pulsation frequencies is listed in Table D.1. The combination of these 9 pulsational frequencies explain 48.1% of variation across the line profiles of HD 147787, illustrated by Figure D.9.

Table 5.3: A summary of the HD 147787 frequencies found in FAMIAS and SIGSPEC. The corresponding amplitudes and uncertainties in the amplitudes A and $\sigma(A)$ calculated in FAMIAS and the maximum spectral significance of the identified frequency in SIGSPEC for the real pulsational frequencies are also listed. (Referenced on page 106.)

	FAMIAS			SIGSPEC	
	Frequency (d^{-1})	**A**	**$\sigma(A)$**	**Frequency (d^{-1})**	**Maximum Sig.**
	Pixel-by-Pixel				
f_1	0.6870	0.7118	0.0369	0.6869	37
f_2	0.9374	0.4371	0.0367	0.9502	31
$1+f_{orb}$	1.0267			1.027	29
f_3	1.2580	0.4130	0.0358	1.258	28
f_4	0.0819	0.3095	0.0379	0.0821	31
f_5	0.8818	0.3000	0.0344	0.8822	23
f_6	0.6781	0.4074	0.0419	0.6781	17
f_7	0.7807	0.2509	0.0358	0.7894	15
f_8	0.0579	0.2608	0.0399	0.0502	38
f_9	0.2103	0.1979	0.0386	0.1821	30
	Zeroth Moment				
f_{10}	0.0490			0.0502	38
f_{11}	0.1178			0.1176	7
f_{12}	0.9016			0.8978	26
f_{13}	2.0185			2.018	6
f_{14}	2.1296			2.119	12
	First Moment				
f_{15}	0.2832			0.2719	25
f_{16}	1.1605			1.172	20
f_{17}	1.1830			1.181	14
f_{18}	0.9358			0.9502	31
f_{19}	0.0176			0.0146	19
f_{20}	1.4597			1.453	7
f_{21}	1.9967			1.991	14
	Second Moment				
f_{22}	0.0828			0.0821	31
f_{23}	0.0587			0.0502	38
f_{24}	0.8070			0.8107	19
f_{25}	0.9202			0.9188	27
f_{26}	1.6917			1.705	12
	Third Moment				
f_{27}	0.2832			0.2719	25
f_{28}	1.1605			1.172	20
f_{29}	0.4907			0.4883	19
f_{30}	0.9295			0.9188	27
f_{31}	0.0997			0.0991	19
f_{32}	0.9522			0.9502	31
f_{33}	1.4435			1.444	9
f_{34}	2.1870			2.175	12

Table 5.4: The identified pulsational frequencies of HD 147787, with the corresponding FAMIAS, SIGSPEC and mean uncertainty estimates. (Referenced on page 108, 108.)

	Frequency (d^{-1})	FAMIAS $\sigma(f)$ (d^{-1})	SIGSPEC $\sigma(f)$ (d^{-1})	$\bar{\sigma}(f)$ (d^{-1})
f_1	0.68700	0.00001	0.00007	0.00004
f_2	0.93740	0.00002	0.00008	0.00005
f_3	1.25799	0.00002	0.00008	0.00005
f_4	0.08189	0.00003	0.00008	0.00005
f_5	0.88180	0.00003	0.0001	0.00006
f_6	0.67812	0.00002	0.0001	0.00006
f_7	0.78074	0.00003	0.0001	0.00007
f_8	0.05790	0.00003	0.00007	0.00005
f_9	0.21027	0.00004	0.00008	0.00006

5.4 Mode Identification

Table 5.5: The zero-point fit parameters of HD 147787. (Referenced on page 110.)

Parameter	Value
$v \sin i$ (km s^{-1})	6.39
Equivalent Width (km s^{-1})	3.91
Intrinsic Width (km s^{-1})	9.30
Velocity Offset (km s^{-1})	-0.15
χ^2	23.98

The initial stellar parameters input prior to mode identification are listed in Table 5.1. The $v \sin i$, equivalent width, intrinsic width and velocity offset, calculated by performing a zero-point fit in FAMIAS[17], are listed in Table 5.5. Figure 5.7 shows the zero-point fit of HD 147787. Note the excellent visual fit of the synthetic line profile to the zero-point line profile, with a correspondingly low $\chi^2 = 23.98$.

Figure 5.8 shows the $v \sin i$ values of the models calculated during the zero-point fit, with their associated χ^2 values. It can be seen that the range of $v \sin i$ values of the best-fitting models is between 0 km s^{-1} to 15 km s^{-1}, which is relatively large. Equations 2.13 and 2.14 were used to calculate the Keplerian breakup velocity and associated critical minimum inclination. Considering the large range of $v \sin i$ values of the best-fitting models, it would be more useful to give a range of $i_{\rm crit}$ values instead of a single one. As such, the Keplerian breakup velocity and range of the critical minimum inclination, based on 0 km s^{-1} $< v \sin i <$ 15 km s^{-1}, are $v_{\rm crit} = 393.1$ km s^{-1} and $0° < i_{\rm crit} < 2.19°$.

Despite the poor constraints on the $v \sin i$, the zero-point fit parameters were fixed before mode identification of the individual frequencies were performed to reduce the parameter

[17] Refer to the section on mode identification methodology (2.4.2) for more information.

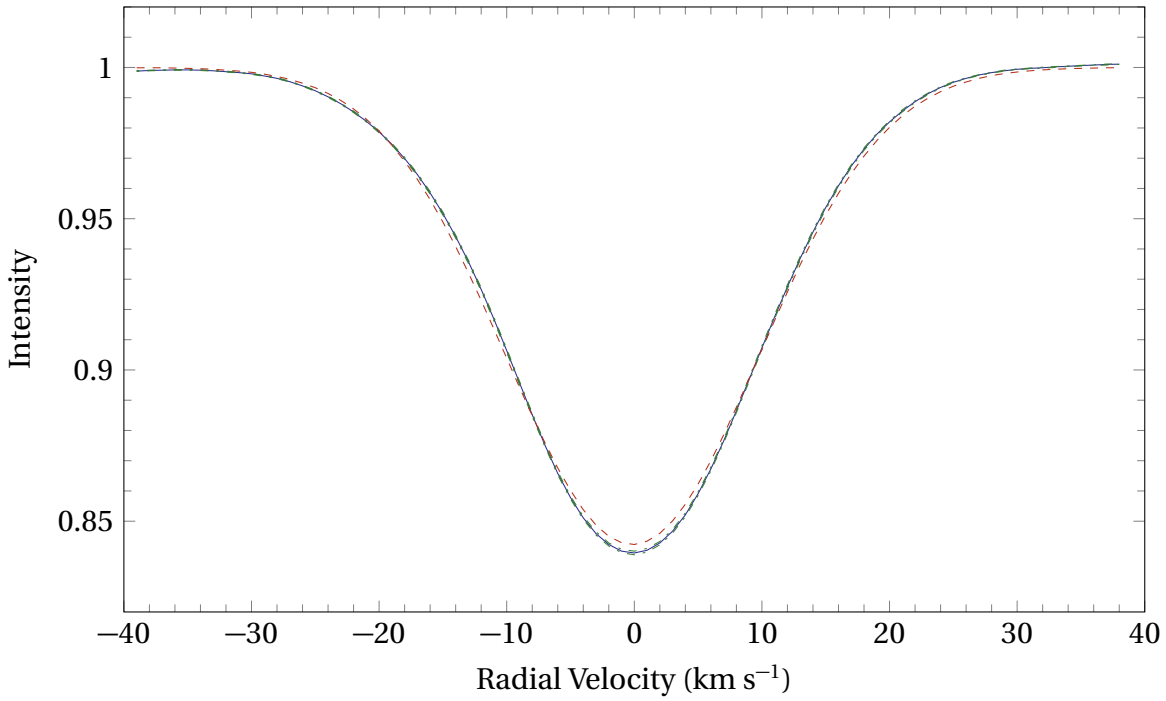

Figure 5.7: The zero-point fit of the HD 147787. The solid blue line represents the zero-point line profile, the two dash dotted green lines (partially obscured by the solid blue line) represent the statistical uncertainty and the dashed red line represents the best-fit synthetic zero-point line profile. Note the excellent visual fit of the synthetic line profile to the zero-point line profile (with a correspondingly low $\chi^2 = 23.98$). (Referenced on page 110.)

space during the amplitude and phase fits[18]. Unfortunately, it was not possible to identify the modes of all of the identified pulsation frequencies. The synthetic amplitude and phase profiles of the best-fitting modes of $f_4 = 0.08189$ d^{-1}, $f_8 = 0.05790$ d^{-1} and $f_9 = 0.21027$ d^{-1} were poor matches to the observational profiles (Figures D.10 to D.12).

Nevertheless, the mode identification of f_1 to f_3, and f_4 to f_7, was successful and featured very well-fitting synthetic amplitude and phase profiles. The best-fitting modes of f_1 to f_3, and f_4 to f_7 are listed in Table 5.6, with their corresponding χ^2 values, inclinations, velocity amplitudes and phases. In addition, the rotational frequency $f_{\rm rot}$ and the co-rotating frequency $f_{\text{co-rot}}$ were calculated using Equations 2.15 and 2.18 in order to determine the physicality of each mode. These are also listed in Table 5.6. The observational amplitudes and phases for each frequency along with the best-fitting synthetic amplitude and phase profiles are shown in Figure 5.9. All of these modes have inclinations that are significantly above $i_{\rm crit}$. In addition, all of the frequencies are significantly greater than $f_{\rm rot}$ at the modelled inclination of the best-fit modes, which all happen to be prograde. Also, the identified pulsation modes are reliable, based on Equation 2.16, as the ratio $|f_{\rm rot}/f_{\text{co-rot}}|$ for all of the frequencies, except for

[18]Refer to the section on mode identification methodology (2.4.2) for more information

$f_6 = 0.67812$ d^{-1}, is below 0.5[19]. The ratio $|f_{\text{rot}}/f_{\text{co-rot}}|$ for $f_6 = 0.67812$ d^{-1} is 0.66, which is still well below 1 and is therefore still reasonable, according to Schrijvers et al. (1997).

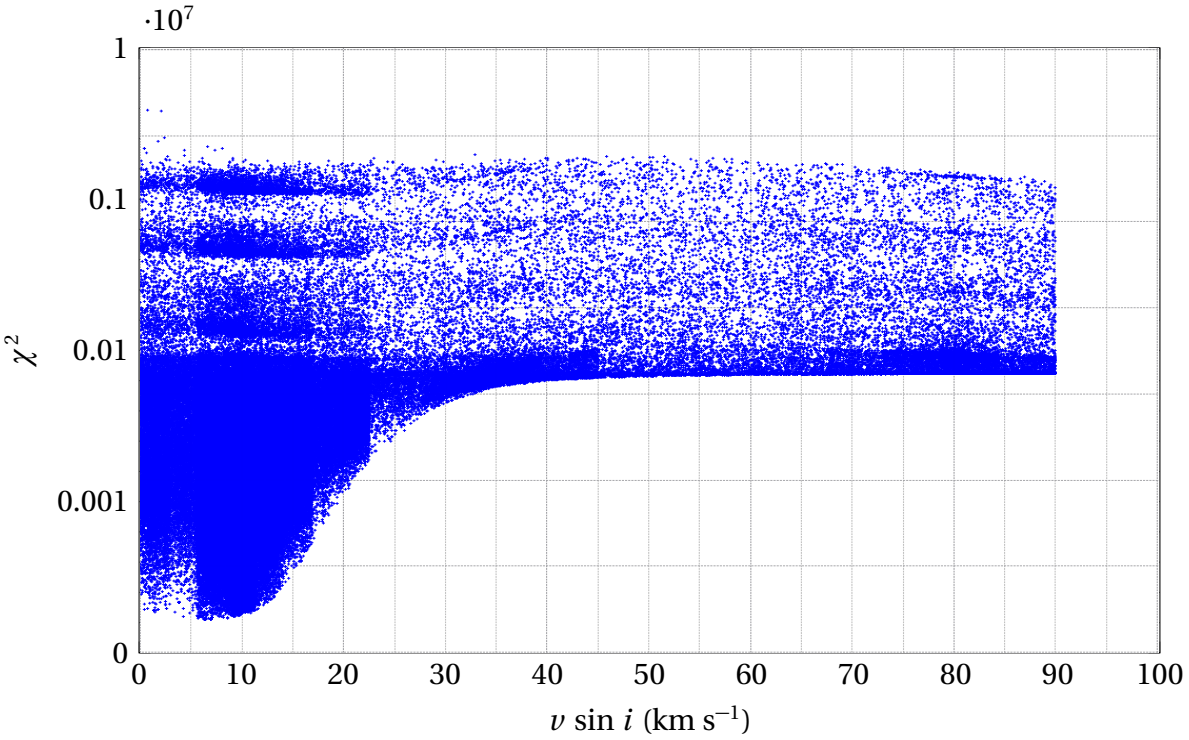

Figure 5.8: The v sin i values of the models fit to the zero-point line profile of HD 147787, with their associated χ^2 values, computed during the zero-point fit of the HD 147787. Each blue dot represents a single model that was fitted to the zero-point line profile of HD 147787. Note the poor level of constraint of the v sin i values during the fit. (Referenced on page 110.)

It must be noted that the best-fit modes of $f_1 = 0.68700$ d^{-1}, $f_5 = 0.88180$ d^{-1} and $f_7 = 0.78074$ d^{-1} were not the modes with the lowest χ^2 values. This is because the modes with the lowest χ^2 values for $f_1 = 0.68700$ d^{-1} $(1,-1)$, $f_5 = 0.88180$ d^{-1} $(1,-1)$ and $f_7 = 0.78074$ d^{-1} $(2,-2)$ were physically inconsistent: the pulsation frequencies were higher than the rotational frequency f_{rot} at the modelled inclination values, which is impossible for retrograde modes.

It was also found that the inclination values of the models with the best-fit ℓ and m values converged to specific ranges. Table 5.7 lists the range of inclination values for each frequency. The inclination ranges of the individual frequencies are not in agreement. The inclination ranges of f_1, f_3, f_5 and f_7 seem to imply that the true inclination of the star is between 70° and 90°. This corresponds to a rotational velocity of 6.4 km s^{-1} to 6.8 km s^{-1} (1.6% to 1.7% of $v_{\text{crit}} =$ 393.1 km s^{-1}). This is significantly below the average for F4-type stars (40 km s^{-1}, McNally, 1965). f_2 and f_6 seem to imply a much smaller inclination of 10° to 40°. This corresponds to a rotational velocity of 10 km s^{-1} to 37 km s^{-1} (2.5% to 9.4% of $v_{\text{crit}} = 393.1$ km s^{-1}). This is at or

[19]Refer to the section on mode identification methodology (2.4.2) for more information.

slightly below the average for F4-type stars (40 km s^{-1}, McNally, 1965).

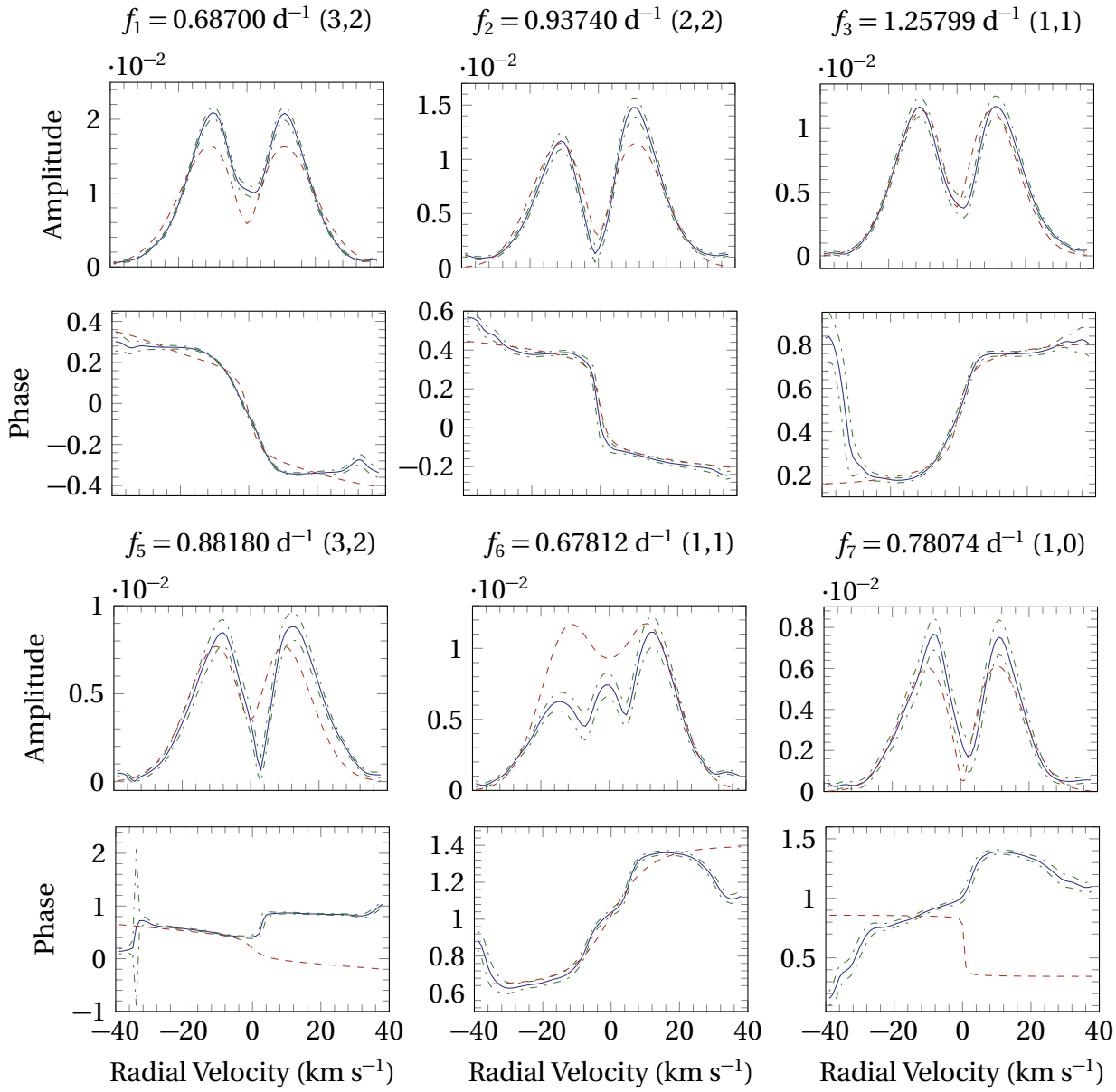

Figure 5.9: The amplitude and phase profiles of the best-fit modes of f_1 to f_3, and f_4 to f_7 of HD 147787. The solid blue lines are the observational profiles, the dash dotted green lines represent the statistical uncertainty and the dashed red lines represent the best-fit synthetic profiles. (Referenced on page 111.)

Table 5.6: The best-fit modes of f_1 to f_3, and f_4 to f_7 of HD 147787, with the corresponding rotational frequencies at the modelled inclinations. (Referenced on page 111, 111.)

Mode	χ^2	Inclination	Vel. Amp. (km s^{-1})	Phase	$f_{\rm rot}$ (d^{-1})	$f_{\rm co\text{-}rot}$ (d^{-1})
			$f_1 = 0.68700$ d^{-1}			
(3, 2)	14.96	81.97	0.645	0.205	0.07	0.55
			$f_2 = 0.93740$ d^{-1}			
(2, 2)	5.03	31.77	0.645	0.362	0.14	0.71
			$f_3 = 1.25799$ d^{-1}			
(1, 1)	3.14	41.14	1.290	0.732	0.11	1.20
			$f_5 = 0.88180$ d^{-1}			
(3, 2)	9.29	84.65	0.645	0.465	0.07	0.75
			$f_6 = 0.67812$ d^{-1}			
(1, 1)	11.90	30.43	0.645	0.267	0.34	0.51
			$f_7 = 0.78074$ d^{-1}			
(1, 0)	3.97	79.96	0.645	0.850	0.07	0.78

Table 5.7: The inclination ranges of the best-fitting models of f_1 to f_3, and f_4 to f_7 of HD 147787. (Referenced on page 112.)

	Frequency (d^{-1})	Inclination range (°)
f_1	0.68700	75 – 90
f_2	0.93740	10 – 50
f_3	1.25799	30 – 90
f_5	0.88180	80 – 90
f_6	0.67812	10 – 40
f_7	0.78074	70 – 90

5.5 Discussion

The frequency and mode identification results show that HD 147787 seems to be a fairly typical γ Doradus[20] star, exhibiting mostly low-frequency variation of low spherical harmonic degree ℓ[21]. However, it does exhibit some very low-frequency pulsations ($f_4 = 0.08189$ d^{-1}, $f_8 = 0.05790$ d^{-1} and $f_9 = 0.21027$ d^{-1}) whose modes could not be identified in this analysis. This may have been due to the fact that the binary orbit frequency $f_{\rm orb} = 0.0251$ d^{-1} is also of a similar magnitude. A larger number of high signal-to-noise spectra would be useful in differentiating these very low frequencies from the noise and from $f_{\rm orb}$. It would be unwise to characterise HD 147787 as a bona-fide γ Doradus star without determining the origin of these very-low frequency pulsations.

Even though the constraints on the v sin i were poor, the best-fit v sin $i = 6.39$ km s^{-1} is

[20] Refer to the section on γ Doradus stars (1.4.1) for more information.
[21] Refer to the section on non-radial pulsational geometry (1.3.5) for more information.

in close agreement with that of De Cat et al. (2009) (7 km s^{-1}). An estimate for the v sin i was calculated using Equation 4.2. Substituting a FWHM= 23 km s^{-1}, the value v sin i = 9.77 km s^{-1} was obtained, which is well within the range defined by the zero-point fit (0 km s^{-1} to 15 km s^{-1}). The strongest frequency detected in this analysis, $f_1 = 0.68700$ d^{-1}, also agrees with that of De Cat et al. (2009) (0.6897 d^{-1}). The second frequency found by De Cat et al. (2009) (1.304 d^{-1}) could be an analogue of $f_3 = 1.25799$ d^{-1} as they had mentioned that they were unable to definitively identify it.

It was mentioned in De Cat et al. (2006) that the components of HD 147787 were distant enough that no ellipsoidal variation was detected. However, the presence of the very-low frequencies whose modes could not be identified, outside of the γ Doradus and of a similar order to the binary orbit frequency $f_{\rm orb} = 0.0251$ d^{-1}, gives pause to this notion. It is possible that such variation was not detected due to its low amplitude in comparison with the primary pulsation frequency. A recent study by Borkovits et al. (2014) of the star HD 183640, an eclipsing binary with a pulsating component whose orbital period (31.973 d) is very similar to HD 147787, revealed ellipsoidal variations that were previously thought to be the beating of the orbital and pulsational frequencies. It would hence be unwise to rule out ellipsoidal variation as an explanation of the very-low frequencies, particularly considering the high spectral significance of frequencies in the 0 d^{-1} to 0.2 d^{-1} region (Figure 5.5).

6 Conclusion and Future Research

6.1 Conclusion

Three binaries were analysed for this thesis: HD 182640, a system with a candidate γ Doradus primary (Koen and Eyer, 2002); HD 3112, a system with a bona fide δ Scuti primary (De Mey et al., 1998); and HD 147787, a system with a candidate γ Doradus primary (De Cat et al., 2009).

The thesis goals set out in the introduction of this thesis (Section 1.6) have largely been met: the orbital elements of all three binaries have been determined to a high degree of precision; higher than any so far in the literature. A large number of frequencies of each star have been identified, explaining from 40% to 50% of the line profile variation of each star. Many of these frequencies agree with previously published frequencies. Mode identification was performed for all three stars, but was unfortunately only completely successful for HD 182640. The mode identification of the frequencies of HD 3112 and HD 147787 was incomplete and possible reasons for the inability to identify the modes of said frequencies was given in the discussion sections of the respective chapters. Table 6.1 is a summary of the frequency and mode identification efforts presented in this thesis.

Table 6.1: A summary of frequency and mode identification results of the three stars analysed for this thesis. (Referenced on page 117.)

Star	No. of Frequencies Identified	% of Variation Explained	No. of Modes Identified
HD 182640	18	42.9	18
HD 3112	17	46.3	1
HD 147787	9	48.1	6

The most significant conclusion of the results from the pulsational analysis is that the method developed for the analysis of binaries with a single pulsating component is viable. This was confirmed by the results of the frequency analysis, where a large number of identified frequencies agreed with previously published results. However, the method was not able to completely eliminate the effects of the binary orbit from the periodograms although the effects were diminished. One may argue that it would be simpler to analyse the line profiles without removing the secondary star and simply prewhiten the periodograms with the binary orbit frequency. However, it is possible that the binary orbit frequency might mask some pulsational frequencies. The removal of the secondary star also enables a smaller radial velocity range to be analysed, reducing computation times.

The frequency and mode identification results of HD 182640 were quite interesting: the frequencies were mostly outside the typical range for γ Doradus[1] stars and were exclusively high-degree[2] ($\ell > 4$) modes. In addition, the significant number of high spectral-significance frequencies in the 0 d^{-1} to 3 d^{-1} range casts doubt as to whether HD 182640 can be classified as a δ Scuti[3] star. Further investigation is required before it is possible to conclude whether HD 182640 is a γ Doradus, or a δ Scuti or hybrid star.

The frequency identification results of HD 3112 agree with the previously published results of Paparo et al. (1996) and De Mey et al. (1998), lending the identification further veracity. The discovery of low-frequency pulsational frequencies is in agreement with the arguments of Balona (2014). The lack of mode identification results for most of the frequency except the primary ($f_1 = 20.2802$ d^{-1}) is unfortunate but can be explained by the fact that HD 3112 experience ellipsoidal variations, an argument reinforced by others (Paparo et al., 1996; Sterken et al., 1997; Templeton et al., 2000). The strongest frequency $f_1 = 20.2802$ d^{-1} was identified as a (1,1) mode but could very well be a radial mode, as suggested by Sterken (1997), Sterken et al. (1997), De Mey et al. (1998) and Templeton et al. (2000). The poor constraining of the v sin i during the zero-point fit[4] is another factor that could have prevented precise mode identification.

The frequencies and modes of HD 147787 are largely typical of γ Doradus stars: all of the identified frequencies are low and the best-fit modes are all low degree ($\ell \leq 3$) ones. However, there were some very low frequencies (< 0.3 d^{-1}) whose modes were not able to be identified. This could be due to the misidentification of those frequencies due to previously undetected ellipsoidal variation. Similar to HD 3112, the v sin i of HD 147787 was poorly constrained during the zero-point fit. Further investigation is required before it is possible to conclude whether HD 3112 is a γ Doradus star.

From these results, it can be seen that binarity affects the pulsational characteristics of the component stars if the components are located close enough to cause tidal distortion of their surfaces. This makes the task of modelling said pulsations more difficult as the shape of the star becomes more oblate at pulsational equilibrium. In addition, the oblateness of the star changes based on the orbital phase for eccentric orbits.

The relationship between γ Doradus and δ Scuti classes is still relatively unclear. HD 3112 seems to be a typical δ Scuti star and HD 147787 seems to be a typical γ Doradus star (ignoring the uncharacterised very-low frequency variations). HD 182640 seems to be in-between the γ Doradus and δ Scuti classes: displaying the strongest variation in the frequency range between the typical frequency ranges of γ Doradus and δ Scuti stars.

[1] Refer to the section on γ Doradus stars (1.4.1) for more information.
[2] Refer to the section on non-radial pulsational geometry (1.3.5) for more information.
[3] Refer to the section on δ Scuti stars (1.4.2) for more information.
[4] Refer to the section on mode identification methodology (2.4.2) for more information

6.2 Future Research

The research scope presented in this thesis can be progressed most obviously by the acquisition of a larger quantity of high signal-to-noise spectroscopic data. This would enhance the number and strength of the pulsational frequencies detected, enabling their characterisation more precisely. Spectroscopic data from space telescopes such as GAIA would be a great boon to this endeavour as they are unaffected by atmospheric distortion and seeing conditions. In some cases, the resolution on these space telescope might be good enough to exclude the secondary component of the binary and obtain data on the primary component without cross-contamination. Supplementing the spectroscopic results with photometric ones would also enable better characterisation of both the binary orbits and the pulsations.

Precise fundamental stellar parameters are important both in the creation of cross-correlated[5] line profiles and in the mode identification process[6]. Large scale surveys devoted to the increasingly more precise measurement of these parameters are still ongoing and would enable more accurate frequency and mode identifications. This would be aided by the development of more sophisticated stellar models incorporating high-order rotational effects and more significantly, ellipsoidal variations, would go a long way in characterising the pulsations of binary pulsators of all classes.

[5]Refer to the section on cross-correlation (2.2.3) for more information.
[6]Refer to the section on mode identification methodology (2.4.2) for more information

Acknowledgements

Personal

First and foremost, I would like to thank my senior supervisor, Associate Professor Karen Pollard, for her invaluable advice and support, and for encouraging me to explore this challenging new frontier in asteroseismology that I would have otherwise not attempted to explore. I would also like to thank my associate supervisor, Professor Mike Reid, for putting up with my antics and for being supportive in all of my endeavours.

Next, I would like to thank my officemates[7] for being a source of great amusement, distraction and cake, as well as profound generosity and hospitality. I would especially like to thank my unofficial supervisor, the HOOTMASTER[8], for his guidance, mentorship and Hoot, and the CAKELORD[9], for putting up with me and for being an all-round awesome guy. Special thanks also go out to THE GOLDEN ONE[10] for being such a warm and generous individual.

I would also like to thank my flatmates[11], a lovely and colourful bunch of individuals. Your warmth and companionship are the reason why our flat felt like a home away from home. I would like to thank my friends, both here in Christchurch[12] and thousands of kilometres away in Singapore[13] and around the world. Thanks for being there for me, in both good times and bad.

Most importantly, I would like to thank my family: Amma, Appa, Shyam, Thatha, Pati, Mama. None of this would have been possible without you. Your love and support are the foundation on which all my success is built.

Last, but certainly not least, I would like to pay homage to the power of heavy metal for giving me the strength and determination to get through the tough times in my life.

[7] Douglas Walker, Peter de Vis, Ariadna Manilla Robles and Amber Malpas
[8] Dr. Christoph Bergmann
[9] Edward James Ashton
[10] Katrin Greßmann
[11] Chong Luo, Dong Viet Anh, Zhiyang Jin, Boney Bun and Tuyen Dinh
[12] Saad Siddiqui, Qian Hu, Euan Mason and Rhiannon Mason
[13] Donovan Koh, V Kumar Sharma, Simon Paul Vincent, Steven Paul Vincent, Pang Tze Wei, Markus Tan, Quek Pearl Ning, David Chang, Stacy Ooi, Seet Rui Feng and many many more.

Professional

I would like to thank the other observers who had gathered the spectra for this research: Emily Brunsden, Fraser Gunn, Pam Kilmartin and Karen Pollard. I would also like to show my appreciation to Dr. John Telting and Dr. Richard Pogge for allowing me to use their animations in this thesis. Special thanks go out Professor Emeritus Thomas O'Haver of the University of Maryland for inspiring the binary analysis methodology and for making his `peakfit.m` MATLAB code available to the public.

I would also like to express my gratitude to Dr. Christoph Bergmann for his Gaussian-fitting and binary orbit-fitting codes that were instrumental in this analysis and for his advice and help throughout this project.

This project has made use of the SIMBAD astronomical data base operated at the CDS in Strasbourg, France and data products from the Wide-field Infrared Survey Explorer, which is a joint project of the University of California, Los Angeles, and the Jet Propulsion Laboratory/California Institute of Technology, funded by the National Aeronautics and Space Administration.

Mode identification results were obtained with the software package FAMIAS developed in the framework of the FP6 European Coordination action HELAS (`http://www.helas-eu.org`).

A Raw FITS Spectrum Examples

This appendix chapter comprises examples of raw FITS spectra from the HERCULES spectrograph:

- Flat-field spectrum (Figure A.1).
- Thorium-Argon spectrum (Figure A.2).
- Stellar spectrum (Figure A.3).

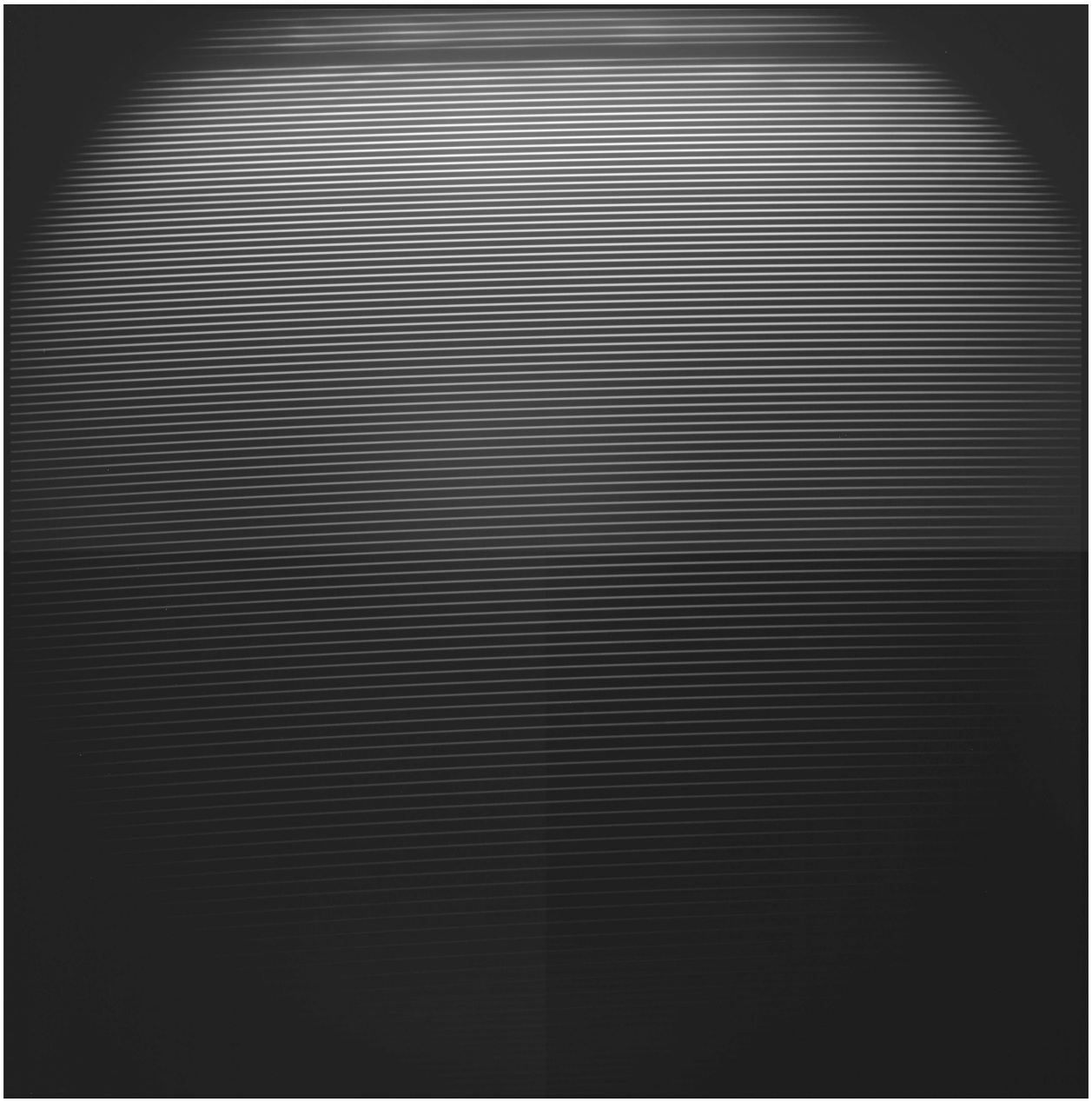

Figure A.1: An example of a flat-field spectrum. The contrast has been increased for greater visibility. The bottom of the image corresponds to the blue parts of the spectrum. Note the distinct lack of absorption lines in the image. (Referenced on page 29, 123.)

Figure A.2: An example of a Thorium-Argon calibration spectrum. The contrast has been increased for greater visibility. The bottom of the image corresponds to the blue parts of the spectrum. Note that the overexposed regions of thorium-argon spectra are removed prior to wavelength calibration. (Referenced on page 29, 31, 123.)

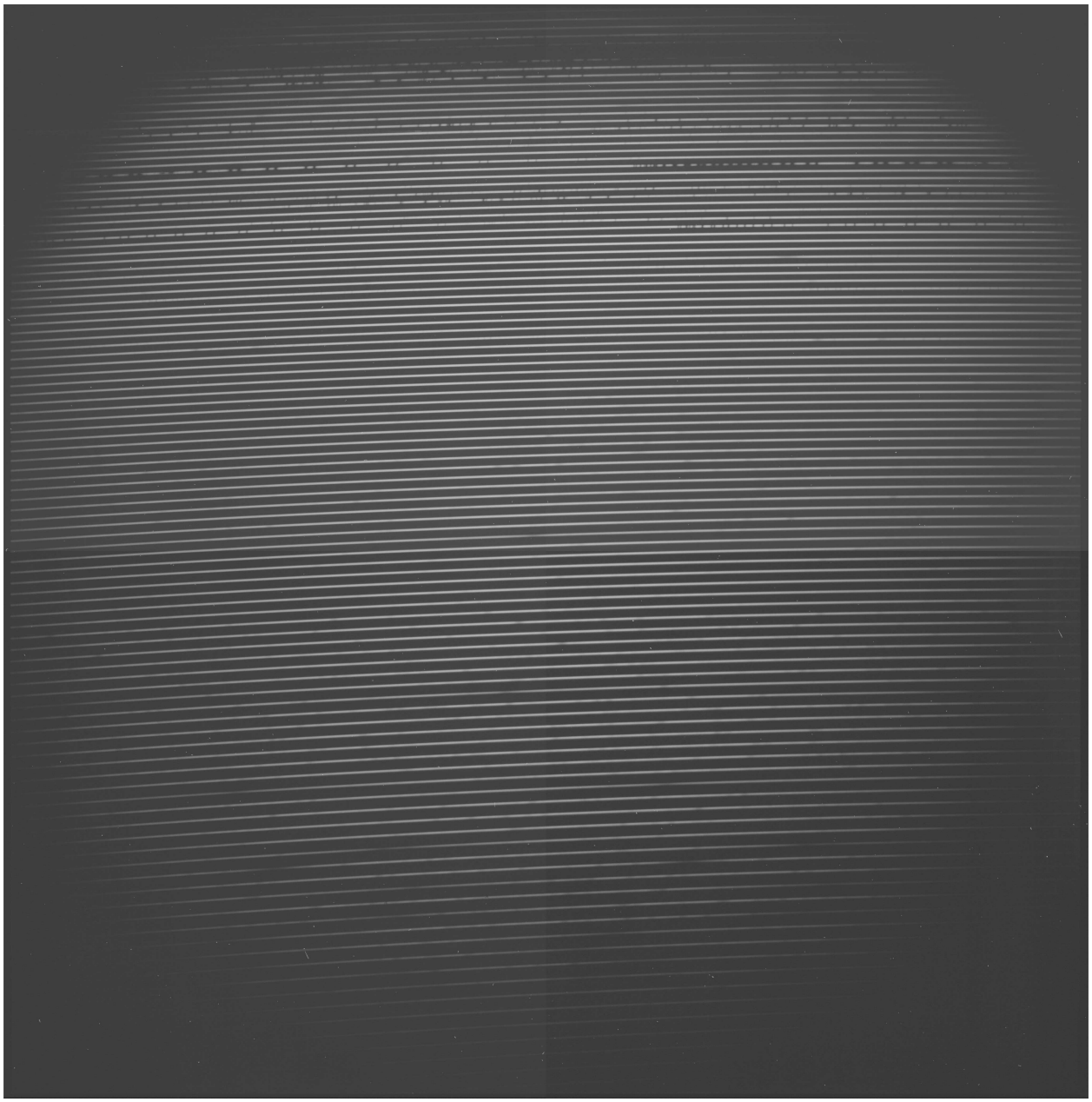

Figure A.3: An example of a stellar spectrum. The contrast has been increased for greater visibility. The bottom of the image corresponds to the blue parts of the spectrum. Note the distinct absorption lines in the image. (Referenced on page 29, 123.)

B Additional Plots and Tables for HD 182640

This appendix chapter comprises various plots and tables pertaining to HD 182640:

- The pixel-by-pixel mean Lomb-Scargle periodograms (Figures B.1 to B.4).
- The zeroth- to third-moment Lomb-Scargle periodograms (Figures B.5 to B.8).
- The reduction in the standard deviation across the line profiles of HD 182640 due to progressive prewhitening of pulsation frequencies (Table B.1) and a graphical representation of this process (Figure B.9).

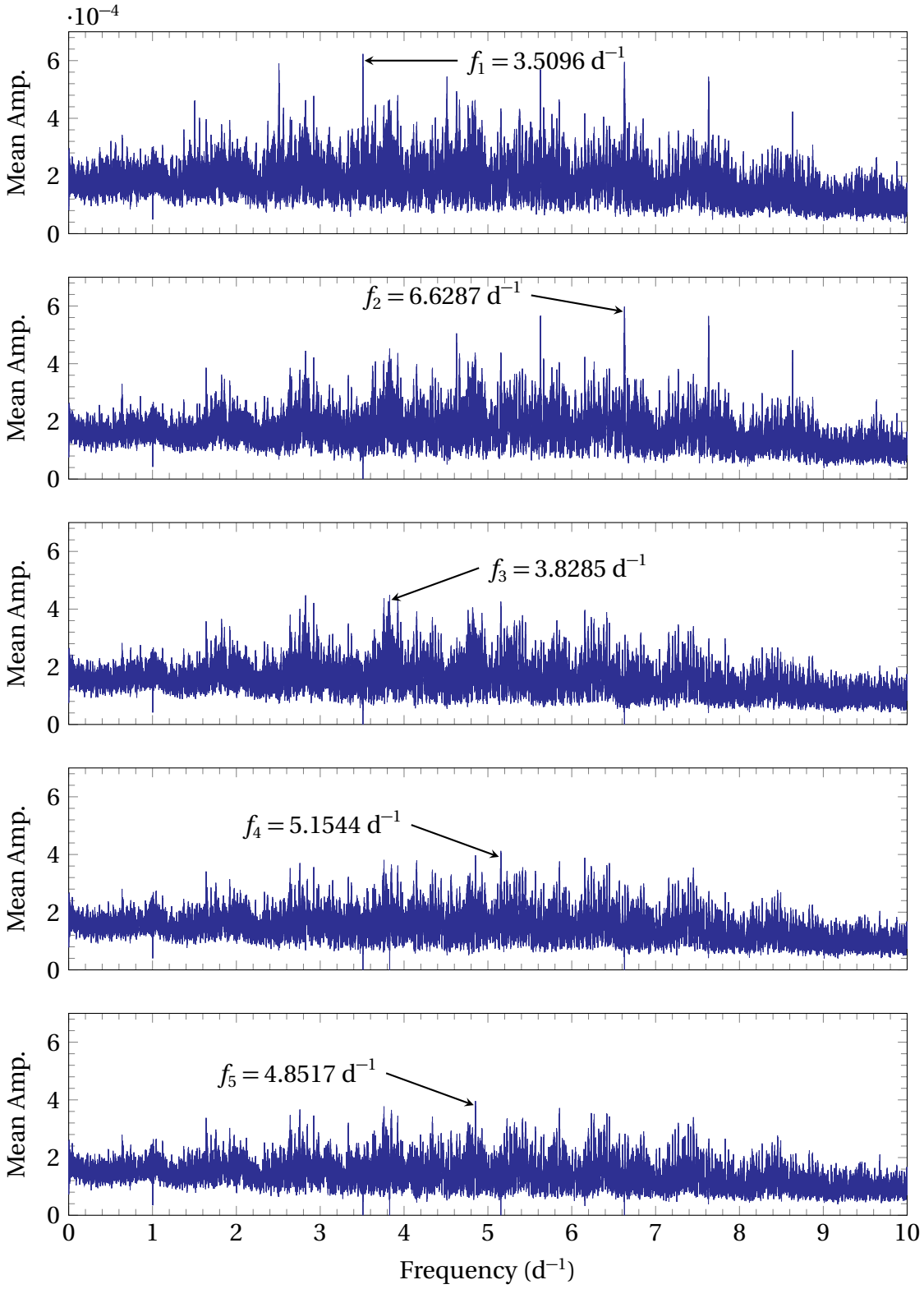

Figure B.1: The pixel-by-pixel mean Lomb-Scargle periodograms of HD 182640 computed by FAMIAS, showcasing the first batch of five frequencies (f_1 to f_5) detected through the pixel-by-pixel method. (Referenced on page 63, 64, 127.)

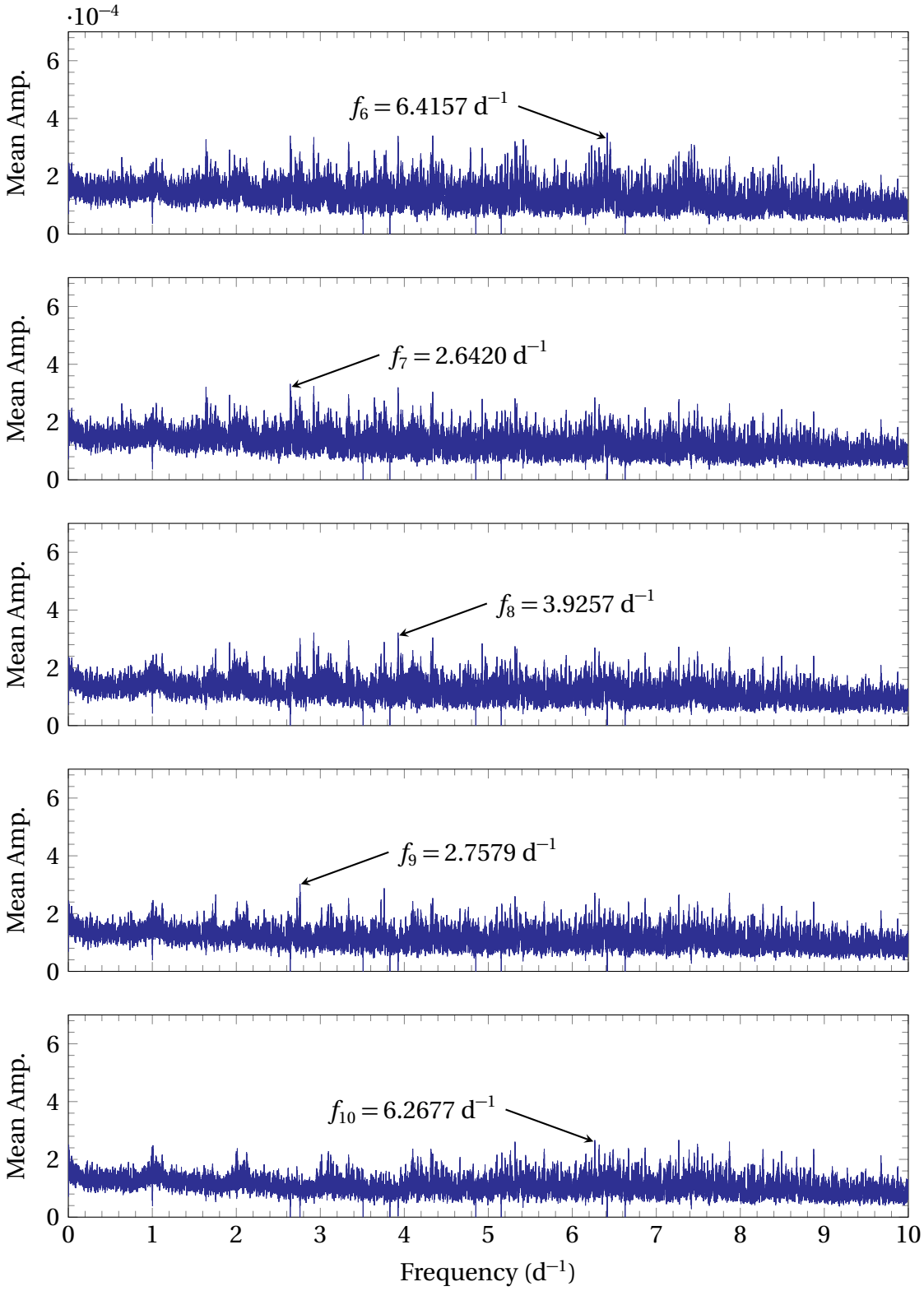

Figure B.2: The pixel-by-pixel mean Lomb-Scargle periodograms of HD 182640 computed by FAMIAS, showcasing the second batch of five frequencies (f_6 to f_{10}) detected through the pixel-by-pixel method.

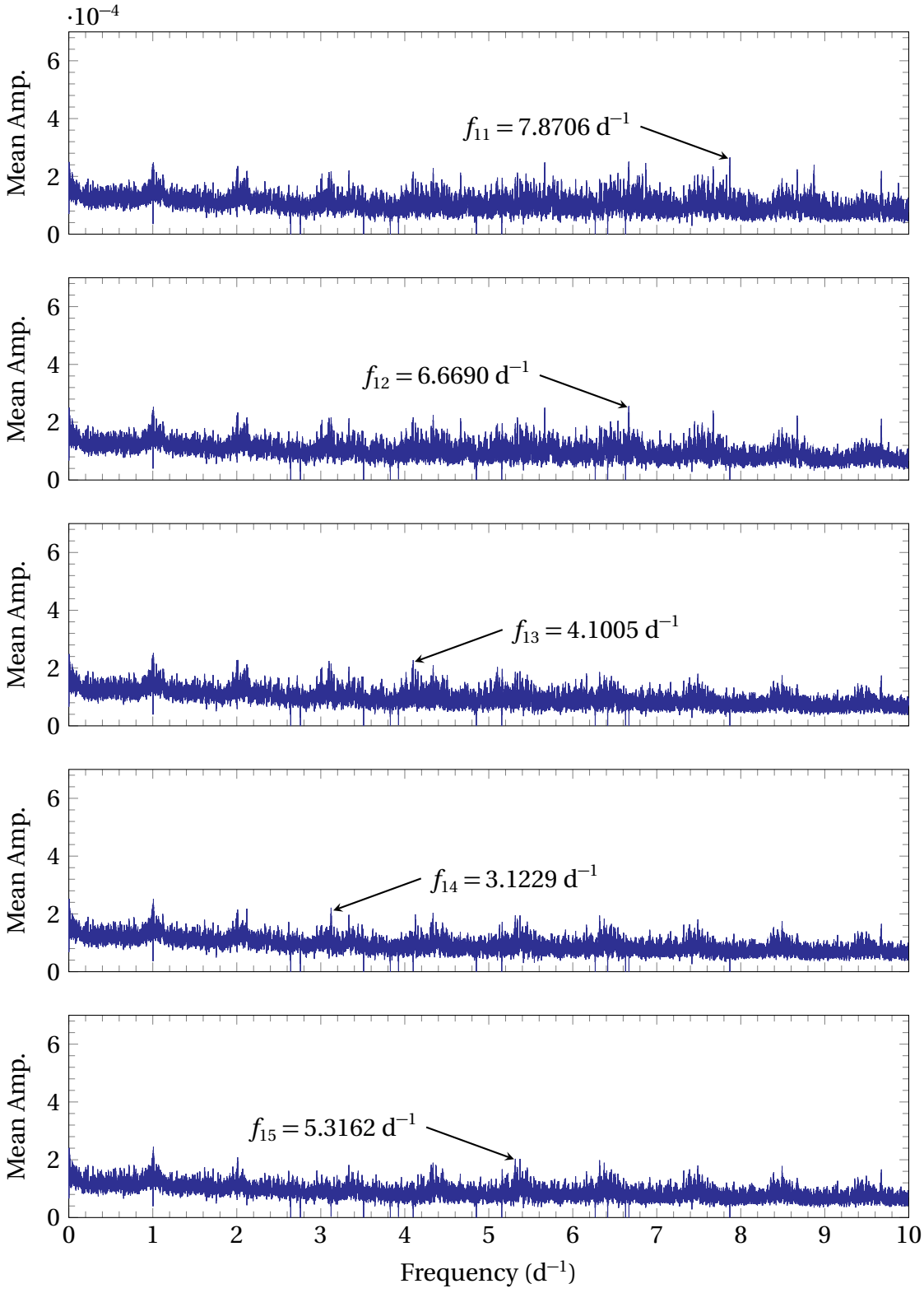

Figure B.3: The pixel-by-pixel mean Lomb-Scargle periodograms of HD 182640 computed by FAMIAS, showcasing the third batch of five frequencies (f_{11} to f_{15}) detected through the pixel-by-pixel method.

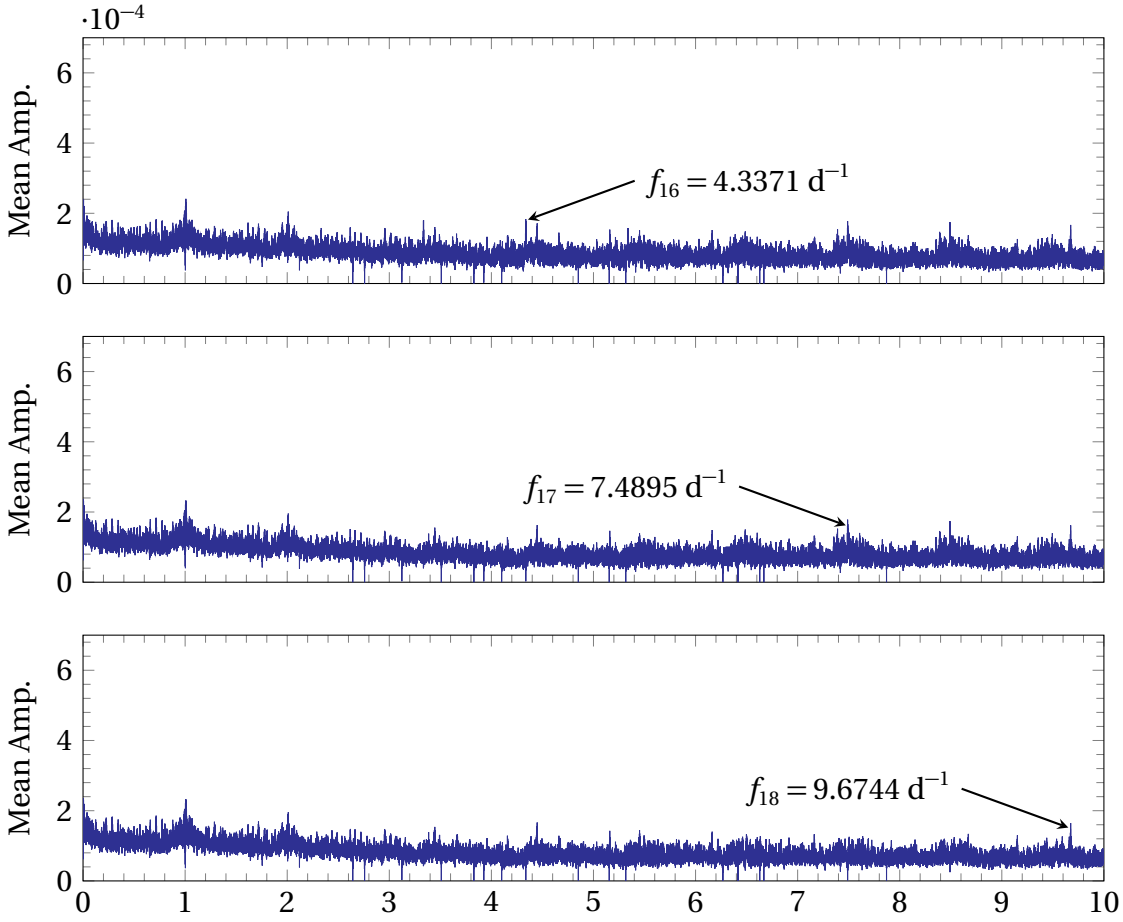

Figure B.4: The pixel-by-pixel mean Lomb-Scargle periodograms of HD 182640 computed by FAMIAS, showcasing the fourth batch of three frequencies (f_{16} to f_{18}) detected through the pixel-by-pixel method.

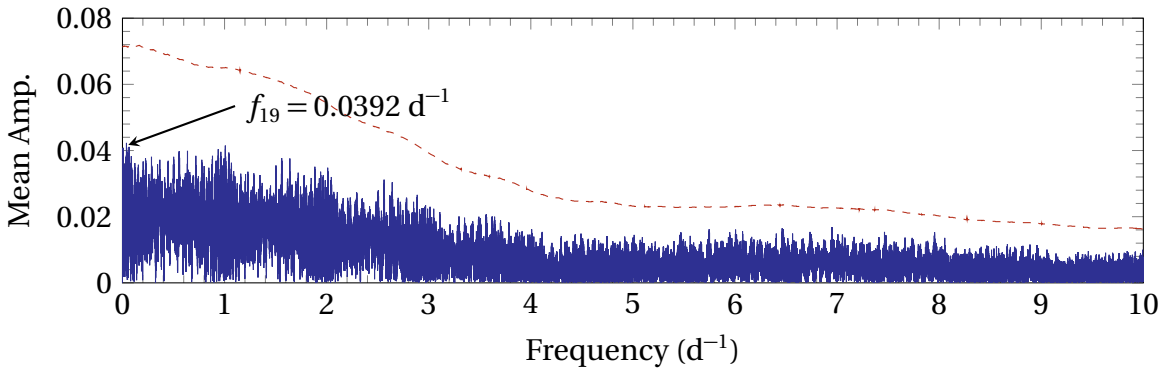

Figure B.5: The zeroth-moment Lomb-Scargle periodograms of HD 182640 computed by FAMIAS, showcasing the only prominent frequency (f_{19}) detected through the zeroth moment of the moment method. The dashed red line represents the significance level at a signal-to-noise ratio of 4. (Referenced on page 63, 75, 127.)

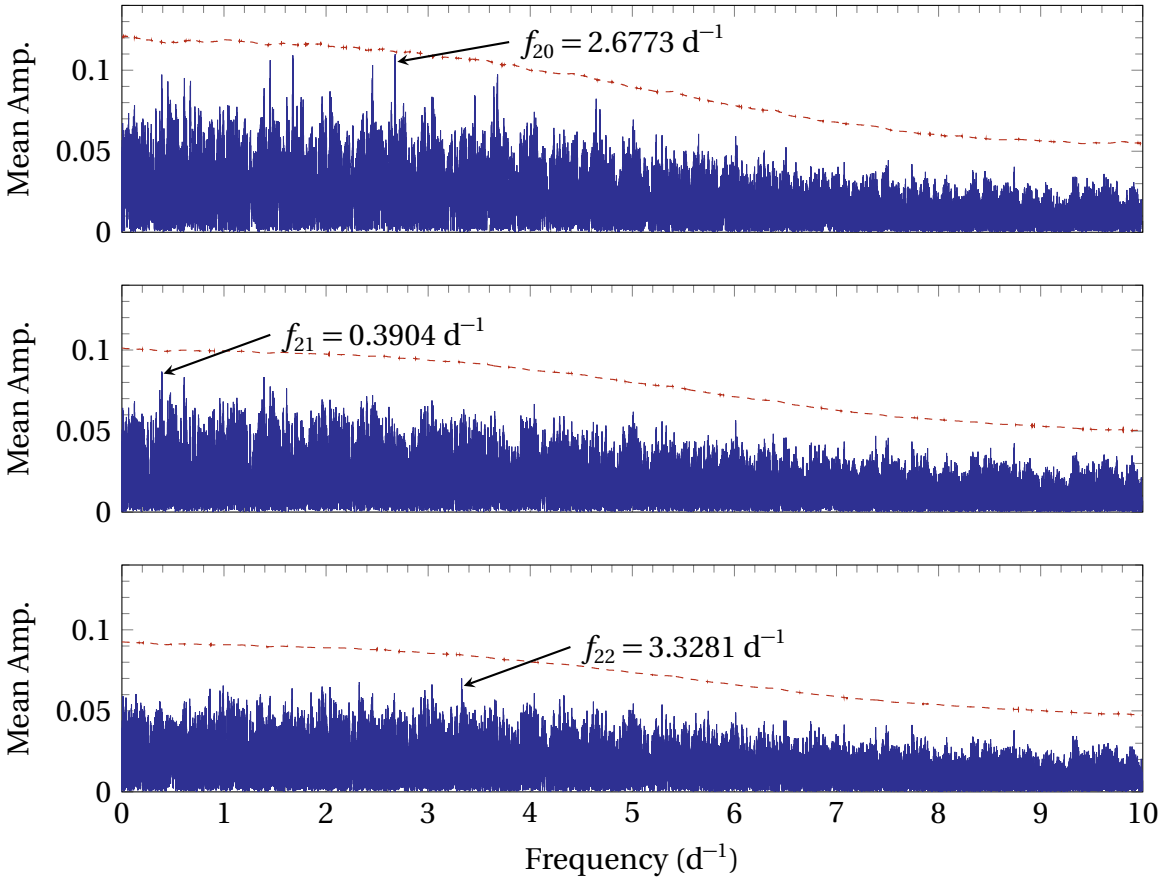

Figure B.6: The first-moment Lomb-Scargle periodograms of HD 182640 computed by FAMIAS, showcasing the three frequencies (f_{20} to f_{22}) detected through the first moment of the moment method. The dashed red line represents the significance level at a signal-to-noise ratio of 4.

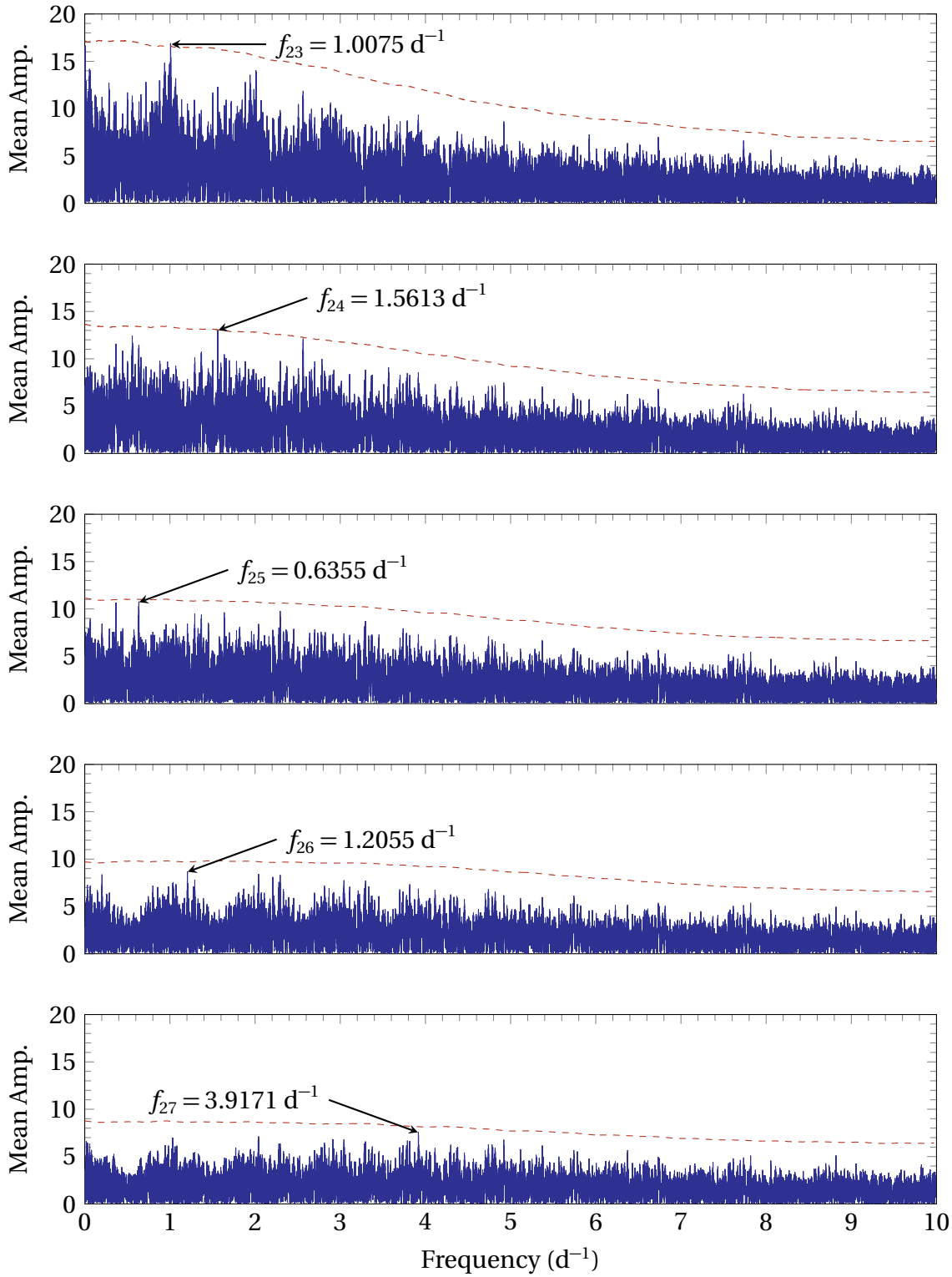

Figure B.7: The second-moment Lomb-Scargle periodograms of HD 182640 computed by FAMIAS, showcasing the five frequencies (f_{23} to f_{27}) detected through the second moment of the moment method. The dashed red line represents the significance level at a signal-to-noise ratio of 4.

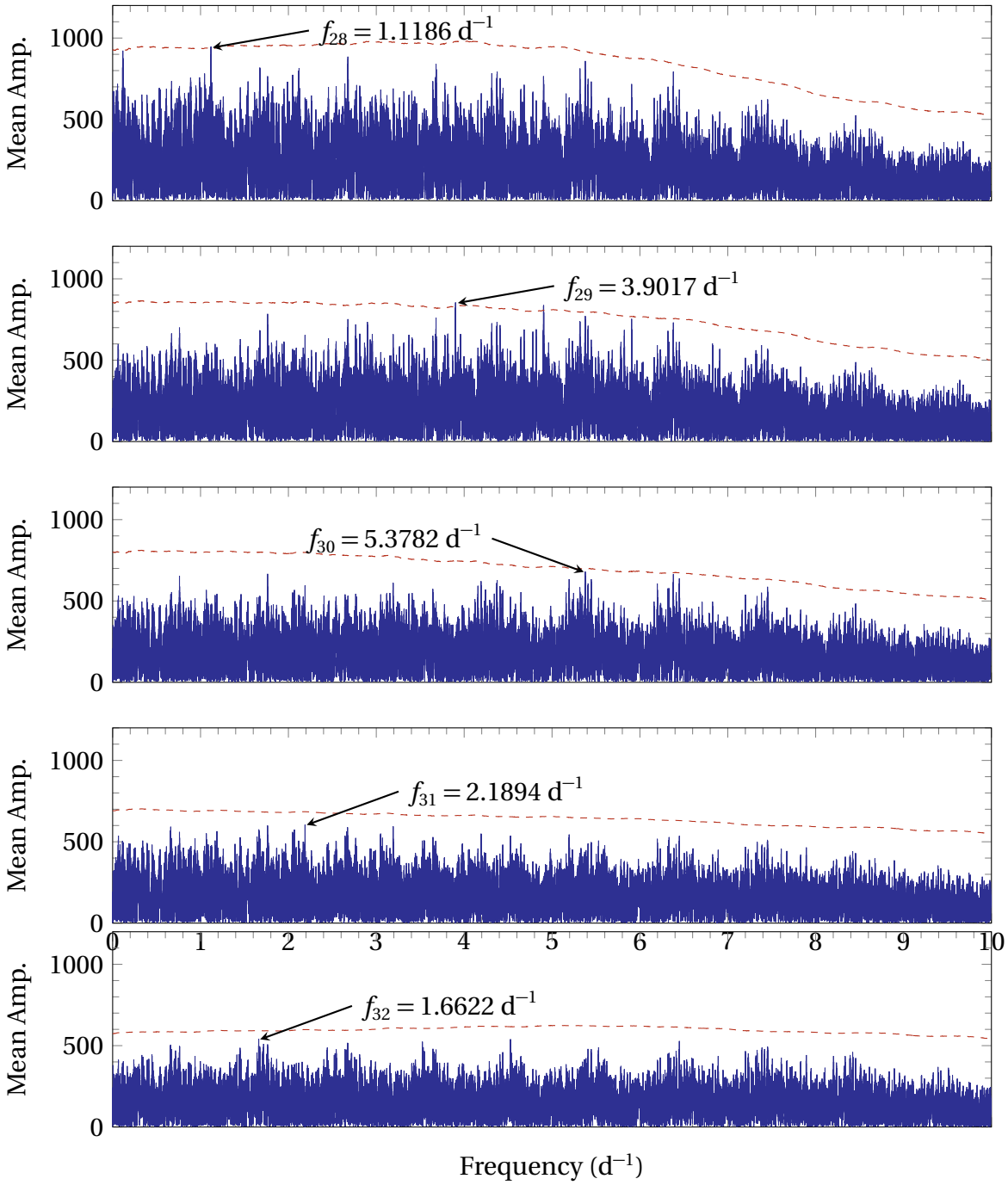

Figure B.8: The third-moment Lomb-Scargle periodograms of HD 182640 computed by FAMIAS, showcasing the five frequencies (f_{28} to f_{32}) detected through the third moment of the moment method. The dashed red line represents the significance level at a signal-to-noise ratio of 4. (Referenced on page 63, 75, 127.)

Frequencies Removed	σ	**% Reduction in σ**
None	0.001384	0
f_1	0.001303	5.8
f_1+f_2	0.001232	11.0
$f_1+f_2+f_3$	0.001187	14.3
$f_1+f_2+f_3+f_4$	0.001146	17.2
$f_1+f_2+f_3+f_4+f_5$	0.001104	20.2
$f_1+f_2+f_3+f_4+f_5+f_6$	0.001074	22.4
$f_1+f_2+f_3+f_4+f_5+\cdots+f_7$	0.001042	24.7
$f_1+f_2+f_3+f_4+f_5+\cdots+f_8$	0.001002	27.6
$f_1+f_2+f_3+f_4+f_5+\cdots+f_9$	0.000971	29.9
$f_1+f_2+f_3+f_4+f_5+\cdots+f_{10}$	0.000946	31.6
$f_1+f_2+f_3+f_4+f_5+\cdots+f_{11}$	0.000923	33.3
$f_1+f_2+f_3+f_4+f_5+\cdots+f_{12}$	0.000896	35.3
$f_1+f_2+f_3+f_4+f_5+\cdots+f_{13}$	0.000872	37.0
$f_1+f_2+f_3+f_4+f_5+\cdots+f_{14}$	0.000853	38.3
$f_1+f_2+f_3+f_4+f_5+\cdots+f_{15}$	0.000838	39.4
$f_1+f_2+f_3+f_4+f_5+\cdots+f_{16}$	0.000822	40.6
$f_1+f_2+f_3+f_4+f_5+\cdots+f_{17}$	0.000806	41.7
$f_1+f_2+f_3+f_4+f_5+\cdots+f_{18}$	0.000791	42.9

Table B.1: The reduction in the standard deviation across the line profiles of HD 182640 from successive prewhitening of the pulsation frequencies. The combination of these frequencies explains 42.9% of the variation across the line profiles of HD 182640. (Referenced on page 66, 127.)

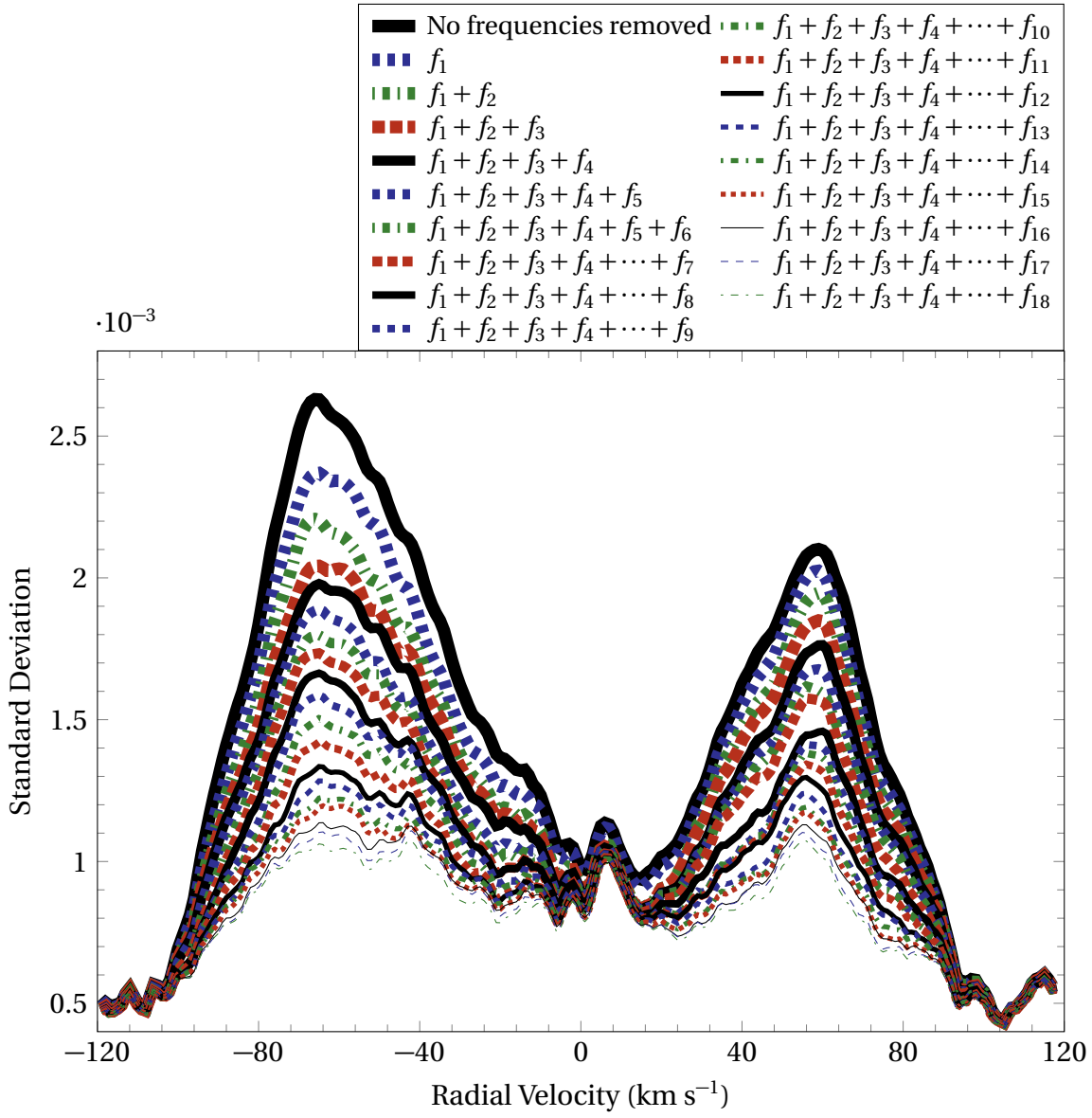

Figure B.9: Reduction in the standard deviation across the line profiles of HD 182640 due to the progressive prewhitening of the 18 identified pulsation frequencies. These 18 frequencies explain 42.9% of the variation across the line profiles of HD 182640. (Referenced on page 66, 127.)

C Additional Plots and Tables for HD 3112

This appendix chapter comprises various plots and tables pertaining to HD 3112:

- The pixel-by-pixel mean Lomb-Scargle periodograms of the 13 d^{-1} to 25 d^{-1} frequency range (Figures C.1 to C.3).
- The zeroth- to third-moment Lomb-Scargle periodograms of the 13 d^{-1} to 25 d^{-1} frequency range (Figures C.4 to C.10).
- The pixel-by-pixel mean Lomb-Scargle periodograms of the 0 d^{-1} to 3 d^{-1} frequency range (Figure C.11).
- The zeroth- to third-moment Lomb-Scargle periodograms of the 0 d^{-1} to 3 d^{-1} frequency range (Figures C.12 to C.16).
- The reduction in the standard deviation across the line profiles of HD 3112 due to progressive prewhitening of pulsation frequencies (Table C.1) and a graphical representation of this process (Figure C.17).
- The amplitude and phase profiles of the best-fit mode of $f_2 = 18.0661$ d^{-1} of HD 3112 (Figure C.18).

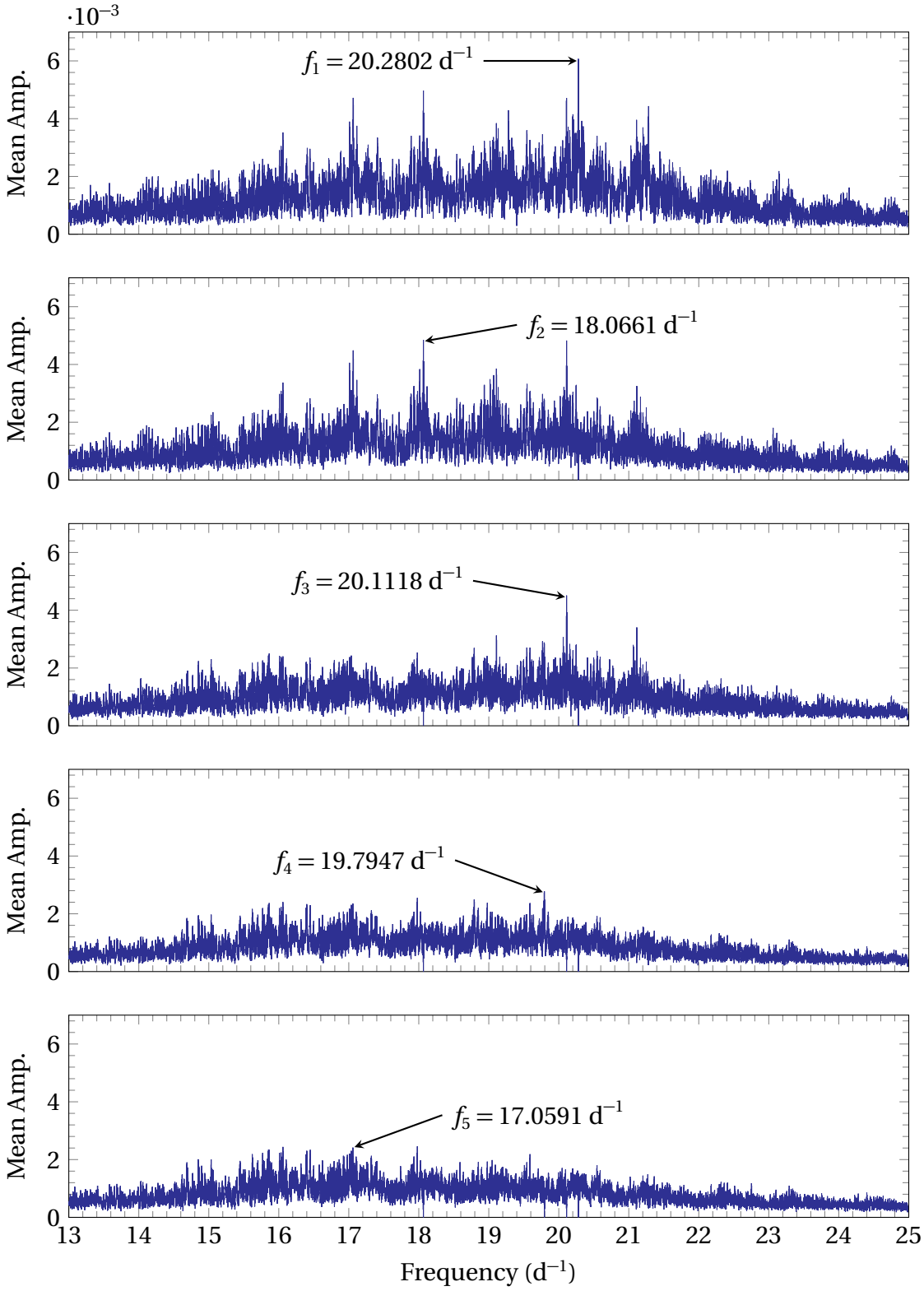

Figure C.1: The pixel-by-pixel mean Lomb-Scargle periodograms of the 13 d^{-1} to 25 d^{-1} frequency range of HD 3112 computed by FAMIAS, showcasing the first batch of five frequencies (f_1 to f_5) detected through the pixel-by-pixel method. (Referenced on page 83, 139.)

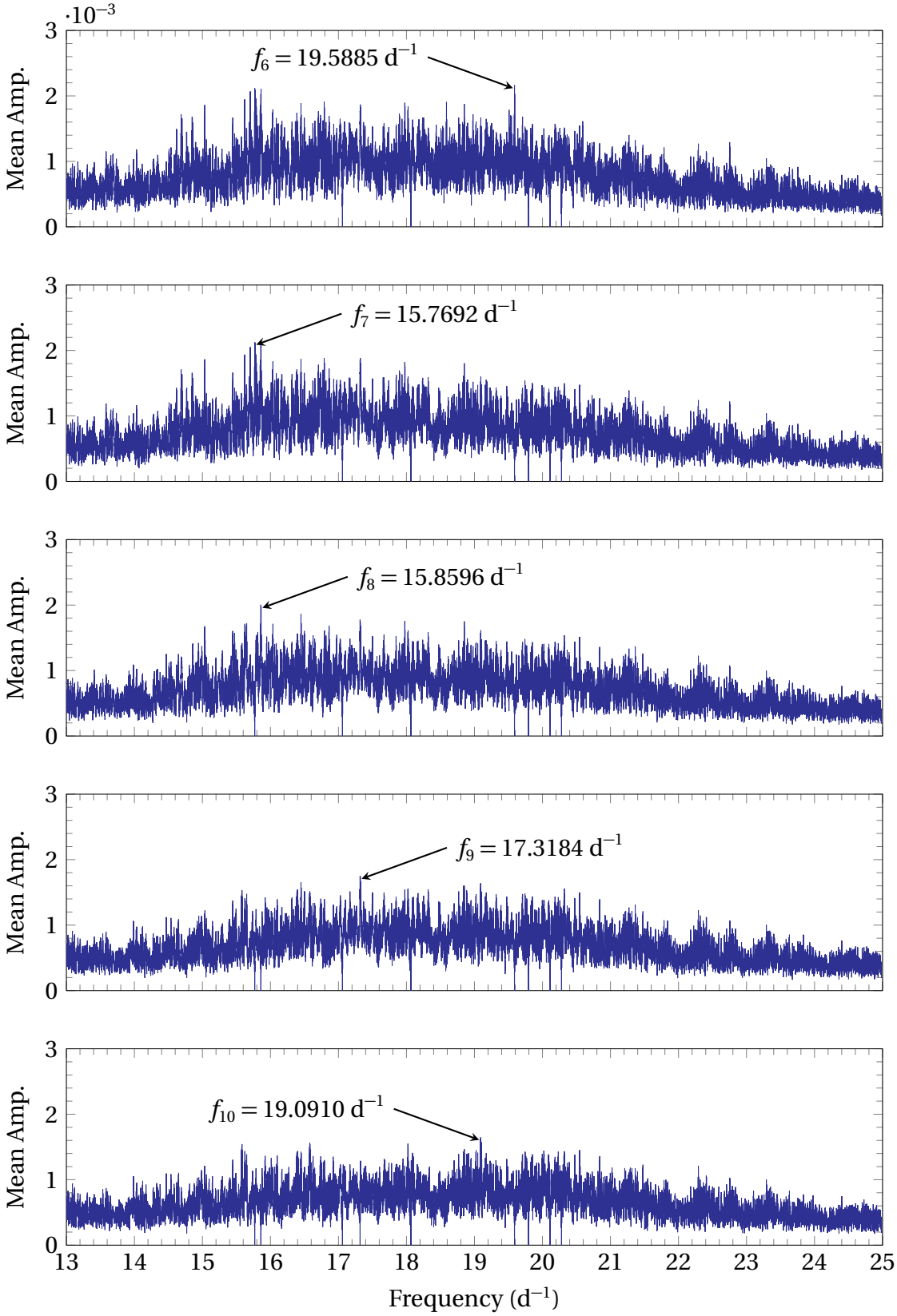

Figure C.2: The pixel-by-pixel mean Lomb-Scargle periodograms of the 13 d^{-1} to 25 d^{-1} frequency range of HD 3112 computed by FAMIAS, showcasing the second batch of five frequencies (f_6 to f_{10}) detected through the pixel-by-pixel method.

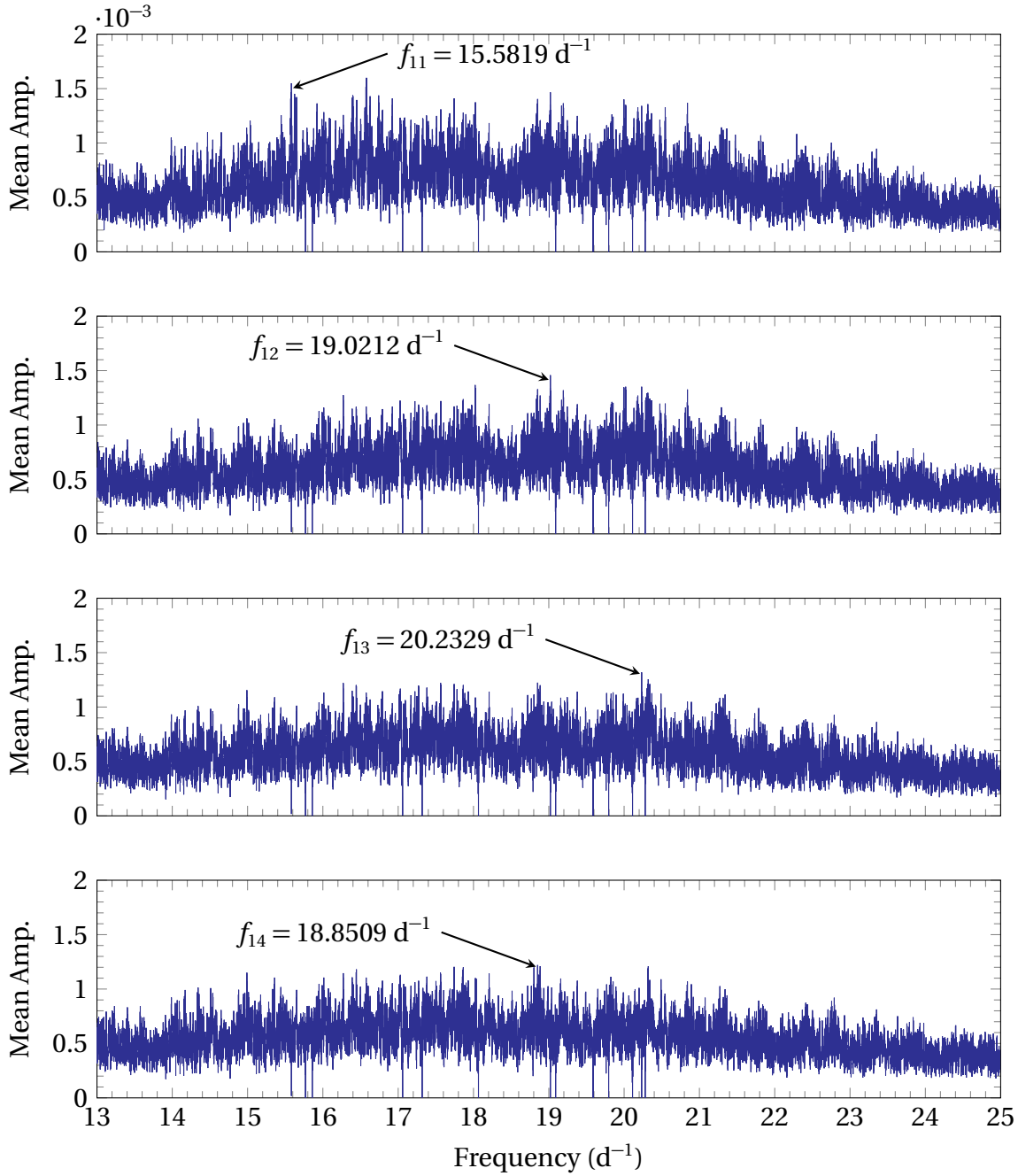

Figure C.3: The pixel-by-pixel mean Lomb-Scargle periodograms of the 13 d^{-1} to 25 d^{-1} frequency range of HD 3112 computed by FAMIAS, showcasing the third batch of four frequencies (f_{11} to f_{14}) detected through the pixel-by-pixel method. (Referenced on page 83, 139.)

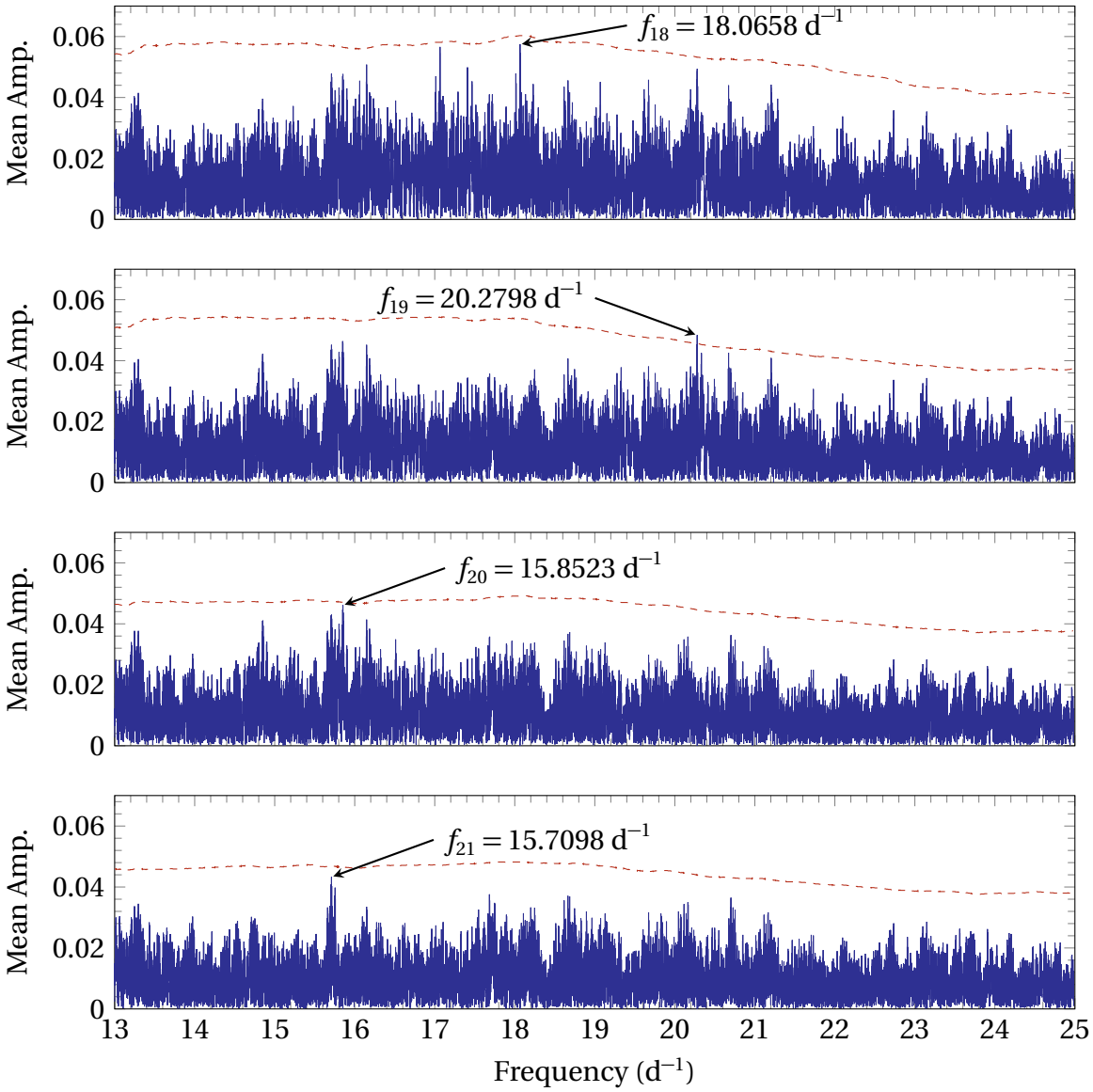

Figure C.4: The zeroth-moment Lomb-Scargle periodograms of the 13 d^{-1} to 25 d^{-1} frequency range of HD 3112 computed by FAMIAS, showcasing the four frequencies (f_{18} to f_{21}) detected through the zeroth moment of the moment method. The dashed red line represents the significance level at a signal-to-noise ratio of 4. (Referenced on page 83, 139.)

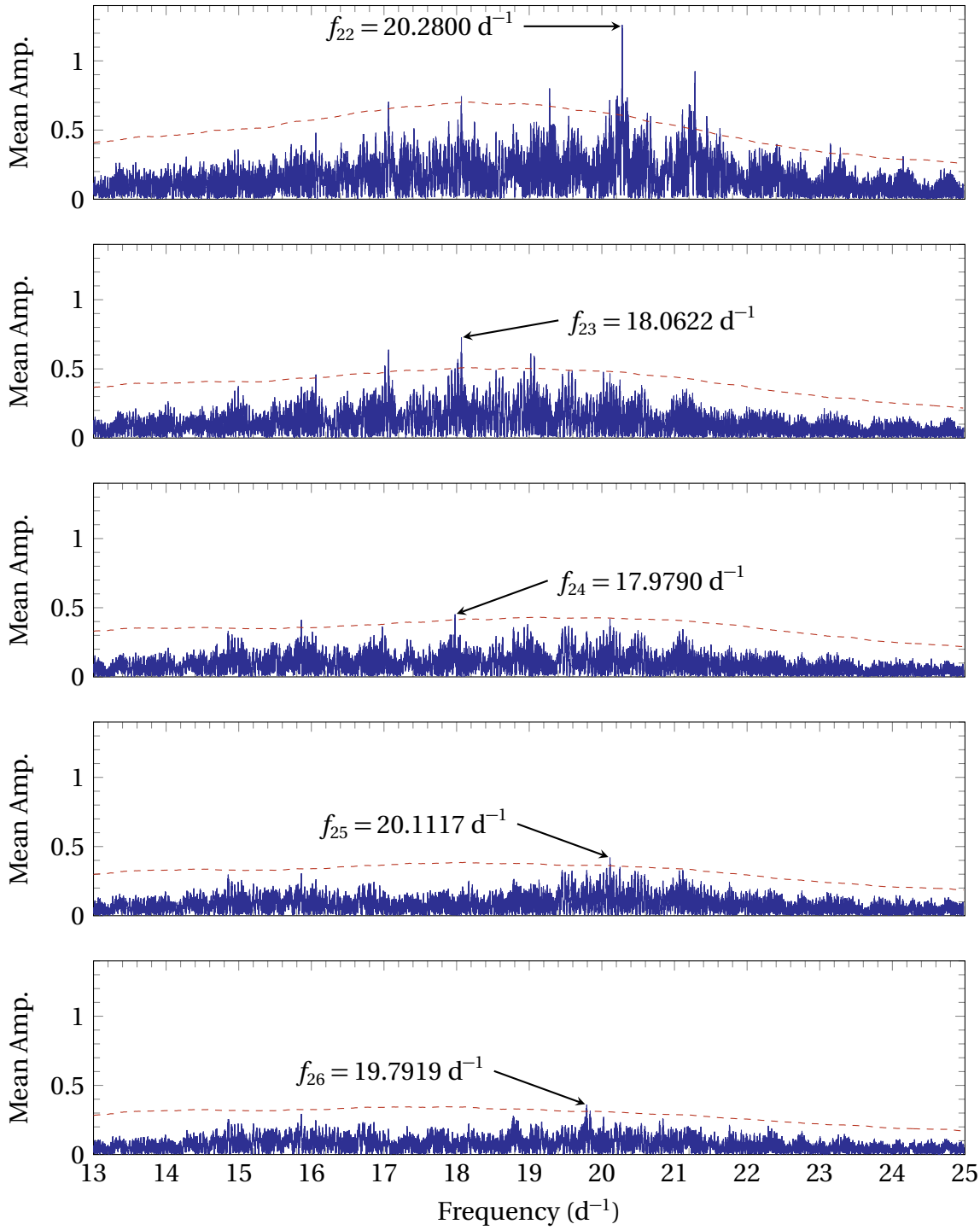

Figure C.5: The first-moment Lomb-Scargle periodograms of the 13 d^{-1} to 25 d^{-1} frequency range of HD 3112 computed by FAMIAS, showcasing the first batch of five frequencies (f_{22} to f_{26}) detected through the first moment of the moment method. The dashed red line represents the significance level at a signal-to-noise ratio of 4.

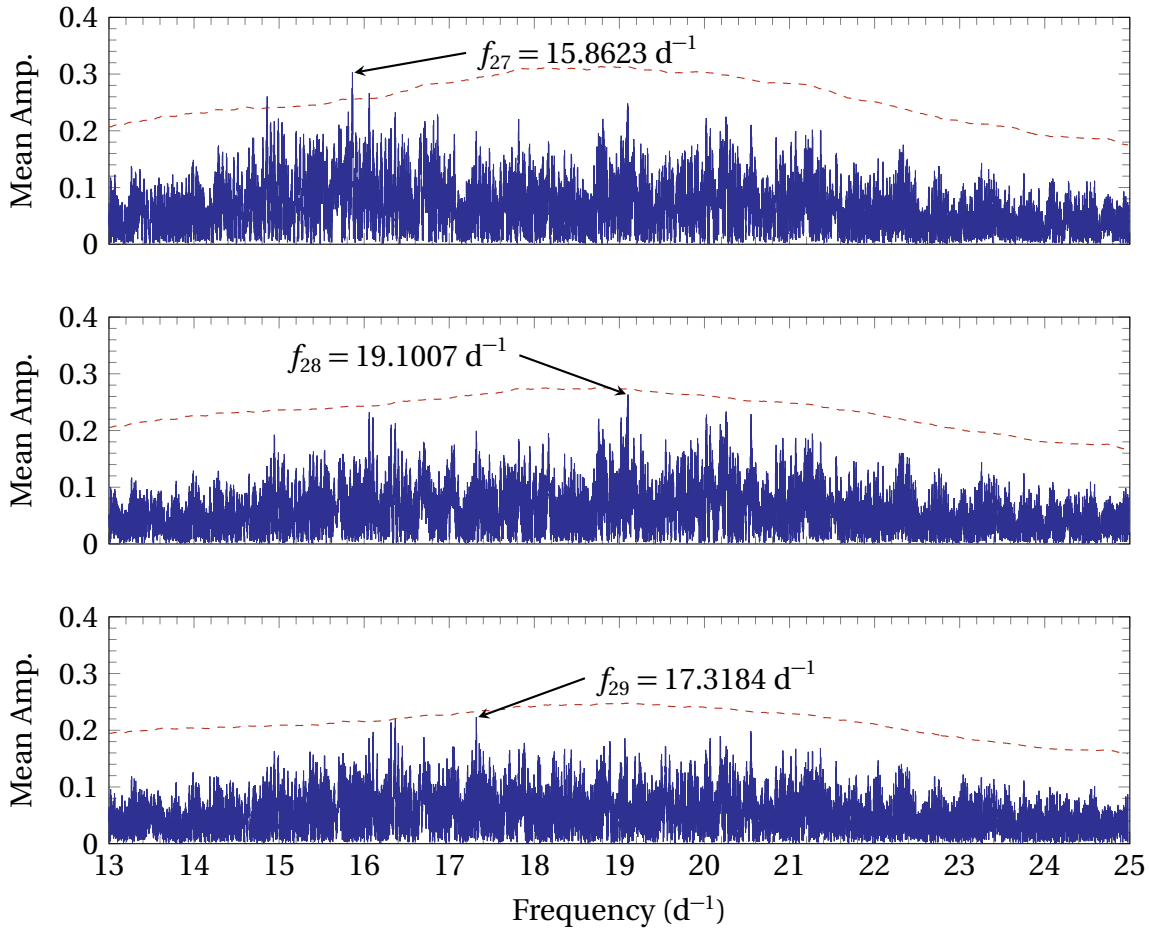

Figure C.6: The first-moment Lomb-Scargle periodograms of the 13 d^{-1} to 25 d^{-1} frequency range of HD 3112 computed by FAMIAS, showcasing the second batch of three frequencies (f_{27} to f_{29}) detected through the first moment of the moment method. The dashed red line represents the significance level at a signal-to-noise ratio of 4.

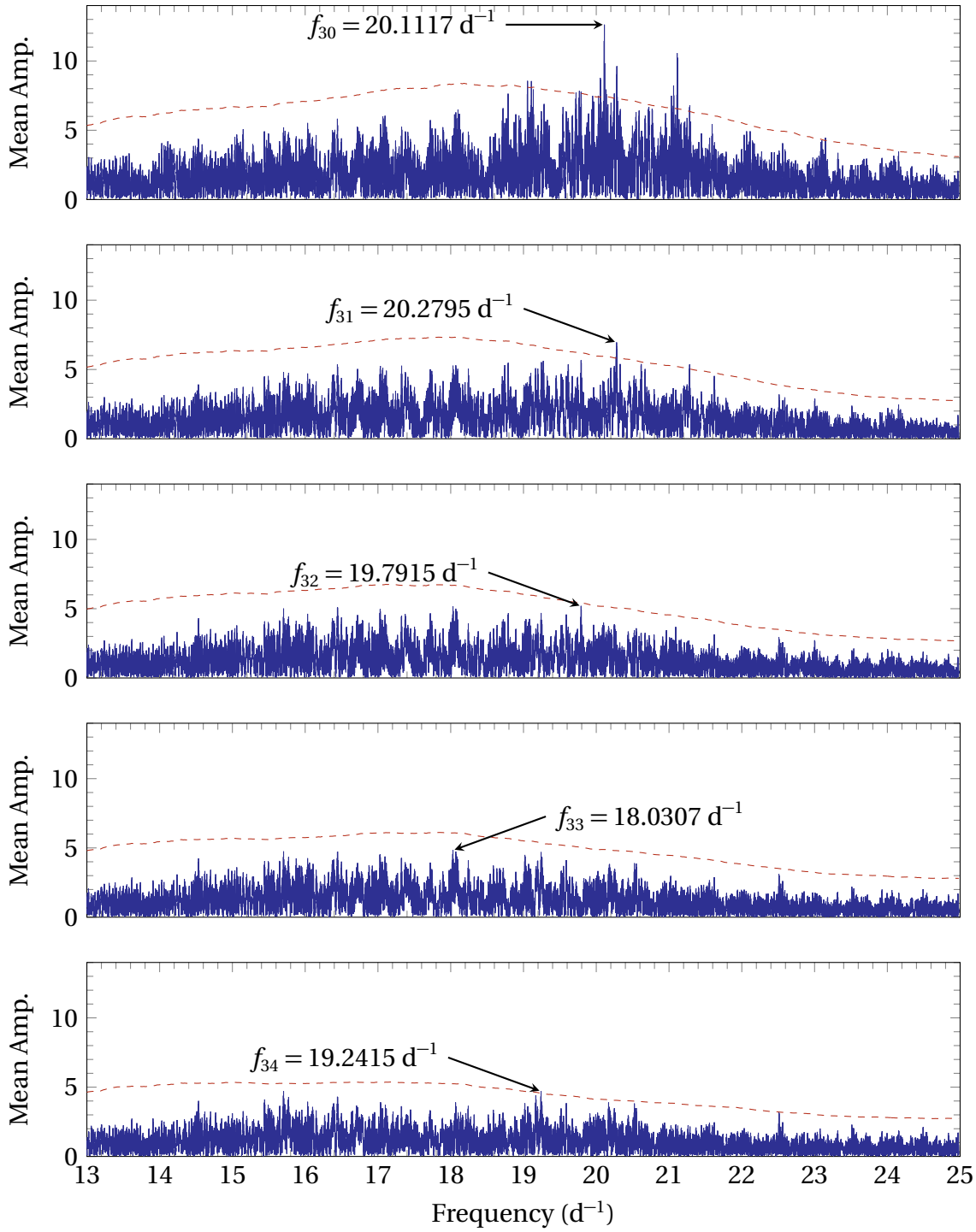

Figure C.7: The second-moment Lomb-Scargle periodograms of the 13 d^{-1} to 25 d^{-1} frequency range of HD 3112 computed by FAMIAS, showcasing the first batch of five frequencies (f_{30} to f_{34}) detected through the second moment of the moment method. The dashed red line represents the significance level at a signal-to-noise ratio of 4.

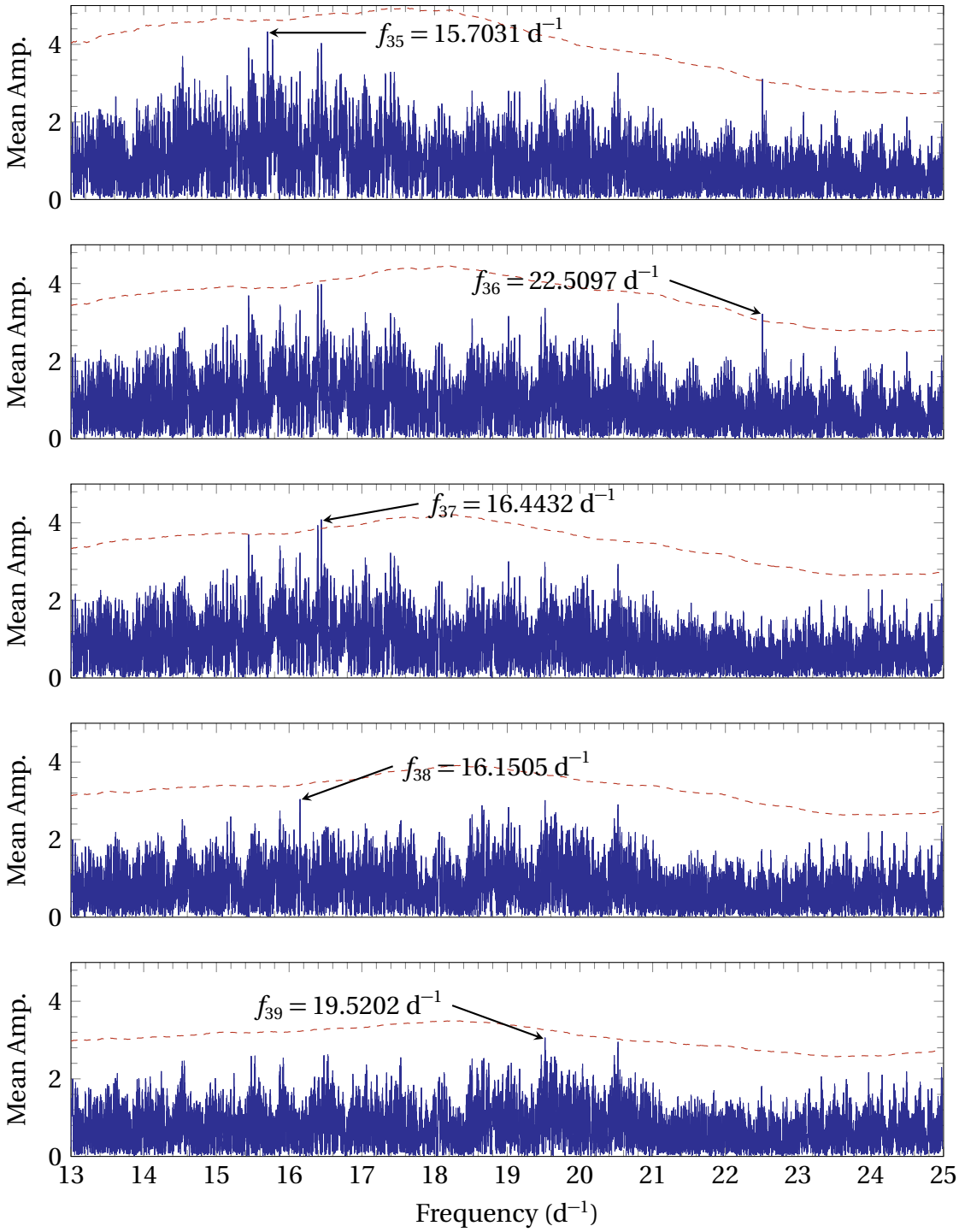

Figure C.8: The second-moment Lomb-Scargle periodograms of the 13 d^{-1} to 25 d^{-1} frequency range of HD 3112 computed by FAMIAS, showcasing the second batch of five frequencies (f_{35} to f_{39}) detected through the second moment of the moment method. The dashed red line represents the significance level at a signal-to-noise ratio of 4.

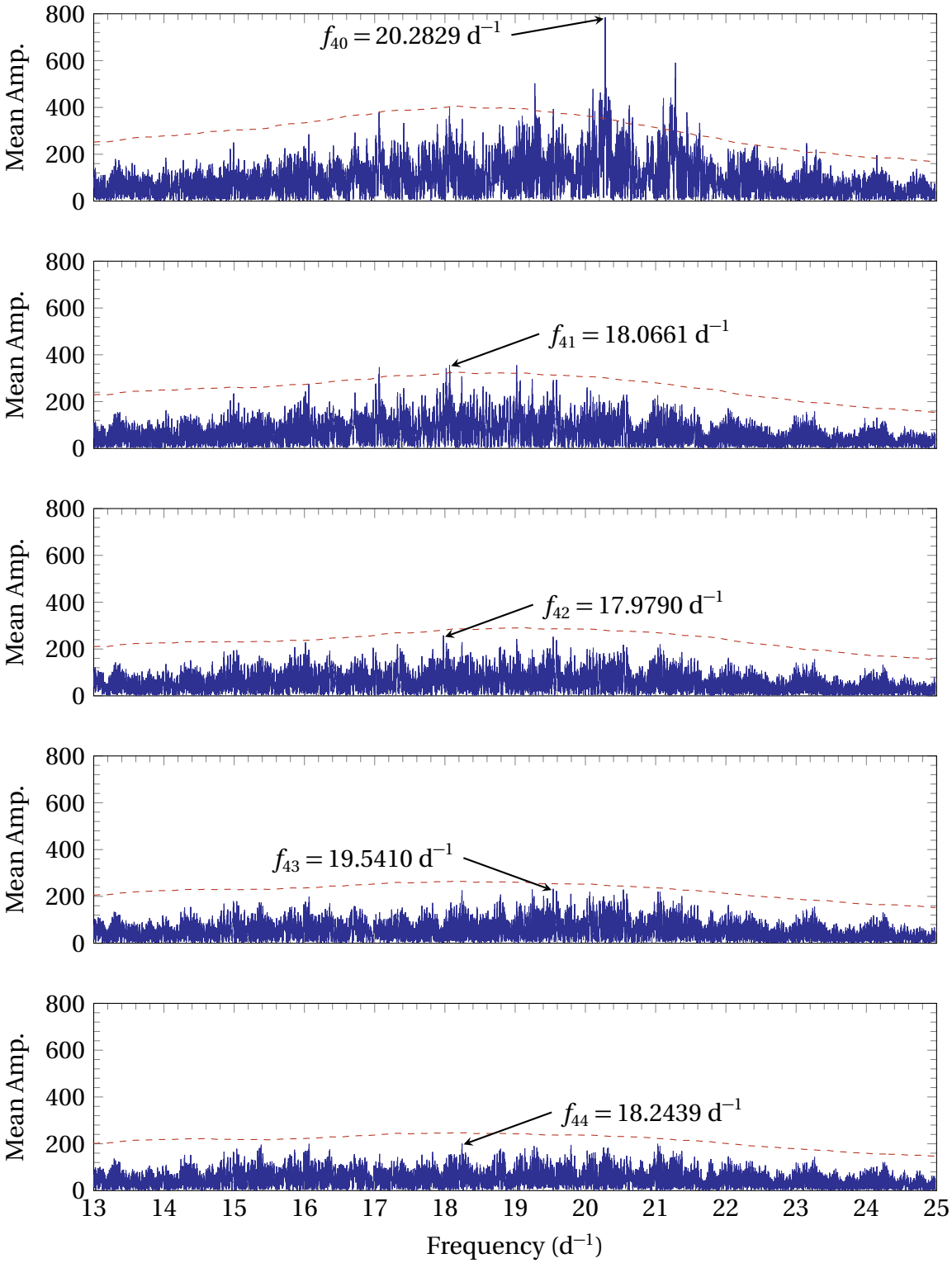

Figure C.9: The third-moment Lomb-Scargle periodograms of the 13 d^{-1} to 25 d^{-1} frequency range of HD 3112 computed by FAMIAS, showcasing the first batch of five frequencies (f_{40} to f_{44}) detected through the third moment of the moment method. The dashed red line represents the significance level at a signal-to-noise ratio of 4.

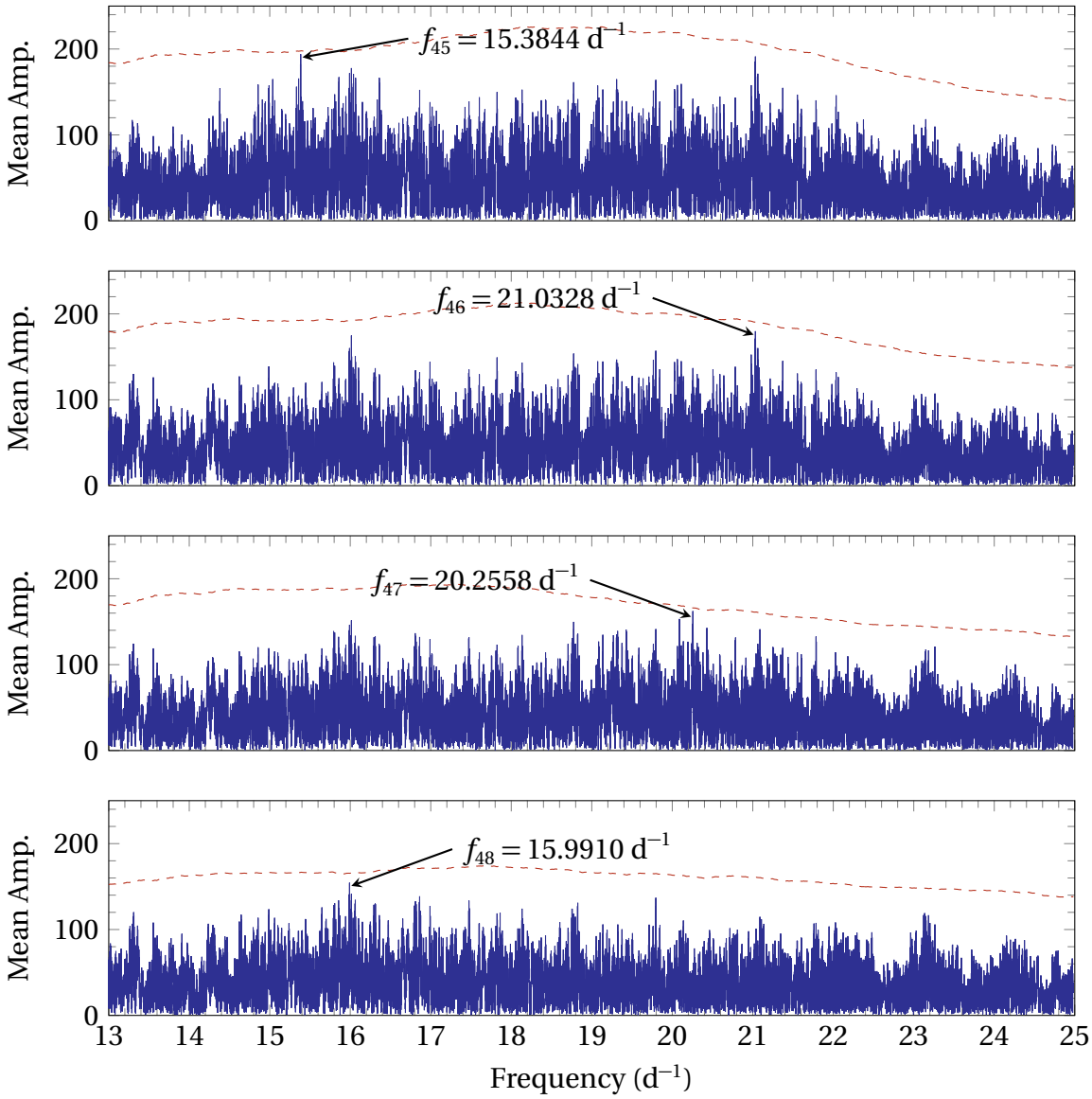

Figure C.10: The third-moment Lomb-Scargle periodograms of the 13 d^{-1} to 25 d^{-1} frequency range of HD 3112 computed by FAMIAS, showcasing the second batch of four frequencies (f_{45} to f_{48}) detected through the third moment of the moment method. The dashed red line represents the significance level at a signal-to-noise ratio of 4. (Referenced on page 83, 139.)

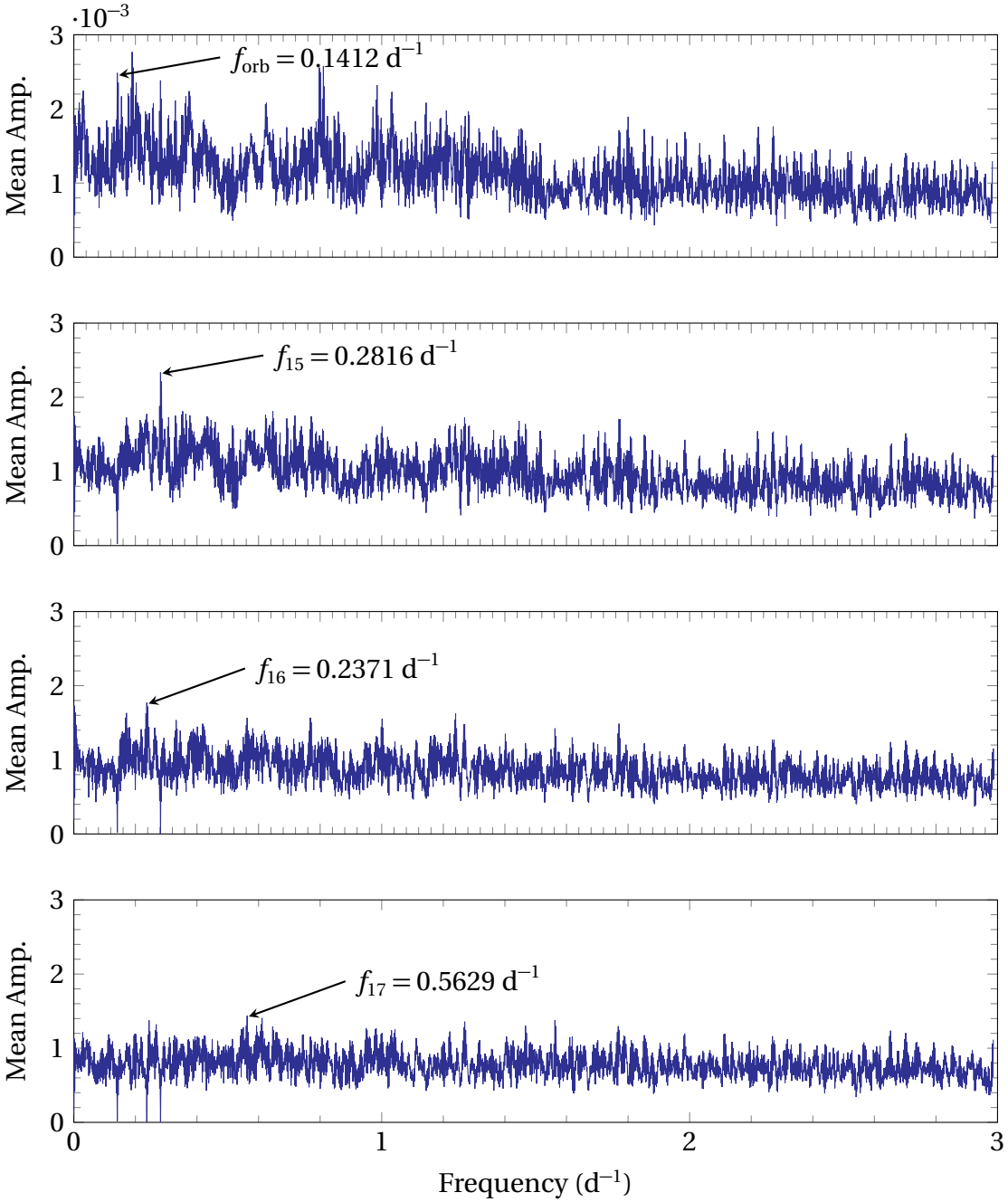

Figure C.11: The pixel-by-pixel mean Lomb-Scargle periodograms of the 0 d^{-1} to 3 d^{-1} frequency range of HD 3112 computed by FAMIAS, showcasing the four frequencies (f_{16} to f_{18} and the binary orbit frequency f_{orb}) detected through the pixel-by-pixel method. (Referenced on page 85, 87, 87, 139.)

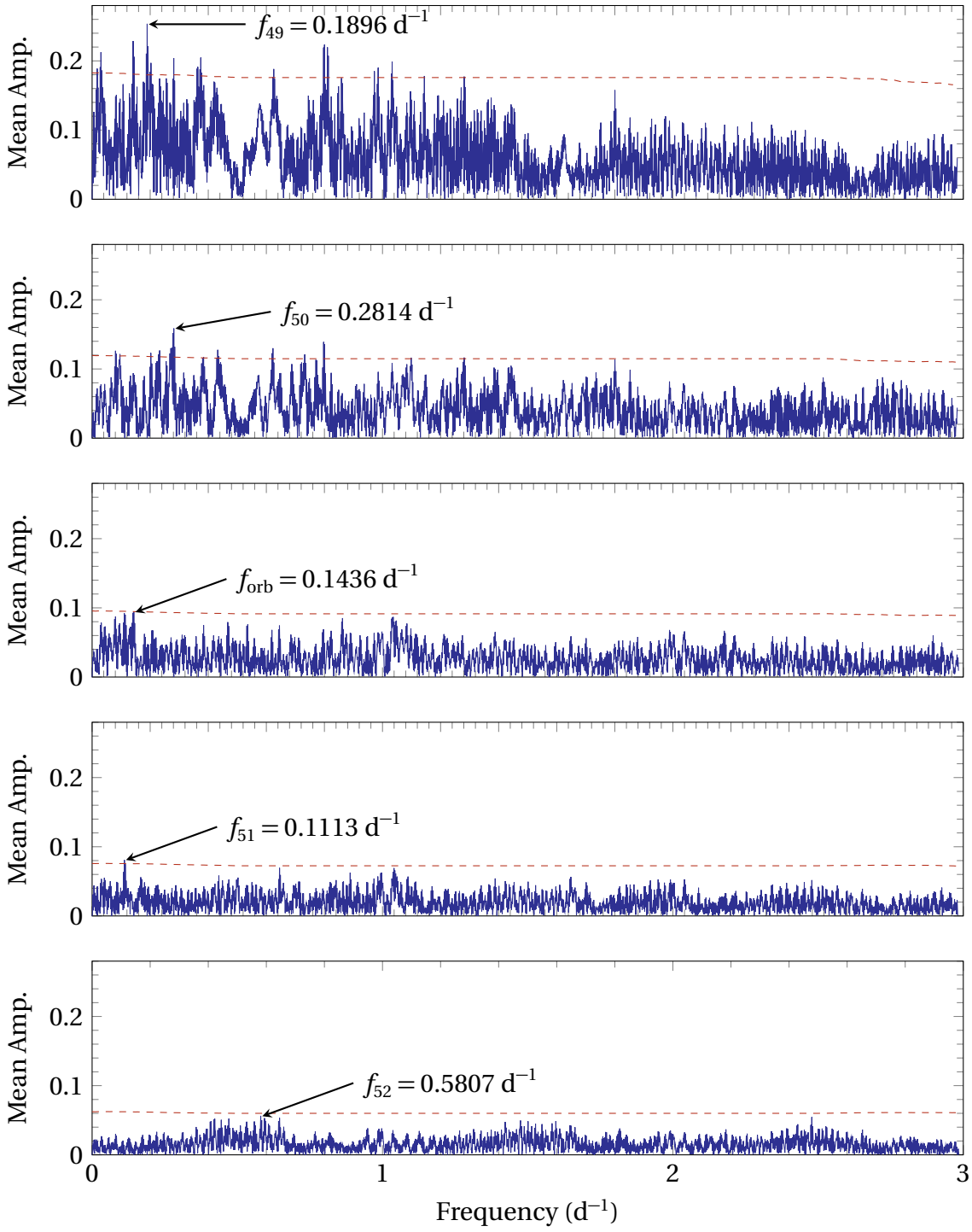

Figure C.12: The zeroth-moment Lomb-Scargle periodograms of the 0 d^{-1} to 3 d^{-1} frequency range of HD 3112 computed by FAMIAS, showcasing the first batch of five frequencies (f_{49} to f_{52} and the binary orbit frequency f_{orb}) detected through the zeroth moment of the moment method. The dashed red line represents the significance level at a signal-to-noise ratio of 4. (Referenced on page 85, 87, 87, 139.)

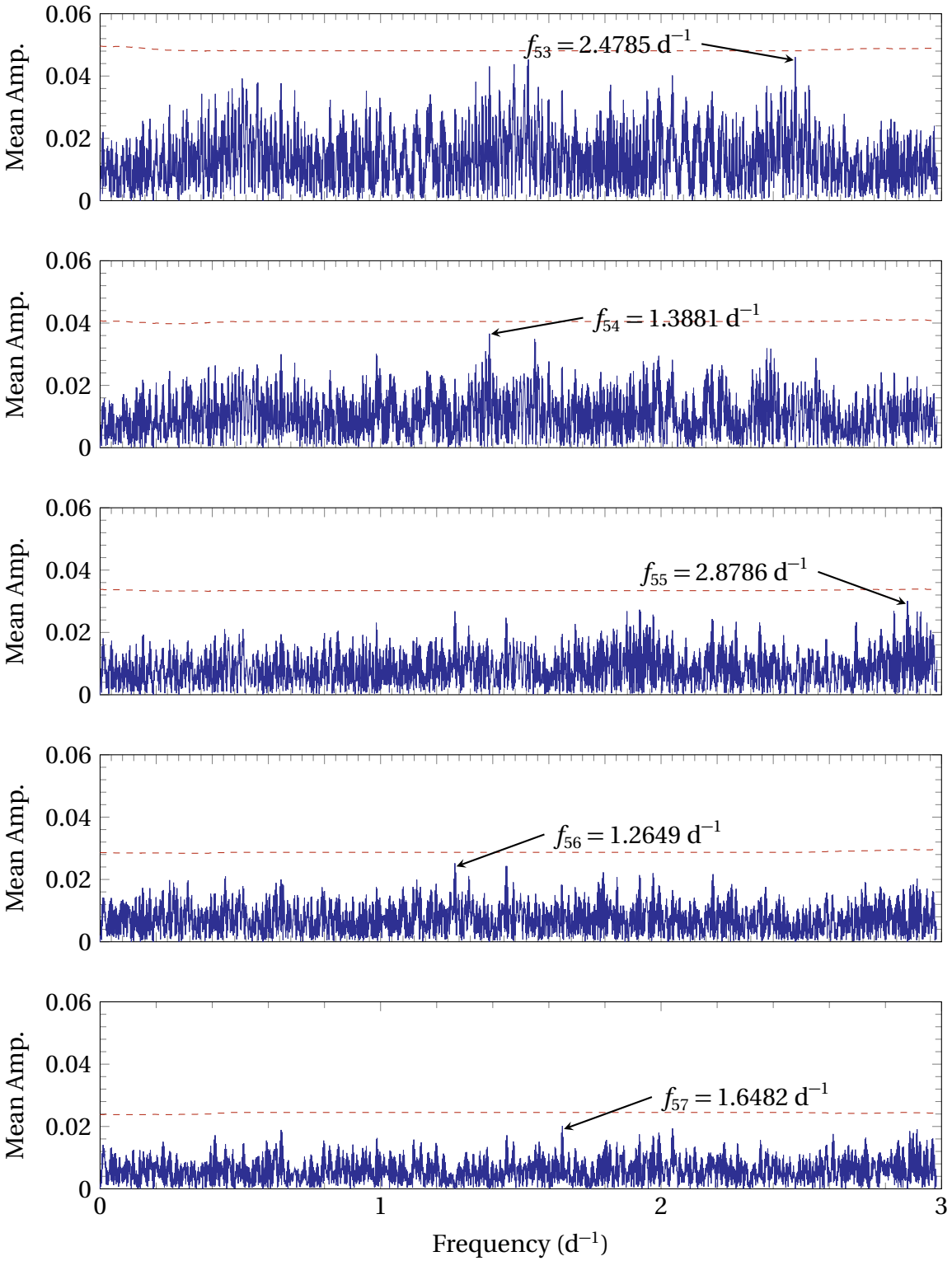

Figure C.13: The zeroth-moment Lomb-Scargle periodograms of the 0 d^{-1} to 3 d^{-1} frequency range of HD 3112 computed by FAMIAS, showcasing the second batch of five frequencies (f_{53} to f_{57}) detected through the zeroth moment of the moment method. The dashed red line represents the significance level at a signal-to-noise ratio of 4.

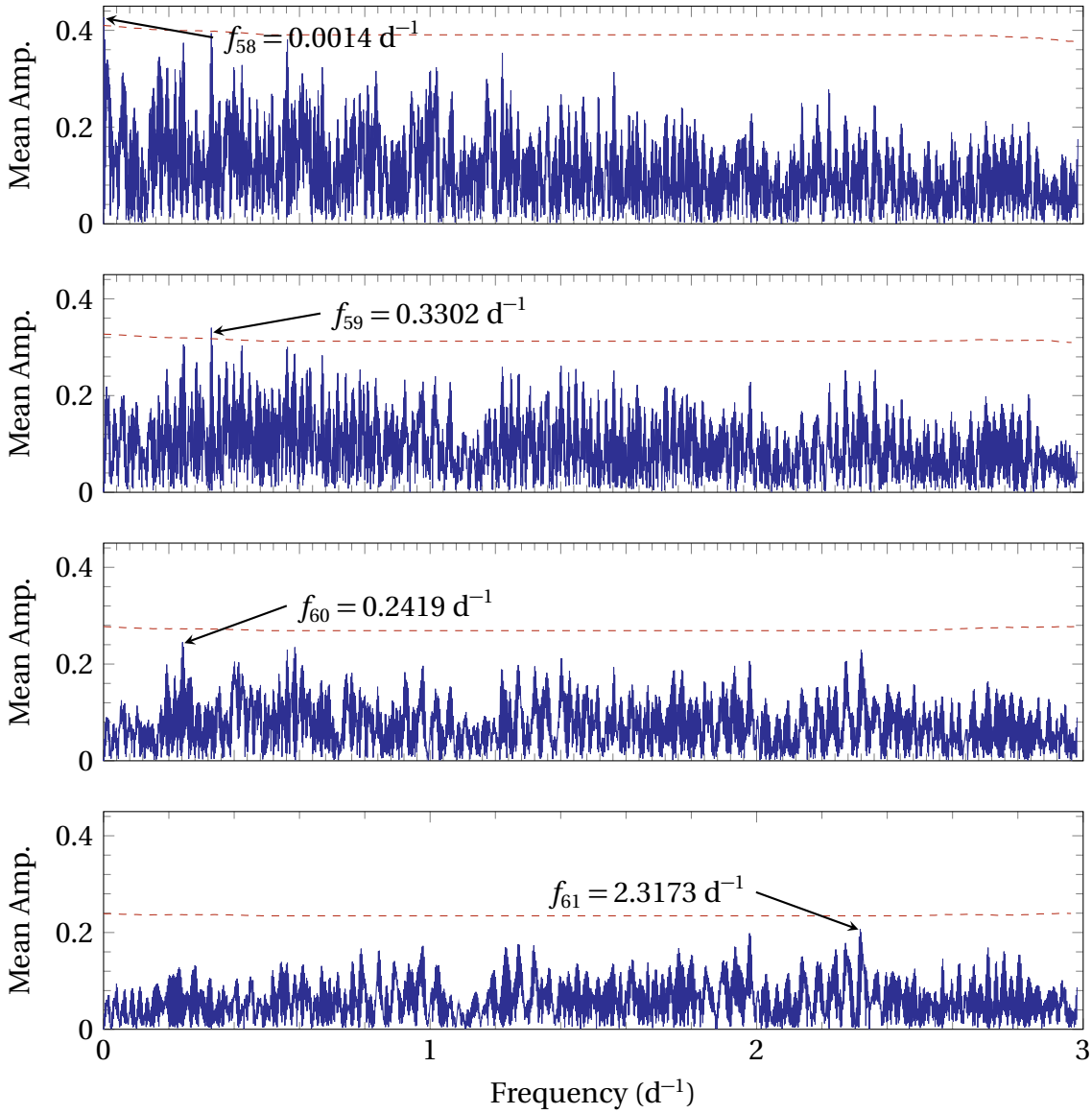

Figure C.14: The first-moment Lomb-Scargle periodograms of the 0 d^{-1} to 3 d^{-1} frequency range of HD 3112 computed by FAMIAS, showcasing the four frequencies (f_{58} to f_{61}) detected through the first moment of the moment method. The dashed red line represents the significance level at a signal-to-noise ratio of 4.

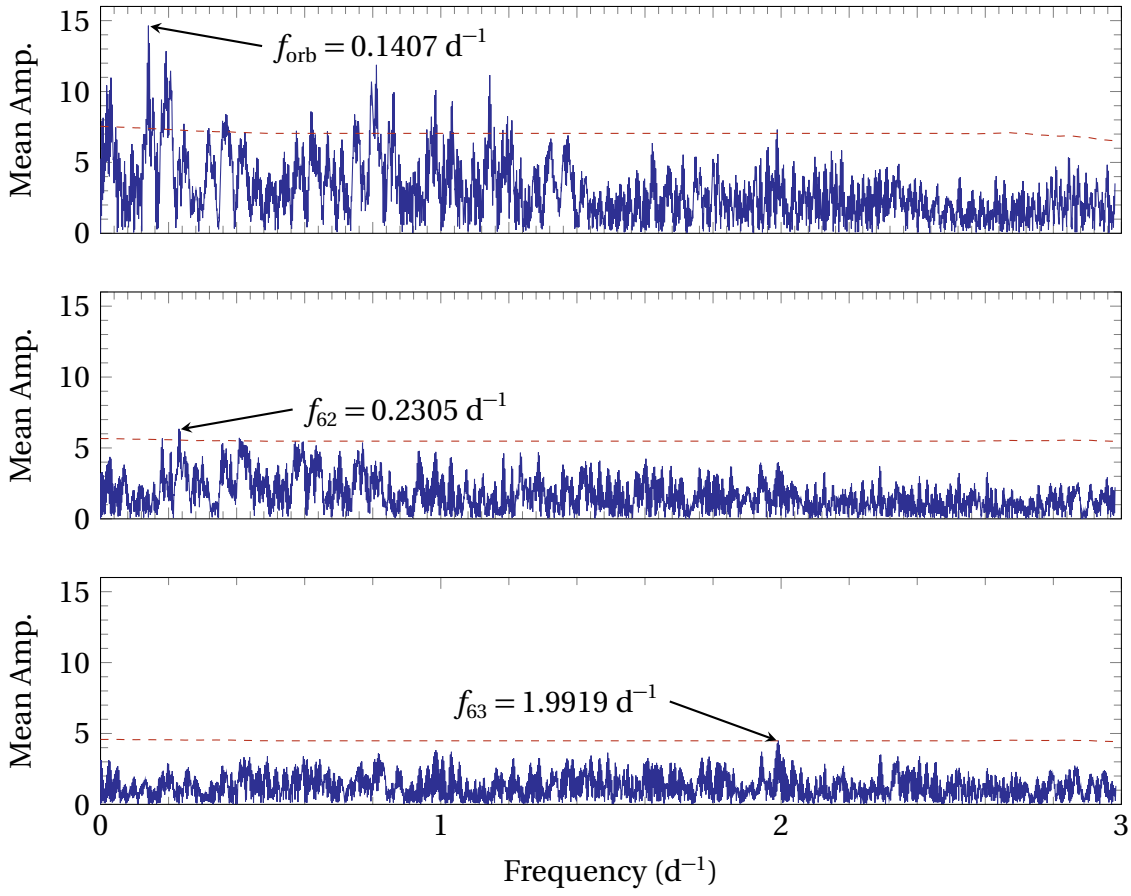

Figure C.15: The second-moment Lomb-Scargle periodograms of the 0 d^{-1} to 3 d^{-1} frequency range of HD 3112 computed by FAMIAS, showcasing the three frequencies (f_{62}, f_{63} and the binary orbit frequency f_{orb}) detected through the second moment of the moment method. The dashed red line represents the significance level at a signal-to-noise ratio of 4.

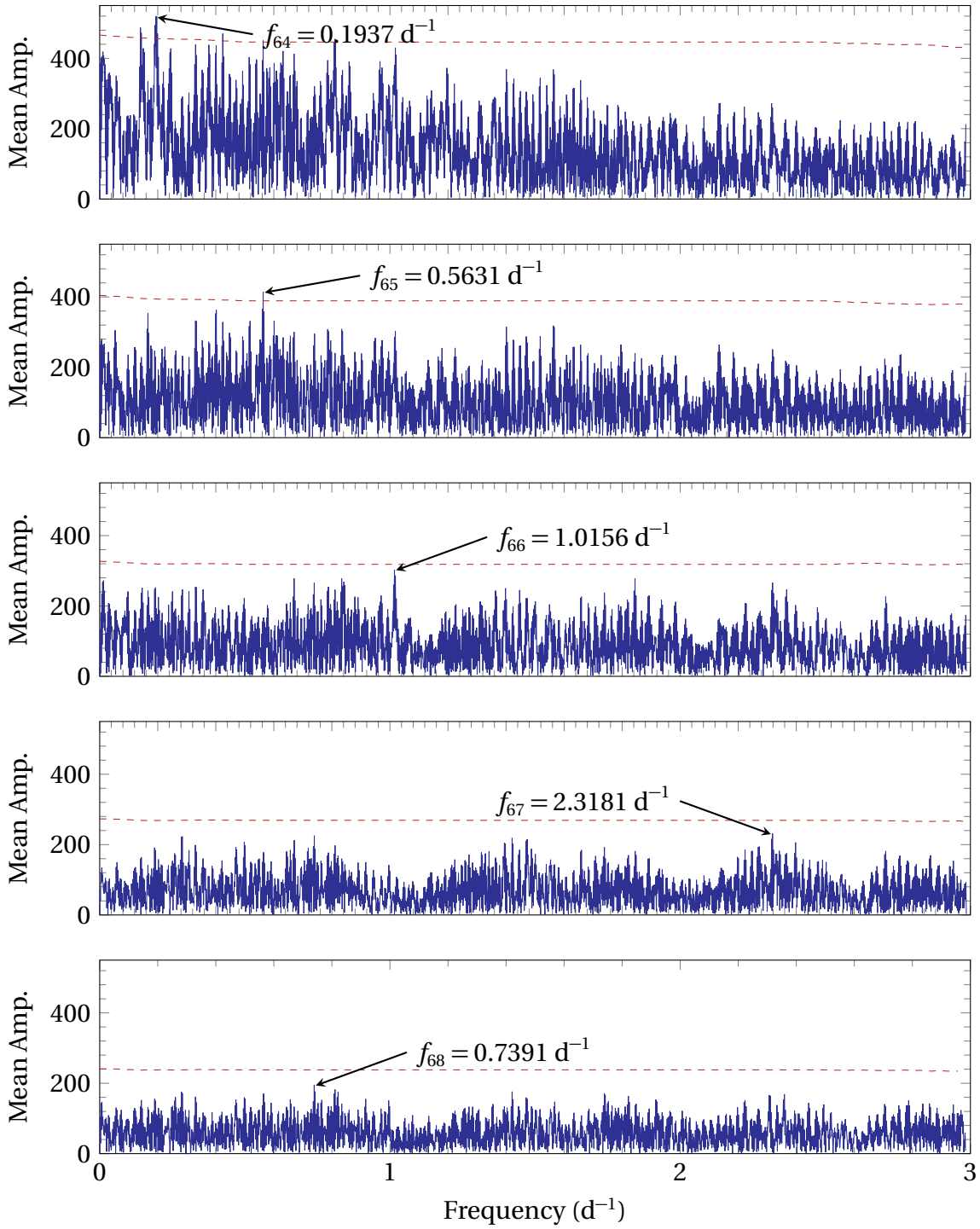

Figure C.16: The third-moment Lomb-Scargle periodograms of the 0 d^{-1} to 3 d^{-1} frequency range of HD 3112 computed by FAMIAS, showcasing the five frequencies (f_{64} to f_{68}) detected through the third moment of the moment method. The dashed red line represents the significance level at a signal-to-noise ratio of 4. (Referenced on page 85, 139.)

Frequencies Removed	σ	**% Reduction in σ**
None	0.01107	0
f_1	0.00991	10.4
f_1+f_2	0.00918	17.0
$f_1+f_2+f_3$	0.00843	23.8
$f_1+f_2+f_3+f_4$	0.00816	26.2
$f_1+f_2+f_3+f_4+f_5$	0.00789	28.7
$f_1+f_2+f_3+f_4+f_5+f_6$	0.00767	30.7
$f_1+f_2+f_3+f_4+f_5+\cdots+f_7$	0.00748	32.4
$f_1+f_2+f_3+f_4+f_5+\cdots+f_8$	0.00729	34.2
$f_1+f_2+f_3+f_4+f_5+\cdots+f_9$	0.00714	35.5
$f_1+f_2+f_3+f_4+f_5+\cdots+f_{10}$	0.00698	36.9
$f_1+f_2+f_3+f_4+f_5+\cdots+f_{11}$	0.00686	38.0
$f_1+f_2+f_3+f_4+f_5+\cdots+f_{12}$	0.00670	39.5
$f_1+f_2+f_3+f_4+f_5+\cdots+f_{13}$	0.00660	40.4
$f_1+f_2+f_3+f_4+f_5+\cdots+f_{14}$	0.00650	41.2
$f_1+f_2+f_3+f_4+f_5+\cdots+f_{15}$	0.00622	43.8
$f_1+f_2+f_3+f_4+f_5+\cdots+f_{16}$	0.00606	45.2
$f_1+f_2+f_3+f_4+f_5+\cdots+f_{17}$	0.00594	46.3

Table C.1: The reduction in the standard deviation across the line profiles of HD 3112 from successive prewhitening of the pulsation frequencies. The combination of these frequencies explains 46.3% of the variation across the line profiles of HD 3112. (Referenced on page 88, 139.)

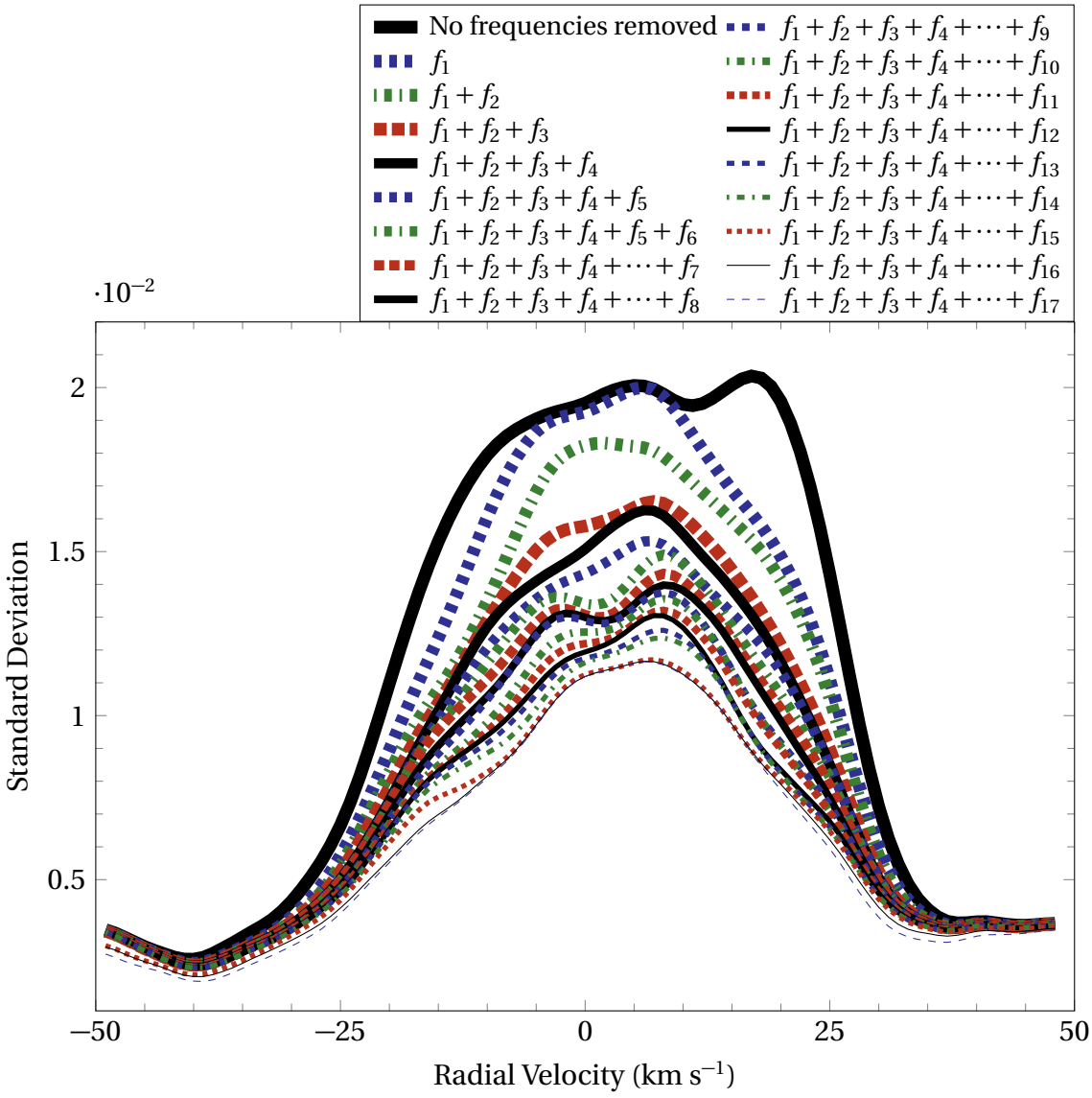

Figure C.17: Reduction in the standard deviation across the line profiles of HD 3112 due to the progressive prewhitening of the 17 identified pulsation frequencies. These 17 frequencies explain 46.3% of the variation across the line profiles of HD 3112. (Referenced on page 88, 139.)

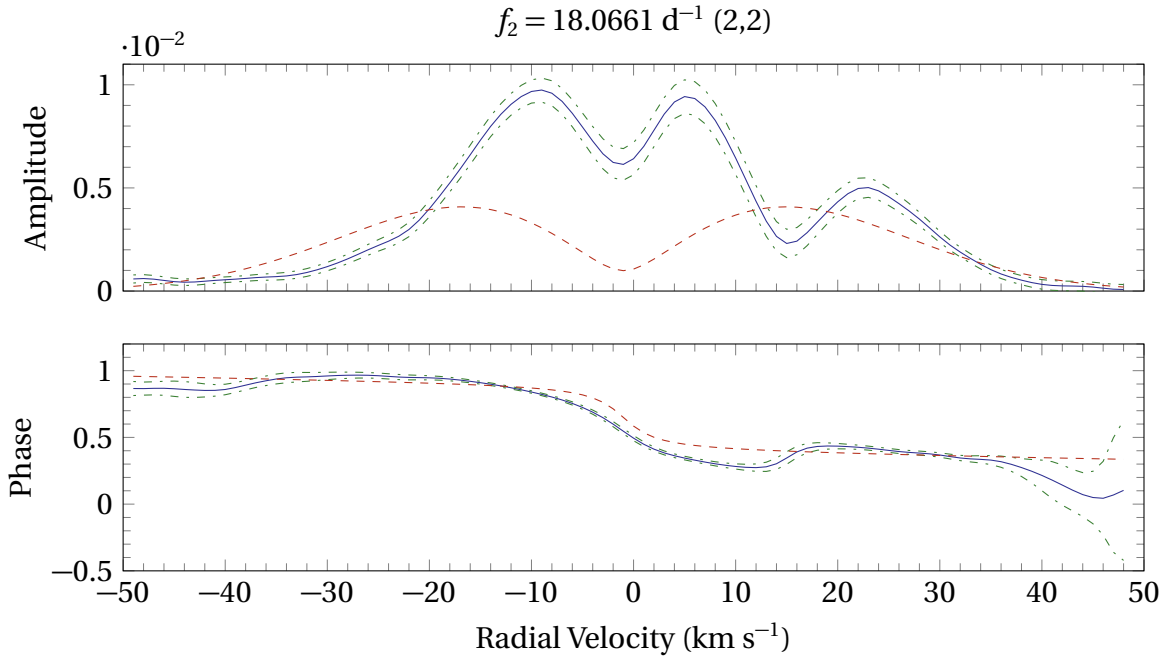

Figure C.18: The amplitude and phase profiles of the best-fit mode (2,2) of $f_2 = 18.0661$ d^{-1} of HD 3112. The solid blue lines are the observational profiles, the dash dotted green lines represent the statistical uncertainty and the dashed red lines represent the best-fit synthetic profiles. Note that although the synthetic phase profile visually matches the observational phase profiles relatively well, the synthetic amplitude profile does not. (Referenced on page 92, 139.)

D Additional Plots and Tables for HD 147787

This appendix chapter comprises various plots and tables pertaining to HD 147787:

- The pixel-by-pixel mean Lomb-Scargle periodograms (Figures D.1 and D.2).
- The zeroth- to third-moment Lomb-Scargle periodograms (Figures D.3 to D.8).
- The reduction in the standard deviation across the line profiles of HD 147787 due to progressive prewhitening of pulsation frequencies (Table D.1) and a graphical representation of this process (Figure D.9).
- The amplitude and phase profiles of the best-fit modes of $f_4 = 0.0819$ d^{-1}, $f_8 = 0.0579$ d^{-1} and $f_9 = 0.2103$ d^{-1} of HD 147787 (Figures D.10 to D.12).

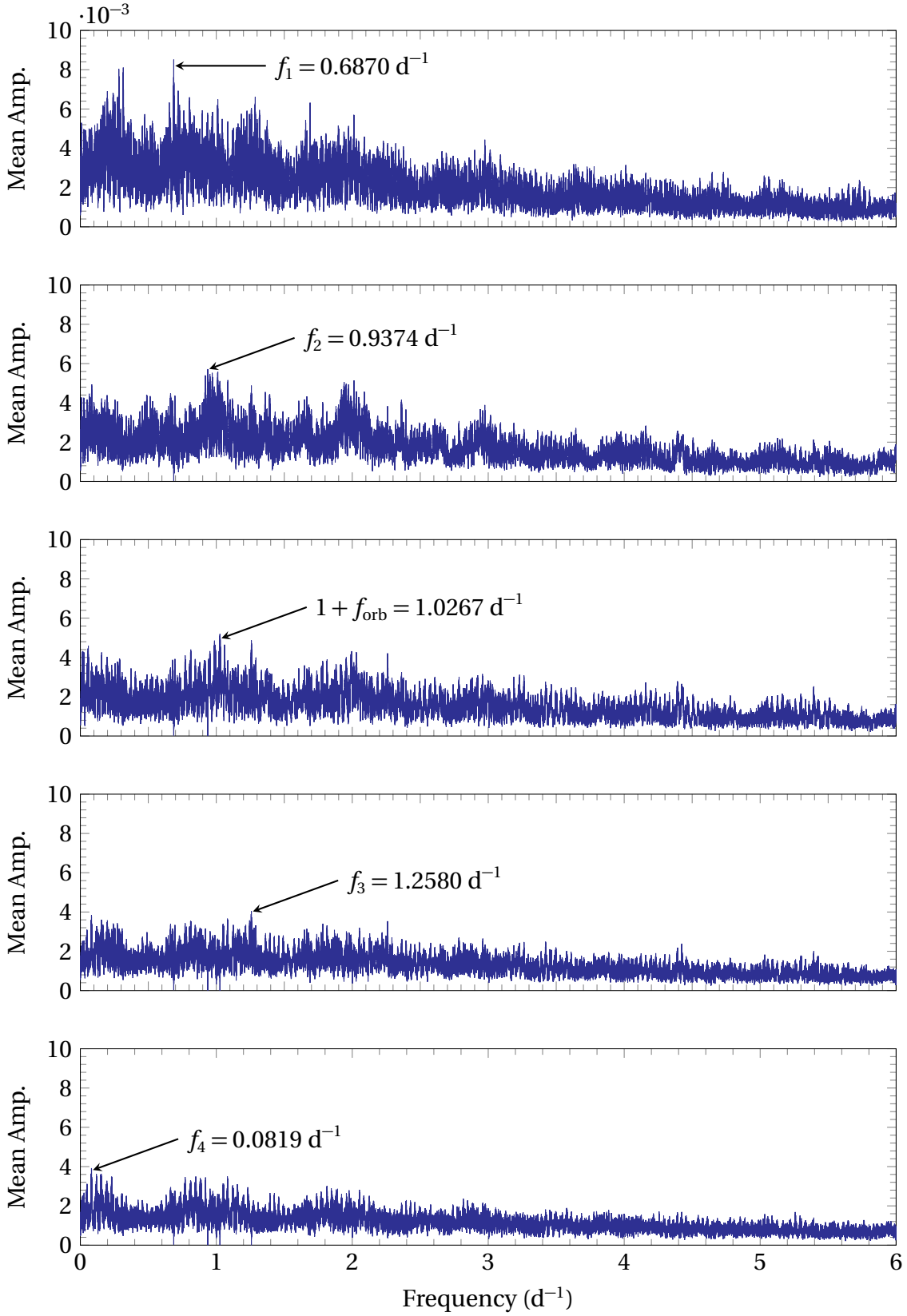

Figure D.1: The pixel-by-pixel mean Lomb-Scargle periodograms of HD 147787 computed by FAMIAS, showcasing the first batch of five frequencies (f_1 to f_4 and the alias of the binary orbit frequency $1+f_{\rm orb}$) detected through the pixel-by-pixel method. (Referenced on page 106, 107, 159.)

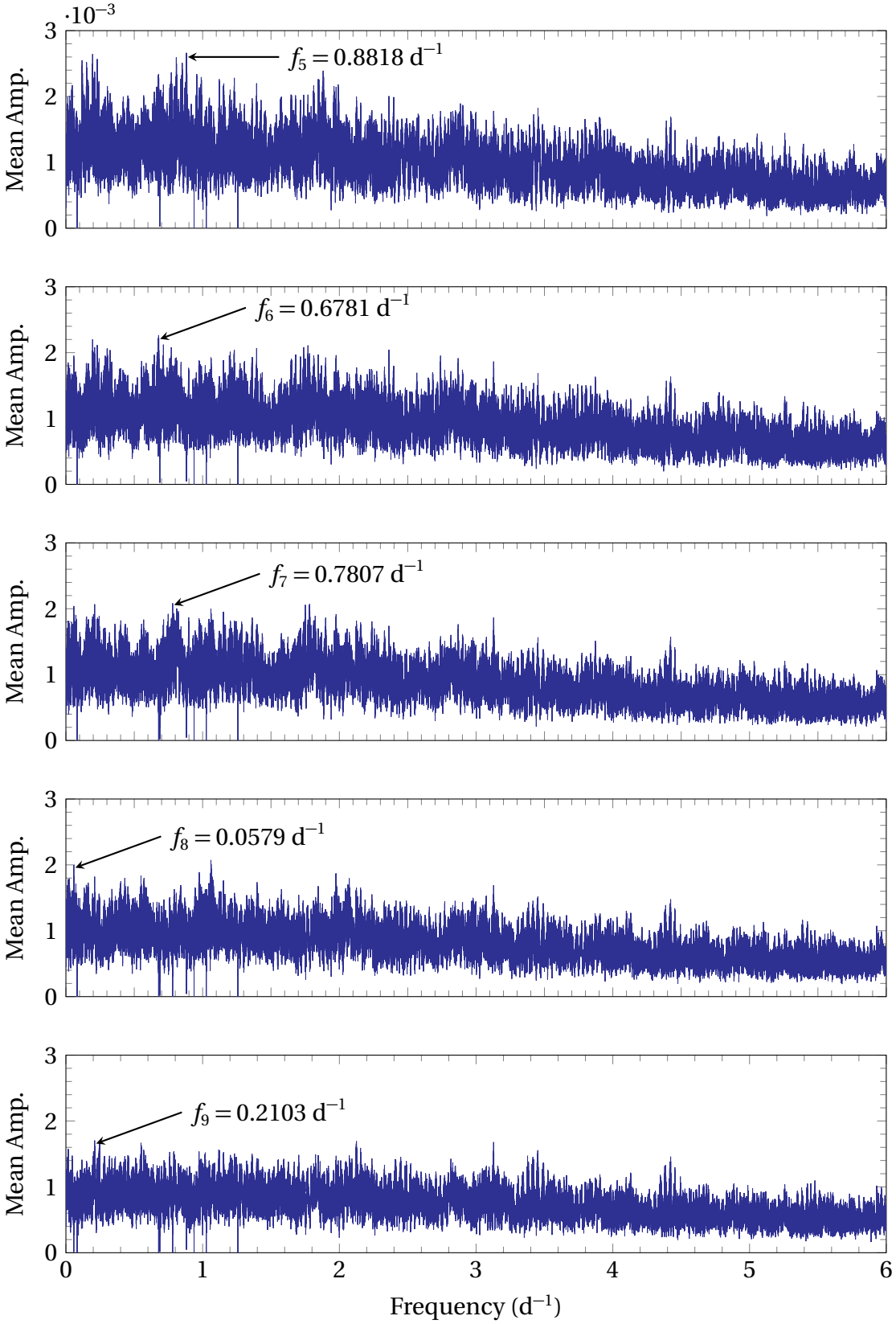

Figure D.2: The pixel-by-pixel mean Lomb-Scargle periodograms of HD 147787 computed by FAMIAS, showcasing the second batch of five frequencies (f_5 to f_9) detected through the pixel-by-pixel method. (Referenced on page 106, 159.)

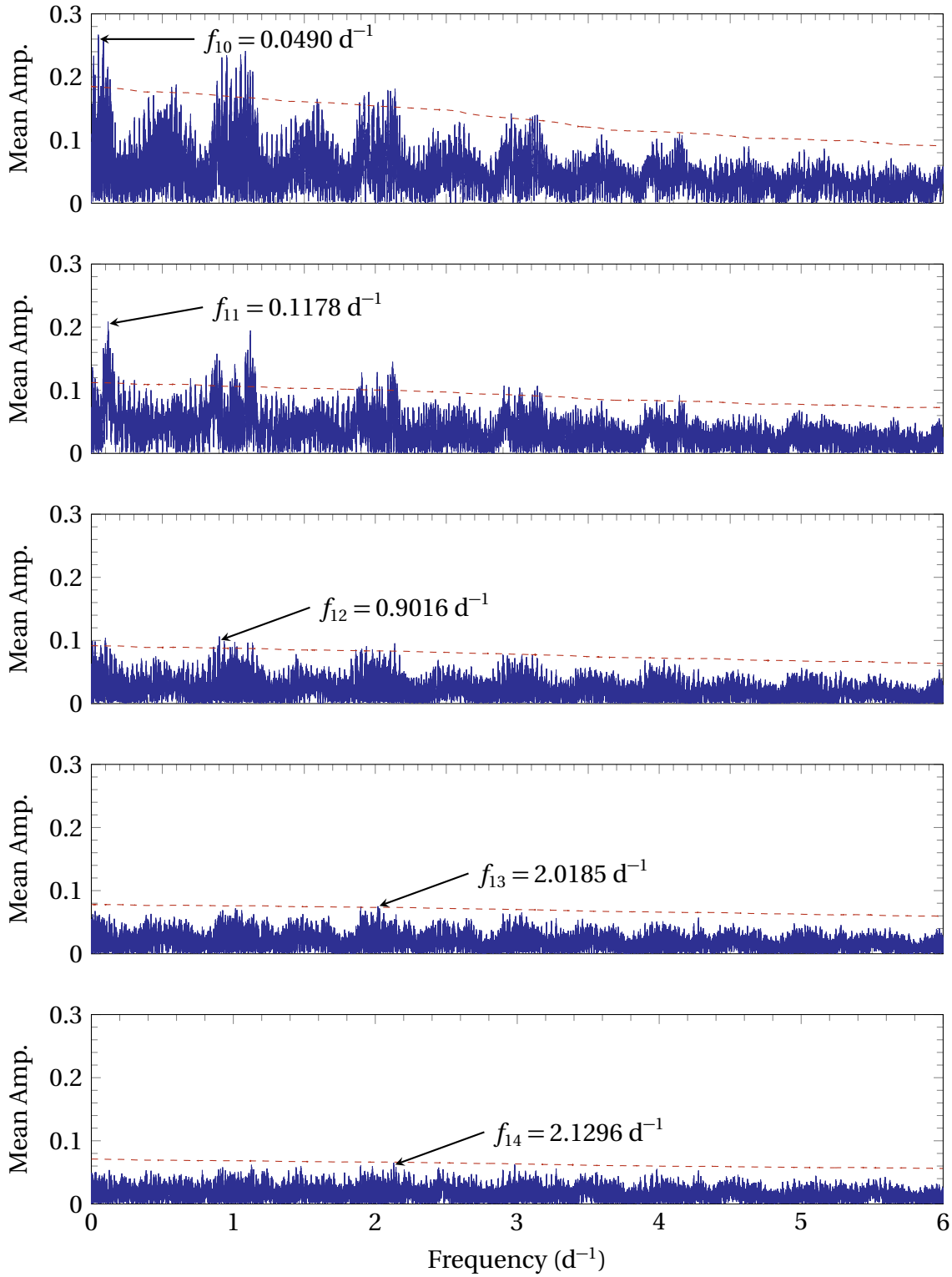

Figure D.3: The zeroth-moment Lomb-Scargle periodograms of HD 147787 computed by FAMIAS, showcasing the five frequencies (f_{10} to f_{25}) detected through the zeroth moment of the moment method. The dashed red line represents the significance level at a signal-to-noise ratio of 4. (Referenced on page 106, 107, 159.)

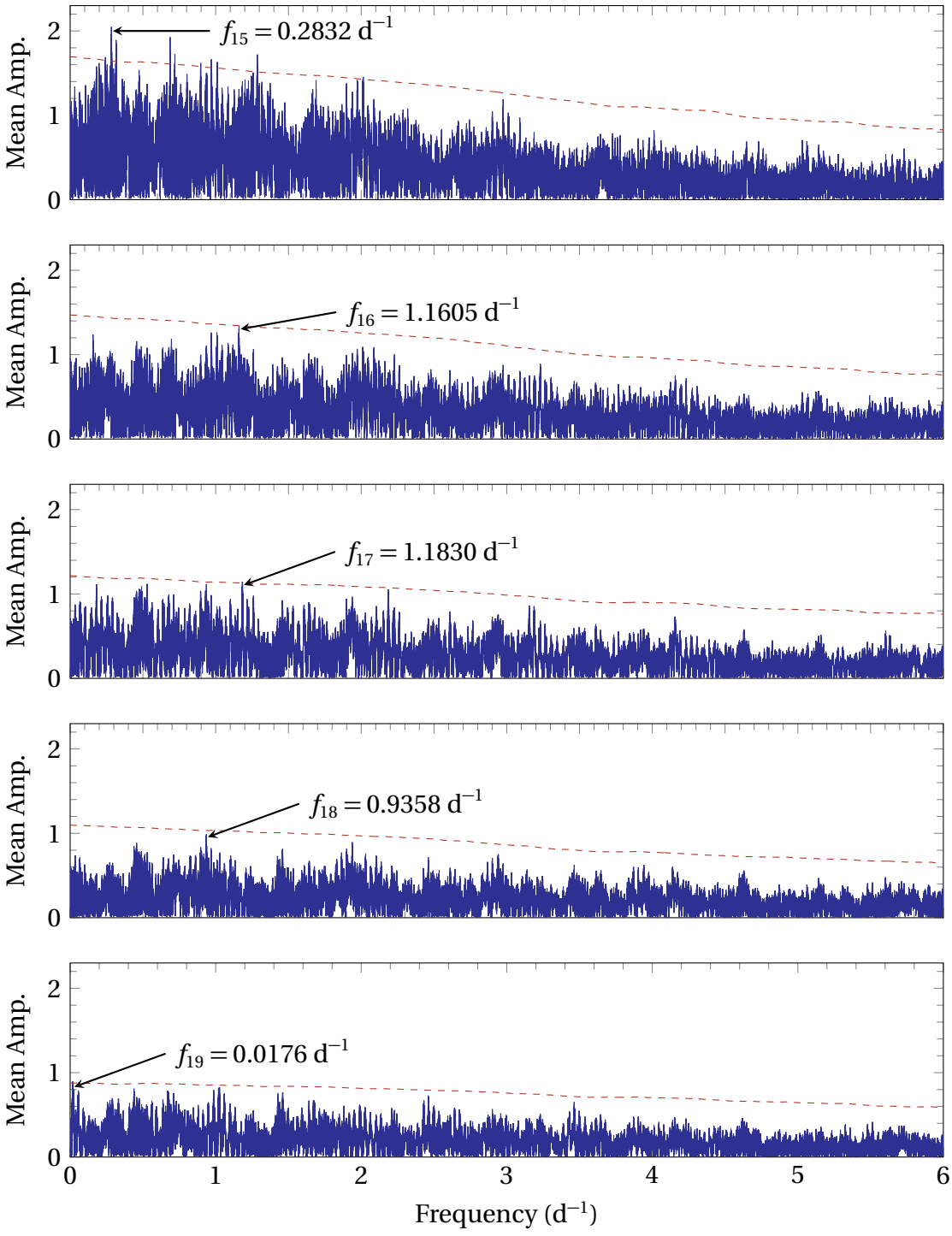

Figure D.4: The first-moment Lomb-Scargle periodograms of HD 147787 computed by FAMIAS, showcasing the first batch of five frequencies (f_{15} to f_{19}) detected through the first moment of the moment method. The dashed red line represents the significance level at a signal-to-noise ratio of 4.

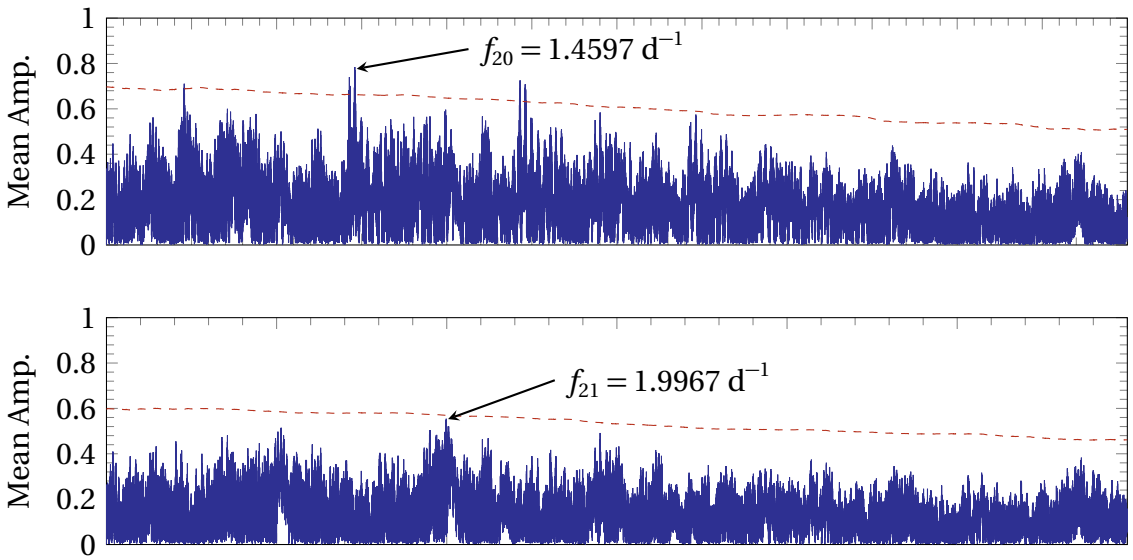

Figure D.5: The first-moment Lomb-Scargle periodograms of HD 147787 computed by FAMIAS, showcasing the second batch of two frequencies (f_{20} and f_{21}) detected through the first moment of the moment method. The dashed red line represents the significance level at a signal-to-noise ratio of 4.

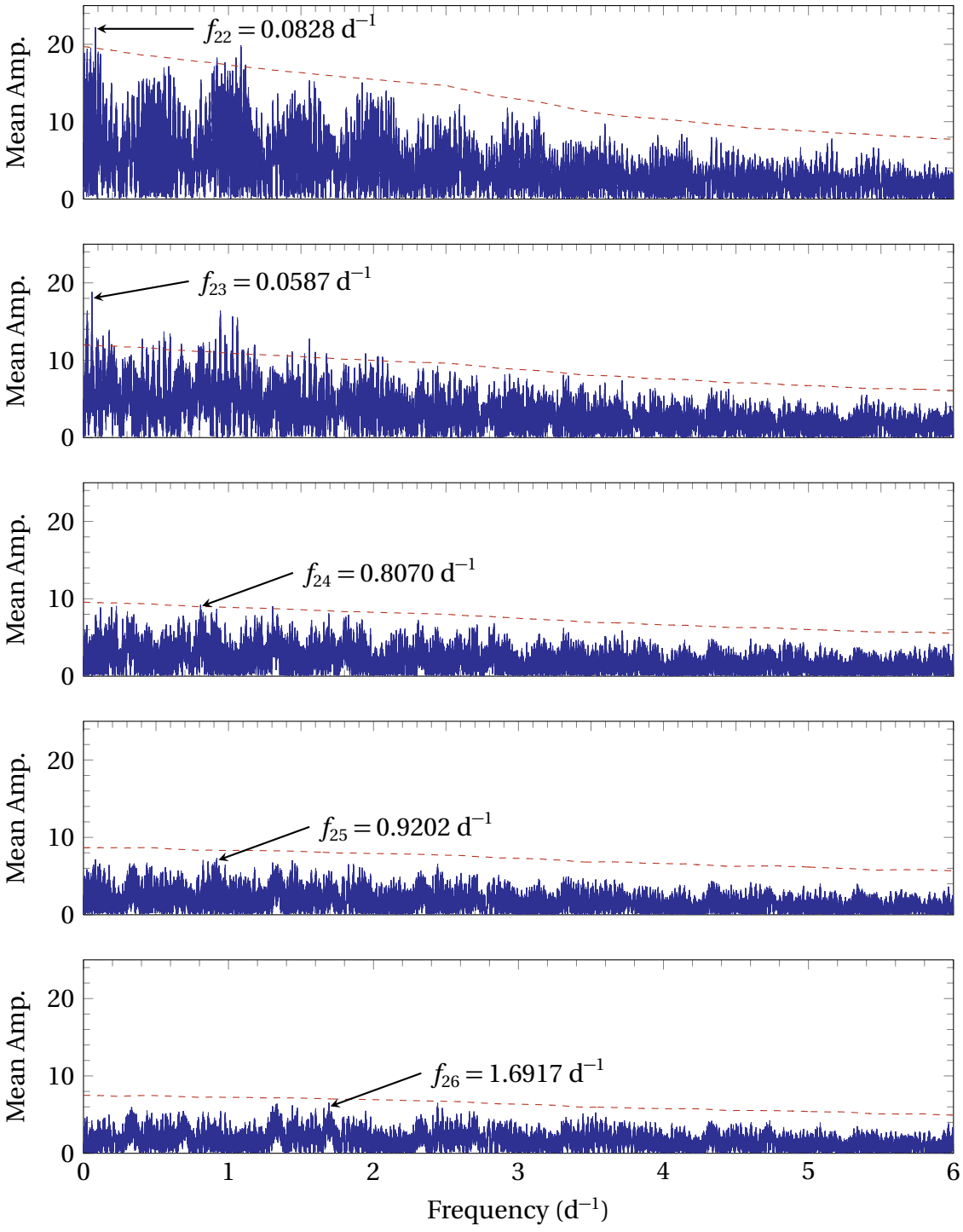

Figure D.6: The second-moment Lomb-Scargle periodograms of HD 147787 computed by FAMIAS, showcasing the five frequencies (f_{22} to f_{26}) detected through the second moment of the moment method. The dashed red line represents the significance level at a signal-to-noise ratio of 4.

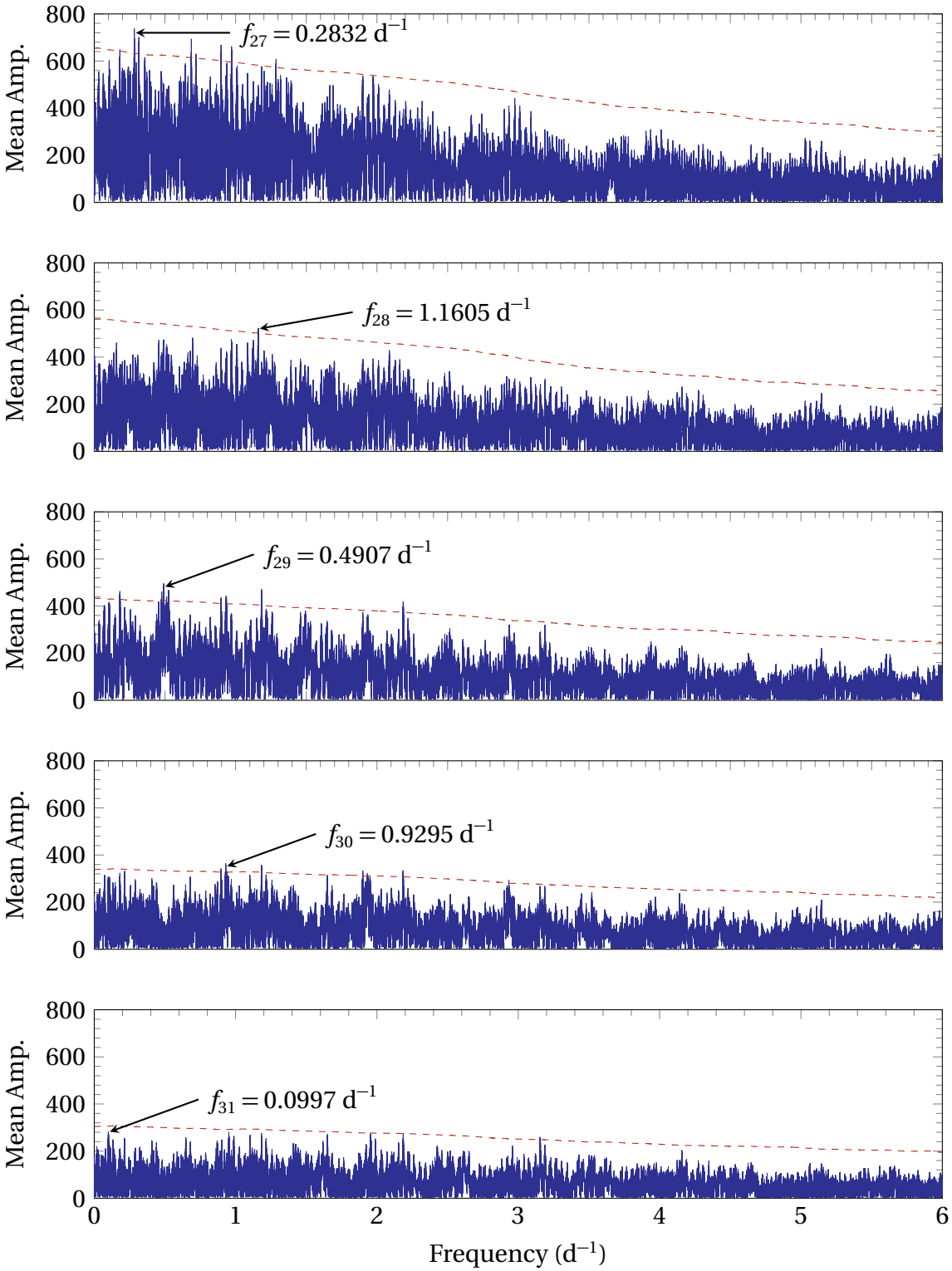

Figure D.7: The third-moment Lomb-Scargle periodograms of HD 147787 computed by FAMIAS, showcasing the first batch of five frequencies (f_{27} to f_{31}) detected through the third moment of the moment method. The dashed red line represents the significance level at a signal-to-noise ratio of 4.

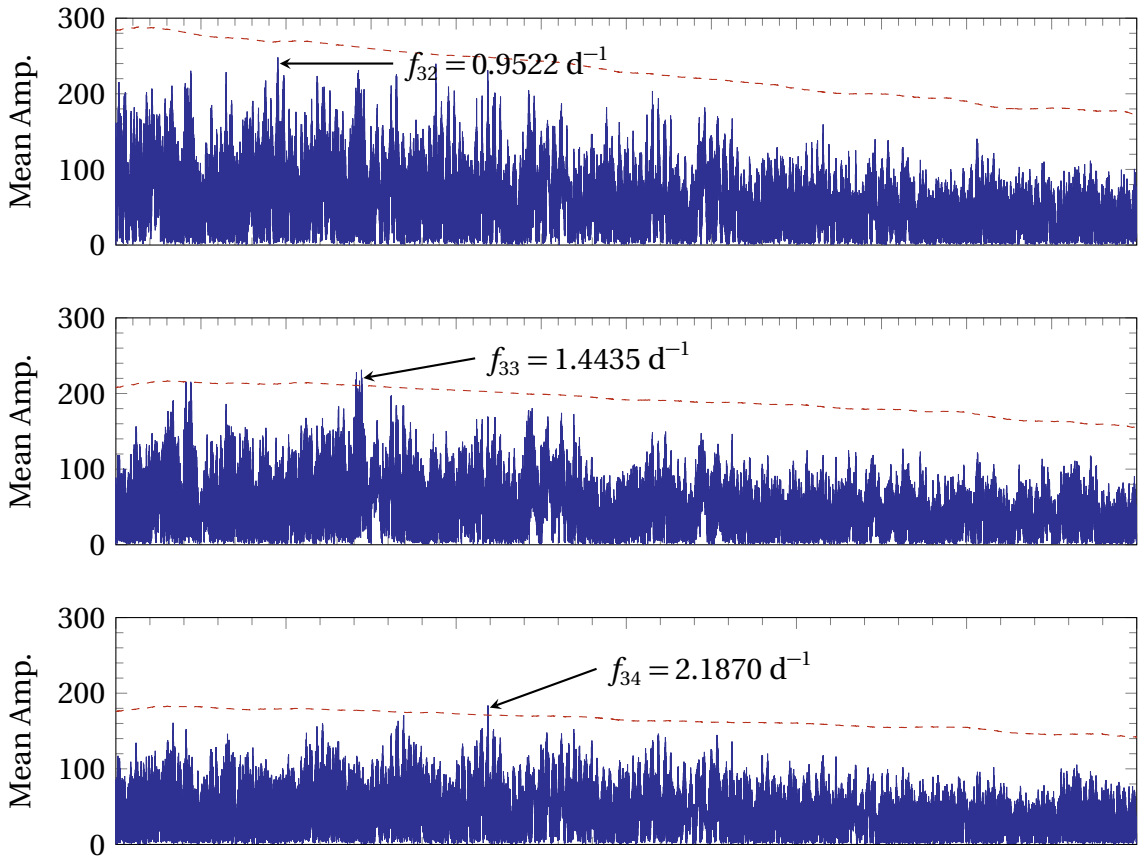

Figure D.8: The third-moment Lomb-Scargle periodograms of HD 147787 computed by FAMIAS, showcasing the second batch of three frequencies (f_{32} to f_{34}) detected through the third moment of the moment method. The dashed red line represents the significance level at a signal-to-noise ratio of 4. (Referenced on page 106, 159.)

Frequencies Removed	σ	**% Reduction in σ**
None	0.01146	0
f_1	0.00973	15.1
f_1+f_2	0.00888	22.5
$f_1+f_2+f_3$	0.00811	29.2
$f_1+f_2+f_3+f_4$	0.00756	34.1
$f_1+f_2+f_3+f_4+f_5$	0.00720	37.2
$f_1+f_2+f_3+f_4+f_5+f_6$	0.00679	40.7
$f_1+f_2+f_3+f_4+f_5+\cdots+f_7$	0.00644	43.8
$f_1+f_2+f_3+f_4+f_5+\cdots+f_8$	0.00613	46.5
$f_1+f_2+f_3+f_4+f_5+\cdots+f_9$	0.00595	48.1

Table D.1: The reduction in the standard deviation across the line profiles of HD 147787 from successive prewhitening of the pulsation frequencies. The combination of these frequencies explains 48.1% of the variation across the line profiles of HD 147787. (Referenced on page 108, 159.)

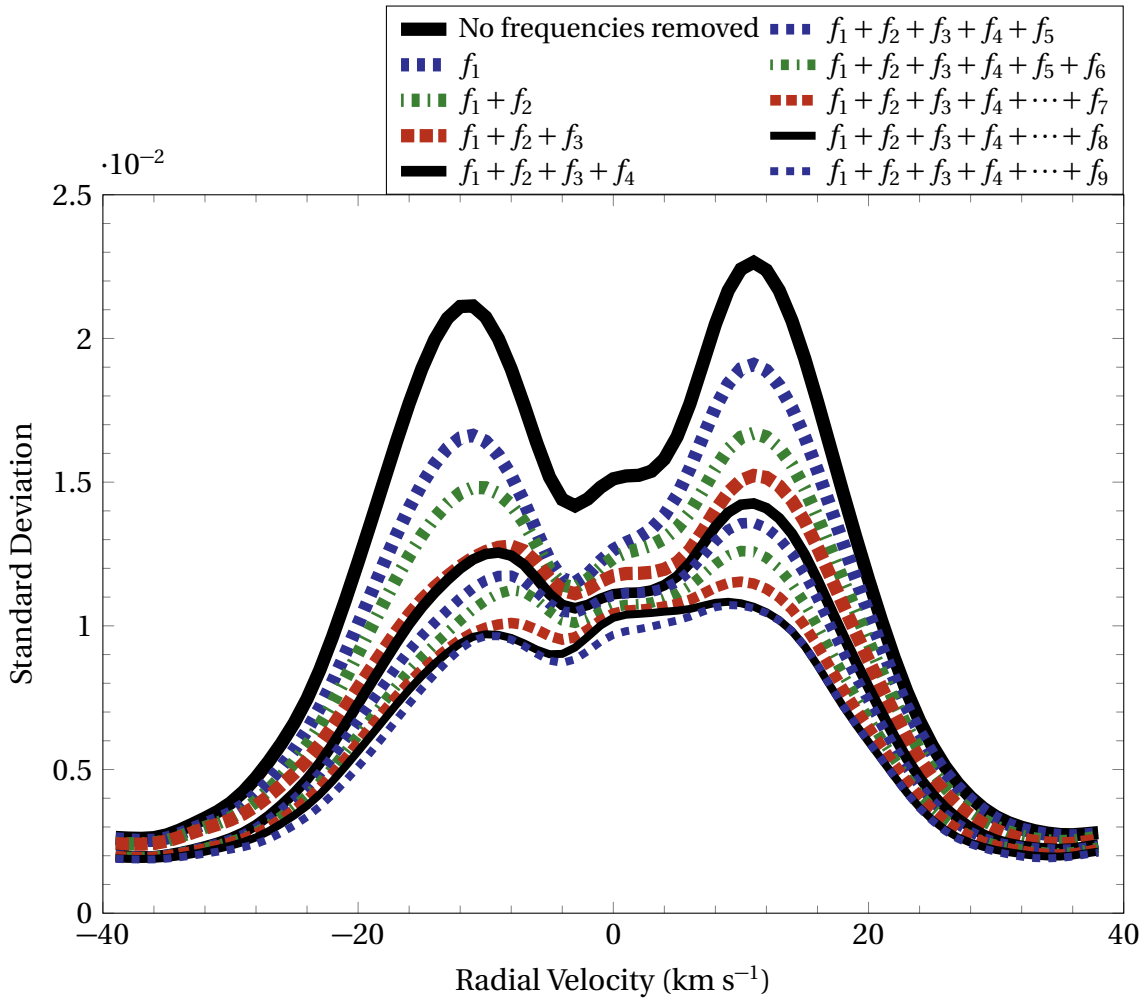

Figure D.9: Reduction in the standard deviation across the line profiles of HD 147787 due to the progressive prewhitening of the 9 identified pulsation frequencies. These 9 frequencies explain 48.1% of the variation across the line profiles of HD 147787. (Referenced on page 108, 159.)

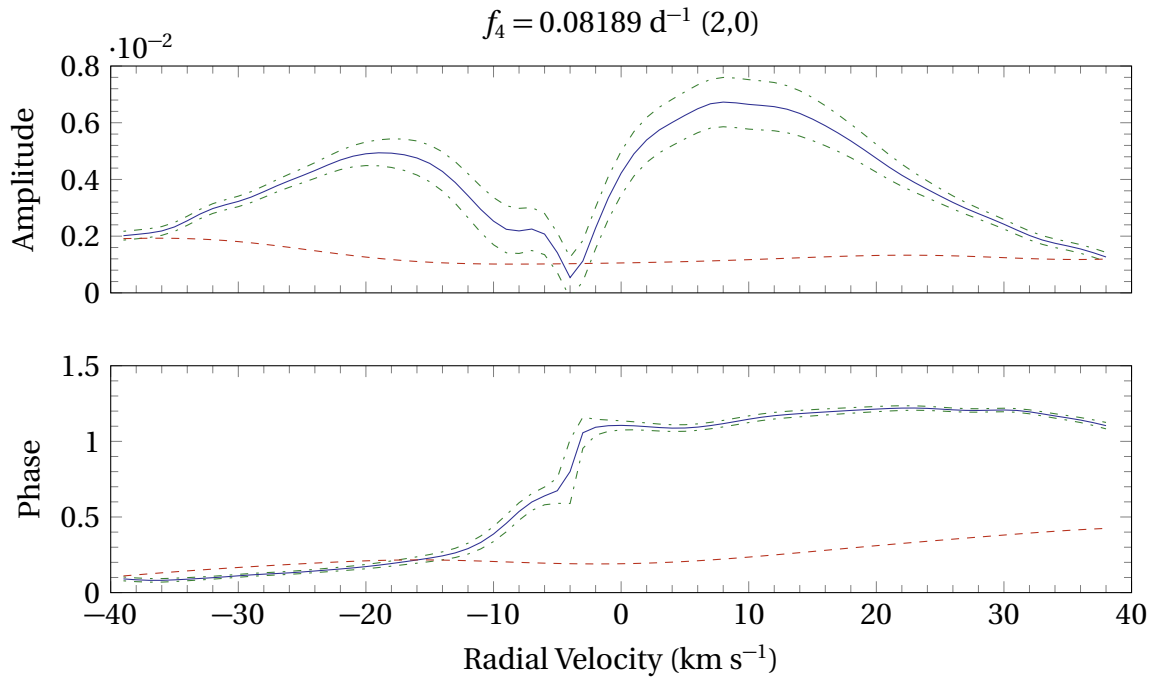

Figure D.10: The amplitude and phase profiles of the best-fit mode of $f_4 = 0.08$ d^{-1} of HD 147787. The solid blue lines are the observational profiles, the dash dotted green lines represent the statistical uncertainty and the dashed red lines represent the best-fit synthetic profiles. Note the poor visual fits of the synthetic amplitude and phase profiles to the observational profiles. (Referenced on page 110, 159.)

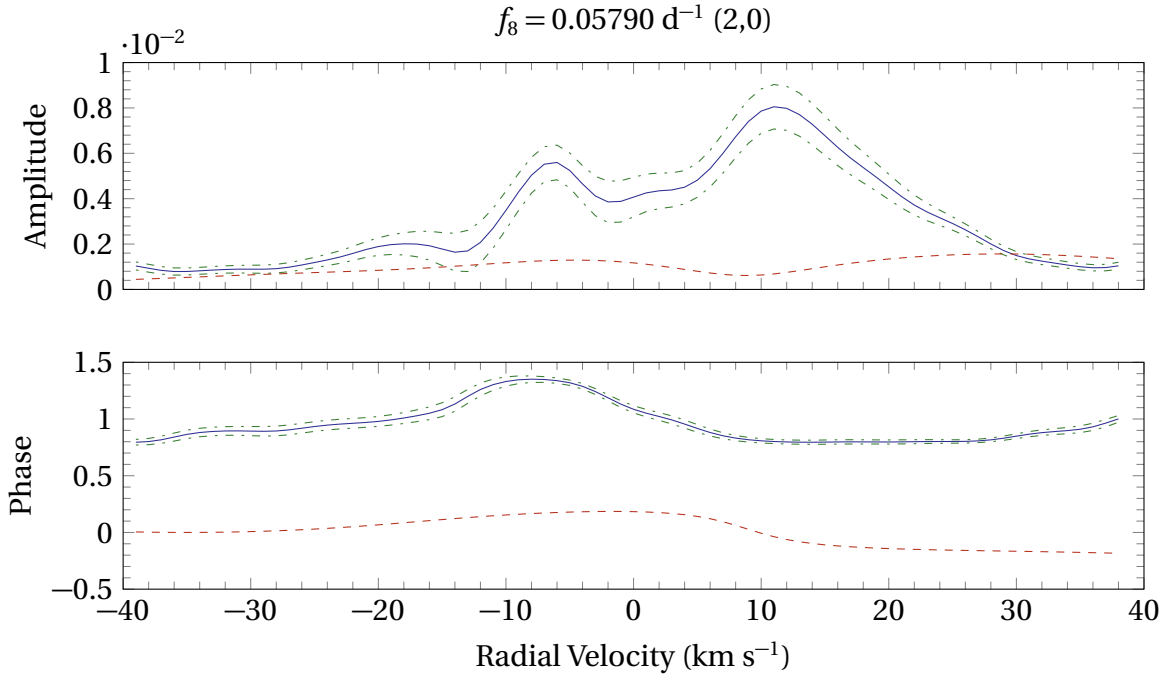

Figure D.11: The amplitude and phase profiles of the best-fit mode of $f_8 = 0.06$ d^{-1} of HD 147787. The solid blue lines are the observational profiles, the dash dotted green lines represent the statistical uncertainty and the dashed red lines represent the best-fit synthetic profiles. Note the poor visual fits of the synthetic amplitude and phase profiles to the observational profiles.

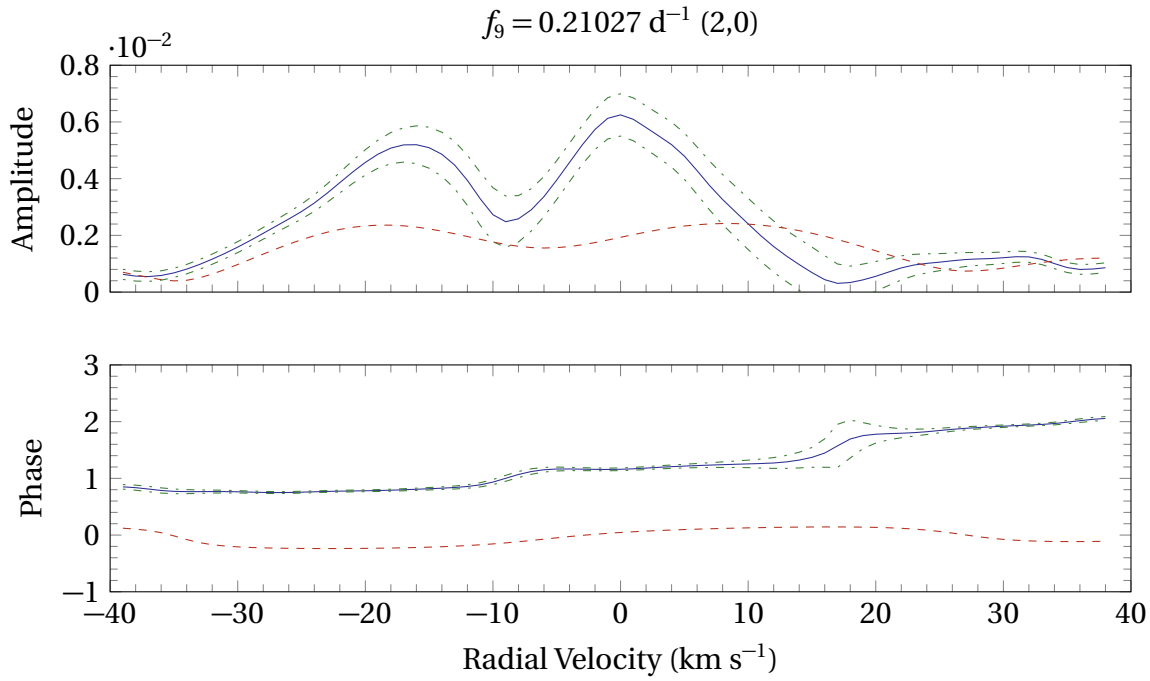

Figure D.12: The amplitude and phase profiles of the best-fit mode of $f_4 = 0.21$ d^{-1} of HD 147787. The solid blue lines are the observational profiles, the dash dotted green lines represent the statistical uncertainty and the dashed red lines represent the best-fit synthetic profiles. Note the poor visual fits of the synthetic amplitude and phase profiles to the observational profiles. (Referenced on page 110, 159.)

References

Abt, H. A. and Biggs, E. S. (1972). Bibliography of stellar radial velocities. New York: Latham Process Corp. (Cited on pages 79 and 102.)

Acevedo-Arreguin, L. A., Garaud, P., and Wood, T. S. (2013). Dynamics of the solar tachocline - III. Numerical solutions of the Gough and McIntyre model. Monthly Notices of the Royal Astronomical Society, 434:720–741. (Cited on page 12.)

Aerts, C. (1996). Mode Identification of pulsating stars from line-profile variations with the moment method: a more accurate discriminant. Astronomy and Astrophysics, 314:115–122. (Cited on pages 9 and 42.)

Aerts, C., Christensen-Dalsgaard, J., and Kurtz, D. W. (2010). Asteroseismology. Astronomy and Astrophysics Library. Springer. (Cited on pages 4, 5, 6, 7, 8, 9, 11, 17, 42, and 43.)

Aerts, C., de Pauw, M., and Waelkens, C. (1992). Mode identification of pulsating stars from line profile variations with the moment method. An example - The Beta Cephei star Delta Ceti. Astronomy and Astrophysics, 266:294–306. (Cited on page 42.)

Aerts, C., Eyer, L., and Kestens, E. (1998). The discovery of new gamma Doradus stars from the HIPPARCOS mission. Astronomy and Astrophysics, 337:790–796. (Cited on pages 13 and 101.)

Agati, J.-L., Bonneau, D., Jorissen, A., Soulié, E., Udry, S., Verhas, P., and Dommanget, J. (2015). Are the orbital poles of binary stars in the solar neighbourhood anisotropically distributed? Astronomy and Astrophysics, 574:A6. (Cited on page 57.)

Alden, H. L. (1936). The apparent orbit of delta Aquilae. Astronomical Journal, 45:193–197. (Cited on page 57.)

Allende, P. C. and Lambert, D. L. (1999). Fundamental parameters of nearby stars from the comparison with evolutionary calculations: masses, radii and effective temperatures. Astronomy and Astrophysics, 352:555–562. (Cited on page 102.)

Ammons, S. M., Robinson, S. E., Strader, J., Laughlin, G., Fischer, D., and Wolf, A. (2006). The N2K Consortium. IV. New Temperatures and Metallicities for More than 100,000 FGK Dwarfs. The Astrophysical Journal, 638:1004–1017. (Cited on pages 58 and 102.)

Antoci, V. (2013). Stochastically excited oscillations on the upper main sequence. In Precision Asteroseismology, number 301 in Proceedings of the IAU Symposium, pages 333–340. (Cited on pages 4 and 7.)

Antoci, V., Handler, G., Carrier, F., Grundahl, F., Matthews, J. M., Hareter, M., Kuschnig, R., and Houdek, G. (2009). The Delta Scuti Star Rho Puppis: the Perfect Target to Probe the Theory Predicting Solar-like Oscillations in Cool Delta Scuti Stars. In American Institute of Physics Conference Series, volume 1170, pages 440–442. (Cited on page 17.)

Baade, D. and Kjeldsen, H. (1997). A spectroscopic search for high azimuthal-order pulsation in broad-lined late F- and early G-stars. Astronomy and Astrophysics, 323:429–441. (Cited on pages 57 and 76.)

Baade, W. (1944). The Resolution of Messier 32, NGC 205, and the Central Region of the Andromeda Nebula. The Astrophysical Journal, 100:137. (Cited on page 13.)

Balona, L. A. (1986). A new version of the moment method, optimised for mode identification in multiperiodic stars. Astronomy and Astrophysics, 398(2):687–696. (Cited on page 42.)

Balona, L. A. (1998). Spectroscopic and Photometric Variations of Pulsating Stars. In A Half Century of Stellar Pulsation Interpretation, volume 135 of Astronomical Society of the Pacific Conference Series, page 120. (Cited on page 13.)

Balona, L. A. (2014). Low frequencies in Kepler δ Scuti stars. Monthly Notices of the Royal Astronomical Society, 437:1476–1484. (Cited on pages 18, 26, 43, 97, and 118.)

Balona, L. A., Daszyńska-Daszkiewicz, J., and Pamyatnykh, A. A. (2015). Pulsation frequency distribution in δ Scuti stars. Monthly Notices of the Royal Astronomical Society, 452:3073–3084. (Cited on pages 18 and 76.)

Balona, L. A. and Dziembowski, W. A. (2011). Kepler observations of δ Scuti stars. Monthly Notices of the Royal Astronomical Society, 417:591–601. (Cited on page 17.)

Balona, L. A. and Evers, E. A. (1999). Mode identification and asteroseismology of delta Scuti stars. Monthly Notices of the Royal Astronomical Society, 302:349–361. (Cited on pages 6 and 8.)

Barnes, S. I. (2004). The design and performance of high resolution echelle spectrographs in astronomy. Unpublished doctoral dissertation, University of Canterbury, Christchurch, New Zealand. (Cited on page 27.)

Beauchamp, A., Wesemael, F., Bergeron, P., Fontaine, G., Saffer, R. A., Liebert, J., and Brassard, P. (1999). Spectroscopic Studies of DB White Dwarfs: The Instability Strip of the Pulsating DB (V777 Herculis) Stars. The Astrophysical Journal, 516:887–891. (Cited on page 3.)

Benomar, O., Takata, M., Shibahashi, H., Ceillier, T., and García, R. A. (2015). Nearly uniform internal rotation of solar-like main-sequence stars revealed by space-based asteroseismology and spectroscopic measurements. Monthly Notices of the Royal Astronomical Society, 452:2654–2674. (Cited on page 12.)

Bergmann, C. M. (2015). Searching for Earth-mass planets around α Centauri. Unpublished doctoral dissertation, University of Canterbury, Christchurch, New Zealand. (Cited on pages 21, 23, 37, 59, 61, 62, 81, and 104.)

Bíró, I. B. and Nuspl, J. (2005). Mode Identification of Nonradial Pulsations by Image Reconstruction in Eclipsing Binary Systems. In Tidal Evolution and Oscillations in Binary Stars, volume 333 of Astronomical Society of the Pacific Conference Series, page 221. (Cited on page 19.)

Bíró, I. B. and Nuspl, J. (2011). Photometric mode identification methods of non-radial pulsations in eclipsing binaries - I. Dynamic eclipse mapping. Monthly Notices of the Royal Astronomical Society, 416:1601–1615. (Cited on page 19.)

Bognár, Z., Lampens, P., Frémat, Y., Southworth, J., Sódor, Á., De Cat, P., Isaacson, H. T., Marcy, G. W., Ciardi, D. R., Gilliland, R. L., and Martín-Fernández, P. (2015). KIC 9533489: a genuine γ Doradus - δ Scuti Kepler hybrid pulsator with transit events. Astronomy and Astrophysics, 581:A77. (Cited on pages 15 and 18.)

Bohm, T., Zima, W., Catala, C., Alecian, E., Pollard, K., and Wright, D. (2008). Discovery of non-radial pulsations in the spectroscopic binary Herbig Ae star RS Cha. Communications in Asteroseismology, 157:47–51. (Cited on page 19.)

Borkovits, T., Derekas, A., Fuller, J., Szabó, G. M., Pavlovski, K., Csák, B., Dózsa, Á., Kovács, J., Szabó, R., Hambleton, K. M., Kinemuchi, K., Kolbas, V., Kurtz, D. W., Maloney, F., Prša, A., Southworth, J., Sztakovics, J., Bíró, I. B., and Jankovics, I. (2014). HD 183648: a Kepler eclipsing binary with anomalous ellipsoidal variations and a pulsating component. Monthly Notices of the Royal Astronomical Society, 443:3068–3081. (Cited on page 115.)

Bouabid, M.-P., Dupret, M.-A., Salmon, S., Montalbán, J., Miglio, A., and Noels, A. (2013). Effects of the Coriolis force on high-order g modes in γ Doradus stars. Monthly Notices of the Royal Astronomical Society, 429:2500–2514. (Cited on page 12.)

Bradley, P. A., Guzik, J. A., Miles, L. F., Uytterhoeven, K., Jackiewicz, J., and Kinemuchi, K. (2015). Results of a Search for γ Dor and δ Sct Stars With the Kepler Spacecraft. The Astronomical Journal, 149:68. (Cited on pages 13 and 17.)

Breger, M. (2000). δ Scuti stars (Review). In Delta Scuti and Related Stars, volume 210, page 3. (Cited on page 17.)

Breger, M., Balona, L., Lenz, P., Hollek, J. K., Kurtz, D. W., Catanzaro, G., Marconi, M., Pamyatnykh, A. A., Smalley, B., Suárez, J. C., Szabo, R., Uytterhoeven, K., Ripepi, V., Christensen-Dalsgaard, J., Kjeldsen, H., Fanelli, M. N., Ibrahim, K. A., and Uddin, K. (2011). Regularities in frequency spacings of δ Scuti stars: the Kepler star KIC 9700322. Monthly Notices of the Royal Astronomical Society, 414:1721–1731. (Cited on page 17.)

Breger, M. and Bischof, K. M. (2002). Close frequency pairs in Delta Scuti stars. Astronomy and Astrophysics, 385:537–545. (Cited on page 6.)

Breger, M., Fossati, L., Balona, L., Kurtz, D. W., Robertson, P., Bohlender, D., Lenz, P., Müller, I., Lüftinger, T., Clarke, B. D., Hall, J. R., and Ibrahim, K. A. (2012a). Relationship between Low and High Frequencies in δ Scuti Stars: Photometric Kepler and Spectroscopic Analyses of the Rapid Rotator KIC 8054146. The Astrophysical Journal, 759:62. (Cited on page 17.)

Breger, M., Hareter, M., Endl, M., Kuschnig, R., Weiss, W. W., Matthews, J. M., Guenther, D. B., Moffat, A. F. J., Rowe, J. F., Rucinski, S. M., and Sasselov, D. (2012b). Delta Scuti stars in the Praesepe cluster observed by the MOST satellite. Astronomische Nachrichten, 333:131. (Cited on page 17.)

Briquet, M. and Aerts, C. (2003). Mode identification from line profile variations. Monthly Notices of the Royal Astronomical Society, 219:111–129. (Cited on pages 42 and 52.)

Brunsden, E. (2013). The Music of the Stars. Unpublished doctoral dissertation, University of Canterbury, Christchurch, New Zealand. (Cited on pages 15, 18, 28, 30, 42, 51, 57, 58, 66, and 75.)

Brunsden, E., Pollard, K. R., Cottrell, P. L., Wright, D. J., Cat, P. D., and Kilmartin, P. M. (2012). Spectroscopic pulsational frequency identification and mode determination of γ Doradus star HD 12901. Monthly Notices of the Royal Astronomical Society, 427(4):3535. (Cited on pages 15 and 49.)

Buzasi, D. L., Bruntt, H., Bedding, T. R., Retter, A., Kjeldsen, H., Preston, H. L., Mandeville, W. J., Suarez, J. C., Catanzarite, J., Conrow, T., and Laher, R. (2005). Altair: The Brightest δ Scuti Star. The Astrophysical Journal, 619:1072–1076. (Cited on page 17.)

Campbell, W. W. and Curtis, H. D. (1903). A list of five stars whose velocities in the line of sight are variable. The Astrophysical Journal, 18. (Cited on page 57.)

Campbell, W. W. and Wright, W. H. (1900). A list of nine stars whose velocities in the line of sight are variable. The Astrophysical Journal, 12:254–257. (Cited on page 17.)

Casagrande, L., Schönrich, R., Asplund, M., Cassisi, S., Ramírez, I., Meléndez, J., Bensby, T., and Feltzing, S. (2011). New constraints on the chemical evolution of the solar neighbourhood and Galactic disc(s). Improved astrophysical parameters for the Geneva-Copenhagen Survey. Astronomy and Astrophysics, 530:A138. (Cited on page 102.)

Chadid, M., De Ridder, J., Aerts, C., and Mathias, P. (2001). 20 CVn: A monoperiodic radially pulsating delta Scuti star. Astronomy and Astrophysics, 375:113–121. (Cited on pages 8 and 9.)

Chang, S.-W., Protopapas, P., Kim, D.-W., and Byun, Y.-I. (2013). Statistical Properties of Galactic δ Scuti Stars: Revisited. The Astronomical Journal, 145:132. (Cited on page 77.)

Chapellier, E., Mathias, P., Weiss, W. W., Le Contel, D., and Debosscher, J. (2012). Strong interactions between g- and p-modes in the hybrid γ Doradus-δ Scuti CoRoT star ID 105733033. Astronomy and Astrophysics, 540:A117. (Cited on pages 12, 15, 18, and 76.)

Claret, A. (2000). A new non-linear limb-darkening law for LTE stellar atmosphere models. Calculations for -5.0 <= log $[M/H]$ <= +1, 2000 K <= $T_{\rm eff}$ <= 50000 K at several surface gravities. Astronomy and Astrophysics, 363:1081–1190. (Cited on page 52.)

Colacevich, A. (1935). The variable radial velocity of δ Scuti. Lick Observatory Bulletin, 17:171–174. (Cited on page 17.)

Cousins, A. W. J., Caldwell, J. A. R., and W., M. J. (1989). The Period of gamma Doradus. Information Bulletin on Variable Stars, 3412:1. (Cited on page 13.)

Cousins, A. W. J. and Lagerwey, H. C. (1971). UBV Observations of Variable Stars. Monthly Notes of the Astronomical Society of South Africa, 30:12. (Cited on page 77.)

Cousins, A. W. J. and Warren, P. R. (1963). Variable Stars Observed During the Cape Bright Star Programme. Monthly Notes of the Astronomical Society of South Africa, 22:65. (Cited on page 13.)

Cox, J. P. (1980). Theory of Stellar Pulsation. Princeton University Press. (Cited on pages 3, 5, and 56.)

Cunha, A. S. (2007). Theory of rapidly oscillating Ap stars. Communications in Asteroseismology, 150:48–54. (Cited on page 6.)

Cunha, M. S., Aerts, C., Christensen-Dalsgaard, J., Baglin, A., Bigot, L., Brown, T. M., Catala, C., Creevey, O. L., Domiciano de Souza, A., Eggenberger, P., Garcia, P. J. V., Grundahl, F., Kervella, P., Kurtz, D. W., Mathias, P., Miglio, A., Monteiro, M. J. P. F. G., Perrin, G., Pijpers, F. P., Pourbaix, D., Quirrenbach, A., Rousselet-Perraut, K., Teixeira, T. C., Thévenin, F., and Thompson, M. J. (2007). Asteroseismology and interferometry. The Astronomy and Astrophysics Review, 14:217–360. (Cited on page 2.)

Daszyńska-Daszkiewicz, J., Dziembowski, W. A., and Pamyatnykh, A. A. (2007). Light and Radial Velocity Variations Due to Low-Frequency Oscillations in Rotating Stars. In Stellar Evolution and Seismic Tools for Asteroseismology - Diffusive Processes in Stars and Seismic Analysis, volume 26 of European Astronomical Society Publications Series, pages 129–136. (Cited on page 12.)

de Bruijne, J. H. J. and Eilers, A. .-C. (2012). Radial velocities for the HIPPARCOS-Gaia Hundred-Thousand-Proper-Motion project. Astronomy and Astrophysics, 546(A61). (Cited on page 79.)

De Cat, P., Eyer, L., Cuypers, J., Aerts, C., Vandenbussche, B., Uytterhoeven, K., Reyniers, K., Kolenberg, K., Groenewegen, M., Raskin, G., Maas, T., and Jankov, S. (2006). A spectroscopic study of southern (candidate) γ Doradus stars. I. Time series analysis. Astronomy and Astrophysics, 449(1):289–292. (Cited on pages 101 and 115.)

De Cat, P., Wright, D. J., Pollard, K. R., Maisonneuve, F., Kilmartin, P. M., and Laney, D. (2009). Is HD 147787 a double-lined binary with two pulsating components? Preliminary results from a spectroscopic multi-site campaign. In Stellar Pulsation: Challenges for Theory and Observation, volume 1170 of American Institute of Physics Conference Series, pages 483–485. (Cited on pages 28 and 117.)

De Cat, P., Wright, D. J., Pollard, K. R., Maisonneuve, F., Kilmartin, P. M., and Laney, D. (2009). Is HD 147787 a double-lined binary with two pulsating components? Preliminary results from a spectroscopic multiâĂŘsite campaign. In American Institute of Physics Conference Series, volume 1170 of American Institute of Physics Conference Series, pages 483–485. (Cited on pages 101, 102, 104, and 115.)

De Mey, K., Daems, K., and Sterken, C. (1998). Theta Tucanae: a binary with a delta Scuti primary. Astronomy and Astrophysics, 336:527–534. (Cited on pages viii, 28, 78, 79, 81, 82, 97, 98, 117, and 118.)

Desmet, M., Briquet, M., Thoul, A., Zima, W., De Cat, P., Handler, G., Ilyin, I., Kambe, E., Krzesinski, J., Lehmann, H., Masuda, S., Mathias, P., Mkrtichian, D. E., Telting, J., Uytterhoeven, K., Yang, S. L. S., and Aerts, C. (2009). An asteroseismic study of the β Cephei star 12 Lacertae: multisite spectroscopic observations, mode identification and seismic modelling. Monthly Notices of the Royal Astronomical Society, 396:1460–1472. (Cited on page 51.)

Dupret, M. A., Grigacéne, A., Garrido, R., Gabriel, M., and Scuflaire, R. (2004). Theoretical instability strips for δ Scuti and γ Doradus stars. Astronomy and Astrophysics, 414:L17–L20. (Cited on pages 5, 15, 16, and 18.)

Dupret, M. A., Grigacéne, A., Garrido, R., Gabriel, M., and Scuflaire, R. (2005a). Convection-pulsation coupling. II. Excitation and stabilization mechanisms in δ Sct and γ Dor stars. Astronomy and Astrophysics, 435:927–939. (Cited on page 15.)

Dupret, M. A., Grigacéne, A., Garrido, R., Gabriel, M., and Scuflaire, R. (2005b). Time-dependent convection seismic study of five γ Doradus stars. Monthly Notices of the Royal Astronomical Society, 360:1143–1152. (Cited on page 15.)

Dupret, M.-A., Grigahcène, A., Garrido, R., De Ridder, J., Moya, A., Suárez, J.-C., Scuflaire, R., Gabriel, M., and Goupil, M.-J. (2006). Theoretical Aspects of g-mode Pulsations in gamma Doradus Stars. Memorie della Societá Astronomica Italiana, 77:366. (Cited on page 15.)

Dziembowski, W. A. and Goode, P. R. (1992). Effects of differential rotation on stellar oscillations - A second-order theory. The Astrophysical Journal, 394:670–687. (Cited on page 55.)

Dziembowski, W. A., Moskalik, P., and Pamyatnykh, A. A. (1993). The Opacity Mechanism in B-Type Stars - Part Two - Excitation of High-Order G-Modes in Main Sequence Stars. Monthly Notices of the Royal Astronomical Society, 265:588. (Cited on page 76.)

Eddington, A. S. (1917). The pulsation theory of Cepheid variables. The Observatory. (Cited on page 3.)

Eddington, A. S. (1926). The Internal Constitution of the Stars, volume 40. Cambridge University Press. (Cited on page 1.)

Eggen, O. J. (1956). ρ Puppis: A New Short-Period Variable Star. Publications of the Astronomical Society of the Pacific, 68:238–241. (Cited on page 17.)

Erspamer, D. and North, P. (2003). Automated spectroscopic abundances of A and F-type stars using echelle spectrographs. II. Abundances of 140 A-F stars from ELODIE. Astronomy and Astrophysics, 398:1121–1135. (Cited on page 58.)

Eyer, L. and Aerts, C. (2000). New Gamma Doradus Stars from the Hipparcos Mission and Geneva Photometry. In IAU Colloq. 176: The Impact of Large-Scale Surveys on Pulsating Star Research, volume 203 of Astronomical Society of the Pacific Conference Series, pages 449–450. (Cited on page 13.)

Eyer, L. and Mowlavi, N. (2008). Variable stars across the observational HR diagram. Journal of Physics Conference Series, 118(1):1–21. (Cited on page 3.)

Fath, E. A. (1935). The Variability of δ Scuti. Publications of the Astronomical Society of the Pacific, 47:232. (Cited on page 17.)

Frolov, M. S. (1970). List of Probable Delta Scuti Stars. Information Bulletin on Variable Stars, 427. (Cited on pages 57 and 75.)

Fuhrmann, K. (2008). Nearby stars of the Galactic disc and halo - IV. Monthly Notices of the Royal Astronomical Society, 384:173–224. (Cited on pages 57, 58, 63, and 76.)

Gamarova, A. Y., Mkrtichian, D. E., and Rodríguez, E. (2005). Mode identification in the eclipsing binary systems with primary pulsating components. In Tidal Evolution and Oscillations in Binary Stars, volume 333 of Astronomical Society of the Pacific Conference Series, page 258. (Cited on page 19.)

Garaud, P. (2002). Dynamics of the solar tachocline - I. An incompressible study. Monthly Notices of the Royal Astronomical Society, 329:1–17. (Cited on page 12.)

Garaud, P. and Garaud, J.-D. (2008). Dynamics of the solar tachocline - II. The stratified case. Monthly Notices of the Royal Astronomical Society, 391:1239–1258. (Cited on page 12.)

García, H. A., Moya, A., Michel, E., Garrido, R., Suárez, J. C., Rodríguez, E., Amado, P. J., Martín-Ruiz, S., Rolland, A., Poretti, E., Samadi, R., Baglin, A., Auvergne, M., Catala, C., Lefevre, L., and Baudin, F. (2009). Asteroseismic analysis of the CoRoT δ Scuti star HD 174936. Astronomy and Astrophysics, 506:79–83. (Cited on page 17.)

García, R. A., Ceillier, T., Salabert, D., Mathur, S., van Saders, J. L., Pinsonneault, M., Ballot, J., Beck, P. G., Bloemen, S., Campante, T. L., Davies, G. R., do Nascimento, Jr., J.-D., Mathis, S., Metcalfe, T. S., Nielsen, M. B., Suárez, J. C., Chaplin, W. J., Jiménez, A., and Karoff, C. (2014). Rotation and magnetism of Kepler pulsating solar-like stars. Towards asteroseismically calibrated age-rotation relations. Astronomy and Astrophysics, 572:A34. (Cited on page 9.)

Gautschy, A. and Saio, H. (1995). Stellar Pulsations Across The HR Diagram: Part 1. Annual Review of Astronomy and Astrophysics, 33:75–114. (Cited on page 3.)

Gautschy, A. and Saio, H. (1996). Stellar Pulsations Across the HR Diagram: Part 2. Annual Review of Astronomy and Astrophysics, 34:551–606. (Cited on page 3.)

Gizon, L. and Solanki, S. K. (2004). Measuring Stellar Differential rotation with asteroseismology. Solar Physics, 220:169–184. (Cited on page 11.)

Glebocki, R. and Gnacinski, P. (2005). VizieR Online Data Catalog: Catalog of Stellar Rotational Velocities (Glebocki+ 2005). VizieR Online Data Catalog, 3244. (Cited on pages 58, 79, 98, and 102.)

Gliese, W. and Jahreiß, H. (1991). Preliminary Version of the Third Catalogue of Nearby Stars. Technical report. (Cited on page 58.)

Gray, D. F. (1975). Atmospheric turbulence measured in stars above the main sequence. The Astrophysical Journal, 202:148–164. (Cited on page 9.)

Gray, D. F. (1988). Lectures on spectral-line analysis: F, G, and K stars, volume 1. The Publisher. (Cited on page 9.)

Gray, D. F. (2005). The Observation and Analysis of Stellar Photospheres. Cambridge University Press, 3rd edition. (Cited on pages 9, 36, and 98.)

Greenwood, A. (2014). Spectroscopic Analysis of γ Doradus Variable Stars. Unpublished master's thesis, University of Canterbury, Christchurch, New Zealand. (Cited on pages 15, 30, 51, and 66.)

Guzik, J. A., Kaye, A. B., Bradley, P. A., Cox, A. N., and Neuforge, C. (2000). Driving the Gravity Mode Pulsations in γ Doradus Variables. The Astrophysical Journal, 542(1):L57–L60. (Cited on pages 5, 14, and 15.)

Handler, G. (1999). The domain of γ Doradus variables in the Hertzsprung-Russell diagram. Monthly Notices of the Royal Astronomical Society, 309(2):L19–L23. (Cited on page 15.)

Handler, G. (2005). Asteroseismology of Delta Scuti and Gamma Doradus Stars. Journal of Astrophysics and Astronomy, 26:241. (Cited on page 6.)

Handler, G. (2013). Asteroseismology. Springer. (Cited on pages 2 and 6.)

Hareter, M. (2012). Preliminary results on Dor and Sct-Dor hybrids in the CoRoT exo-field of LRa01. Astronomische Nachrichten, 333:1048. (Cited on pages 13 and 18.)

Hearnshaw, J. B. (2009). Astronomical Spectrographs and their History. Cambridge University Press. (Cited on page 27.)

Hearnshaw, J. B., Barnes, S. I., Kershaw, G. M., Frost, N., Graham, G., Ritchie, R., and Nankivell, G. R. (2002). The HERCULES Échelle Spectrograph at Mt. John. Experimental Astronomy, 13(2):59–76. (Cited on page 27.)

Henroteau, F. (1923). A spectrographic study of stars of classes A and F. Publications of the Dominion Observatory Ottawa, 8:59–82. (Cited on pages 57 and 75.)

Henry, G. W., Fekel, F. C., and Henry, S. M. (2011). A Volume-limited Photometric Survey of 114 γ Doradus Candidates. The Astronomical Journal, 142:39. (Cited on pages 13 and 15.)

Hoffleit, D. (1964). Catalogue of bright stars, 3rd rev. ed. New Haven, Conn.: Yale University Observatory. (Cited on page 101.)

Hoffleit, D. and Warren, Jr., W. H. (1995). VizieR Online Data Catalog: Bright Star Catalogue, 5th Revised Ed. (Hoffleit+, 1991). 5050. (Cited on pages 79 and 98.)

Hogeveen, S. J. (1990). The mass-ratio distribution of visual binary stars. Astrophysics and Space Science, 173:315–342. (Cited on page 19.)

Hogeveen, S. J. (1992). The mass-ratio distribution of spectroscopic binary stars. Astrophysics and Space Science, 196(2):299–336. (Cited on page 19.)

Holmberg, J., Nordström, B., and Andersen, J. (2009). The Geneva-Copenhagen survey of the solar neighbourhood. III. Improved distances, ages, and kinematics. Astronomy and Astrophysics, 501:941–947. (Cited on page 102.)

Hubeny, I. and Lanz, T. (2011). Synspec: General Spectrum Synthesis Program. Astrophysics Source Code Library. (Cited on pages xiii and 33.)

Jones, S. H. (1928). Radial velocity determinations : including a spectroscopic determination of the constant of aberration, the orbits of 13 spectroscopic binary stars, and the radial velocities of 434 stars. Annals of the Cape Observatory, 10. (Cited on page 101.)

Kaiser, A., Weiss, W., Guenther, E., Balaguer, L., Maceroni, C., and Ribas, I. (2009). The Domain of δ Scuti Stars: First CoRoT IRa01 Results. In Stellar Pulsation: Challenges for Theory and Observation, volume 1170, page 432. (Cited on page 17.)

Kallinger, T., Reegen, P., and Weiss, W. W. (2008). A heuristic derivation of uncertainty for frequency determination in time series data. Astronomy and Astrophysics, 481(2):571–574. (Cited on page 47.)

Kamper, K. W., Legget, D., and McCarthy, Jr., D. W. (1989). Astrometric-spectroscopic binary star orbits. III - Alpha Ophiuchi and Delta Aquilae. Astronomical Journal, 98:686–691. (Cited on pages 57 and 63.)

Katz, D., Soubiran, C., Cayrel, R., Barbuy, B., Friel, E., Bienaymé, O., and Perrin, M.-N. (2011). Probing the Galactic thick disc vertical properties and interfaces. Astronomy and Astrophysics, 525:A90. (Cited on page 58.)

Kaye, A. B., Handler, G., Krisciunas, K., Poretti, E., and Zerbi, F. M. (1999). Gamma Doradus Stars: Defining a New Class of Pulsating Variables. Publications of the Astronomical Society of the Pacific, 111(7):840–844. (Cited on pages 13 and 15.)

Keen, M. A., Bedding, T. R., Murphy, S. J., Schmid, V. S., Aerts, C., Tkachenko, A., Ouazzani, R.-M., and Kurtz, D. W. (2015). KIC 10080943: a binary star with two γ Doradus/δ Scuti hybrid pulsators. Analysis of the g modes. Monthly Notices of the Royal Astronomical Society, 454:1792–1797. (Cited on page 19.)

King, J. R. and Liu, T. (1990). The Delta Scuti variable AI Canum Venaticorum - Short-period variables, spectroscopic binaries, and the Bright Star Catalogue. Publications of the Astronomical Society of the Pacific, 102:328–337. (Cited on pages 57 and 75.)

Koen, C. and Eyer, L. (2002). New periodic variables from the Hipparcos epoch photometry. Monthly Notices of the Royal Astronomical Society, 331:45–59. (Cited on pages 28, 57, and 117.)

Krisciunas, K. (1993). A new class of pulsating stars. In American Astronomical Society Meeting Abstracts, volume 25 of Bulletin of the American Astronomical Society, page 1422. (Cited on page 13.)

Kurtz, D. W. (1980). On the stability of observed frequencies in Delta Scuti stars - A reanalysis of Theta Tuc. Monthly Notices of the Royal Astronomical Society, 193:61–77. (Cited on page 77.)

Kurtz, D. W., Cunha, M. S., Saio, H., Bigot, L., Balona, L. A., Elkin, V. G., Shibahashi, H., Brandão, I. M., Uytterhoeven, K., Frandsen, S., Frimann, S., Hatzes, A., Lueftinger, T., Gruberbauer, M., Kjeldsen, H., Christensen-Dalsgaard, J., and Kawaler, S. D. (2011). The first evidence for multiple pulsation axes: a new rapidly oscillating Ap star in the Kepler field, KIC 10195926. Monthly Notices of the Royal Astronomical Society, 414:2550–2566. (Cited on pages 7 and 8.)

Kurucz, R. L. (1970). ATLAS: A Computer Program For Calculating Stellar Atmospheres. Smithsonian Astrophysical Observatory Special Report, 309. (Cited on page xi.)

Lafrasse, S., Mella, G., Bonneau, D., Duvert, G., Delfosse, X., and Chelli, A. (2010). VizieR Online Data Catalog: JMMC Stellar Diameters Catalogue - JSDC (Lafrasse+, 2010). VizieR Online Data Catalog, 2300. (Cited on pages 79 and 102.)

Lambert, D. L. and Reddy, B. E. (2004). Lithium abundances of the local thin disc stars. Monthly Notices of the Royal Astronomical Society, 349:757–767. (Cited on page 102.)

Lampens, P. and Boffin, H. M. J. (2000). δ Scuti Stars in Stellar Systems: a Review. In Delta Scuti and Related Stars, volume 210 of Astronomical Society of the Pacific Conference Series, pages 309–325. (Cited on page 17.)

Landolt, A. U. (1969). UBV Observations of Selected Double Systems, II. Publications of the Astronomical Society of the Pacific, 81:443. (Cited on page 101.)

Lee, Y.-H., Kim, S. S., Shin, J., Lee, J., and Jin, H. (2008). Incidence of High-Amplitude δ Scuti-Type Variable Stars. Publications of the Astronomical Society of Japan, 60:551–555. (Cited on page 18.)

Liakos, A., Niarchos, P., Soydugan, E., and Zasche, P. (2012). Survey for δ Sct components in eclipsing binaries and new correlations between pulsation frequency and fundamental stellar characteristics. Monthly Notices of the Royal Astronomical Society, 422:1250–1262. (Cited on page 19.)

Lund, M. N., Miesch, M. S., and Christensen-Dalsgaard, J. (2014). Differential Rotation in Main-sequence Solar-like Stars: Qualitative Inference from Asteroseismic Data. The Astrophysical Journal, 790:121. (Cited on pages 7 and 11.)

Mantegazza, L. (2000). Mode Detection from Line-Profile Variations. In Delta Scuti and Related Stars, volume N of Astronomical Society of the Pacific Conference Series. (Cited on pages 42 and 51.)

Mantegazza, L. and Poretti, E. (2005). High-degree non-radial modes in the Delta Scuti star AV Ceti. Communications in Asteroseismology, 146:33–36. (Cited on pages 8 and 76.)

Mathias, P., Gillet, D., Aerts, C., and Breitfellner, M. G. (1997). A spectroscopic study of the delta Scuti star rho Puppis. Astronomy and Astrophysics, 327:1077–1086. (Cited on page 18.)

Mathias, P., Le Contel, J.-M., Chapellier, E., Jankov, S., Sareyan, J.-P., Poretti, E., Garrido, R., Rodríguez, E., Arellano Ferro, A., Alvarez, M., Parrao, L., Peña, J., Eyer, L., Aerts, C., De Cat, P., Weiss, W. W., and Zhou, A. (2004). Multi-site, multi-technique survey of γ Doradus candidates. I. Spectroscopic results for 59 stars. Astronomy and Astrophysics, 417:189–199. (Cited on page 19.)

Maxted, P. F. L., Serenelli, A. M., Miglio, A., Marsh, T. R., Heber, U., Dhillon, V. S., Littlefair, S., Copperwheat, C., Smalley, B., Breedt, E., and Schaffenroth, V. (2013). Multi-periodic pulsations of a stripped red-giant star in an eclipsing binary system. Nature, 498:463–465. (Cited on page 19.)

McDonald, I., Zijlstra, A. A., and Boyer, M. L. (2012). Fundamental parameters and infrared excesses of Hipparcos stars. Monthly Notices of the Royal Astronomical Society, 427:343–357. (Cited on pages 79 and 102.)

McNally, D. (1965). The distribution of angular momentum among main sequence stars. The Observatory, 85:166–169. (Cited on pages 70, 112, and 113.)

Miesch, M. S. (2005). Large-Scale Dynamics of the Convection Zone and Tachocline. Living Reviews in Solar Physics, 2:1–137. (Cited on page 11.)

Montalbán, J. and Dupret, M.-A. (2007). Effect of convective outer layers modeling on non-adiabatic seismic observables of δ Scuti stars. Astronomy and Astrophysics, 470:991–1002. (Cited on page 18.)

Montgomery, M. H. and Odonoghue, D. (1999). A derivation of errors for least squares fitting to time series data. Delta Scuti Star Newsletter, 13:28. (Cited on page 44.)

Muñoz, B. J., Asensio, B. A., and Allende, P. C. (2013). A PCA approach to stellar effective temperatures. Astronomy and Astrophysics, 553:A95. (Cited on page 58.)

Oke, J. B. and Gunn, J. E. (1983). Secondary standard stars for absolute spectrophotometry. The Astrophysical Journal, 266:713–717. (Cited on page 9.)

Önehag, A. (2008). The calibration of Strömgren uvby Hβ photometry for late-type stars: a model atmosphere approach. Physica Scripta Volume T, 133(1):014021. (Cited on page 58.)

Osvalds, V. (1958). The astrometric orbit of delta Aquilae. Astronomical Journal, 63:222–228. (Cited on page 57.)

Paparó, M. and Sterken, C. (2000). The delta Scuti star theta Tucanae. III. Observational guidelines for mode identification. Astronomy and Astrophysics, 362:245–254. (Cited on page 78.)

Paparo, M., Sterken, C., Spoon, H. W. W., and Birch, P. V. (1996). Complex behaviour of the δ Scuti star θ Tucanae. I. Frequencies in the light variation. Astronomy and Astrophysics, 315:400–410. (Cited on pages viii, 77, 78, 97, 98, and 118.)

Pasinetti-Fracassini, L. E., Pastori, L., Covino, S., and Pozzi, A. (2001). Catalogue of Apparent Diameters and Absolute Radii of Stars (CADARS) - Third edition - Comments and statistics. Astronomy and Astrophysics, 367:521–524. (Cited on page 58.)

Paunzen, E. (2015). A new catalogue of Strömgren-Crawford uvbyβ photometry. Astronomy and Astrophysics, 580:A23. (Cited on pages 57, 77, and 101.)

Perryman, M. A. C., Lindegren, L., Kovalevsky, J., Hoeg, E., Bastian, U., Bernacca, P. L., Crézé, M., Donati, F., Grenon, M., Grewing, M., van Leeuwen, F., van der Marel, H., Mignard, F., Murray, C. A., Le Poole, R. S., Schrijver, H., Turon, C., Arenou, F., Froeschlé, M., and Petersen, C. S. (1997). The HIPPARCOS Catalogue. Astronomy and Astrophysics, 323:L49–L52. (Cited on page 13.)

Pesnell, W. D. (1987). A new driving mechanism for stellar pulsations. The Astrophysical Journal, 314:598–604. (Cited on page 15.)

Petersen, J. O. (1973). Masses of double mode cepheid variables determined by analysis of period ratios. Astronomy and Astrophysics, 27:89–93. (Cited on page 5.)

Pigulski, A., Kołaczkowski, Z., Ramza, T., and Narwid, A. (2006). High-amplitude delta Scuti stars in the Galactic Bulge from the OGLE-II and MACHO data . Memorie della Societá Astronomica Italiana, 77:223. (Cited on page 5.)

Pollard, K. R. (2009). A Review of γ Doradus Variables. In Stellar pulsation: challenges for theory and observation, volume 1170 of American Institute of Physics Conference Proceedings, pages 455–466. (Cited on page 13.)

Pollard, K. R., Brunsden, E., Cottrell, P. L., Davie, M., Greenwood, A., Wright, D. J., and De Cat, P. (2014). Mode identification from spectroscopy of gravity-mode pulsators. In Precision Asteroseismology, volume 301 of Proceedings of the IAU Symposium, pages 477–478. (Cited on page 28.)

Poretti, E. (2003). Asteroseismology of HADS stars: V974 Oph, a radial pulsator flavoured by nonradial components. Astronomy and Astrophysics, 409:1031–1035. (Cited on page 18.)

Ramm, D. J. (2004). A Spectroscopic Study of Detached Binary Systems Using Precise Radial Velocities. Unpublished doctoral dissertation, University of Canterbury, Christchurch, New Zealand. (Cited on pages 23 and 32.)

Reegen, P. (2007). SigSpec. I. Frequency- and phase-resolved significance in Fourier space. Astronomy and Astrophysics, 467:1353–1371. (Cited on pages xiii and 42.)

Reegen, P. (2011). SigSpec User's Manual. Communications in Asteroseismology, 163(3). (Cited on pages xiii and 42.)

Reese, D., Lignières, F., and Rieutord, M. (2006). Acoustic oscillations of rapidly rotating polytropic stars. II. Effects of the Coriolis and centrifugal accelerations. Astronomy and Astrophysics, pages 621–637. (Cited on pages 9 and 11.)

Rodrigo, B. C., Suárez, J. C., Solano, E., and Rodón, J. R. (2015). TOUCAN: A VO tool for asteroseismology. Scientific preparation and exploitation of the PLATO mission. In Highlights of Spanish Astrophysics VIII, pages 834–839. (Cited on page 12.)

Rodríguez, E. and Breger, M. (2001). delta Scuti and related stars: Analysis of the R00 Catalogue. Astronomy and Astrophysics, 366:178–196. (Cited on page 17.)

Rodríguez, E., López-González, M. J., and López de Coca, P. (2000). A revised catalogue of delta Sct stars. Astronomy and Astrophysics Supplement Series, 144:469–474. (Cited on page 17.)

Rowe, J. F., Matthews, J. M., Cameron, C., Bohlender, D. A., King, H., Kuschnig, R., Guenther, D. B., Moffat, A. F. J., Rucinski, S. M., Sasselov, D., Walker, G. A. H., and Weiss, W. W. (2006). Discovery of hybrid γ Dor and δ Sct pulsations in BD+18 4914 through MOST spacebased photometry. Communications in Asteroseismology, 148:34–43. (Cited on pages 13, 15, and 18.)

Saio, H. (2013). Prospects for Asteroseismology of Rapidly Rotating B-Type Stars. In Lecture Notes in Physics, volume 865 of Studying Stellar Rotation and Convection, pages 159–177. (Cited on page 11.)

Samus, N. N., Durlevich, O. V., and et al. (2009). VizieR Online Data Catalog: General Catalogue of Variable Stars (Samus+ 2007-2013). VizieR Online Data Catalog, 1. (Cited on page 101.)

Sbordone, L., Bonafacio, P., Castelli, F., and Kurucz, R. L. (2004). ATLAS and SYNTHE under Linux. Memorie della Societá Astronomica Italiana Supplement, 5(93). (Cited on page xi.)

Schmid, V. S., Themeßl, N., Breger, M., Degroote, P., Aerts, C., Beck, P. G., Tkachenko, A., Van Reeth, T., Bloemen, S., Debosscher, J., Castanheira, B. G., McArthur, B. E., Pápics, P. I., Fritz, V., and Falcon, R. E. (2014). Discovery of binarity, spectroscopic frequency analysis, and mode identification of the δ Scuti star 4 CVn. Astronomy and Astrophysics, 570:A33. (Cited on page 19.)

Schrijvers, C. and Telting, J. H. (2002). Identification of non-radial pulsation modes in the close-binary beta Cephei star nu Centauri. Astronomy and Astrophysics, 394:603–615. (Cited on page 19.)

Schrijvers, C., Telting, J. H., Aerts, C., Ruymaekers, E., and Henrichs, H. F. (1997). Line-profile variations due to adiabatic non-radial pulsations in rotating stars. I. Observable characteristics of spheroidal modes. Astronomy and Astrophysics Supplement Series, 121. (Cited on pages 53 and 112.)

Schröder, C., Reiners, A., and Schmitt, J. H. M. M. (2009). Ca II HK emission in rapidly rotating stars. Evidence for an onset of the solar-type dynamo. Astronomy and Astrophysics, 493:1099–1107. (Cited on page 58.)

Schulz, N. S. (2012). The Formation and Early Evolution of Stars: From Dust to Stars and Planets. Springer. (Cited on page 54.)

Shrijvers, C., Telting, J. H., Aerts, C., Ruymaekers, E., and Henrichs, H. F. (1997). Line-profile variations due to adiabatic non-radial pulsations in rotating stars. I. Observable characteristics of spheroidal modes. Astronomy and Astrophysics Supplement Series, 121:343–368. (Cited on page 56.)

Sipahi, E. and Dal, H. A. (2014). A γ Doradus candidate in eclipsing binary BD And? New Astronomy, 26:62–71. (Cited on page 19.)

Skuljian, J. (2004). HRSP - A Dedicated Échelle Reduction Software Package for HERCULES. IAU Colloqium 193, 310:575. (Cited on pages xii and 33.)

Sódor, Á., Chené, A.-N., De Cat, P., Bognár, Z., Wright, D. J., Marois, C., Walker, G. A. H., Matthews, J. M., Kallinger, T., Rowe, J. F., Kuschnig, R., Guenther, D. B., Moffat, A. F. J., Rucinski, S. M., Sasselov, D., and Weiss, W. W. (2014). MOST light-curve analysis of the γ Doradus pulsator HR 8799, showing resonances and amplitude variations. Astronomy and Astrophysics, 568:A106. (Cited on pages 13 and 15.)

Starrfield, S. G., Cox, A. N., Hodson, S. W., and Pesnell, W. D. (1983). The discovery of nonradial instability strips for hot, evolved stars. The Astrophysical Journal, Part 2 - Letters to the Editor, 268:L27–L32. (Cited on page 3.)

Sterken, C. (1997). The δ Scuti star θ Tucanae. II. UVBY colour variations and pulsational/orbital properties. Astronomy and Astrophysics, 325:563–568. (Cited on pages 77, 78, 98, and 118.)

Sterken, C., De Mey, K., and Gray, R. O. (1997). On the spectrum of Theta Tucanae. Journal of Astronomical Data, 3. (Cited on pages 78, 79, 97, 98, and 118.)

Stobie, R. S. and Shobbrook, R. R. (1976). Frequency analysis of the Delta Scuti star, Theta Tucanae. Monthly Notices of the Royal Astronomical Society, 174:401–409. (Cited on page 77.)

Suárez, J. C., García Hernández, A., Moya, A., Rodrigo, C., Solano, E., Garrido, R., and Rodón, J. R. (2014). Measuring mean densities of δ Scuti stars with asteroseismology. Theoretical properties of large separations using TOUCAN. Astronomy and Astrophysics, 563:A7. (Cited on page 12.)

Suchkov, A. A. and Makarov, V. V. (2002). ROSAT View of Hipparcos F Stars. In American Astronomical Society Meeting Abstracts, volume 34 of Bulletin of the American Astronomical Society, page 1112. (Cited on page 102.)

Templeton, M. R., Bradley, P. A., and Guzik, J. A. (2000). Asteroseismology of the Multiply Periodic δ Scuti Star θ Tucanae. The Astrophysical Journal, 528:979–988. (Cited on pages 78, 79, 97, 98, and 118.)

Townsend, R. H. D. (1997). Spectroscopic modelling of non-radial pulsation in rotating early-type stars. Monthly Notices of the Royal Astronomical Society, 284:839–858. (Cited on page 12.)

Townsend, R. H. D. (2003a). Asymptotic expressions for the angular dependence of low-frequency pulsation modes in rotating stars. Monthly Notices of the Royal Astronomical Society, 340:1020–1030. (Cited on page 12.)

Townsend, R. H. D. (2003b). A semi-analytical formula for light variations due to low-frequency g modes in rotating stars. Monthly Notices of the Royal Astronomical Society, 343(1):125–136. (Cited on pages 9 and 12.)

Ulusoy, C., Stateva, I., Iliev, I. K., and Ulaş, B. (2014). Frequency and spectrum analysis of γ Doradus type Kepler target KIC 6462033. New Astronomy, 30:28–31. (Cited on page 15.)

Uytterhoeven, K., Moya, A., Grigahcène, A., Guzik, J. A., Gutiérrez-Soto, J., Smalley, B., Handler, G., Balona, L. A., Niemczura, E., Fox Machado, L., Benatti, S., Chapellier, E., Tkachenko, A., Szabó, R., Suárez, J. C., Ripepi, V., Pascual, J., Mathias, P., Martín-Ruíz, S., Lehmann, H., Jackiewicz, J., Hekker, S., Gruberbauer, M., García, R. A., Dumusque, X., Díaz-Fraile, D., Bradley, P., Antoci, V., Roth, M., Leroy, B., Murphy, S. J., De Cat, P., Cuypers, J., Kjeldsen, H., Christensen-Dalsgaard, J., Breger, M., Pigulski, A., Kiss, L. L., Still, M., Thompson, S. E., and van Cleve, J. (2011). The Kepler characterization of the variability among A- and F-type stars. I. General overview. Astronomy and Astrophysics, 534:A125. (Cited on page 13.)

van Leeuwen, F. (2007). Validation of the new Hipparcos reduction. Astronomy and Astrophysics, 474(2):653–664. (Cited on pages 57, 77, and 101.)

Waelkens, C., Aerts, C., Kestens, E., Grenon, M., and Eyer, L. (1998). Study of an unbiased sample of B stars observed with Hipparcos: the discovery of a large amount of new slowly pulsating B stars. Astronomy and Astrophysics, 330:215–221. (Cited on page 13.)

Warner, P. B., Kaye, A. B., and Guzik, J. A. (2003). A Theoretical γ Doradus Instability Strip. The Astrophysical Journal, 593(2):1049–1055. (Cited on page 16.)

Wells, D. C., Greisen, E. W., and Harten, R. H. (1981). FITS - a Flexible Image Transport System. Astronomy and Astrophysics Supplement Series, 44:363. (Cited on page xi.)

White, T. R., Bedding, T. R., Gruberbauer, M., Benomar, O., Stello, D., Appourchaux, T., Chaplin, W. J., Christensen-Dalsgaard, J., Elsworth, Y. P., García, R. A., Hekker, S., Huber, D., Kjeldsen, H., Mosser, B., Kinemuchi, K., Mullally, F., and Still, M. (2012). Solving the Mode Identification Problem in Asteroseismology of F Stars Observed with Kepler. The Astrophysical Journal Letters, 751:L36. (Cited on page 8.)

Wright, C. O., Egan, M. P., Kraemer, K. E., and Price, S. D. (2003). The Tycho-2 Spectral Type Catalog. The Astronomical Journal, 125:359–363. (Cited on page 79.)

Wright, D. J. (2008). Spectroscopic Mode Identification in a Sample of Non-radially Pulsating Stars. Unpublished doctoral dissertation, University of Canterbury, Christchurch, New Zealand. (Cited on pages 30, 36, and 51.)

Wright, D. J., Chené, A.-N., De Cat, P., Maraois, C., Mathais, P., Macintosh, B., Isaacs, J., Lehmann, H., and Hartmann, M. (2011). Determination of the Inclination of the Multiplanet Hosting Star HR 8799 Using Asteroseismology. The Astrophysical Journal Letters, 728(1). (Cited on page 99.)

Zacharias, N., Finch, C. T., Girard, T. M., Henden, A., Bartlett, J. L., Monet, D. G., and Zacharias, M. I. (2013). The Fourth US Naval Observatory CCD Astrograph Catalog (UCAC4). The Astronomical Journal, 145:44. (Cited on page 101.)

Zboril, M. (1996). Versions of CCP7 SYNSPEC Code. In M.A.S.S: Model Atmospheres and Spectrum Synthesis, volume 108 of Astronomical Society of the Pacific Conference Series, pages 193–197. (Cited on pages xiii and 33.)

Zhou, A.-Y. (2014). Pulsating Components in Binary and Multiple Stellar Systems — A Catalog of Oscillating Binaries. Astronomy and Astrophysics, 14(6). (Cited on page 19.)

Zima, W. (2006). A new method for the spectroscopic identification of stellar non-radial pulsation modes. I. The method and numerical tests. Astronomy and Astrophysics, 455(1):227–234. (Cited on pages 2, 42, 51, and 53.)

Zima, W. (2008a). FAMIAS - A userfriendly new software tool for the mode identification of photometric and spectroscopic time series. Communications in Asteroseismology, 157:387. (Cited on pages xi, 41, and 53.)

Zima, W. (2008b). FAMIAS User Manual. Communications in Asteroseismology, 155:17–121. (Cited on pages xi, 7, 8, 41, 49, 51, 52, 53, and 56.)

Zorec, J. and Royer, F. (2012). Rotational velocities of A-type stars. IV. Evolution of rotational velocities. Astronomy and Astrophysics, 537:A120. (Cited on page 58.)

Zwintz, K., Fossati, L., Guenther, D. B., Ryabchikova, T., Baglin, A., Themessl, N., Barnes, T. G., Matthews, J. M., Auvergne, M., Bohlender, D., Chaintreuil, S., Kuschnig, R., Moffat, A. F. J., Rowe, J. F., Rucinski, S. M., Sasselov, D., and Weiss, W. W. (2013). Regular frequency patterns in the young δ Scuti star HD 261711 observed by the CoRoT and MOST satellites. Astronomy and Astrophysics, 552:A68. (Cited on page 17.)